Ventricular Septation in a Mouse Model of Down Syndrome

Htun, Mint

Awarding institution:
King's College London

Ventricular Septation in a Mouse Model of Down Syndrome

Mint Ravinand Htun

King's College London

and

The Francis Crick Institute

PhD Supervisors:

Prof. Jeremy B.A. Green & Prof. Victor L.J. Tybulewicz

A thesis submitted to King's College London for the degree of

Doctor of Philosophy

December 2023

Declaration

I, Mint Ravinand Htun, confirm that the work presented in this thesis is my own. Where information has been derived from other sources, I confirm that this has been indicated in the thesis.

Abstract

Down syndrome (DS) arises from trisomy of human chromosome 21 (Hsa21) and is the most common cause of congenital heart defects (CHD). Approximately half of all DS births present with a form of CHD, a significant contributor to infant mortality in the condition. These defects result from aberrant heart septation during development. However, the developmental origins of CHD in DS remain poorly understood. The Dp1Tyb mouse model of DS, containing a duplication of a region of mouse chromosome 16 orthologous to a large stretch of Hsa21, recapitulates many CHD seen in human DS. This project aimed to characterise the cardiac development of Dp1Tyb embryos by identifying morphological and cellular behaviours driving the CHD phenotype.

Key stages of chamber septation between E10.5 to E13.5 were 3D reconstructed from images in Dp1Tyb hearts to form a developmental timeline. This analysis revealed no significant differences in muscular septum growth nor the closure of the interventricular communication of the Dp1Tyb embryos. Investigation into the endocardial cushions, transient structures crucial to heart septation and valve formation, revealed dysmorphic outflow tract cushions (OFTC). Underlying this phenotype, the Dp1Tyb OFTC were comprehensively quantified through cellular packing, apoptosis and proliferation through serial sections. Dp1Tyb OFTC were found to have reduced cellular packing through its structure at both stages and a decrease in proliferating cells in the proximal region. The Dp1Tyb OFTC mesenchyme occupied larger section areas at its proximal anatomy while retaining its low cell density phenotype, suggesting more extracellular matrix in this region.

To determine if excess extracellular matrix impacted the material stiffness of the OFTCs, Atomic Force Microscopy was deployed to test the structure's stiffness, which may be the first example of the technique on fresh OFTC tissue. Due to the preliminary nature of the experiment and results, there were no conclusive findings. Exploration of mechanosensitive-YAP nuclear expression, showed a reduction in nuclear translocation in distal regions of the Dp1Tyb OFTC, suggesting altered mechanosensitive pathways.

Overall, the work presented in this thesis begins to unravel the cellular behaviours underpinning OFTC development, its contribution to ventricular septation and how this is altered in the Dp1Tyb. The data identifies these structures as

probable contributors to the formation of CHD in the DS mouse model Dp1Tyb. The thesis further covers and discusses possible dysregulated pathways and causative genes from Hsa21 that contribute to the DS phenotypes, in addition to avenues for future experimentation.

Acknowledgement

Through this PhD and the writing of this thesis, I have had the support of the most amazing people, without them, I'm not sure I would have been able to do any of this.

Firstly, I extend my gratitude to my two supervisors Prof. Jeremy Green and Prof. Victor Tybulewicz for the opportunity to pursue this PhD in their labs and for their support and guidance. Jeremy, thank you for the memorable discussions we had on Tuesday afternoons about all scientific possibilities and for challenging me to think outside of the box with this project. Victor, I am thankful for your mentorship throughout this process, I will cherish all the memories from lab retreats and cocktail weeks we shared as a lab.

I'd like to thank past and present members of both labs, especially Rifdat and Eva who were always there to listen and give advice. Callan, Rebecca, Micaela, Leon, Yushi, Victor Y, Harvey – thank you so much for your friendship and all the lunches (at exactly 12.00!) that we shared. Jack, I am lucky to call you a friend – thank you for supporting me in the final stages of the PhD, it's been a journey to say the least but we both made it through!

A special thanks to all the people at the Crick that have made this work possible. The BRF for looking after my mice, Fabrice for his HREM guidance, and Experimental Histopathology for putting up with my hundreds and hundreds of slides. Olivia, thank you for all your help on the AFM.

To my friends at the Crick, in particular, Theresa, Toby, Alice and Haixi, thank you for keeping me sane and having endless amounts of tea with me.

Louis, I don't have the words to express how grateful I am for you. You have been my rock throughout this PhD and my biggest supporter. You believed in me in the many times I did not.

To Otto, you'll never understand this because you're a dog but thank you for being by my side even at the hardest of times.

I'd also like to thank Gillian and Jeremy for supporting me and making sure I was properly fed, especially in the last few months of this PhD.

A special mention to my friends Rheanna, Mara and Hawo – thank you for always listening to my ramblings, even if they didn't make sense. I promise to stop talking about embryonic hearts from now on.

Thank you to my family, your love, support and sometimes blind faith in me kept me going. To my parents, Aung and Noy, I wouldn't be here without you and your encouragement. To my brother, Nicky, thank you for always being there for me – this was truly the hardest climb (at least a V12)!

Finally, I want to express my gratitude to everyone I've mentioned here again for everything they've done for me. I've made it through because of them.

Table of Contents

Table of figures

List of tables

Abbreviations

§§	Subsection
AA	Aortic arch
AFM	Atomic force microscopy
AVC	Atrioventricular cushions
AVSD	Atrioventricular septal defects
BMP	Bone morphogenetic protein
CHD	Congenital heart defect
CNCC	Cardiac neural crest cells
DMP	Dorsal mesenchymal protrusion
DORV	Double outlet right ventricle
DS	Down Syndrome
DSCR	Down Syndrome Critical Region
E	Embryonic day
ECM	Extracellular matrix
EndoMT	Endothelial-to-mesenchymal transition
FHF	First heart field
H&E	Haematoxylin and esoin
HA	Hyaluronic acid
HH	Hedgehog
HREM	High resolution episcopic microscopy
Hsa21	Human chromosome 21
IVC	Interventricular communication
kPCA	Kernel principal component analysis
MFI	Mean fluorescence intensity
Mmu	Mouse chromosome
mVS	Muscular ventricular septum
OA	Overriding aorta
OFT	Outflow tract
OFTC	Outflow tract cushion
PA	Pharyngeal arch
PDA	Patent ductus arteriosus
PFA	Paraformaldehyde
PHH3	Phospohistone H3
PROMASS	Proliferation, rearrangement, orientation of division, matrix, addition/apoptosis, sise and shape
PTA	Persistent truncus arteriosus
ROI	Region of interest
scRNA-seq	Single-cell RNA sequencing
SHF	Second heart field
SHG	Second harmonic generation

Shh	Sonic hedgehog
TdT	Terminal deoxynucleotidyl transferase
TGA	Transposition of the great arteries
ToF	Tetralogy of Fallot
TUNEL	Terminal deoxynucleotidyl transferase dUTP nick end labelling
VMTK	Vascular modelling toolkit
VSD	Ventricular septal defect
YAP	Yes-associated protein

Chapter 1. Introduction

1.1 Trisomy 21/Down Syndrome

Down syndrome (DS) was first described by the physician Langdon Down in 1862, who published a wider report describing the clinical presentations of the disorder in 1866 (Zaman and Fortea, 2022). DS is a genetic disorder caused by an extra copy of human chromosome 21 (Hsa21), also known as Trisomy 21. The chromosomal aberrations underlying DS were identified by geneticist Jérôme Lejeune and paediatric cardiologist Marthe Gauthier in 1959 (Lejeune *et al.*, 1959).

1.1.1 Epidemiology and risk

DS is the most common form of aneuploidy in humans with an occurrence of approximately 1 in 700 births worldwide (Antonarakis, 2017). The number of individuals with DS has risen in recent decades due to the survival of babies and children with DS, alongside life expectancy increasing to 60-65 years (Bittles and Glasson, 2004). The most common cause leading to trisomy is chromosomal nondisjunction during cell division, where there is a failure of the chromosome pair separating, from either the egg or the sperm, to separate during meiosis (Oliver *et al.*, 2008). Thus, all subsequent cells have three copies of the chromosome as development progresses. In some rare cases, mosaic DS can occur where patients are found to have both euploid cells and cells with three copies of Hsa21. The vast majority of chromosomal nondisjunction in Trisomy 21 occurs from the maternal meiotic process (93%), followed by paternal spermatogenesis (5%) and then from mitosis (2%) (Vraneković *et al.*, 2012). The only risk factor that has been linked to DS is parental age, specifically advanced maternal age (>35 years of age) (Nagaoka, Hassold and Hunt, 2012), where the probability of having a child with DS increases from ~1 in 500 when below the age of 35 to ~1 in 50 after (Loane *et al.*, 2013).

1.1.2 Phenotypes

Individuals with DS nearly always present with a spectrum of physical, neurological and intellectual phenotypes affecting multiple systems, all of which vary in severity and penetrance. DS is the most common cause of intellectual disability, which can range from mild to moderate, presenting as a developmental delay with adults typically reaching a mental ability equivalent to 8–9-year-olds (Malt *et al.*, 2013). This cognitive impairment is characterised by deficits in episodic memory, verbal short-term memory, and irregular speech patterning. As DS individuals age, they become prone to developing early-onset Alzheimer's disease, with 15% of those above the age of 40 diagnosed and increasing to 50-70% by the age of 60 (Head *et al.*, 2012). Both children and adults with DS have an increased risk of epileptic seizures, which occur in 5-10% of children but in 50% of adults over 50 with DS (McVicker *et al.*, 1994; Altuna *et al.*, 2021).

As with neurological and intellectual disability, the physical phenotypes also range in severity and penetrance except for impaired motor coordination, hypotonia, and craniofacial dysmorphology which are all found at nearly 100% penetrance in individuals with DS (Hernandez and Fisher, 1996). Approximately half of people with DS have visual and auditory impairments. Vision problems include strabismus, where the eyes do not move in synchronisation, cataracts, and glaucoma (Weijerman and de Winter, 2010). Hearing defects are very common in people with trisomy 21, with approximately 85% of the group reported to have hearing loss in at least one ear (Kreicher *et al.*, 2018). Hearing problems in DS are associated with otitis media with effusion, an accumulation of fluid in the middle ear that can lead to chronic ear infections and contribute to hearing loss (Sait *et al.*, 2022). Up to 50% of babies with DS are born with a congenital heart defect (CHD), compared to 1-2% of the general population. Those diagnosed with CHD at birth often require surgical intervention in early childhood as it is a major contributor to infant mortality (Stoll *et al.*, 2015).

Less penetrant phenotypes include impairment of the endocrine system with thyroid dysfunction (Amr, 2018) and gastrointestinal anomalies ranging from celiac disease to Hirschsprung disease (Holmes, 2014). Children with DS are at a significantly increased risk of developing specific types of blood cancer compared to the general population; the risk of developing acute lymphoblastic leukaemia is increased by 20-fold (Verma *et al.*, 2023) and the risk of acute myeloid leukaemia is

increased by 400-fold in children with DS under the age of 5 (Marlow *et al.*, 2021). Interestingly, individuals with DS have an overall decreased risk of developing solid cancers, which is thought to be due to tumour suppressor genes on Hsa21 having increased expression in trisomy (Nixon, 2018).

1.1.3 Genetics of Down Syndrome

The described DS phenotypes arise from an additional copy of Hsa21, either in the form of whole trisomy with the whole chromosome or as partial trisomy, wherein only specific segments of chromosome are in triplicate. The presence of extra genetic material from the third copy of Hsa21 results in the overexpression of the ~230 protein-coding genes found on the chromosome. It is thought that the presence of the third copy of one or a combination of these genes gives rise to the DS phenotypes described rather than too much chromosomal material (Yahya-Graison *et al.*, 2007). These genes are termed “dosage-sensitive genes”. The identification of specific dosage-sensitive genes would uncover the mechanisms driving the observed DS phenotypes. This understanding would not only shed light on the molecular mechanisms underlying the phenotypes but also pave the way for the identification of pathways for which targeted therapeutics can be developed to better manage DS.

The search for the dosage-sensitive genes on Hsa21 has been approached with both human and mouse genetics. The rare existence of partial trisomy 21 has helped to identify regions of Hsa21 that are seemingly responsible for specific phenotypes. The first region found to be important in the development of some phenotypes was mapped to the telomeric region of the chromosome, this region was subsequently named the “Down Syndrome Critical Region” (DSCR) (McCormick *et al.*, 1989; Delabar *et al.*, 1993). The DSCR hypothesis initially put forward that at least one gene in the region was dosage-sensitive and therefore responsible for some of the phenotypes. However, advances in both human and mouse genetics have moved away from the single DSCR hypothesis (Olson *et al.*, 2004), instead providing evidence that multiple loci (with some outside the DSCR) from Hsa21 are causative of the different phenotypes (Barlow *et al.*, 2001; Korbel *et al.*, 2009; Lyle *et al.*, 2009). Systematic mapping of the regions orthologous to Hsa21 in transgenic mice developed by the Tybulewicz lab (Lana-Elola *et al.*, 2016) has recently identified

that three copies of the gene *Dyrk1a* are sufficient to cause the CHD phenotype (Lana-Elola *et al.*, 2023) as well as the craniofacial dysmorphology (Redhead *et al.*, 2023). Yet, the mapping panel also suggests that with both phenotypes there are more dosage-sensitive genes to be found.

1.1.4 Down Syndrome mouse models

The collection of phenotypes associated with DS prompted a need for animal models to further understand the aetiology of these pathologies, as there are limited options for exploring the mechanism in humans. While partial trisomies were crucial to understanding the genetics of DS, the regions of Hsa21 in partial trisomies varied in size and location of the chromosome as well as the natural genetic variation that exists from individual to individual. Thus, a more genetically controlled and robust animal model was required to study DS. Consequently, mice are the most common model organism for this purpose with many mouse models of DS available.

Hsa21 has syntenic regions on 3 different mouse chromosomes (Mmu) – Mmu10, Mmu16 and Mmu17, with the largest stretch of synteny on Mmu16 (Gupta *et al.*, 2016). Mapping of Hsa21 to mouse chromosomes has allowed for DS models to be developed by duplicating these regions. The first mouse model of DS was the Ts65Dn mouse which was generated from a chance translocation event from γ-irradiation (Davisson *et al.*, 1990). This was followed by the Ts1Cje (Sago *et al.*, 1998) mouse a few years later. Both mouse models contain duplications of regions of Mmu16 orthologous to Hsa21 and have been extensively used in studies to show recapitulation of some DS phenotypes, allowing for the first identifications of dosage-sensitive genes. However, both models – which are still in use – include regions of aneuploidy from other chromosomes, Ts65Dn was found to also be trisomic for 60 genes on Mmu17 that do not map to Hsa21 and the Ts1Cje has 7 genes in monosomy from Mmu12 (Duchon *et al.*, 2011). The additional aneuploidies have made the interpretations of any results from these models difficult to conclusively pin on the Hsa21 syntenic genes. A later mouse model, the Tc1 strain, featured a freely segregating Hsa21 which also demonstrated some DS phenotypes including CHDs (O'Doherty *et al.*, 2005), but this strain was later discovered to be mosaic for Hsa21 as the chromosome was not intact (Gribble *et al.*, 2013).

Advances in chromosomal engineering have ushered in a new generation of DS models created using Cre/LoxP methods which allowed much more precise duplications of regions from the mouse genome. Mouse models made from this method do not have freely segregating chromosomes as the regions are duplicated onto the telomeric region of a chromosome and thus are not true trisomies. This means that any phenotypes observed from these models are the result of increased gene dosage of the syntenic genes, rather than as a consequence of too much chromosomal material from a freely segregating chromosome that could disrupt cellular function.

The first mouse models created using the Cre/LoxP system to separately map Hsa21 syntenic regions from Mmu10, Mmu16 and Mmu17 were the Dp(10)1Yey/+, Dp(16)1Yey/+, and Dp(17)1Yey/+ respectively (Li *et al.*, 2007). These were followed by the Dp1Tyb mice which were produced in the same fashion and identical to the Dp(16)1Yey with duplication of Mmu16. Dp1Tyb was subsequently followed up with the engineering of strains with partial trisomies for successively smaller regions of Mmu16 to generate the most comprehensive mapping panel of the region to date (Figure 1.1). The Dp1Tyb mouse strain shows similar cardiac defects as seen in human DS when harvested at embryonic day (E) 14.5 as well as craniofacial dysmorphology in the adult mouse (Lana-Elola *et al.*, 2016; Toussaint *et al.*, 2019). The genetic mapping panel has allowed for more precise identification of dosage-sensitive regions responsible for the craniofacial and heart phenotypes observed and to confirm the involvement of *Dyrk1a* in both. The heart phenotypes will be discussed in detail in subsection (§§) 1.4.2 below.

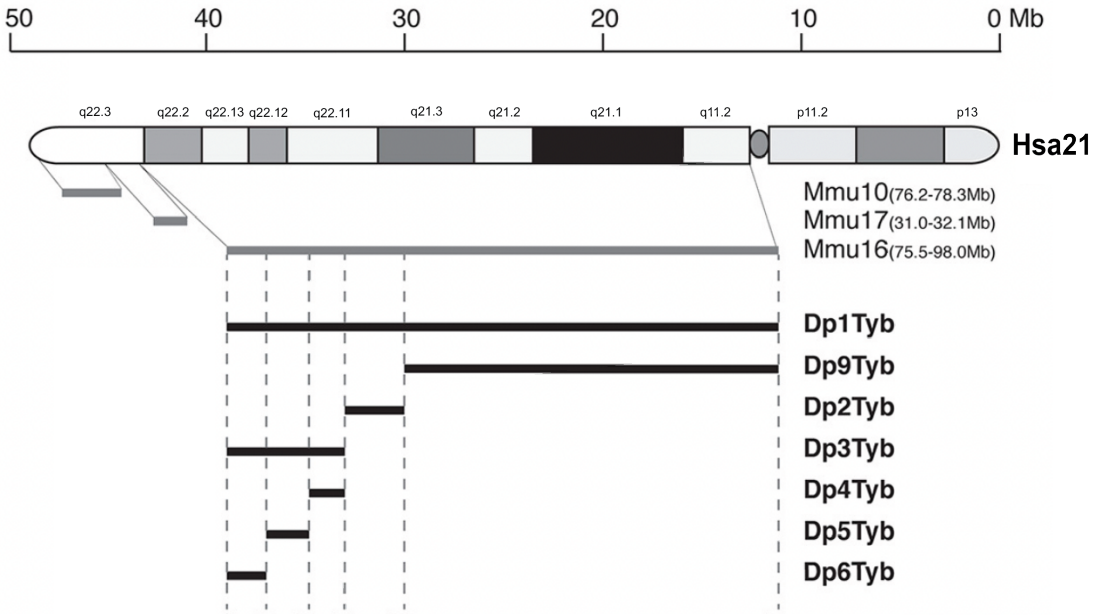

Figure 1.1 Genetic mapping panel of Dp1Tyb, a mouse model for Down Syndrome, and subsequent models. A genetic mapping panel showing the 7 mouse strains modelling Down Syndrome, with a representation of Hsa21 and conserved regions of synteny on Mmu10, Mmu17 and Mmu16. The 7 mouse strains with partial trisomies are shown here aligned to their orthologous regions in Hsa21. Adapted from Lana-Elola *et al.*, 2016.

Mouse model	Number of Hsa21 orthologous genes
Dp1Tyb	145
Dp9Tyb	76
Dp2Tyb	33
Dp3Tyb	39
Dp4Tyb	13
Dp5Tyb	12
Dp6Tyb	14

Table 1.1 Mouse models of Down Syndrome and number of duplicated Hsa21-orthologous genes. Mouse models Dp1Tyb, Dp9Tyb, Dp2Tyb, Dp3Tyb, Dp4Tyb, Dp5Tyb and Dp6Tyb along with the number of duplicated genes orthologous to Hsa21. The genes in these mouse models are duplicated from Mmu16.

1.1.5 Congenital heart defects in Down Syndrome

As stated above, an estimated 50% of babies with DS are born with a CHD. The most common types of CHD in trisomy 21 are atrioventricular septal defects (AVSD) which make up ~40% of all heart defects, followed by ventricular septal defects (VSD) at ~30% (Benhaourech *et al.*, 2016; Bergström *et al.*, 2016). Defects in the development of the aorta and the pulmonary artery are also seen in DS. These are known as outflow tract defects and are usually concomitant with AVSDs and VSDs (Dimopoulos *et al.*, 2023). The developmental origins of all these heart defects remain unclear, particularly regarding when a morphological or cellular phenotype emerges. This is especially true in trisomy 21, where limited literature exists on the developmental aspects.

1.2 Heart development

The mammalian heart is the first functional organ to develop and is a complex organogenesis that requires a multitude of cell lineages and cellular processes. The heart is responsible for the circulation of oxygenated blood throughout the body and for transporting deoxygenated blood to the lungs for gas exchange. Failure of proper heart development can impair its functionality and lead to adverse consequences on overall health. Cardiogenesis begins as a cardiac crescent which morphs into the primitive heart tube, undergoing heart looping and septation to form the four-chambered heart. In this section, I will describe the morphology of the developing heart and its key structures and stages in detail, starting with the cardiac crescent and ending with the process of chamber septation.

1.2.1 The cardiac crescent

The heart originates from the primitive streak, a region of the epiblast in early embryogenesis. The primitive streak is an elongated blastoporal slit through which some epiblast cells ingress to make the mesoderm and endoderm, the epiblast cells that do not ingress become the ectoderm. Some ingressed nascent mesodermal cells move laterally initially but then migrate to the anterior of the embryo as two

bilateral sheets that meet at the midline to form a horse-shoe shape, which is termed the cardiac crescent (Ivanovitch *et al.*, 2017). At this point in cardiogenesis, the cells in the cardiac crescent take on two distinct cardiac progenitor populations, defined by their positioning and molecular markers. These two groups are the first heart field (FHF) and the second heart field (SHF) (Figure 1.2) (Tyser, 2023).

The FHF cells were initially difficult to characterise due to their quickly differentiating to form immature cardiomyocytes as the cardiac crescent is forming, but the advent of RNA-sequencing technology has allowed the FHF cells to be defined by expression of specific markers. Because the FHF cells differentiate quickly and progressively, the balance of the various markers (such as TBX5 and HAND1) used to identify them changes with the stage of development (Kelly *et al.*, 2014). The cells are quickly recruited to the heart tube simultaneous to the remodelling and folding of the mesoderm to form the initial linear heart tube with an arterial (cranial) and venous (caudal) pole (Miyamoto and Kwon, 2022). The FHF will go on to give rise to the left ventricle and most of the atria. The SHF cells are easier to define as a population due to their contact with the endoderm and their sustained proliferative state (Dyer and Kirby, 2009). Other than positioning, the SHF can be defined with the expression of the genes *Fgf10* and *Isl1*, the SHF can be further grouped into two populations, with the posterior SHF expressing *Tbx5* but not *Tbx1*, and the anterior SHF expressing *Tbx1* but not *Tbx5* (De Bono *et al.*, 2018). As the SHF proliferates, the cells contribute to a new pool of cardiac progenitors that will form part of the outflow tract (OFT) and the right ventricle at the arterial pole of the heart tube and part of the atria and inflow tract from the venous pole of the structure (Ivanovitch, Esteban and Torres, 2017).

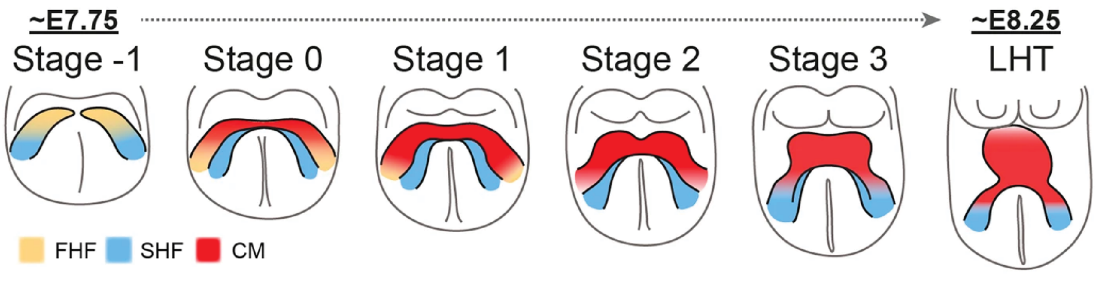

Figure 1.2 Formation of the cardiac crescent in mice. A schematic of the stages of cardiac crescent development to the formation of a linear heart tube. The two cardiac progenitor populations are coloured to show their positioning; the first heart field (FHF)

is seen in yellow, and the second heart field (SHF) in blue with cardiomyocytes (CM) from these progenitors are coloured red. LHT = linear heart tube. Adapted from (Tyser et al., 2021)

1.2.2 Growth and looping of the heart tube

The linear heart tube is a hollow structure organised into three layers: the visceral pericardium forms the external surface, the next layer inward consists of cardiomyocytes, and the inside layer is a lining of endocardial cells (Mathew and Bordoni, 2023). The two inner layers are separated by cardiac jelly which is made of extracellular matrix proteins. At this point in development, the heart tube is patterned along the cranial-caudal axis according to which areas will give rise to what heart chambers. The two caudal arms at the venous (caudal) pole of the heart are where the precursor cells to the atrial chambers reside, which will move in positioning after heart looping. The arterial (cranial) pole of the heart is the outlet, where the OFT is forming.

Looping of the heart tube occurs simultaneously with an increase in length as cells from the SHF migrate into the arterial pole of the heart, populating the OFT and contributing to the primordium of what will become the right ventricle (Buijtendijk *et al.*, 2020). Elongation of the heart tube leads bending of the structure, forming a ventricular loop which is supported by the caudal inlet where the atrial progenitors are and the OFT at the cranial end. The OFT at this stage (E11 in the mouse), feeds into the arteries arising from the aortic sac which is connected to the increasing number of pharyngeal arches (PA) (Anderson *et al.*, 2014). Once looping has occurred, chamber compartmentalisation starts to occur with the ballooning of the ventricular loop, forming the primitive ventricular chambers (Christoffels *et al.*, 2000).

1.2.3 Atrioventricular cushions

During heart looping, the walls of the inlet and outlet swell with cardiac jelly into the lumen of the heart tube to form pairs of endocardial cushions at both locations, these transient structures primarily consist of extracellular matrix (ECM) secreted by the myocardium and are initially acellular (Camenisch *et al.*, 2001) (Figure 1.3A). The

inlet endocardial cushions will become the atrioventricular cushions (AVC) and the outlet cushions become the outflow tract cushions (OFTC). These structures are crucial for proper heart development both contributing to ventricular septation and the formation of valves. The OFTCs are additionally responsible for the patterning of the arterial vessels.

The AVCs are the endocardial cushions that will give rise to the tricuspid and mitral valves. The two cushions are positioned adjacent to one another, with a dorsal or inferior AVC and a ventral or superior AVC (Figure 1.3B-C). The AVCs become increasingly cellularised between E9-E9.5 with endocardial-to-mesenchymal transition (EndoMT), prompted by signals secreted from the myocardium (Ma *et al.*, 2005). Fluid shear stress, as the heart begins to beat and haemodynamic load is exerted on the endocardium, triggers the migration of endocardially-derived mesenchymal cells into the cushion structure (Granados-Riveron and Brook, 2012). These cells invade and cellularise the cushion, which is now a dense matrix of hyaluronan, collagens, versican and proteoglycans (Silva *et al.*, 2021). The cushions continue to swell and grow as the mesenchymal cells from proliferation and matrix production until superior and inferior AVCs fuse at the midline (Figure 1.3C) (Web *et al.*, 1998). The fusion event will separate the atrioventricular canal into the left and right orifices, where the atrioventricular valves will develop with the help of lateral cushions that will form a leaflet in each of the valves (Figures 1.3C-E). Furthermore, the AVCs reside at the atrioventricular junction and the atrial septal complex and thus are key structures in both ventricular and atrial septation (discussed in §§1.2.5).

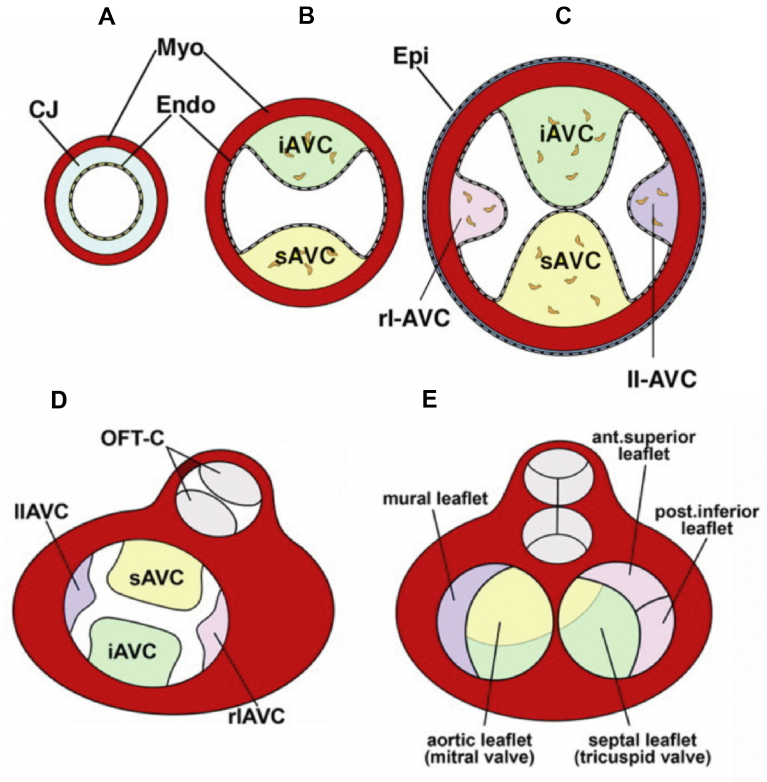

Figure 1.3 Schematic of the atrioventricular cushions and their development in to valves. (A) Layers of the heart tube where the atrioventricular cushions (AVC) will form. (B) Formation of the inferior and superior atrioventricular cushions. (C) Growth of the AVCs and formation of the right and left lateral leaflets. (D-E) Fate of the superior AVC, inferior AVC and lateral leaflets. CJ, cardiac jelly; Myo, myocardium; Endo, endocardium; Epi, epicardium; OFT-C, outflow tract cushions; iAVC, inferior AV cushion; sAVC, superior AV cushion; llAVC, left lateral AV cushion; rlAVC, right lateral AV cushion. Adapted from Snarr, Kern and Wessels (2008).

1.2.4 Outflow tract development and septation

The OFT is the arterial pole of the heart loop and is a transient structure through development. It extends from the right ventricle into the aortic sac and has historically been separated into the distal and proximal (conus and truncus), demarcated by a transient dog-leg bend of the structure seen during development (Kramer, 1942; Ya *et al.*, 1998). However, it has been recently proposed by Anderson *et al.* (2023) that the OFT should be considered a tripartite structure, with the pulmonary trunk as the most distal portion, the middle the pulmonary root, and the infundibulum (“funnel”) as the connection of the OFT to the right ventricle. The inner walls of the OFT begin to

swell with a myriad of ECM proteins like hyaluronan, proteoglycans, collagens and fibronectin (Lockhart *et al.*, 2011), to form a jelly layer lined at the interior lumenal face with an endocardial layer. These swellings form the OFTCs, where two separate structures are formed – the parietal and the septal cushions.

The OFTCs are often referred to as the "conotruncal" cushions, as the OFT was first described to have a conus and truncus (Kramer, 1942). The OFTCs are endocardial cushions like the AVCs, although are structurally distinct and have different cellular origins. The OFTCs consist of the parietal and septal cushions which spiral helically around each other, eventually fusing at their interface (in a distal-to-proximal sequence) to septate the OFT into the pulmonary artery and the aorta. Their ability to remodel, fuse and partition the common arterial trunk is crucial for not only the patterning of the great vessels but to ventricular septation, as the proximal end of the septal cushion extends proximally into the ventricular space to fuse to the crest of the muscular ventricular septum (mVS). Furthermore, the OFTCs give rise to the two semilunar (arterial) valves – the pulmonary valve and the aortic valve – that prevent backflow in the mature heart.

The OFTCs begin similarly to the AVCs, with a swelling of the internal wall of the (in this case arterial) pole of the heart tube. They cellularise through both EndoMT of the endocardial cells lining the swelling and through additional contributions from a subset of the neural crest, the cardiac neural crest cells (CNCC). Both cell types form the mesenchymal cells of the OFTC and can be tracked through their expression of *Sox9* (Akiyama *et al.*, 2004). The mesenchymal cells then undergo proliferation to expand and continually cellularise the OFTCs to form the aortopulmonary septum and septate the OFT. This process is dependent on the condensation of the CNCC within the cushions, as the condensation of CNCC goes on from the myocardial bridge to remodel the OFTC and form to aortopulmonary septum (Kirby *et al.,* 1983; Scholl and Kirby, 2009). CNCC also migrate further into the proximal cushions to form the semilunar valves and contributes to the membranous interventricular septum during ventricular septation (Jain *et al.*, 2011).

Concurrent to this process, the OFTC form the semilunar valves with intercalated leaflet valve swellings (Figure 1.4A-C). These cellularised swellings are the precursors of the anterior and posterior leaflets of the valves originating from the SHF and do not contribute to OFT septation. The distal OFTCs and intercalated

swellings remodel to form the arterial valves by sculpting to form the thin fibrous leaflets of the arterial valves (Henderson *et al.*, 2022).

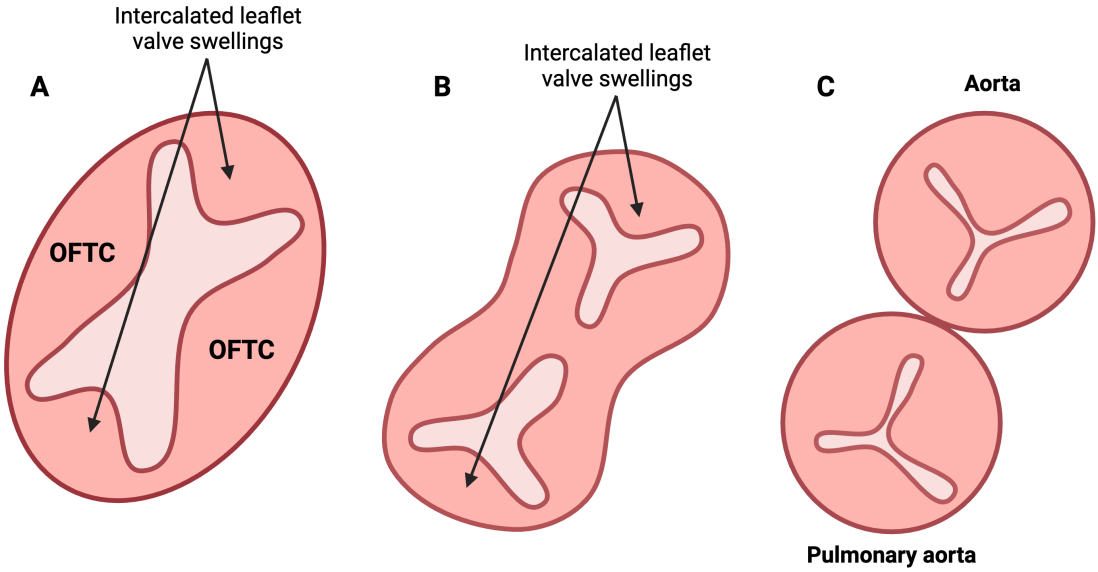

Figure 1.4 Schematic showing the formation of the semilunar (arterial) valves. (A) The common outflow tract is shown with the two OFTCs and the intercalated leaflet valve swellings. (B) The OFTCs have fused at the midpoint leaving two lumen each bordered by the intercalated leaflet valve swellings and remaining distal OFTCs. (C) The OFT septated in to the aorta and pulmonary artery shown with remodelled arterial valve leaflets originating from the OFTCs and intercalated leaflet valve swellings. OFTC, outflow tract cushions; OFT, outflow tract.

The OFT-proper becomes anatomically distinct from other regions of the looped heart at E10.5 when the outer curvature begins ballooning into the common ventricle. The OFT is at this point a solitary lumen (with a myocardial wall formed from SHF progenitor cells) that emerges from the ventricular loop at the proximal end and connects to the margins of the pericardial cavity at the distal end, before becoming continuous with the aortic sac (Anderson *et al.*, 2023). Before OFTC formation, CNCC, a subset of neural crest cells, delaminate from the neural tube and migrate into the OFT and the OFTC via the carotid, aortic and pulmonary PAs (George *et al.*, 2020; Graham *et al.*, 2023). Some of the CNCC are deposited at the PAs, differentiating into smooth muscle of the aortic arch arteries to maintain the persistence of these structures (Waldo *et al.*, 1998). At the same time as the OFTCs

are forming, the dorsal wall of the aortic sac protrudes into the cavity of the distal OFT in preparation for septation.

The OFT straightens at E11.5, losing its dog-leg bend. The OFTCs continue to cellularise with SHF-derived cells from EndoMT and CNCC. The septal and proximal cushions spiral around each other as the myocardial wall rotates, completing rotation at E12.5 (Bajolle *et al.*, 2006). At this stage, the distal OFTC begin forming nascent semilunar valves, along with the formation of intercalated valve swellings which will become the anterior and posterior leaflets of the arterial valves (Henderson *et al.*, 2022). Both the parietal and septal distal OFTC at this stage fuse to each other, originating from areas of condensed mesenchymal CNCC cells within each cushion, to form the intrapericardial arterial trunks. Additionally, the fusing OFTC also fuse to the protrusion of the dorsal wall of the aortic sac (Anderson *et al.*, 2012). This fused structure initially forms the aortopulmonary septum before becoming extracavitary space that will separate the pulmonary and aortic trunks (Anderson *et al.*, 2023). This process will move progressively from the distal to the proximal OFT.

At the same stage, the middle of the OFT is not yet septated and the OFTCs have not fused, but the primordium of the arterial roots can be identified as areas of condensed mesenchyme that extend towards the proximal cushions in both septal and parietal OFTCs. The proximal face of the septal OFTC begins to fuse to the crest of the muscular septum (described in §§1.2.5) and subsequently muscularises. Fusion of the proximal cushions is complete by E13.5, where the central core of the structure are CNCC-derived cells which begin to decrease in size to become extracavitary tissues that will eventually separate the pulmonary artery and aorta at what was the proximal OFT (Anderson *et al.*, 2023).

1.2.5 Formation of the aortic arch arteries

During heart development, the aortic arches develop in tandem to provide the heart with the necessary plumbing to deliver blood to and from the organ. Adult mammals have left-sided asymmetric aortic arch (AA) arteries, though embryonically this develops bilaterally in five pairs, from cranial to caudal in the developing embryo. AA arteries develop from the aortic sac between the PA, which are bulges located along

the lateral surface of the embryo's neck and head. The PAs all have endodermal, mesodermal and ectodermal components, with the endodermal layer responsible for the patterning of the AAs (Piotrowski and Nüsslein-Volhard, 2000). The PA endoderm also forms the pharyngeal glands such as the thymus and parathyroid glands (Graham *et al.*, 2005). Some of the PA mesenchyme is derived from CNCC which contributes to the persistence of the AA arteries after their remodelling.

The five pairs of arteries that form are never present at the same time during development, with regression of formed structures and asymmetrical regression within the pairs to form the left-sided asymmetrical patterning seen in adult mammals. In murine development, the first and second AA arteries form at E9.0, remodel at E10.5 and regress by E11.5, with its distal remnants contributing to portions of the maxillary arteries. The third pair of AA arteries form the common carotid arteries bilaterally and the internal carotid arteries, undergoing extensive remodelling at E12.5. The right fourth AA artery contributes to the right proximal subclavian artery, whereas the left gives rise to the medial AA. The fifth AA never forms or incompletely forms and regresses, failure to regress results in an extremely rare cardiovascular defect: Persistent Fifth Aortic Arch (Shan *et al.*, 2023). The final and most caudal pair of AA arteries are the last to form at E10.5 and give rise to components of the pulmonary artery and pulmonary trunk. The right artery lengthens and thins due to the rotation of the OFT, causing the portion distal to the pulmonary trunk to regress, with the remnants forming the right pulmonary artery. The left artery forms the ductus arteriosus, connecting the aorta to the pulmonary artery (Anderson and Bamforth, 2022). This structure is present in all foetuses and closes shortly after birth.

1.2.6 Chamber formation and septation

After heart looping, the heart begins to form its atrial and ventricular chambers. The ventricular chambers start to form at the ventral outer curvature of the heart loop, where myocardial protrusions begin to extend into the lumen of the heart to form the early trabeculation. These finger-like protrusions form through oriented cell division of trabecular cardiomyocytes into the ventricular lumen (Li *et al.*, 2016). Further cardiomyocyte division parallel to the ventricular wall lengthens and thickens the ventricular walls. The left and right ventricles begin to be separated by the

interventricular septum, which comprises a muscular and membranous component, the latter of which is formed from the AVCs and the OFTCs and is the last step in ventricular septation. Proper development of the ventricular septum begins with the muscular septum (E10.5-E12.5), which then fuses to the septal OFTC to set up the left and right ventricles to have separate arterial vessels (E12.5-13.5) (Figures 1.5A-B'). Septation is finalised by the protuberance of AVCs into the ventricles, closing the remaining shunting between the left and right chambers (E13.5-14.5). The precise timing of complete septation is unknown in the mouse, with literature describing the heart to finish septation between E13.5 and 14.5 (Savolainen *et al.*, 2009). However this is unlikely to be consistent across all mouse strains, as development of other structures such as bone microstructure and somite formation have been found to differ between strains (Thiel *et al.*, 1993; Papageorgiou *et al.*, 2020).

The formation of the ventricular septum occurs concomitantly with the ballooning of the ventricular loop, where the bulboventricular groove develops. The mVS originates at the bulboventricular groove on the floor of the common ventricle and can first be structurally identified at E10.5 in the mouse. The mVS grows cranially towards the inner heart curvature and the endocardial cushions through the oriented proliferation of cells localised in the ventricular walls. Trabeculation near the growing mVS is recruited to the structure to add to its outgrowth. The crest of the mVS then fuses to the septal OFTC which overhangs into the right ventricle. The proximal region of the OFTC at this stage forms a "shelf" (a structure which forms the roofing of the interventricular communication) above the right ventricle and the remaining interventricular communication (IVC) (Figures 1.5A'-B', circled region). The attachment of the mVS to septal OFTC restricts the remaining IVC to the posterior of the ventricles, where the aortic root will be (Figure 1.5B'-C). The remnant of the IVC is closed by the fusion of the right ridge of the AVC to the remaining right crest of the mVS (Figure 1.5D), sealing the shunting between the left and right ventricles. This leaves the right ventricle access to the pulmonary arterial root and the left ventricle to the aortic root.

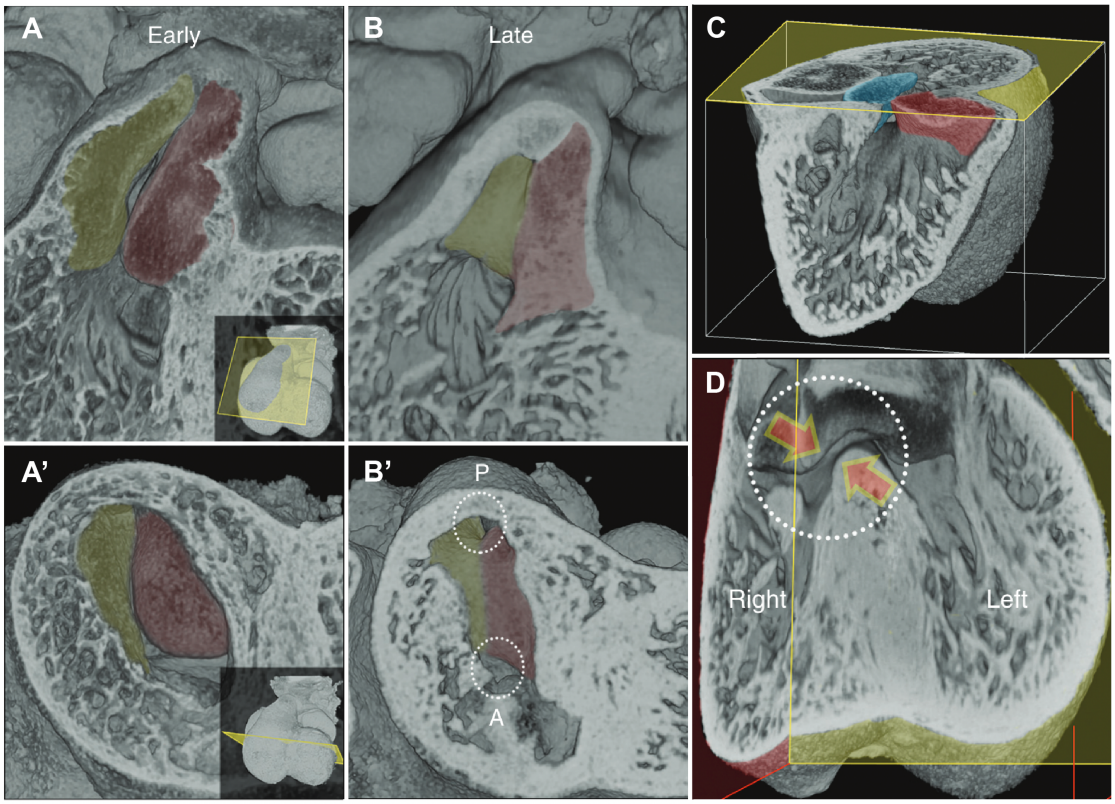

Figure 1.5 Proximal outflow tract cushions and ventricular septation. (A-A') Frontal and axial views of the proximal outflow tract cushions at early E12.5. The parietal cushion is coloured yellow and the septal cushion in red. (B-B') Frontal and axial views of the proximal outflow tract cushions at late E12.5 where the aortic and pulmonary roots are identifiable (dashed circles). (C) E12.5 heart eroded from the right with axial erosion to show fusion of the septal cushion (red) with the ventricular septum and positioning of the superior atrioventricular cushion (blue). (D) Remaining interventricular communication and the structure needed to close it are indicated by red arrows at E13.5 (upper arrow points to the bottom end of the superior atrioventricular cushion; lower arrow points to right-ventricular side of the crest of the muscular ventricular septum). A, aortic root; P, pulmonary root. Adapted from (Mohun and Anderson, 2020)

The mVS is a mixture of cells with left and right ventricular identities as confirmed by lineage tracing studies, which is likely what has made the hunt for a definitive 'ventricular septum' marker difficult: the closest thing to a marker for the mVS is lysozyme M, a bacteriolytic enzyme expressed by immune cells, which is expressed in some but not all cells within the mVS (Stadtfeld *et al.,* 2007). The mVS also contains a small contribution from the neural crest: a study by (Tang *et al.*, 2019)

demonstrated the presence of CNCC in the mouse mVS through a lineage-tracing study using Wnt1-Cre. However, it is unknown how and if these neural crest cells contribute to the ventricular septation process from the mVS.

While the ventricles are forming, the atria are forming symmetrically. The proper development of the atrium is dependent on the formation of the lungs and the associated pulmonary vasculature: the vessels developing around the lung buds connect to the primary inlet of the heart tube via the pulmonary vein as the primary atrium expands in preparation for atrial septation (Anderson *et al.*, 2002). The process begins with the primary atrial septum growing caudally towards the AVCs, the space between the leading edge of the septum and the AVCs is the primary atrial foramen (Figure 1.6A). As this foramen decreases in size with the leading edge of the primary atrial septum fusing to the dorsal mesenchymal protrusion (DMP) at the atrioventricular junction, the upper edge of the primary septum perforates and forms a secondary interatrial communication (secondary foramen) which maintains the right-to-left blood flow through the heart at this stage (Figures 1.6B-C). To the right of the primary atrial septum, the secondary atrial septum extends downwards to cover most of the primary atrial septum with the remaining foramen now called the foramen ovale. The primary and secondary atrial septa fuse with a flap remaining over the foramen ovale throughout development, closing up by atrial pressure postnatally (Annabi *et al.*, 2023) (Figure 1.6D).

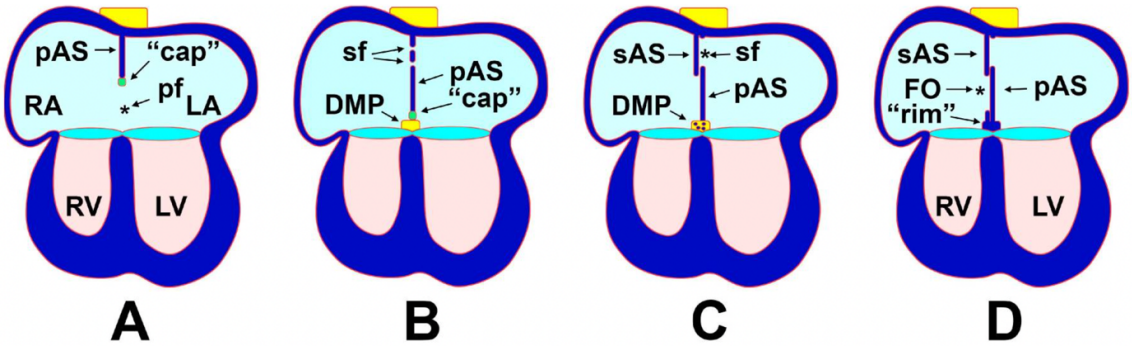

Figure 1.6 Atrial septation. (A) Growth of the primary atrial septum. (B) Formation of the secondary foramen and location of the dorsal mesenchymal protrusion (C) Growth of the secondary atrial septum. (D) Complete atrial septation with the foramen ovale present. pAS, primary atrial septum; pf, primary foramen; sf, secondary foramen; sAS, secondary atrial septum; DMP, dorsal mesenchymal protrusion; FO, foramen ovale. Adapted from (Burns et al., 2016).

1.2.7 Comparisons between mouse and human heart development

Much of our understanding of cardiac morphogenesis has emerged from studying mouse development and using mouse genetics to understand the underlying mechanisms. Nevertheless, it is important to discern the distinctions between heart morphogenesis in mice and humans to understand the impact and translation of our findings for the development of CHD in humans. The gestational period for heart morphogenesis in mice and humans is quite different even with the heart being the first functional organ to develop in both species. In humans, complete heart septation takes place over the first two months of gestation whereas in mice it takes approximately 14.5 days from conception. The rest of development and other organogenesis is complete in less than a week after heart septation in the mouse, but in humans, the gestation period lasts for another 7 months.

As both are mammals, the anatomical structures of mouse and human hearts are very similar. The hearts of both species have four chambers, the two atria separated by the interatrial septum and the two ventricles separated by the ventricular septum. Comparative studies have shown that processes such as heart looping, OFT development, ventricular and atrial septation (described above) are very similar in mice and humans (Krishnan *et al.*, 2014). However, there has been some debate amongst anatomists on the differences in the structure of the atrioventricular septal junction. The structure formed by the final stages of ventricular septation where the AVC fuses with the mVS and septal OFTC complex to close the remaining IVC is traditionally described to be the membranous portion of the ventricular septum in both mice and humans. In humans, this structure is thin and fibrous whereas in the mouse the corresponding structure is muscular and thick (Wessels and Sedmera, 2003). This is thought to be due to a combination of delayed delamination of the tricuspid valve septal leaflet (Webb, Brown and Anderson, 1996) and myocardialisation of the mesenchymal tissues (Kruithof *et al.*, 2003) in the mouse. This is a tantalising part of the anatomy to have a discrepancy between human and mouse, as the membranous septum is the location of most variations of VSDs.

1.3 Congenital heart defects

CHDs are defined as any condition with a structural abnormality in the heart or the great vessels existing from birth. Here I will discuss the most common types of CHDs and their aetiology and delve further into some of the key pathways in heart development and how their dysregulation can result in CHD phenotypes.

1.3.1 Prevalence of congenital heart defects

CHDs constitute the most common category of congenital anomaly (Yu *et al.*, 2022) and is the main cause of non-communicable diseases in regions without access to adequate and timely intervention (Su *et al.*, 2022). Signs and symptoms vary between the different types of defects, ranging from non-existent to acute. Surgical intervention is often required and long-term outcomes are generally positive where surgery is provided. The prevalence of CHDs has remained stable globally in the last three decades, suggesting that there has not been an improvement in prevention strategies, likely stemming from our lack of understanding of the mechanisms underlying heart malformations.

1.3.2 Ventricular septal defects

The most common type of CHD clinically is the VSD, where there is shunting between the left and right ventricular chambers allowing for the mixing of oxygenated and non-oxygenated blood. The extent of IVC size varies, ranging from a pinhole to a complete lack of the ventricular septum. With smaller shunting, the communication can close without medical intervention after birth. VSDs are often found in isolation but also in conjunction with other defects such as OFT or atrial septal defects. There are 4 different types of VSDs (Dakkak and Oliver, 2023):

1. Type 1: Shunting is located below the aortic valves in the outlet septum of the right ventricle (Figure 1.7A). It is also known as the infundibular or outlet VSD, representing 6% of all VSDs in most populations except for the Asian population where its prevalence increases to 30%.

2. Type 2: Communication is found in the membranous ventricular septum; this is commonly referred to as the membranous VSD or the perimembranous VSD if the shunting partially involves the mVS (Figure 1.7B). This is the most common of the VSDs, accounting for 80% of all diagnosed isolated VSDs.
3. Type 3: This VSD is found by the atrioventricular valves by the inlet portion of the muscular septum (Figure 1.7C). This type occurs in 8% of diagnosed VSDs but is most associated with patients with DS.
4. Type 4: Shunting in the mVS, where in some cases more than one communication can be found (Figure 1.7D). These muscular VSDs represent 20% of VSDs in infants but not adults, as they have a tendency to close as the patients age.

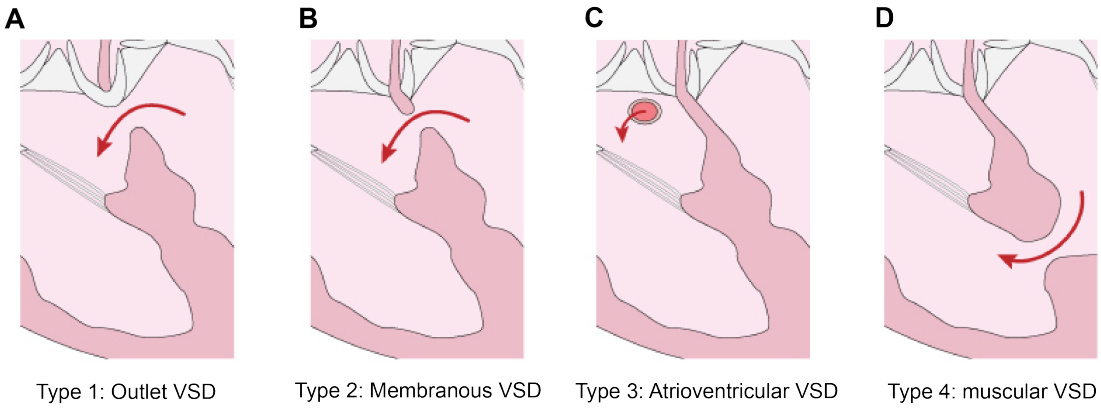

Figure 1.7 Schematic of the four types of ventricular septal defects. (A) Illustration of an outlet VSD. (B) Membranous or perimembranous VSD. (C) Atrioventricular inlet VSD. (D) Muscular VSD. VSD, Ventricular septal defect. Adapted from “vhlab.umn.edu”.

The aetiology of VSDs lies in the aberrant development of the ventricular septum, in either the muscular or membranous components. Causes of developmental aberrations are heterogeneous and likely involve both environmental and genetic factors. Chromosomal abnormalities are one major, known cause of defects, as discussed in this thesis, appearing in nearly half of all patients diagnosed with trisomy 21. Isolated VSDs in particular account for 21.5% of all CHDs diagnosed in DS (Benhaourech *et al.*, 2016). It is also a phenotype of trisomy 18, also known as Edward’s syndrome, where CHDs have a higher penetrance in 90% of cases with VSDs making up 77% (Bruns and Martinez, 2016). VSDs are also a common phenotype of DiGeorge Syndrome, also known as 22q11.2 deletion syndrome.

Similar to DS, DiGeroge Syndrome is a congenital disorder which presents with a broad range of phenotypes stemming from the microdeletion of the 22q11.1 location on chromosome 22 (McDonald-McGinn *et al.*, 2015). This deletion results in developmental failure of the pharyngeal pouches, located between the PAs in the developing embryo, causing cardiac, pharyngeal, parathyroid and thymic defects (Zhang *et al.*, 2006). In DiGeorge syndrome, the causative gene is thought to be TBX1 (Gao *et al.*, 2013). This gene is expressed in SHF but not CNCC and mice with inactivated Tbx1 have been shown to have VSDs and OFT defects (Zhang *et al.*, 2018). Other T-Box transcription factors also play a critical role in heart development and, unsurprisingly, variants of TBX2, TBX3, TBX5, TBX18 and TBX20 are associated with CHDs like VSDs (Bolunduț *et al.*, 2023). Of these genes, TBX5 and TBX20 are of particular interest to ventricular septum development, as patterning of TBX20 and TBX5 gene expression in myocardium and cardiomyocytes correlate with the position of the ventricular septum (Takeuchi *et al.*, 2003). Single gene defects have also given clues to the cellular mechanisms that lead to VSDs, such as Nkx2-5 haploinsufficiency, where Nkx2-5 is required for proliferation of SHF cells and morphogenesis of the OFT (Winston *et al.*, 2012).

To summarise, VSDs are multifactorial in aetiology with multiple points of failure possible in heart development. As indicated through single gene defects, a complex network of genetic regulation is involved in the multiple cellular processes that lead to proper septation. Furthermore, while VSDs often occur in isolation, it is also common to find them alongside other CHDs, for instance, as a key constituent of AVSDs, as will be discussed below, and one of the four components of Tetralogy of Fallot (ToF) which consists of a VSD, an overriding aorta, pulmonary stenosis and right ventricular hypertrophy.

1.3.3 Atrioventricular septal defects

AVSDs are a subset of CHDs where there is a combination of 3 defects:

1. An atrial septal defect where there is shunting at the atrial level
2. VSD, as described above
3. A common atrioventricular valve in place of mitral and tricuspid valves.

DS is the most common disorder associated with AVSDs: 35-40% of CHDS in DS being AVSD and of 40-50% of all AVSDs diagnosed being comorbid with DS (Benhaourech *et al.*, 2016). A further 20% of AVSDs are associated with other chromosomal disorders, such as DiGeorge syndrome, and the remainder are not found to be associated with a broader condition. Most syndromic AVSDs are *de novo* mutations while 3.5% of AVSD cases show a familial pattern of inheritance (Pugnaloni *et al.*, 2020). AVSDs are thought to arise during cardiogenesis from the AVC maldevelopment due to defective ECM deposition which impacts the fusion of the superior and inferior AVCs, leading to the common atrioventricular valve or "bridging leaflet". Further studies have suggested that the failure of the DMP (the dorsal protrusion that emerges from the middle of the AVC) to develop properly impacts the process of atrial septation, tracing back to its origins from the SHF (Briggs *et al.*, 2012; Burns *et al.*, 2016).

As DS is the most frequent disorder associated with AVSDs, much interest has been focused on genes in the DSCR of Hsa21, in particular DSCAM, COL6A1, COL6A2, DYRK1A and DSCR1. Of these genes, DSCR1 and DYRK1A have been two genes of interest where overexpression has been shown to inhibit the expression of NFAT target genes which are commonly associated with cardiogenesis and mitochondrial function (Bushdid *et al.*, 2003). Transgenic mice overexpressing DYRK1A and DSCR1 were found to have a failure in atrioventricular valve elongation at E13.5, where a failure of elongation results in failure to form proper valve leaflets (Arron *et al.*, 2006). Genes such as COL6A1 and COL6A2 have been implicated in AVSD pathogenesis due to the ECM of AVCs being rich with Collagen VI, where it has been speculated that increased deposition of Collagen VI leads to hyperplastic AVCs and impacts AVC differentiation leading to malformed valves which affect cardiac septation (Gittenberger-De Groot *et al.*, 2003).

Aside from trisomy 21, other chromosomal disorders such as Deletion 8p23 and Deletion 3p25 are associated with AVSDs, with candidate genes GATA4 and CRELD1 respectively identified as the causative genes in the deleted regions (Pugnaloni *et al.*, 2020). Interestingly, both genes are involved with Sonic Hedgehog signalling (Shh); GATA4 interacts with transcription factors to drive DMP progression through Shh signalling (Zhou *et al.*, 2017) and CRELD1 mutations have been shown to modulate Shh signalling in the SHF (Robinson *et al.*, 2003).

Interestingly, many other syndromic and monogenic disorders associated with AVSD are ciliopathies, i.e., disorders involving ciliary dysfunction. Cilia are involved with Shh signalling in the development of the DMP, where mice with knockout of the Shh pathway components exhibited loss of the DMP tissue resulting in failure to form the septal complex at the atrioventricular junction. This was suggested as a premature differentiation of the SHF leading to fewer cells contributing to the DMP (Goddeeris *et al.*, 2008). Notably, there is also evidence to suggest that trisomy 21 dysregulates cilia formation and function from studies conducted in trisomic cell lines (Galati *et al.*, 2018). In humans, ciliopathies such as Joubert syndrome and Ellis-van Creveld syndrome present with a constellation of phenotypes but consistently display AVSDs as one of the most penetrant phenotypes (Klena *et al.,* 2017; Al-Dairy *et al.*, 2022). Other components of the Hedgehog (HH) signalling components are implicated in other CHDs, for instance, intracardiac HH signalling has been found to participate in the formation of the mVS through myocardial proliferation in the ventricular walls which contributes to the outgrowth of the mVS and disruption of this pathway results in VSDs in transgenic mice (Wiegering *et al.,* 2017).

As discussed, AVSDs are complex in their causation with many studies indicating that the fault lies with the improper development of the atrioventricular junction. While many studies point to dysmorphic DMP development as the origin of AVSDs, other studies indicate the development and maturation of the AVCs as the fault. The latter is more inclusive of the 3 defects that make up AVSDs as outlined above, as the AVCs are the structure involved in all of the defects independently.

The AVCs are the junction at which the DMP is found for atrial septation and they the structure that gives rise to the atrioventricular valves. However, it is also the last component to fuse to the membranous ventricular septum to complete ventricular septation.

1.3.4 Outflow tract defects

Within the scope of CHDs, OFT defects and abnormalities of the arterial vessel development and patterning are estimated to contribute to 30% of all CHDs

diagnosed (Thom *et al.*, 2006). OFT defects are often found concurrent with VSDs. There are 4 major types of structural OFT defects (Figure 1.8):

1. Persistent truncus arteriosus (PTA): a common arterial trunk instead of separate pulmonary and arterial vessels exiting the heart.
2. Double outlet right ventricle (DORV): both the pulmonary artery and aorta drain from the right ventricle.
3. Transposition of the great arteries (TGA): reversed positioning of pulmonary and aortic arteries.
4. Overriding aorta (OA): the aorta is positioning above a VSD and receives blood from both ventricles.

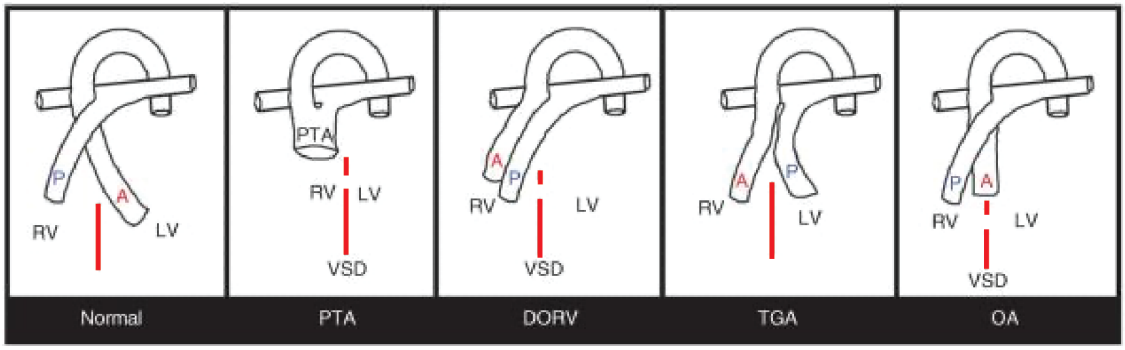

Figure 1.8 The four major structural outflow tract defects. A simplified cartoon of the aorta and pulmonary artery positioning from the right ventricle (RV) and left ventricle (LV) in a normal heart. The ventricular septum is shown as the red line. The following panels showcase the arterial patterning in persistent truncus arteriosus (PTA), double outlet right ventricle (DORV), transposition of the great arteries (TGA) and overriding aorta (OA). Adapted from Neeb et al. (2013).

Structural OFT defects are caused by the disturbance of morphogenetic patterning of the arterial pole of the heart that becomes the OFT and the rotation (helical twist) of the septum (myocardial wall) that runs along and divides the OFT to form the separate great arteries (Bajolle *et al.*, 2006). As discussed in §§1.2.4, proper development of the OFT is dependent on OFTC cushion development which relies on the contribution of not only the SHF, but also migration of CNCCs from the PAs and ECM production. With the proper OFT development dependent on the participation of extracardiac progenitor populations, various potential failures in these processes could lead to OFT defects.

SHF cells colonise the OFT in early cardiac development during heart tube development and cardiac looping, arriving at the arterial pole and undergoing EndoMT to establish a mesenchymal population in the OFTCs. Many studies have observed that defective proliferation and function of SHF-derived cells in the OFT lead to hypoplastic cushions which result in concomitant CHDs (Cai *et al.*, 2003; Waldo *et al.*, 2005). This was taken further in chick embryos where removal of SHF progenitors leads to OA with some exhibiting ToF (Ward *et al.*, 2005). Ablation of specific SHF-associated genes like *Isl1* and *Mef2c* in mice has also resulted in OFT defects, failure of heart tube elongation, looping and underdeveloped heart chambers (Cai *et al.*, 2003; Dodou *et al.*, 2004). The same cardiac defects were also observed with cell cycle inhibition in SHF progenitors before migration (van den Berg *et al.*, 2009). This highlights the importance of the SHF and its ability to proliferate within the developing OFT, where defects in these processes directly result in OFT and heart development abnormalities.

The endocardium lines the lumenal faces of the OFTCs to contribute to the morphogenesis of the OFTC and modulate OFT myocardial proliferation. Signalling from the myocardium prompts the endocardium to undergo EndoMT to seed the OFTC, this process is modulated by *Nfatc1* which coordinates the location and timing through suppression of *Snai1* and *Snai2*, which are needed for the initiation of EndoMT (Kovacic *et al.*, 2019). The endocardium also regulates cardiomyocyte proliferation and differentiation through multiple signalling pathways such as Notch, VEGF and FGF (Wu *et al.*, 2011). Cardiomyocyte proliferation has also been found to be regulated by the Hippo-YAP (yes-associated protein) where proliferation was found to be impaired with deletion of Yap in embryonic mice prior to embryonic lethality (Xin *et al.*, 2011). Recently, Yap has been identified as being involved in valvulogenesis and cell proliferation in both the OFTCs and AVCs in mice. Additionally, Yap-mediated mechanotransduction was found to underlie the cell proliferation alongside valve shape (Wang *et al.*, 2023).

CNCC are also vital in the development and remodelling of the OFT. Disruption of neural crest development results in a collection of conditions known as neurocristopathies, such as Waardenburg, DiGeorge, Hirschsprung and CHARGE syndromes. These and many other neurocristopathies count OFT defects among their multi-systemic phenotypes (Keyte and Hutson, 2008). The importance of the CNCC in the OFT was established by (Kirby and Waldo, 1990), where ablation of

CNCC in chick embryos led to an array of abnormal patterning of the pulmonary and aortic arteries and structural OFT deformities. Involvement of the CNCC in the remodelling of the OFT has been shown to include its septation: CNCC form the condensates at the distal OFTC that initiate the septation of the common trunk into separate pulmonary and arterial vessels (Waldo *et al.*, 1998). The CNCC are governed by multiple different pathways throughout their journey from the neural tube to the OFT, and interference with these pathways specifically in the CNCC has led to structural OFT abnormalities and VSDs. These pathways are involved at different steps in the CNCC, from migration to proliferation and differentiation at their destination. For example, a pathway affecting CNCC differentiation is Notch, where suppression of Notch signalling components in the CNCC resulted in reduced CNCC differentiation into cardiac smooth muscle in mice, resulting in OFT defects and VSDs (High *et al.*, 2007). Another example is Bone morphogenetic proteins (BMP). Dysregulation of various BMP pathway components resulted in various structural OFT defects (Délot *et al.*, 2003). Bmp signalling has been shown to promote OFTC development through repression of Vegfa to regulate EndoMT within the cushion and control the influx of CNCC in to the OFT (Ma *et al.*, 2005; Bai *et al.*, 2013). Additionally, the deletion of *Dullard,* a repressor of BMP, in CNCC of mouse embryos causes a premature and asymmetric septation of the OFT ultimately leading to embryonic lethality, suggesting that the pathway is highly important in cardiogenesis as a whole (Darrigrand *et al.*, 2020). Many other pathways are found to affect the development of the OFT through the CNCC or SHF-derived cells but are beyond the scope of discussion for this project.

1.3.5 Other heart defects

Another heart defect often diagnosed in infants is persistent ductus arteriosus (PDA), where there is a remaining shunt between the pulmonary trunk and the aorta, formed from the modified left 6th pharyngeal AA. The ductus arteriosus, also known as the arterial duct, is a foetal blood vessel connecting the pulmonary trunk and the aorta that alleviates pressure on the developing embryonic lungs, allowing blood flow to bypass them. This structure closes shortly after birth. But in some cases, this communication remains open, leading to the mix of oxygenated and nonoxygenated

blood. PDA accounts for 5-10% of CHDs but is greatly increased for premature newborns (Dice and Bhatia, 2007). Oftentimes PDA may close of its own accord but some persistent PDA will require surgical operations. ToF is another notable CHD, as described above it consists of four specific defects. ToF is considered one of the more severe CHDs, with surgical treatment advised soon after birth as newborns are at risk of becoming cyanotic. ToF has been associated with DS with 13% of DS CHD cases identified prenatally as ToF, with some cases concurring with AVSD (9%) (Mogra *et al.*, 2011).

1.3.6 Management of congenital heart defects

Symptoms of CHDs are dependent on their severity, with clinical presentations ranging from rapid breathing, cyanosis, fainting and heart murmurs. In groups at high risk, such as those at risk of DS, prenatal screening is advised to manage outcomes. Some defects require surgical intervention but some do not if there are no adverse effects on quality of life or, as described above in some VSDs, the shunting closes on its own. Modern surgical treatment is usually minimally invasive and has favourable outcomes. DS patients were found to have better outcomes in most cardiac defects than those without DS, in particular after repair of AVSDs (Evans *et al.*, 2014). The exception to this was for the repair of perimembranous VSDs, where the outcome of the group was worse due to a higher risk of post-operative inflammation and pulmonary infections as well as a higher likelihood of needing permanent pacemaker implantation after the operation (Furlong-Dillard *et al.*, 2018; Sarno *et al.*, 2020). Patients are often monitored through the remainder of their lives for any other cardiac-associated health problems.

1.4 Studying congenital heart defects in Down Syndrome

As described above, approximately half of all infants with DS are born with a CHD. However, the developmental mechanisms that lead to these defects within the DS are unknown and the identification of causative genes has been debated. Usage of mouse models has greatly helped our understanding of CHDs in trisomy 21, but the developmental aetiology is still unclear.

1.4.1 Congenital heart defects in mouse models of Down Syndrome

As described above in §§1.1.4, many mouse models of DS exhibit similar phenotypes to that of the human condition. CHDs have been characterised in many of the DS mouse models, such as the Ts1Cje (Ferrés *et al.*, 2016), Ts65Dn (Moore, 2006), Dp16(1)Yey (Liu *et al.*, 2014) and Dp1Tyb (Lana-Elola *et al.*, 2016). Although as previously discussed the Ts65Dn and Ts1Cje are difficult to interpret due to aneuploidy of addition genes outside of Mmu16. The Dp1Tyb model has been shown to recapitulate a similar spectrum of heart defects as those seen in DS infants, including VSDs and AVSDs and these have been characterised in 3D data sets (Lana-Elola *et al.*, 2016). Additionally, the Dp1Tyb mouse has given rise to a genetic mapping panel to break down Mmu16 into smaller regions to identify dosage-sensitive genes that are sufficient in three copies to cause CHDs in the model (Lana-Elola *et al.*, 2023).

1.4.2 Dp1Tyb mouse model heart defects

The Dp1Tyb mouse model has an extra copy of 148 genes on Mm16 that are syntenic to Hsa21, replicating the increased gene dosage that is likely responsible for the DS phenotype in the model. It has also been subjected to comprehensive phenotyping where it was found to recapitulate many complex phenotypes seen in DS (Lana-Elola *et al.*, 2021). The CHDs in Dp1Tyb embryos were phenotyped at E14.5 when chamber septation should be complete, using the 3D imaging modality High-Resolution Episcopic Microscopy (HREM) which allows for highly detailed preservation of the heart structural anatomy (Weninger *et al.*, 2006). The model was found to have a significantly higher proportion of embryos with heart defects at E14.5 compared to their wild-type littermates, with 62% of the Dp1Tyb embryos exhibiting some type of CHD (Lana-Elola *et al.*, 2016). The CHD were further categorised into types with the most commonly occurring being a VSD either in isolation or concurrent with other defects, followed by AVSDs and then OFT defects (Table 1.2). The OFT defects observed in the Dp1Tyb mice were OA and DORV. Dp1Tyb hearts were found to have these two OFT defects in 15.2% of samples (7.6% OA and 7.6%

DORV) compared to 3.8% in wild-type control group (unpublished data, Lana-Elola). The OFT defects were consistently found with other defects such as VSD and AVSD.

Notably, the AVSDs in the Dp1Tyb mice were defined by their common arterial valve (bridging leaflet) and were always found in conjunction with a VSD. Interestingly, the Dp1Tyb showed no perturbations in growth, volume or shape of the DMP, suggesting that the AVSDs phenotyped in the model are not caused by malformation of the DMP contrary to other studies. It is noted here that the wild-type control embryos in this study have a surprisingly high number of defects than would be expected which may be from phenotyping the defects too early, this will be further expanded on in the General Discussion (Chapter 7).

Types of defects			Wt	Dp 1Tyb
Single defects	Septal defects	ASD	1	0
		pVSD	3	9
		mVSD	0	0
	OFT defects	OA	0	0
		DORV	0	0
	AVSD		0	0
Multiple defects	OFT + VSD		1	2
	pVSD+ mVSD		1	3
	VSD + AVSD		1	3
	OFT + VSD + AVSD		0	5
Total number of CHD			7	24
Embryos analyzed			26	39
% of CHD			26.9	61.5

Table 1.2 Cardiovascular anomalies in E14.5 Dp1Tyb embryos. The table shows the number of hearts with different cardiac defects found in Dp1Tyb embryos and their wild-type littermate controls. ASD, atrial septal defect; pVSD, perimembranous ventricular septal defect; mVSD, membranous ventricular septal defect; OA, overriding aorta; DORV, double outlet right ventricle; OFT, outflow tract. Adapted from Lana-Elola *et al.*, 2016.

1.4.3 Genetic mapping panel of Mmu16

As described above, the region of Mmu16 that is duplicated in the Dp1Tyb was further broken down to generate mice with three copies of smaller regions to identify

the critical regions that are sufficient to cause CHD in DS. The mapping panel (Figure 1.1) was used to show that Dp3Tyb, which contains the duplication of 39 genes, was sufficient to cause heart defects at frequencies indistinguishable from those in Dp1Tyb. Another DS mouse model strain, Ts1Rhr, which contains the same duplications as the Dp3Typ except for 8 genes, showed no evidence of an increased frequency of CHDs (Liu *et al.*, 2011a), thereby narrowing the candidate gene(s) to 8. Further crossing with other strains in the mapping panel determined that there were two or more loci of dosage-sensitive genes and that one of the genes must reside in the aforementioned 8-gene region in the Dp3Tyb (Lana-Elola *et al.*, 2016).

A subsequent investigation has revealed that *Dyrk1a* is one of the causative genes of CHD in DS, this was shown by selectively knocking down its copy number in the Dp1Tyb to 2 copies and thus restoring *Dyrk1a* gene dosage. The Dp1Tyb.*Dyrk1a*$^{+/+/-}$ embryos showed a rescue in the number of heart defects identified when compared to the Dp1Tyb (which is *Dyrk1a*$^{+/+/+}$) and their wild-type littermates. Identification of one of the causative genes has allowed exploration into the mechanism by which it may affect heart development and thus affect septation.

1.4.4 Dysregulated pathways associated with heart defects in Dp1Tyb

Single-cell RNA sequencing (scRNA-seq) of Dp1Tyb and wild-type hearts at E13.5 revealed several transcriptionally altered gene sets associated with known molecular pathways. The Dp1Tyb hearts were found to have signatures of decreased proliferation and oxidative phosphorylation, increased immune responses (as marked by increased inflammatory and interferon responses) and activation of epithelial-to-mesenchymal transition pathways. The decreased proliferation signature was further validated using flow cytometry, where an increased proportion of cardiomyocytes and endocardial cells were found to be in G1 and decreased in S-phase, which is consistent with reduced proliferative capacity. More specifically, scRNA-seq revealed that the proliferative defects stemmed from the downregulation of E2F target genes; E2F transcription factors are needed for transitioning cells from G1 to S (Fischer *et al.*, 2022). This defect was transcriptionally rescued in the Dp1Tyb.*Dyrk1a*$^{+/+/-}$ hearts: reducing the copy number of *Dyrk1a* back to two restored the transcriptional profile of E2F target genes to be similar to wild-type. Mitochondrial

dysfunction was suggested as the origin of the reduced oxidative phosphorylation transcriptomic signature in the Dp1Tyb hearts. This was confirmed through flow cytometry and confocal microscopy for analysis of mitochondrial shape, which was found to be abnormal. The phenotype was again reversed when the same assays were performed on Dp1Tyb.*Dyrk1a*$^{+/+/-}$ hearts, suggesting that an extra copy of Dyrk1a is also required for mitochondrial dysfunction.

In addition to the identified dysregulated pathways, pregnant mice were treated with Leucettinib-21, a selective Dyrk1a inhibitor (Lindberg *et al.*, 2023), daily from E5.5 to E13.5 for scRNA-seq and E14.5 for the presence of CHDs. Firstly, treatment with the inhibitor resulted in a partial recovery of rates of heart defects in Dp1Tyb embryos (Lana-Elola *et al.*, 2023). Secondly, Leucettinib-21 caused a partial reversal of the decreased oxidative phosphorylation and proliferative transcriptomic signature in the Dp1Tyb embryonic hearts. These results were consistent with *Dyrk1a* being one of the causative genes (even if, based on the mapping panel, there remains at least one more gene that contributes to these phenotypes to be uncovered). As yet, it is unclear how *Dyrk1a* causes any of the phenotypes, as it is ubiquitously expressed in the heart rather than the specific affected structures. Additionally, it is not known how reduced proliferation or mitochondrial dysfunction affects cardiogenesis and the septation process.

1.5 Summary and Aims

The underlying developmental and cellular mechanisms of CHD are still not well understood, in particular how the presence of a third copy of Hsa21 perturbs heart development in DS to result in half of DS infants being born with a heart defect. While much of the focus has been on identifying the causative dosage-sensitive genes and the pathways associated, there has been startlingly little characterisation of how trisomy 21 affects different stages of heart development. Additionally, while much work has been done to describe the process of chamber septation from an anatomical and descriptive perspective, there is little quantitation of the process. With access to 3D imaging modalities, there is a wealth of metrics that could be gleaned from such datasets that would provide detailed quantification of anatomical changes necessary to trace the origins and proximate physical mechanisms of CHDs in DS.

Similarly, there has been sparse characterisation of the cellular processes that lead to failure of septation in DS models especially as approached from a more developmental perspective. As work by Lana-Elola and colleagues (2023) have found, the Dp1Tyb mouse model has been found to have cellular phenotypes like reduced proliferation in the heart and mitochondrial defects. But there has not yet been an identification of when some of these phenotypes first arise, in what structures and how they go on to impact morphology and septation processes. Furthermore, the focus of CHDs in many DS mouse models has been on AVSDs and VSDs whereas there has been identification of OFT abnormalities in the models. As summarised above, the development of the OFT and OFTCs are critical aspects of proper heart septation, from contributing to the ventricular septum to patterning the arterial vessels. This area of research remains relatively unexplored when compared to other aspects of septation like the AVCs.

Thus, the key aim of this thesis is to answer the question: What are the developmental steps that lead up to septation and how does this process differ in DS to result in CHD?

This question can be subdivided into the following aims:

- Create a detailed developmental timeline of the heart anatomy as it leads up to ventricular septation.
- Quantitatively characterise the morphological changes during this period and how this differs in the Dp1Tyb.
- Identify if any other structures involved in ventricular septation are affected in the Dp1Tyb.
- Elucidate cellular processes of ventricular septation in Dp1Tyb to explain any changes in morphology and how they could impact proper septation.

Chapter 2. Materials & Methods

2.1 Mice

C57BL/6J.129P2-Dp(16Lipi-Zbtb21)1TybEmcf/Nimr (Dp1Tyb) was the primary mouse strain used in this project. These animals were bred in the Biological Research Facility at The Francis Crick Institute and were backcrossed to C57BL/6 for at least 10 generations. Male Dp1Tyb mice were crossed with female C57BL/6 mice to generate embryos for the experiments. Pregnant females were killed via cervical dislocation and dissected immediately for the embryos. Genotyping of the animals was done through the Transnetyx service with ear clippings. All animal work was approved by the Ethical Review panel of the Francis Crick Institute and performed under Project Licences granted by the UK Home Office.

2.2 Embryo collection

When a vaginal plug is found after putting the male Dp1Tyb and female C57BL/6 mouse together for mating, the embryos were counted as being E0.5 with mating assumed to happen at midnight. Once the embryos have reached the required embryological day after the vaginal plug (in this case E10.5, E11.5, E12.5 and E13.5), the mother was sacrificed with cervical dislocation followed by a secondary check with exsanguination. Embryos were dissected immediately and placed into ice-cold phosphate-buffered saline (PBS).

2.3 Embryo processing

2.3.1 Dissection and fixation

Embryos were dissected out of the uterine sac in ice-cold PBS using fine-tipped forceps under a dissecting microscope. For E13.5 embryos, the heart was dissection out of the body. The yolk sac or tail of embryos was used for genotyping through Transnetyx. After dissection, embryos were placed in 4% paraformaldehyde (PFA)

for 15 minutes followed by distilled water (dH_2O) for 1 hour. Embryos were then stored in 4% PFA at 4°C until further processing.

2.3.2 Paraffin embedding

Whole fixed embryos were washed in PBS for 3 X 15 minutes before undergoing dehydration in a series of ethanol dilutions: 30%, 50%, 70% 80%, 90% and 100% for 1 hour each at room temperature (21°C). Embryos and hearts were then placed in cassettes and into xylene, which was changed 3 times at 1 hour each followed by paraffin wax (60°C) twice for 1.5 hours each. Embryos and hearts then were embedded in the desired orientation for the stage and experiment. When the blocks were solidified, they were stored at 4°C until microtome sectioning. All paraffin embedding was done by Experimental Histopathology at the Francis Crick Institute.

2.4 High-resolution Episcopic Microscopy

2.4.1 Preparation for high-resolution episcopic microscopy

Fixed embryos and hearts were washed in PBS 3 X 15 minutes followed by dehydration in serial dilutions of ethanol: 30%, 50%, 70%, 90% and 100% for 1 hour each in a fume hood. Embryos and hearts were further incubated in a prepared solution of JB-4 resin (Polysciences, 00226-1) and 0.40mg/100 ml Eosin B (Sigma Aldrich, 861006) mixed with ethanol at a 1:1 ratio for another hour before incubating in the pure JB-4 mixture overnight. To embed the embryos, the JB-4 mixture was mixed with Solution B from the JB-4 embedding kit (Polysciences, 00226-1) to help catalyse the resin solidification while embryos were placed in a custom polyethylene embedding mould. The catalysed JB-4 was poured over the embryos until covered in the mould. Under a dissecting scope, the embryos were adjusted to the desired orientation with fine-tipped forceps until the resin polymerised and set. A plastic chuck (block) base (Indigo Scientific) is placed over the mould and topped with mineral oil to aid the polymerisation process overnight. The resin blocks were removed from the mould and placed at 100°C overnight to harden. The blocks were stored at 4°C until sectioning.

2.4.2 Sectioning and imaging

The blocks were mounted on to the HREM machine (Indigo Scientific) and sectioned until the beginning of the embryo specimen. The cut surface of the microtome is imaged through an Olympus MVX10 microscope with a JENOPTIK ProgGres GRYPHAX camera mounted over the microtome and block. The focus of the camera was adjusted on the sample in the first section the tissue was visible. The sectioning was then automated in synchrony with image capturing with UV light illumination, a fan was mounted onto the HREM machine and was continuously blowing air to prevent the freshly cut sections from obstructing the camera. Sectioning was set to 2.55 µm for all embryos in this project.

2.5 Reconstruction of embryos in 3D

2.5.1 Image processing

The raw images obtained from High-resolution episcopic microscopy (HREM) were colour-inverted and adjusted in Adobe Photoshop (2022) using Levels and Curves functions to ensure good contrast between the background and the sample. The images were further cropped to just the embryo and changed to 8-bit to reduce file size.

2.5.2 3D reconstruction

Processed datasets for each embryo were imported into the 3D image analysis software Dragonfly (Object Research Systems, version 2021.1). The resolution of the datasets was determined as 2.55 x 2.55 x 2.55 µm.

2.5.3 Limb bud staging

The embryos were staged according to limb bud development through an online system developed by (Musy *et al.,* 2018) called eMOSS which can be accessed at

https://limbstaging.embl.es/. The staging system relies on an image of a limb and user input of the limb outline. The polyline is matched to a database of pre-staged limbs from C57Bl6/J mouse embryos using the maximum likelihood principle which gives the parameters of an assumed probability distribution over different stages, the stage with the highest probability is taken as the "microstage" of the embryo (Boehm *et al.,* 2011). For each whole embryo reconstructed, the left hindlimb was used to input into the eMOSS system for their microstage (Figures 2.1A-L'). As at E13.5 only the hearts were embedded and sectioned, the left hindlimb was imaged through the dissecting microscope and at the time of dissection. For each outline, eMOSS would return a plot of the shape created by user-input outlines (grey circles in Figures 2.1B, E, H, K) and how they fit the lines within its database that were matched to embryonic stages (solid black line in Figures 2.1B, E, H, K). This was accompanied by two age probability graphs of each submitted image:

(1) The chi values (Figure 2.1C, F, I, L) indicate the reliability of the estimation where the higher the value the less reliable the estimation is, however, the value increases with age due to morphological variability.

(2) The probability density as a function of limb age (Figure 2.1C', F', I', L').

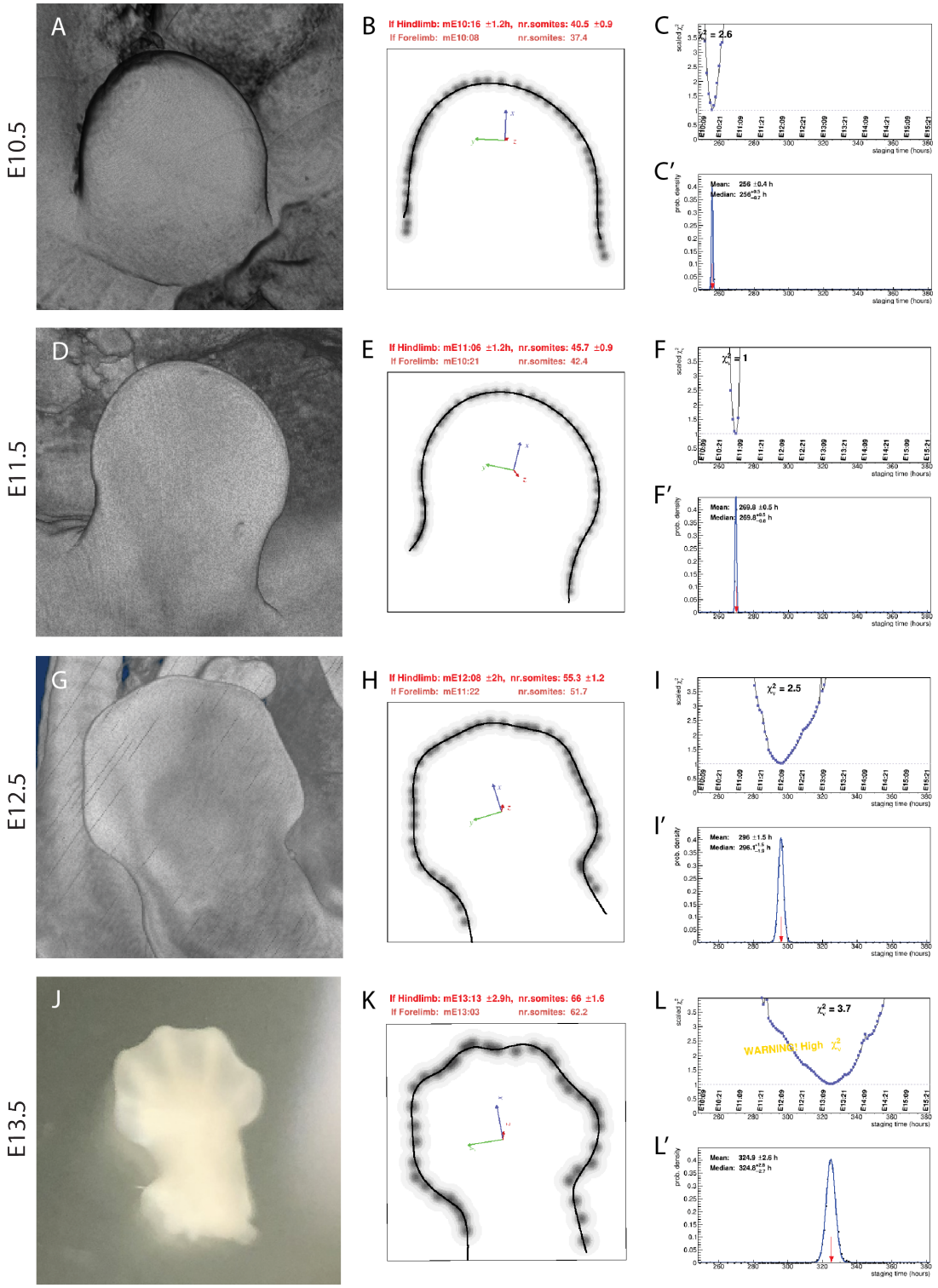

Figure 2.1 Limb-bud microstaging of E10.5 to E13.5 embryos. (A) E10.5 limb from a 3D reconstruction. (B) Points from user-input limb outline (dots) and closest matching limb from the database (line) for E10.5. (C-C') Embryonic age probability graphs for E10.5 limb example. (D) E11.5 limb from a 3D reconstruction. (E) Points from user-input limb outline (dots) and closest matching limb from database (line) for E11.5. (F-F')

Embryonic age probability graphs for E11.5 limb example. (G) E12.5 limb from a 3D reconstruction. (H) Points from user-input limb outline (dots) and closest matching limb from database (line) for E12.5. (I-I') Embryonic age probability graphs for E12.5 limb example. (J) E13.5 limb imaged from a microscope during dissection. (K) Points from user-input limb outline (dots) and closest matching limb from database (line) for E13.5. (L-L') Embryonic age probability graphs for E13.5 limb example.

2.6 Morphometric analysis

Morphometric analysis was performed on the processed 3D image data sets obtained from HREM.

2.6.1 Anatomical measurements

The HREM data sets were loaded into the Dragonfly software (Object Research Systems, version 2021.1). Each dataset was resliced in the right-ward sagittal orientation, the section plane was adjusted at an oblique until the plane was at the midline of mVS and in line with the crest of the structure. This plane was imported to FIJI for measurements of the length of the mVS and the morphometrics of the IVC. The IVC was measured first by using the "polygon selection" tool to outline the IVC. From this shape, the perimeter, area and circularity were recorded. A circle was fitted to this shape using its centroid as the circular origin and the radius was recorded. This circle was expanded, while keeping the same origin, to the outer edge of the mVS. The IVC circle radius was subtracted from the mVS circle radius to obtain the length of the septum.

2.6.2 Segmentation and mesh construction

In Dragonfly software (Object Research Systems, version 2021.1), the OFTCs were segmented from the images using "active contour" selections. This involved manually outlining the cushion perimeter at even intervals throughout the OFTC structure. The software interpolated the outlines between the manual input and was checked in every orientation after for correct boundaries, if it was not then more manual outlines would be added for better interpolation. These outlines were used to create a 3D

mesh that could be saved as a .stl file. The same was done for the mVS of the E12.5 embryos for the approximation analysis.

The .stl mesh files of the OFTC were imported into MeshLab (2021.05) where a bounding box was applied to each cushion mesh to record the length of the cushions. To measure the length of fused cushion at E12.5, the Measuring Tool in Meshlab was used to draw a line from the distal tip to the lowest point of the "dip".

In the creation of the E13.5 lumen meshes, a custom Python-based segmentation algorithm (Appendix §§8.1) was applied to the HREM data for Dp1Tyb and wild-type E13.5 hearts. The algorithm was written with Jon Smith (Software engineering and AI, the Francis Crick Institute). The resulting segmentation was then opened in ChimeraX (1.6.1) (Meng *et al.,* 2023) where a surface was created and saved as a .stl mesh. The mesh was cleaned in MeshLab (2021.05) by decimating the mesh to 10% of the points and the atrial lumens were removed. Isolation of the IVC "bridge" was achieved by building an alpha complex of the shape (Gardiner, Behnsen and Brassey, 2018) and removing the ventricles to isolate the bridge.

2.6.3 Centerline and cross-section analysis of meshes

Segmented E13.5 lumens described above were loaded in to 3D Slicer (version 5.6.1) for Windows (Fedorov *et al.*, 2012). The images were segmented by applying a mask over the binary structures and casted as a surface. The surface mesh was trimmed to just the IVC bridge. The extension Vascular Modelling ToolKit (VMTK) (version 144582e) was used to apply find the centerline using "Extract Centerline" by applying 2 end points on either ventricular end of the trimmed mesh. The VMTK tool "Cross-section Analysis" was then used to find the cross-sectional area and diameter. The data was saved as a .csv to access the minimum values for each metric.

2.6.4 Approximation analysis

The segmented septal OFTC cushion and corresponding mVS mesh for E12.5 embryos were imported into Python script (Python version 3.7.6) written to calculate the distance from points on one mesh to its closest neighbouring point on the second mesh. The distances can then be projected onto the first mesh to visualise these

values as a heatmap topography. With the septal OFTC and the corresponding mVS were segmented I input them into a Python script (Appendix §§8.2) that visualised the two objects and calculated the distance from points on the first mesh to its closest neighbouring point on the secondary mesh. This was achieved by organising the data with a 3D KD-tree (K-Dimensional Tree) using the Python SciPy library, this organised all the coordinates of every point (in x, y and z) on the meshes into K-dimensional space. The co-ordinates were partitioned into a data structure resembling a binary search tree using the values of each x, y and z coordinate, allowing for approximation of coordinates that are "clustered" in the same branch i.e. the closest neighbours of any given coordinate. Using this analysis, the closest neighbouring point on the secondary mesh was found for any point on the first mesh and the distance was calculated. As the data for each mesh pair was collected, I concatenated the data for Dp1Tyb and wild-type hearts into separate files to plot a histogram of the data. The script requires the following Python libraries: pyvista, scipy, numpy, os, pandas, seaborn.

2.6.5 Land-mark free morphometric analysis

Quantitative morphometrics analysis was performed on E13.5 OFTC meshes segmented from Dp1Tyb and wild-type hearts in Dragonfly. A wild-type mesh was selected as a reference mesh to align all the other meshes in the data set to. The meshes were registered using two different software. The initial alignment was made with GeoMagic software (2014) with the help of Dr Saorise O'Toole (King's College London) using N-Point Alignment, with 9 "landmarks" chosen to register to the reference mesh. The meshes were then aligned a second time with WearCompare software (O'Toole *et al.*, 2019) using broader areas.

Once aligned, the meshes were input into a Python-based land-mark free morphometric pipeline (Toussaint *et al.*, 2021) with the help of Dr Yushi Redhead. As the meshes were aligned with Geomagic and WearCompare, the meshes were entered into the atlas construction and shape statistics portions of the pipeline. The output meshes with volumetric changes and point displacements were visualised using Paraview (5.10.0).

2.7 Microtome sectioning

Embryos embedded in paraffin blocks were placed on a cold plate for an hour and trimmed with a razor blade to the appropriate size for the embryo. The block was then sectioned on a Leica RM2255 microtome with disposable microtome blades (Fisher Scientific, Epredia™ 3053835) Blocks were sectioned at 4 µm thickness, with every section from the start of the OFT to the end kept, sections were placed into a water bath of deionised water at 45°C before mounting on SuperFrost plus glass slides (Fisher Scientific, Epredia™ J1800AMNZ). The slides were placed in a 37°C oven overnight to dry.

2.8 Immunohistochemistry

All staining except for Alcian blue was stained using the Tissue-Tek Prisma® *Plus* autostainer (Sakura Finetek) and coverslip applied with the Tissue-Tek® Glas™ *g2* Automated Glass Coverslipper (Sakura Finetek).

2.8.1 Haematoxylin and eosin

Haematoxylin and eosin (H&E) staining was the histological technique used for paraffin-sectioned E12.5 embryos to visualise the OFTC anatomy. The slides were processed in the automatic stainer under the following protocol:

1. Xylene 2 x 2 minutes
2. Alcohol 100% 2 x 30 seconds
3. Alcohol 95% 1 x 30 seconds
4. Alcohol 70% 1 x 30 seconds
5. Water 1 x 30 seconds
6. Haematoxylin (Harris) 1 x 5 minutes
7. Water 1 x 1 minute 30 seconds
8. Acid alcohol 0.5% x 20 seconds
9. Water 1 x 1 minute
10. Scott's tap water x 1 minute
11. Water 1 x 1 minute

12. Eosin x 5 minutes
13. Water 1 x 1 minute 30 seconds
14. Alcohol 100% 3 x 30 seconds
15. Xylene 1 x 30 seconds
16. Xylene x 1 minute

2.8.2 Alcian blue and haematoxylin

Prior to staining, the Alcian Blue solution was prepared with 3% glacial acetic acid (in dH2O), 1% Alcian Blue solution (1g of Alcian Blue per 100ml of 3% acetic acid) at pH2.5 and 1% of freshly prepared periodic acid. The solution was then passed through filter paper to remove any remaining residue that could affect the staining. Paraffin sections were rehydrated in xylene with the following dewaxing protocol on the autostainer:

1. Xylene 2 x 30 seconds
2. Alcohol 100% 2 x 30 seconds
3. Alcohol 95% 1 x 30 seconds
4. Alcohol 70% 1 x 30 seconds
5. Water 1x 30 seconds

Rehydrated slides were placed in the Alcian Blue solution for 30 minutes and then under running tap water for 3 minutes followed by a 5-minute wash in dH2O. Slides were then counterstained with haematoxylin in the automatic stainer with the following protocol:

1. Water 1 x 30 seconds
2. Haematoxylin (Harris) 1 x 5 minutes
3. Water 1 x 1 minute 30 seconds
4. Acid alcohol 0.5% x 20 seconds
5. Water 1 x 1 minute
6. Scott's tap water x 1 minute
7. Water 1 x 1 minute
8. Alcohol 100% 3 x 30 seconds
9. Alcohol 100% 2 x 1 minute
10. Xylene 2 x 30 seconds

2.8.3 Image acquisition and analysis

Sectioned stained with H&E and Alcian blue and haematoxylin were imaged using the Zeiss Axio Scan.Z1 Slide scanner. This imaging modality allowed for automated imaging and multiplexing the slides, with up to 100 slides in one run. The images were acquired with the brightfield microscopy setting using the 10X objective. For each embryo, every fourth section was imaged, leaving a 12 µm gap between the acquired image and the next. All image analysis was performed in FIJI with custom-written macros for cell counting (Appendix §§8.3).

2.9 Immunofluorescence staining

DAPI (Sigma Aldrich, D9542) at dilution 1:10000 in dH2O was used as the nuclear counterstain for all the immunofluorescence-stained slides.

2.9.1 Staining for Sox9, TUNEL, and Phospho-histone3

TUNEL staining was achieved with the Click-iT™ Plus TUNEL Assay Kit, Alexa Fluor 647 dye (Fisher Scientific, Invitrogen™ C10619) with the supplied protocol adapted and optimised for this experiment. Paraffin sections were rehydrated by xylene following the above protocol on the autostainer. 100 µm of 4% PFA was added to each slide with a pipette and placed into a humid chamber at 37°C for 10 minutes. Slides were then washed 2 x 5 minutes in PBS and placed in boiling citrate butter (2.8 ml 1M citric acid, 12.75 ml 1M sodium citrate, filled to 1.4 L dH2O) in the microwave or a further 10 minutes at lower power for antigen retrieval. Slides were allowed to cool down to room temperature in the citrate buffer solution. Slides were washed 3 x 5 minutes PBS and 1 X 5 minutes in dH2O. 100 µl of TdT reaction buffer from the TUNEL kit was added to each slide and allowed to incubate for 10 minutes at 37°C while the following TdT mixture was prepared for 25 slides: 1175 µl TdT Reaction Buffer, 25 µl EdUTP, 50 µl TdT enzyme. The slides were tapped onto tissue to remove excess buffer before applying 50 µl of the prepared TdT mixture to every slide and incubating for 1 hour at 37°C in a humid chamber. Slides were then washed in dH2O for 5 minutes, PBS + 0.1% TritonX100 (Sigma Aldrich, X100-1L) (PBST) for

5 minutes and PBS for 5 minutes. The following TUNEL reaction buffer was prepared and vortexed for 25 slides while the slides were washing: 1125 µl Click-iT plus TUNEL Supermix and 125 µl 10X Click-iT Plus TUNEL Reaction Buffer Additive. The reaction buffer was immediately added to the slides and incubated for 30 minutes at 37°C in a dark humid chamber. After the incubation, the slides are rinsed in PBS for 5 minutes and blocked with 5% goat serum (Sigma Aldrich, G9023) in PBST for a minimum of 1 hour. The slides were rinsed in PBS for 5 minutes before applying 1:250 rabbit anti-Sox9 (Sigma Aldrich, AB5535) and 1:300 mouse anti-Phospho-Histone H3 (Ser10) (6G3) (Cell Signalling Technology, 9706) in 5% goat serum PBST overnight in a dark humid chamber at 4°C.

The following day, slides were rinsed in PBST 2 x 5 minutes before adding the secondary antibodies and incubated for 1 hour at room temperature in a dark humid chamber. The secondary antibodies used were Goat anti-Mouse IgG H&L Alexa Fluor 488 (Abcam, ab150113) and Goat anti-Rabbit IgG H&L Cy3 (Invitrogen, A10520). The slides were then washed 2 x 5 minutes in PBST then 2 x 5 minutes PBS before adding 1:10000 DAPI to counterstain nuclei for 10 minutes at room temperature in a dark humid chamber. The slides were washed for the time with 2 x 5 minutes in PBST then 2 x 5 minutes PBS before adding the coverslip (VWR, 631-0147) was added with VectaMount Aqueous Mounting Medium (Vector Laboratories, H-5501-60).

2.9.2 Staining for Sox9 and YAP

Immunofluorescence staining for Sox9 and YAP was achieved through the Leica BOND-III Fully Automated IHC and ISH Staining System using rabbit anti-Sox9 (Sigma Aldrich, AB5535) and rabbit anti-YAP (D8H1X) (Cell Signalling Technology, 14074) primary antibodies. Anti-Sox9 antibody was used with a dilution of 1:500, followed by 20 minutes of antigen retrieval with ER1 and an Opal 520 secondary antibody (Akoya, FP1487001KT) at 1:500 dilution. The anti-YAP antibody was used at a dilution of 1:200, followed by a 20 minute antigen retrieval with ER2 and Opal 570 secondary antibody (Akoy, FP1488001KT) at 1:500 dilution. This staining was carried out by Experimental Histopathology at the Francis Crick Institute.

2.9.3 Image acquisition and analysis

All immunofluorescence stainings were imaged using the Zeiss Axio Imager.Z1 fitted with the Zeiss Apotome.2 unit using the 10X and 20X objectives. All images were acquired using the same laser intensity, gain and exposure. Acquired images were acquired and pre-processed using Zeiss Zen Microscopy Software. For each embryo immunolabelled with TUNEL, SOX9 and PPH3 immunofluorescence, every eighth section was imaged, leaving a 32 µm gap between the acquired image and the next.

2.10 Immunofluorescence image analysis

All image analysis was performed within FIJI software and R (2023-03-0).

2.10.1 Nuclear segmentation with StarDist

StarDist (Schmidt *et al.*, 2018; Weigert *et al.*, 2020) was used for automated segmentation of the nuclei in the DAPI channel. Briefly, StarDist is a deep-learning model that can be user-trained to automatically segment star-convex shapes. I trained the model using my DAPI images in a serverless Jupyter Notebook on "Google Colaboratory". The notebook can be accessed at:
https://colab.research.google.com/github/HenriquesLab/ZeroCostDL4Mic/blob/master/Colab_notebooks/StarDist_2D_ZeroCostDL4Mic.ipynb
Further details on how I trained my deep-learning model of StarDist is described in §§5.2.3. Once the nuclei were segmented, X-Y coordinates of each nuclear centroid were saved on FIJI as a .csv file that was imported into an R script written to automate the extraction and concatenation of data (Appendix §§8.4).

2.10.2 Sox9 expression intensity

The nuclear mask generated from Stardist was applied to the Sox9 channel and the mean fluorescence intensity (MFI) was saved for each nuclear mask. Concurrently, an area of Sox9 negative tissue in the heart was chosen to record the background signal for Sox9 negative nuclei by applying the StarDist model and measuring the

maximum fluorescence signal in the Sox9 channel. The number of Sox9-positive cells was determined by any cell with an upper-quartile signal (based on the minimum and maximum values within individual nuclear masks) higher than that of the maximum background value. The group of Sox9 positive cells were further split into high signal and low signal by normalising all remaining intensity values between 0 and 1, values below 0.5 were placed in the low signal group and values above 0.5 were placed in the high signal group. This calculation was done through an R script where other data was concatenated alongside (Appendix §§8.4).

2.10.3 Cell density and inter-nuclear spacing

The area was calculated by the border of the Sox9 cells in the cushion and divided by the number of nuclei from the nuclear segmentation to give the cell density as cells/μm^2. Internuclear spacing analyses were performed in R by amending a script previously developed in the Green lab (Economou *et al.*, 2013; Brock *et al.*, 2016). The script extracts the X-Y coordinates from the nuclear segmentations described in §§2.10.1 and applies the internuclear spacing script to it. The Deldir package identified the nearest neighbouring nuclei to each nucleus and drew a line between the centroid and its neighbours' centroids. From this, the average distance between each nucleus centroid to its neighbours was calculated. These values were then assigned a colour code on a user-defined scale, which was visualised through a double corona connecting each centroid to the neighbouring centroids with Voronoi tessellation. This tiles the image with polygons which were in turn coloured using the colour code for each cell, thus generating a heatmap of internuclear spacing. Expanding on the original R script, I extracted the individual values for the average distance between each cell and its neighbours which could be averaged to give a numerical value of average internuclear spacing throughout the queried region (Appendix §§8.4).

2.10.4 Phospho-Histone H3

PHH3-positive cells were counted in FIJI and compared to the Sox9 image channel to determine whether the PHH3-positive cell was also Sox9-positive.

2.10.5 TUNEL quantification

TUNEL staining was thresholded using “Otsu” filter in FIJI for each section. The thresholded image was binarized and then analysed for the size of each puncta and the number of puncta. Within the R script mentioned above, data for each section would be extracted and calculated for the average puncta size and number of puncta for each section (Appendix §§8.4).

2.11 Atomic force Microscopy

Atomic force microscopy (AFM) and analysis of generated force curves were performed by Olivia Courbot, Elosegui-Artola Lab (the Francis Crick Institute).

2.11.1 Tissue preparation

Embryos were harvested from crosses of Dp1Tyb mice to C57Bl6 mice at E12.5 and E13.5. The embryos were immediately placed in ice-cold PBS and dissected out of the uterine sac. The yolk sac and tail were used for genotyping through Transnetyx so the experiment was performed blind to genotype. The embryonic hearts from each embryo were dissected using fine-tipped forceps, the OFT was dissected from the hearts with a micro scalpel. The OFT was further bisected into the distal and proximal halves and mounted onto 35 mm glass bottom Petri dishes (ibidi, 81158). Prior to dissection these dishes were coated with 5 µm of the tissue-substrate adhesive Cell-Tak (Corning, 354240) in a laminar flow hood and left to dry. Each half of the OFT was mounted on the dish with the bisected axis facing downwards, excess PBS was aspirated from the tissue. Droplets of PBS were pipetted on the sides of the dish to keep the environment humid as the tissue was allowed to adhere dish for 2 hours at 4°C. Immediately before probing with the AFM, the samples were gently flooded with room-temperature PBS.

2.11.2 Atomic Force Microscopy

AFM was performed by Olivia Courbot using the AFM NanoWizard 4 (Bruker) mounted onto a Zeiss LSM 710 Confocal Microscope with a motorised precision stage. A pre-calibrated rectangular cantilever with a 5μm spherical bead was used (Bruker, SAA-SPA-5UM). The sensitivity was s=9.09nm/V and the spring constant (pre-calibrated) was k=0.152N/m. The sensitivity was measured using contact-free calibration with the software JPK SPM v7.0 using thermal noise measurement.

2.11.3 F-D curve generation and analysis

Force curves were generated from a mapping grid of 10 x 10 points over a 10 μm x 10μm area (i.e. 1 μm intervals). For each sample, two mapping grids were placed in the centre of the tissue as much as possible to ensure cushion tissue was being measured and not the myocardium. Young's modulus was calculated using a Hertz Model for each force curve in the 10 x 10 grid. Force curve analysis was performed with the JPK SPM Data Processing software v7.0.173 under "Hertz-fit" analysis. Some curves were rejected if they were noisy, demonstrated adherence to tissue or did not achieve a constant baseline. This analysis was subject to the expertise of Olivia Courbot, who screened all generated force curves.

2.12 Statistics

All statistical analysis was performed using GraphPad Prism version 9.5.1 for Mac under the Francis Crick Institute licence, GraphPad Software, Boston, Massachusetts USA, www.graphpad.com. All statistical tests used are stated in the legend of each figure panel or text. Numerical P-values are shown in the relevant graphs. A P-value of <0.05 was taken as statistically significant in all analyses.

Chapter 3. Analysis of the morphological changes leading to ventricular septation in Dp1Tyb hearts

3.1 Introduction

As described in detail in Chapter 1, the primitive heart tube continually remodels through looping and ballooning to become a more recognisable 4-chambered structure between E10.5 and E14.5. The anatomical changes through heart development were initially described in histological sections at different embryonic stages and inferring the changes that occur between them. However, since the heart has a complex three-dimensional structure, it is difficult to capture these developmental changes in just one orientation or sectioning plane.

Other studies have tracked heart development in 3D using techniques such as micro CT, but until recently such images were not high enough resolution to type cardiac defects (Li-Villarreal *et al.*, 2023). An imaging modality that has provided the resolution needed to reconstruct high-fidelity 3D embryonic data is high-resolution episcopic microscopy (HREM) (Weninger *et al.*, 2006, 2014; Mohun and Weninger, 2011). This technique has been used by the Tybulewicz lab to identify different CHD in Dp1Tyb embryos at E14.5 (Lana-Elola *et al.*, 2016) and was thus a suitable choice to explore the development of Dp1Tyb hearts prior to this stage.

In the mouse, ventricular septation happens between E10.5 and E14.5 after heart looping has occurred. At approximately E10.5, the primitive mVS begins as a bud on the floor of the common ventricle. This structure grows cranially towards the inner heart curvature where it begins fusing to the septal OFTC at approximately E12.5, located at the top of the IVC (Mohun and Anderson, 2020). The OFTCs continue to fuse with the septum over the next embryonic day (E13.5) until the AVC push into the remaining IVC and close it, together forming the membranous septum. The approximation of these structures and their fusion to form the final ventricular septum is, perhaps surprisingly, not well defined.

While there is plenty of literature on the occurrence and types of CHD identified in other mouse models of Down Syndrome (Shinohara *et al.*, 2001; Dunlevy *et al.*, 2010; Liu *et al.*, 2011b; Lana-Elola *et al.*, 2016), there appear to be no thorough 3D developmental studies on heart development in these models for stages prior to

typing the different defects, typically at E14.5 or later. As CHD are a consequence of these septation events not occurring properly, there are likely to be structural abnormalities prior to phenotyping the defects at E14.5 that could, in principle, be detected with a systematic characterisation of the ventricular septation process in earlier embryonic stages.

In this chapter, I therefore set out to capture the process of ventricular septation in embryos aged E10.5-E13.5 in 3D by exploiting HREM imaging to characterise the anatomical changes taking place and compare them in Dp1Tyb versus wild-type embryos. I was able to directly compare the developmental processes of the two genotypes to not only have detailed tracking of the structural changes in normal septation (with publication of similar descriptions coinciding with these studies (Anderson *et al.*, 2019; Mohun and Anderson, 2020)) but also to determine if this differs in the mutant, and at what time point in the process any anatomical abnormalities can be identified. By using microstaging techniques to break down the developmental timeline while describing the anatomical changes, I was also able to analyse if the pacing of ventricular septation differs between the genotypes and control for intra-litter developmental age variability.

3.2 Results

3.2.1 Utilising High Resolution Episcopic Microscopy to visualise ventricular septation

The HREM technique was used in this study to assess the structural anatomy of developing wild-type and Dp1Tyb embryos to characterise how the IVC closes and whether this was anatomically different in the mutant embryos. I collected embryos from wild-type females crossed to Dp1Tyb males at E10.5, E11.5, E12.5 and E13.5 with the assumption that conception would occur at midnight (Figure 3.1).

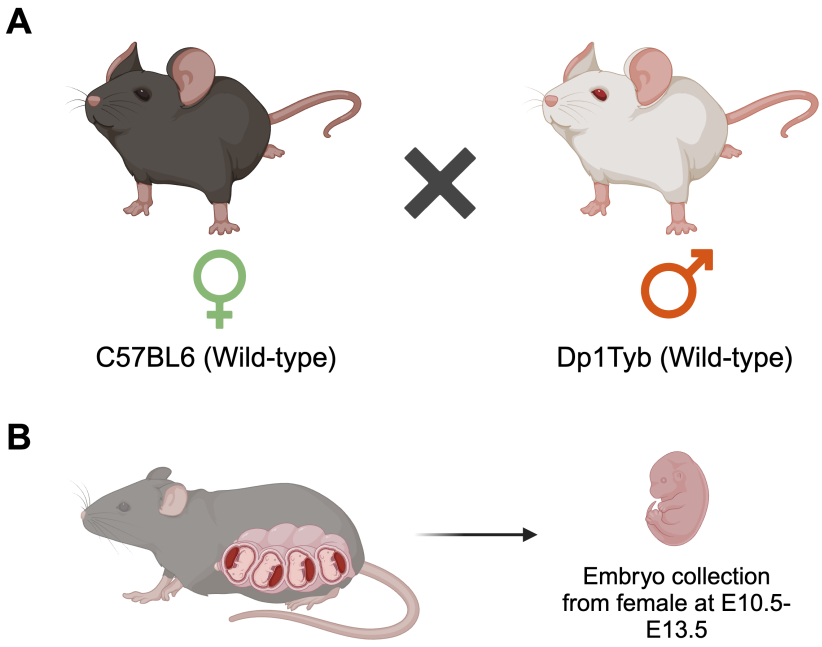

Figure 3.1 Diagram of mouse cross for Dp1Tyb mouse embryos. (A) Female C58BL6 (wild-type) mouse was crossed to male Dp1Tyb mouse to produce embryos. (B) Female mouse was sacrificed to obtain embryos at E10.5, E11.5, E12.5 and E13.5; embryos obtained were either wild-type or Dp1Tyb genotype.

Dissected embryos were fixed, as described in the Methods chapter, in 4% PFA for 15 minutes and then treated with distilled water for an hour to lyse red blood cells, before fixing in 4% PFA overnight. This method does not arrest the heart consistently in diastole, which may have produced some anatomical variability between samples. The embryos were prepared for HREM by dehydration and incubation in the embedding medium, an eosin-dyed methacrylate resin, JB4. The dyed JB4 creates high contrast between the tissue and the remainder of the resin block but also permeates different tissues to differing degrees to provide some histological differentiation. The HREM machine consists of an automated microtome mounted such that the cut face of the block can be imaged with a camera to capture every successive surface cut by each strike of the blade, creating a data set of images that are perfectly in register (see Figure 3.2 for a flow diagram of the protocol). These images preserve the anatomical structure of the samples but do not provide cellular resolution.

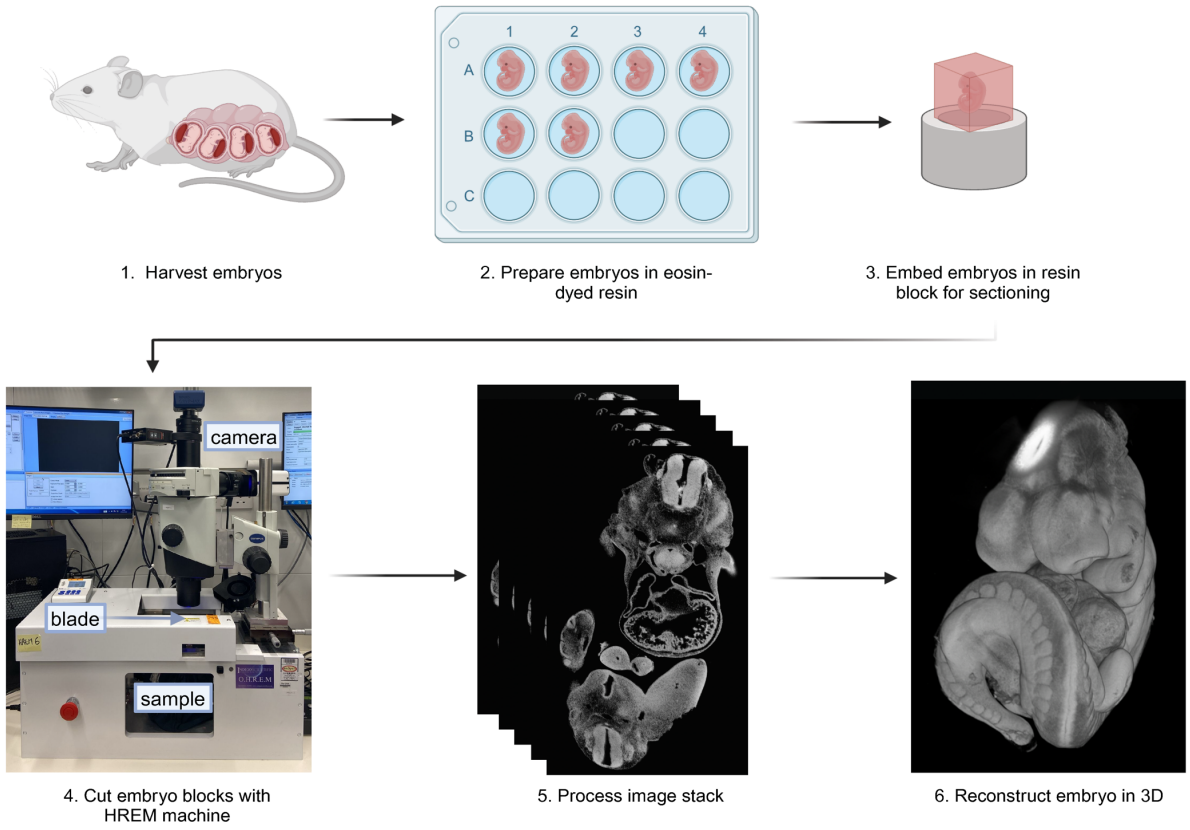

Figure 3.2 Processing embryonic samples with High-Resolution Episcopic Microscopy. The diagram shows a schematic representing the process starting with harvesting the embryos from the pregnant female (1), incubating the embryos in the resin fluid (2) and a cured resin block containing an embryo embedded within (3). The next steps show an image of the HREM machine set-up with the camera and microtome blade components (4), the collected and processed image stack (5) and the final reconstruction of the image stack in 3D (6).

For embryonic stages E10.5 to E12.5, whole embryos were embedded, cut and imaged, which took approximately 7-8 hours per block using 2.55 µm z-steps. At E13.5 the heart was dissected from each embryo and embedded on its own. This was unavoidable due to the embryos becoming too large to fit within the embedding trays, but it also provided two benefits in streamlining the process: firstly, two hearts could be embedded in the same block, and, secondly, the time taken to cut the blocks was reduced to approximately 3 hours. As HREM section images are fully in register, entire embryos and hearts could be reconstructed in 3D with no anatomical deformation using Dragonfly software. Dragonfly further allowed for seamless

reorientation of slicing planes, so the embryos could be viewed in any orientation and saved as a new stack in that plane. An example of a fully reconstructed embryo can be seen in Figure 3.3A, with the same embryo rotated to the frontal plane recessed until the heart is visible (Figure 3.3B).

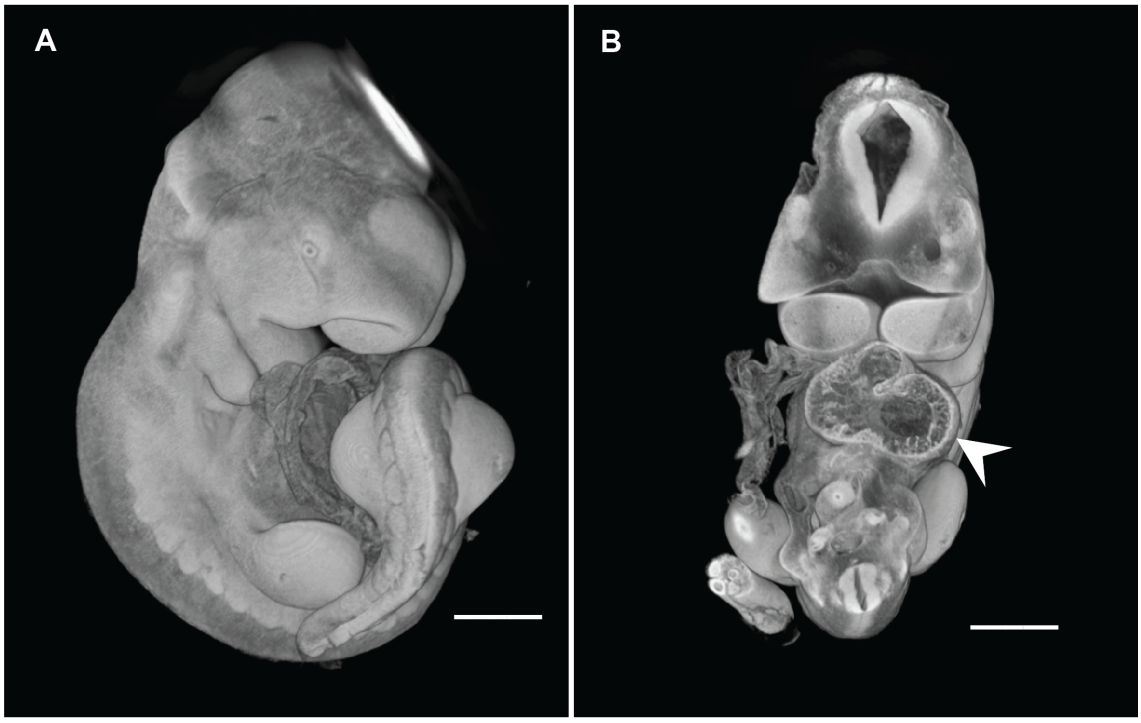

Figure 3.3 Reconstruction of an E10.5 embryo from High-Resolution Episcopic Microscopy. (A) 3D reconstruction of an E10.5 embryo viewed from the right. (B) The same embryo recessed into the frontal plane to show the heart structure (white arrowhead). Scale bars are 500 μm.

With whole embryos reconstructed, I was able to use other parts of the anatomy than the heart to assess what stage the embryos were with finer temporal resolution than just the day of harvesting. I wanted to achieve more precise staging of the embryos during ventricular septation for consistency and to be able to detect variation in the timing of closely-spaced events, with the final stages of septation and fusion of endocardial cushions and mVS occurring in a 48-hour time window between E12.5 and E14.5. In addition to this, embryos within the same litter have been reported to develop at different speeds (Miyake *et al.*, 1996) and the rate of embryonic development also varies according to the mouse strain used (Miyake *et al.,* 1997). The time of harvest was kept consistent throughout the collection of this

data, with sacrifice and harvest occurring at 13.30 GMT. Regardless, the embryos in this chapter were staged according to limb bud development through an online system called eMOSS (Musy *et al.*, 2018).

The spread of embryonic ages for the collected embryos from a given nominal stage meant that many of the developmental stages from different embryonic days overlapped (Table 3.1). For example, the minimum age for a Dp1Tyb embryo collected at E12.5 is younger than the oldest E11.5 Dp1Tyb embryo. E12.5 embryos also appeared to have the largest age range of any of the collected stages, spanning 1.25 and 1.75-day ranges in wild-type and Dp1Tyb groups respectively, whereas no other collected stage had age ranges over 1 day. Aside from actual intra-litter variability in age, some variability clearly arose from the software itself: slightly different angles in the picture of the hindlimb submitted and the number of points used to construct the linear outline of the limb were two factors I noticed impacting the staging. To try and reduce variability from these two factors I checked the orientation of the limb to be as flat as possible in the image by rotating and rolling the 3D image. When outlining the limb, I ensured that I was using a minimum of 25 points for any given image. Finer temporal resolution of embryonic age means that I can disaggregate any morphological changes that would be due to differing developmental age within a collected stage from real changes occurring due to the genotype.

Embryonic Stage	Genotype	Minimum age (days)	Maximum age (days)	Age range (days)	Mean age + SEM (days)
E10.5	WT	10.04	10.29	0.25	10.14 ± 0.04
	Dp1Tyb	10.08	10.63	0.55	10.23 ± 0.04
E11.5	WT	10.50	11.25	0.75	10.96 ± 0.07
	Dp1Tyb	10.67	11.25	0.58	10.96 ± 0.04
E12.5	WT	11.58	12.83	1.25	12.07 ± 0.11
	Dp1Tyb	11.13	12.88	1.75	12.09 ± 0.11
E13.5	WT	14.00	14.00	0.00	14.00 ± 0.00
	Dp1Tyb	13.38	14.13	0.75	13.88 ± 0.08

Table 3.1. Age of limb-bud staged embryos collected from E10.5 to E13.5 for wild-type and Dp1Tyb embryos. The table shows the minimum and maximum ages for all embryos staged by limb morphometry in eMOSS and the mean and range for each embryonic stage collected. E10.5 – wild type n = 5, Dp1Tyb n = 17; E11.5 – wild-type n = 11, Dp1Tyb n = 16; E12.5 – wild-type n = 12, Dp1Tyb n = 16; E13.5 – wild-type n = 3, Dp1Tyb = 9.

Limb-based micro-stage is plotted against harvest day in Figure 3.4. Though the spread of the microstages for each embryonic stage was variable, there was no statistical difference found between the two genotypes when tested ($p > 0.05$, Mann Whitney U-tests). Thus, there was no evidence of a general developmental retardation in the Dp1Tyb embryos versus wild-type littermates. With the caveat that there can be discrepancies in stage between different body parts, I proceeded to use both the microstage (also referred to as the embryonic age) from limb-bud staging and the traditional embryonic stage for quantification.

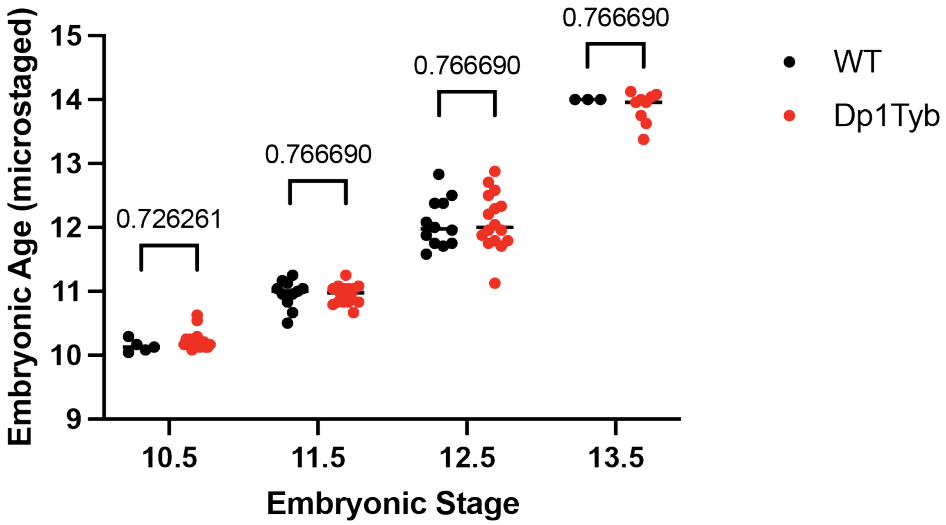

Figure 3.4 Microstage comparison of wild-type and Dp1Tyb embryos within collected embryonic stages. A graph showing the spread of embryonic ages of wild-type and Dp1Tyb embryos staged by limb bud morphology, the samples were collected at E10.5, E11.5, E12.5 and E13.5. Statistics performed with Mann-Whitney U tests. E10.5 – wild type n = 5, Dp1Tyb n = 17; E11.5 – wild-type n = 11, Dp1Tyb n = 16; E12.5 – wild-type n = 12, Dp1Tyb n = 16; E13.5 – wild-type n = 3, Dp1Tyb = 9.

3.2.2 Interventricular septation in Dp1Tyb hearts

Using the reconstructed embryos and hearts described previously, I isolated the hearts to quantify two main metrics: the shape of the IVC and the length of the mVS. The rationale behind measuring the IVC and its shape was to investigate the size of the remaining communication between the two genotypes at the same developmental stage, thereby assessing how much ventricular septation had progressed and if this was impacted in the Dp1Tyb embryos. In measuring the mVS length, I was able to determine if the overall growth of the mVS differed in the mutants.

To define the mVS, I utilised the plane reslicing function in Dragonfly to find the mid-sagittal plane of the heart where the mVS consisted of as much solid (i.e. untrabeculated) myocardium as possible. I assumed that the smallest foramen of the IVC would be in the same plane for stages E10.5 to E12.5 but not E13.5, when the smallest IVC foramen is at an oblique angle to the apical mVS structure; this particular stage will be explored and discussed further in the chapter using a different quantitation.

Heart morphology changes greatly within the studied stages, going from an unseptated structure to forming discrete chambers by partitioning with the growth of a muscular wall, all while ballooning and growing in proportion to the rest of the embryo (Moorman *et al.*, 2003).

In wild-type and Dp1Tyb hearts at E10.5, the gross morphology of the heart appeared similar. The wild-type heart had a fully unseptated common ventricle with a ventricular bud at the caudal floor of the ventricles (Figure 3.5A) and in the sagittal plane from the righthand side, the IVC remained rounded and unrestricted (Figure 3.5B). The Dp1Tyb E10.5 hearts showed a similar anatomy in the frontal plane with the presence of a ventricular bud in a common ventricle (Figure 3.5C), and the same rounded IVC foramen in the sagittal plane (Figure 3.5D). At E10.5 in both genotypes, the mVS appeared to be somewhat trabeculated with a number of lumens, but these were small and dispersed, unlike the extensive trabecular voids found on the inner walls of the ventricles.

By E11.5, the mVS had become a more substantial structure. As can be seen in the wild-type heart at E11.5 in the frontal plane (Figure 3.5E), the clear lumen of the common ventricle had become smaller, with the trabecular network becoming much more extensive. The mVS had also grown cranially towards the inner heart curvature where the medial wall of the proximal OFT bends as it exits from the primitive right ventricle. In the sagittal plane, the E11.5 hearts of both genotypes exhibited a more developed mVS with a more solid myocardial structure compared to the previous stage (Figures 3.5E-H), the IVC had become smaller and less round as the superior and inferior AVC began to extrude into the IVC.

In the next stage collected, E12.5, the crest of the mVS started to contact and initiate fusion with the proximal septal OFTC, this process is described in the literature (Mohun and Anderson, 2020) as happening at E12.5. In the wild-type frontal plane, the ventricular trabeculation-free lumen was increasingly restricted as the trabeculation extends far into the lumen in comparison to the previous stage; however, the mVS became a more discrete solid structure (Figure 3.5I). In the wild-type sagittal plane, the mVS appeared structurally similar to E11.5 but taller, the biggest change is the change in the shape of the IVC where the foramen shape was non-circular as the superior atrioventricular cushion continues to push into the IVC space in preparation for completing ventricular septation (Figure 3.5J). These

observations in the Dp1Tyb heart were the same in the frontal plane (Figure 3.5K) as was the midsagittal view (Figure 3.5L).

The final stage of heart development collected for this study was E13.5. The heart at this stage was a much more recognisably adult-heart-like structure, with two almost-discrete ventricles, septating atria and arterial vessels developing from the distal OFT. Wild-type hearts in the frontal plane showed the mature mVS as a solid structure with a small distance between its crest and the atrioventricular and OFTCs immediately above (Figure 3.5M). Sectioning the image in the plane of the mVS (previously defined as the midsagittal plane) did not always capture the foramen (IVC) at its narrowest point (Figure 3.5N) due both to the now-complex shapes of the cushions and ensuring the correct remodelling of the pulmonary and aortic outlets.

In the Dp1Tyb E13.5 hearts, the anatomy was indistinguishable from the wild-type in both the frontal plane (Figure 3.5O) and the sagittal (Figure 3.5P). The apparent discrepancies at E13.5 between the plane of the smallest foramen and the mid-plane of the mVS suggested that to connect the developmental trajectory of the Dp1Tyb embryos with its failure to close the ventricular foramen, a different approach to quantifying the foramen patency was needed at this stage.

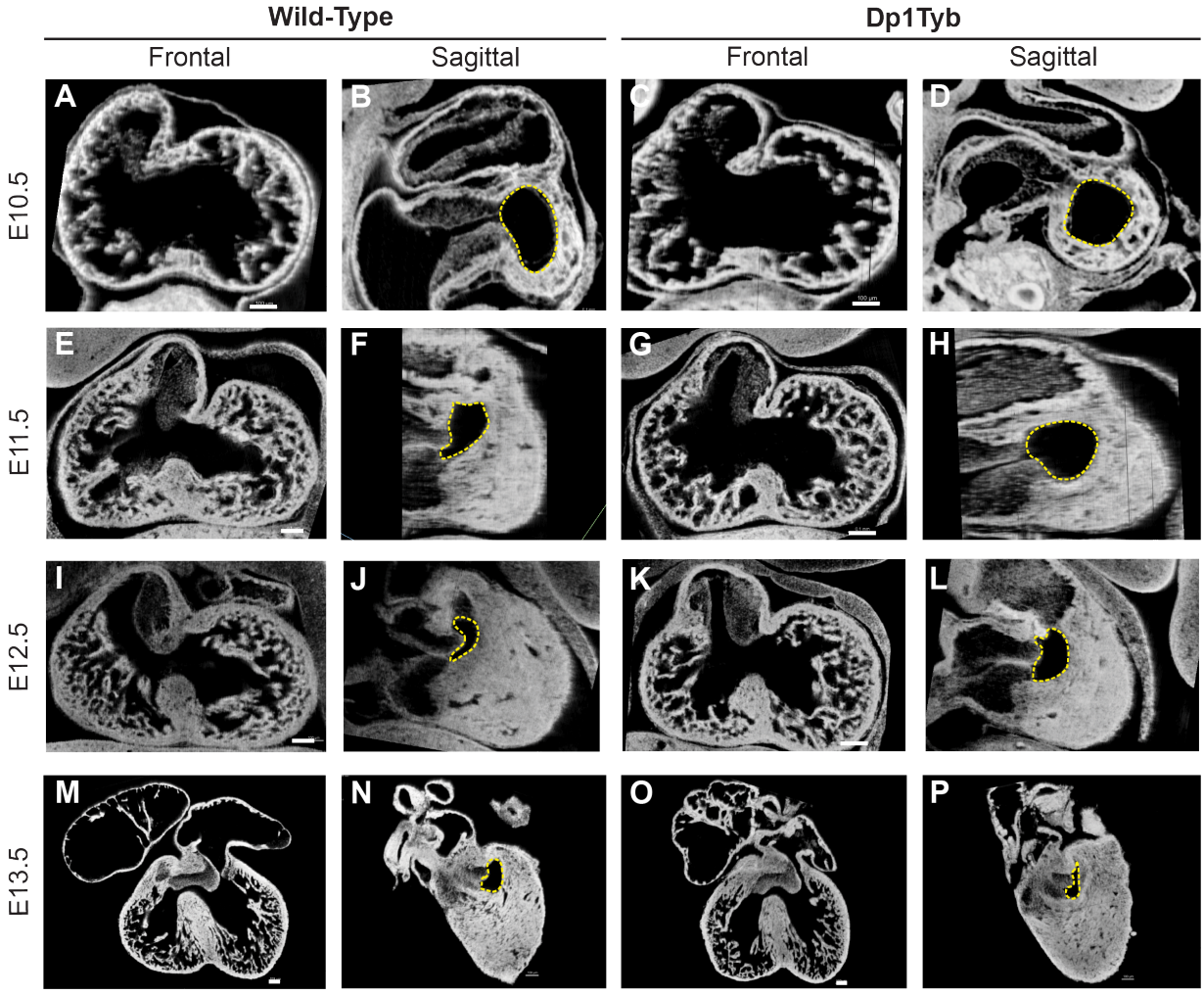

Figure 3.5 High-resolution episcopic microscopy images of wild-type and Dp1Tybe hearts from E10.5 to E13.5. Interventricular communication outlined in yellow. (A) Frontal section of a wild-type E10.5 heart. (B) Sagittal section of an E10.5 wild-type heart. (C) Frontal section of E10.5 Dp1Tyb heart. (D) Sagittal section of E10.5 Dp1Tyb heart. (E) Frontal section of a wild-type E11.5 heart. (F) Sagittal section of an E11.5 wild-type heart. (G) Frontal section of E11.5 Dp1Tyb heart. (H) Sagittal section of E11.5 Dp1Tyb heart. (I) Frontal section of a wild-type E12.5 heart. (J) Sagittal section of an E12.5 wild-type heart. (K) Frontal section of E12.5 Dp1Tyb heart. (L) Sagittal section of E12.5 Dp1Tyb heart. (M) Frontal section of a wild-type E13.5 heart. (N) Sagittal section of an E13.5 wild-type heart. (O) Frontal section of E13.5 Dp1Tyb heart. (P) Sagittal section of E13.5 Dp1Tyb heart. Scale bars are 100 μm.

To quantify the narrowing of the IVC and the growth of the mVS in both genotypes, I initially used the sagittal planes of the embryo/heart defined as the mid-plane of the mVS (Figure 3.6A). Once this plane was found I imported the image into

FIJI for analysis. The metrics of the IVC were obtained by outlining the foramen as a region of interest (ROI) (yellow dashed line in Figure 3.6B) and analysing the shape to acquire the area, the perimeter, and the circularity. Since the mVS has a saddle-shaped surface where it forms the ventricular limit of the IVC and an ill-defined base where it joins the heart wall at the bottom of the ventricles, measurement of its height would be very sensitive to the angle of the line used to take that measurement in the sagittal plane. To avoid subjectivity, I devised the following procedure: With ROI selected, I used the function “Fit Circle” to obtain a circular approximation of the IVC ROI and calculate the radius by halving the diameter of the circle (Figure 3.6B, blue circle with radius denoted with blue double-headed arrow). Using the same circle, I expanded the shape to the outer perimeter of the caudal mVS while keeping the origin the same (Figure 3.6B, green circle with radius as green double-headed arrow), then calculated the radius the same way. The length of the mVS was calculated by subtracting the radius of the IVC-fitted circle from the radius of the larger circle encapsulating the mVS.

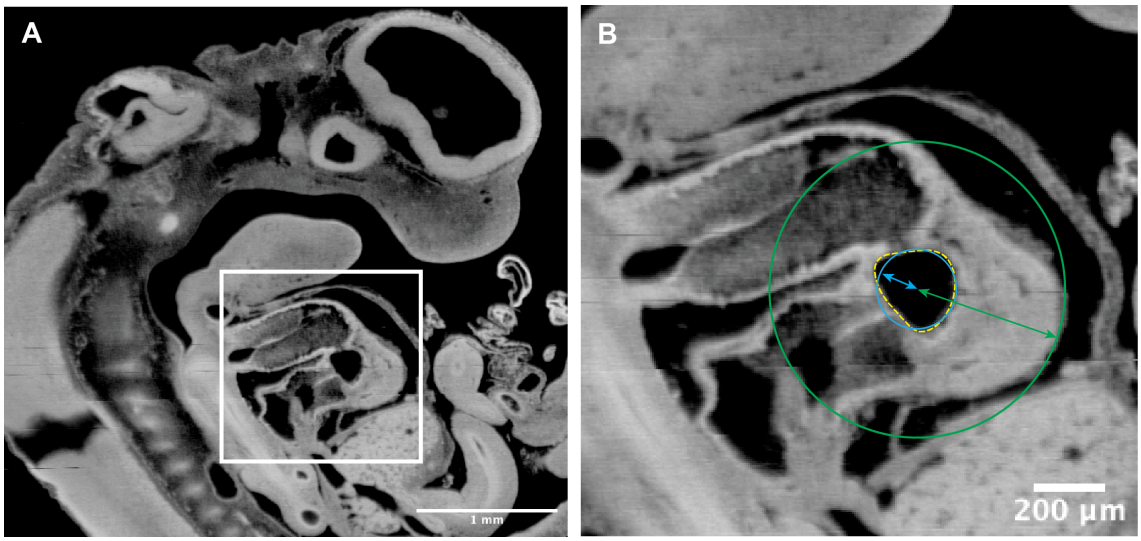

Figure 3.6 Strategy for measuring interventricular communication and muscular ventricular septum growth. (A) A sagittal section of an E11.5 heart with the heart outlined by the white square. (B) Inset of the white square from (A) with the heart, the yellow dashed line shows the perimeter of the interventricular communication, the blue circle is fitted to the communication and its radius is shown with the double-headed blue arrow, the green circle shows the enlargement of the blue circle until it reaches the outer edge of the muscular septum of the heart with the double-headed green arrows indicated the circle’s radius.

There was a wide variance in the area of the IVC in the earlier embryonic stages, but the mean area remained similar at approximately 0.04 mm^2 between E10.5 and E11.5; the IVC narrowed and decreased measurably at E12.5 before almost closing up at E13.5 (Figure 3.7A). In all 4 embryonic stages observed, there was no apparent difference in the area of the IVC between wild-type and Dp1Tyb hearts. This was highly surprising, given that the VSD phenotype of Dp1Tyb scored at E14.5 definitively implies a genotype-dependent IVC size difference just one day later. Although the phenotypic difference could be due to a very late effect (see below), it was possible that real, albeit small, differences might have been masked by experimental variability. The variability of the area in each embryonic stage and the lack of difference between genotypes was still present when the measurements were matched to embryonic age from limb-bud staging (Figure 3.7B). For example, many E10.5 samples in both genotypes were clustered closely in age but the IVC area ranged from as little as 0.01 mm to nearly 0.06 mm. Explanations of this may be from natural variation within the population, the heart developing at a different rate from the limb bud, and/or some inconsistency in the planes of the section from sample to sample. The section plane used for measurement was found through tilting the erosion plane back and forth and cross-checking in the frontal plane to ensure a mid-sagittal section. The latter point is more explanatory in the earlier stages given that the main landmark I used to find the plane is the midline of the mVS, which was not fully formed and recognisable at E10.5. At the final stage collected (E13.5), some embryos appeared to have almost closed the IVC but others had not, despite being microstaged to E14.0, even though it is described that chamber septation is completed at E14.5. As previously mentioned, these could be due to the plane at which the measurement was taken as the smallest foramen remaining was not always at the crest of the mVS.

The perimeter of the IVC area surprisingly did not vary much between any of the stages nor was there a statistical difference between wild-type and Dp1Tyb hearts (Figure 3.7C). As described in Figure 3.5, the IVC changed from the circular shape seen at E10.5 and E11.5 to a progressively more folded crescent shape from the AVC extruding into the IVC space after E12.5 (Figures 3.7J and L). This resulted in the perimeter not decreasing with the area as the foramen took on a more complex shape in the later stages. When the values were matched to its microstage, the downward trend in the perimeter length in both genotypes was not much smoother

than when discrete day-stages were used and did not reveal any difference associated with genotype (Figure 3.7D). Linked to measuring the perimeter as a proxy for how the foramen shape changes, the last metric I measured for the IVC was circularity. When divided into embryonic stages, E10.5 and E11.5 appeared to have rounded foramen which becomes deformed as the circularity score decreases at E12.5 and even more so at E13.5; there were no significant changes between the circularity of the IVC at any of the stages (Figures 3.7E-F).

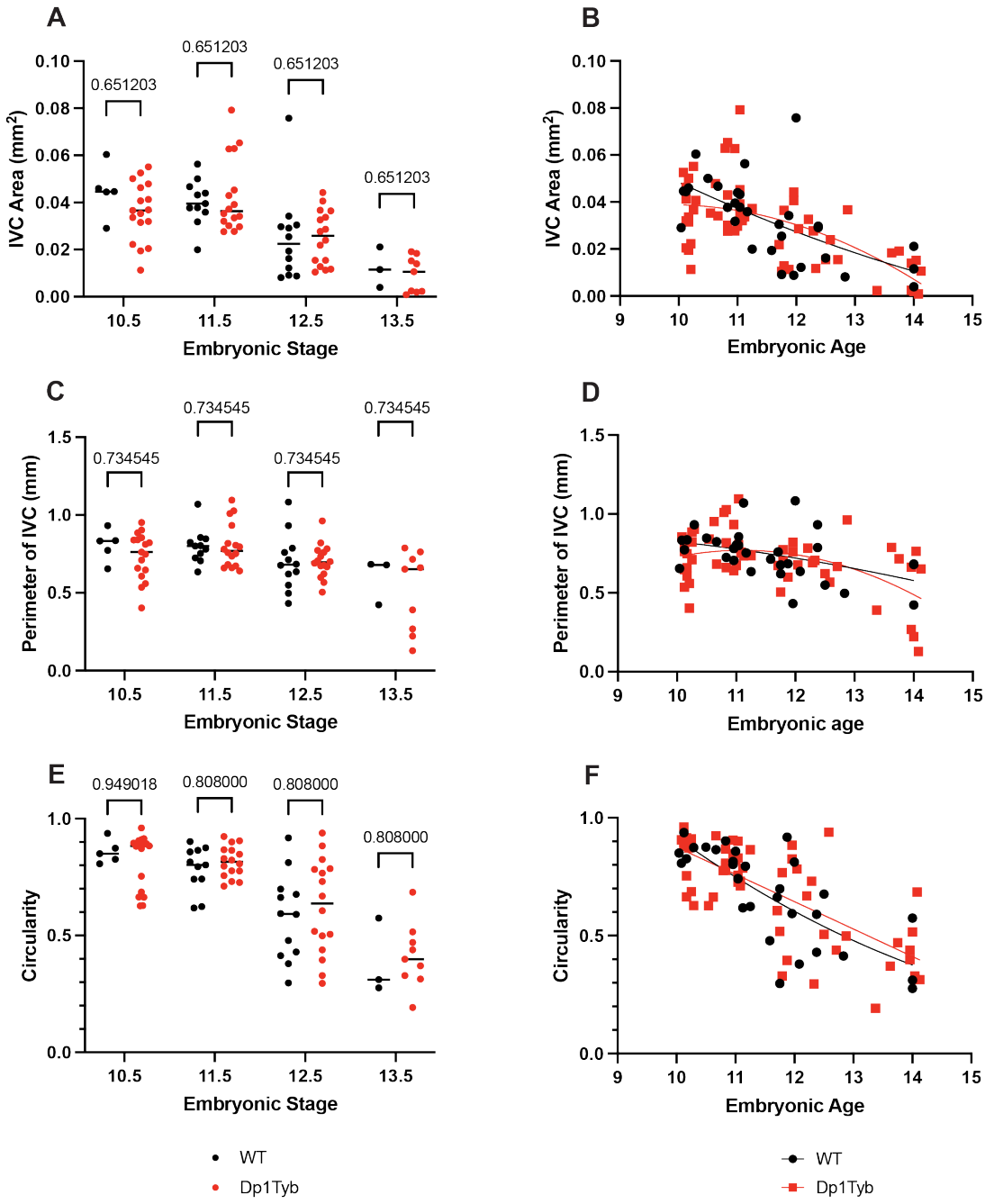

Figure 3.7 Area, perimeter, and circularity of the interventricular communication of wild-type and Dp1Tyb embryos from E10.5 to E13.5. (A, B) Area (C, D) Perimeter (E, F) Circularity of interventricular communication for wild-type and Dp1Tyb embryos for embryos E10.5-E13.5 separated into stages at harvest (A,B,C), or by embryonic age microstaged with limb-bud morphometry (B, D, F). Lines in B, D, and F show non-linear quadratic regression for each genotype. Hypothesis tests in A, C and E performed with Mann-Whitney U tests. E10.5 – wild type n = 5, Dp1Tyb n = 17; E11.5 – wild-type n = 11, Dp1Tyb n = 16; E12.5 – wild-type n = 12, Dp1Tyb n = 16; E13.5 – wild-type n = 3, Dp1Tyb = 9.

Measurements of the mVS likewise revealed no statistical difference between the wild-type and Dp1Tyb hearts at any of the stages analysed. In contrast to the IVC measurements, the mVS measurements were closely clustered in all stages except for E12.5, at which there was a big range of length in both genotypes using either staging method (Figures 3.8A-B).

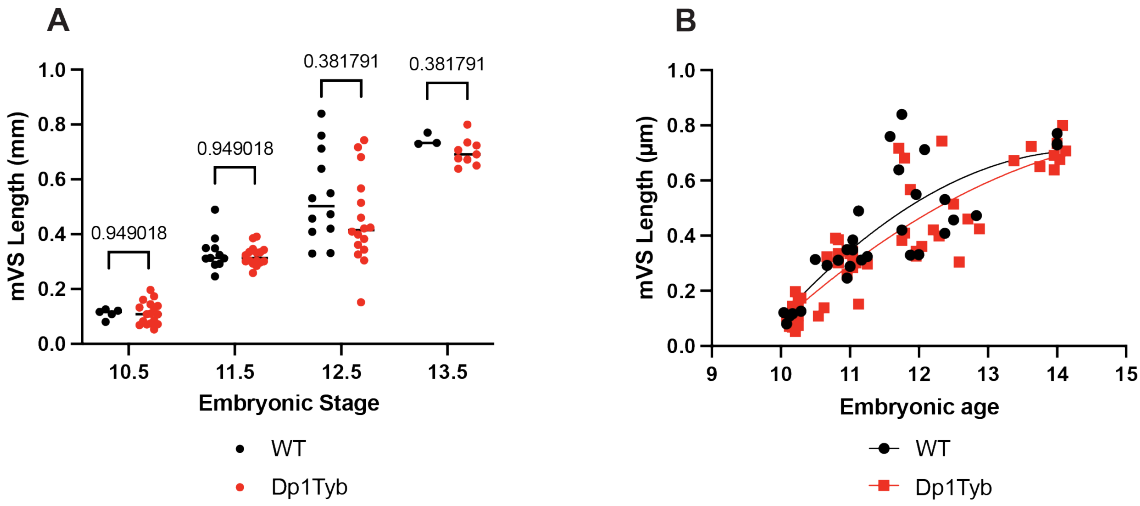

Figure 3.8 Length of the muscular ventricular septum in wild-type and Dp1Tyb embryos from E10.5 to E13.5. (A) Graph showing the length of the muscular ventricular septum when wild-type and Dp1Tyb embryos are separated into their stages based on day of embryo collection. (B) A graph showing the length of the muscular ventricular septum of wild-type and Dp1Tyb embryos matched to their embryonic ages determined by limb-bud morphometry. The lines show a non-linear quadratic regression fit of the results. Statistics performed with Mann-Whitney U test. E10.5 – wild type n = 5, Dp1Tyb n = 17; E11.5 – wild-type n = 11, Dp1Tyb n = 16; E12.5 – wild-type n = 12, Dp1Tyb n = 16; E13.5 – wild-type n = 3, Dp1Tyb = 9.

It is possible the VSD phenotype described in Lana-Elola *et al.* (2016) at E14.5 in the Dp1Tyb may arise in neither the mVS itself or in how the IVC immediately above the crest of the mVS is closing up, but from the structures that are out of its plane. The proximal regions of OFTC play a crucial role in the formation of the ventricular septum and is found at the right ventricular face of the mVS, which achieves contact and fusion at an oblique to the measuring plane. I believe that finding a way to analyse the morphometry in 3D would be a useful approach to

investigate this oblique closure that becomes evident at E12.5 and E13.5 samples. In the next parts of this chapter, I will discuss how I assessed the morphology of the E12.5 and E13.5 hearts using 3D-based methods.

3.2.3 Assessing ventricular septation in 3D

The stage at which the septal OFTC is described to contact the mVS is E12.5, where the IVC becomes the secondary IVC (Anderson *et al.,* 2019). As this process involves two 3D structures coming together, I wanted to visualise and quantify the closing of this distance to assess if this process is affected in the Dp1Tyb hearts. To do this, I segmented the septal OFTC and the mVS in 3D using the existing HREM data (Figure 3.9A) and using Dragonfly to outline the structures manually and interpolate between the manual segmentations to generate the 3D volume. A description of how the OFTCs were segmented is discussed in §§4.2.1, the E12.5 OFTCs used in the morphometric analyses of the next chapter are the same used in this approximation analysis.

A python script (Appendix §§8.2) was used to calculate the closest distance of points on the surface of the mVS mesh to the septal OFTC mesh through a 3D kd-tree analysis. The distances were then mapped onto the first mesh as a heat map based on a user-defined scale, allowing for visualisation of which points on the mesh were closer or further from the secondary mesh (Figure 3.9B). The values could be restricted to just the crest of mVS by capping the values at 0.075 mm to gain a detailed heat map of the distances at the interface between the proximal septal OFTC and the surface of the mVS apex (Figure 3.9C).

In addition to the visualisation, the script saved the values of the restricted distances; in this case, I kept every value less than 0.075mm for a coordinate distance. These values were then separated by genotype and plotted as a histogram with a kernel density estimate to represent a smooth probability density curve. The histograms were then interpreted as a representation of the interface between the proximal cushion and the apical mVS as they are about to fuse or with some surfaces having partially fused already. A representation of a histogram plot from a heart where the cushion and mVS were partially in contact is shown in Figure 3.9E, where the plot skewed towards the smaller distances and with values falling in the smallest

distance range. In contrast, the plot in Figure 3.9F shows a heart where the two structures have not yet fused as the smallest distances exceeded 0.05 mm.

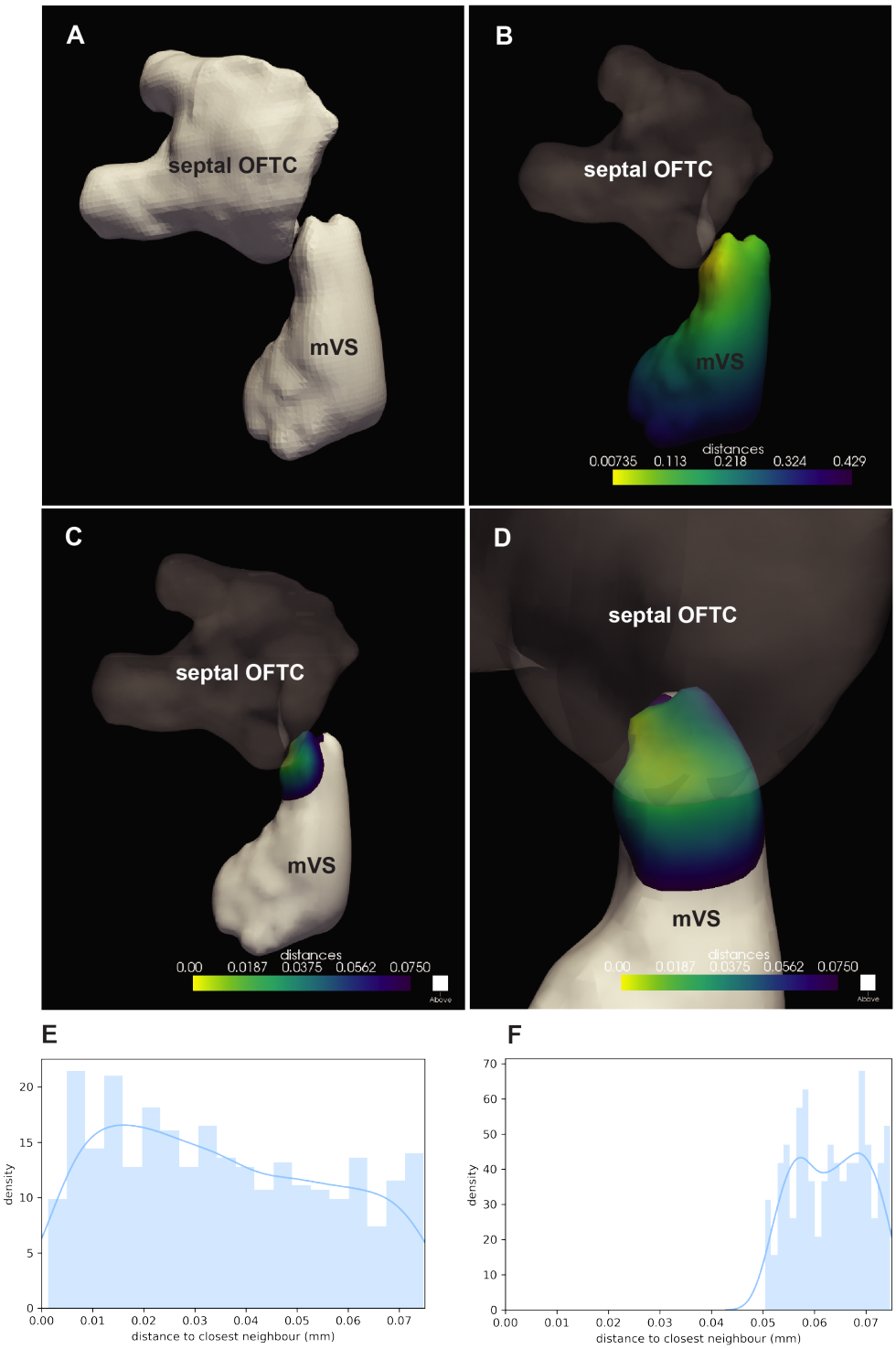

Figure 3.9 Approximation analysis of the septal outflow tract cushion and the muscular ventricular septum in 3D from E12.5 embryos. (A) The septal outflow tract cushion (sOFTC) and the corresponding muscular ventricular septum (mVS) are

segmented as 3D objects. (B) Distances of points on the septum mesh to the cushion mesh are represented as a heat map on the septum mesh. (C) Heat map of distances on the muscular ventricular septum mesh to the cushion mesh restricted to 0.075 mm. (D) Alternative orientation of (C) zoomed in. (E) Representative histogram of distances between septum and cushion meshes where the objects are in contact, the line represents the kernel density estimate. (F) Representative histogram of distances between septum and cushion meshes where the objects are further away from one another, the line represents the kernel density estimate.

I plotted the values in a density histogram to determine if there was a difference in the distance between the two mesh interfaces for Dp1Tyb and wild-type hearts. The histogram showed that there was no difference between Dp1Tyb and wild-type in the mesh-to-mesh distance distribution measured this way (Figure 3.10A). Additionally, the analysis showed that the minimum distance between the apical mVS and the proximal septal OFTC was not significantly different between the genotypes (Figure 3.10B). The same was done for the mean distance of all the points on the mVS to their neighbours on the septal cushion mesh; this metric gave an approximation to the shape of the mVS, with smaller values suggesting a more elongated structure than larger values where there were more points with shorter distances, therefore, closer to the septal cushion mesh overall (Figure 3.10C). Like the minimum distance measurement, there was no statistical significance or change between wild-type and Dp1Tyb hearts. The results taken together indicated that at E12.5 the way the apical surface of the mVS comes to meet and fuse with the septal OFTC to form the secondary IVC was not (yet) different in the Dp1Tyb versus wild-type hearts.

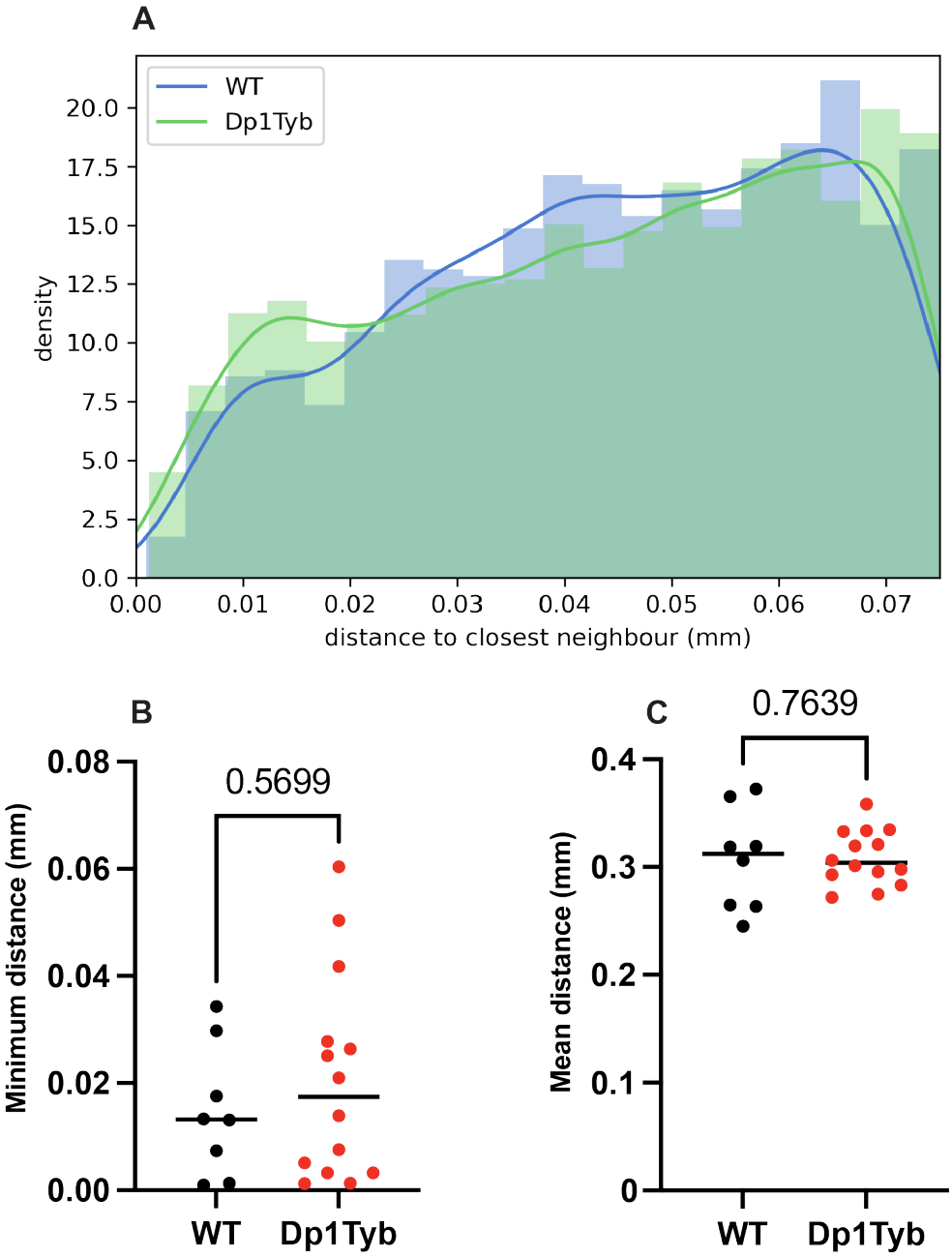

Figure 3.10 Quantification of the distances of points on the muscular ventricular septum mesh to the septal outflow tract cushion mesh in wild-type and Dp1Tyb hearts at E12.5. (A) Histogram of the distances between points on the muscular septum mesh to its closest neighbour on the septal outflow tract cushion mesh, restricted to distances up to 0.075 mm. The lines represent kernel density estimates. (B) Plot showing the minimum distance between cushion and septum for each wild-type and Dp1Tyb sample. (C) The mean distance of all points of the septum mesh to the cushion mesh for wild-type and Dp1Tyb hearts. Statistics performed were Mann-Whitney U tests. Wild-type n = 8, Dp1Tyb n = 14.

Exploring the next embryonic stage, E13.5, in 3D was of particular interest as this is the stage right before complete septation. It was the group of data that I had the most difficulty in analysing due to the smallest IVC foramen being at an oblique to the midline of the mVS and not susceptible to the above method used for E12.5 because cushion-mVS fusion was largely complete. This suggested that the best way to look at this data would be to construct the remaining lumen of the ventricles by extracting the empty space and creating that as an object of its own (yellow outlines in Figures 3.11A-C). This was a difficult process as the main body of the lumen is connected to spaces in between the dense network of trabeculation at this stage. Usage of active contour algorithms such as Ballooning (Federici *et al.*, 2012), where a starting seed was placed in the middle of the lumen and expanded to fill all the connected space as if a balloon was inflating, was not successful nor ultimately applicable due to the complexity of the trabeculation and the processing capability needed to run through a stack of approximately 500 images sections per sample. Instead, the solution devised was to develop a script (Jon Smith, Sofware Engineering and AI, the Francis Crick Institute) that automated making every image in the stack binary and invert this so the highlighted result represented the empty spaces i.e. the lumen (Figure 3.11A'-C'). The script then used a Connected Components algorithm to isolate the largest lumen (which should be the ventricles) by detecting connected objects through the image stack using the pixel connectivity from one section to the next in the stack (Appendix §§8.1).

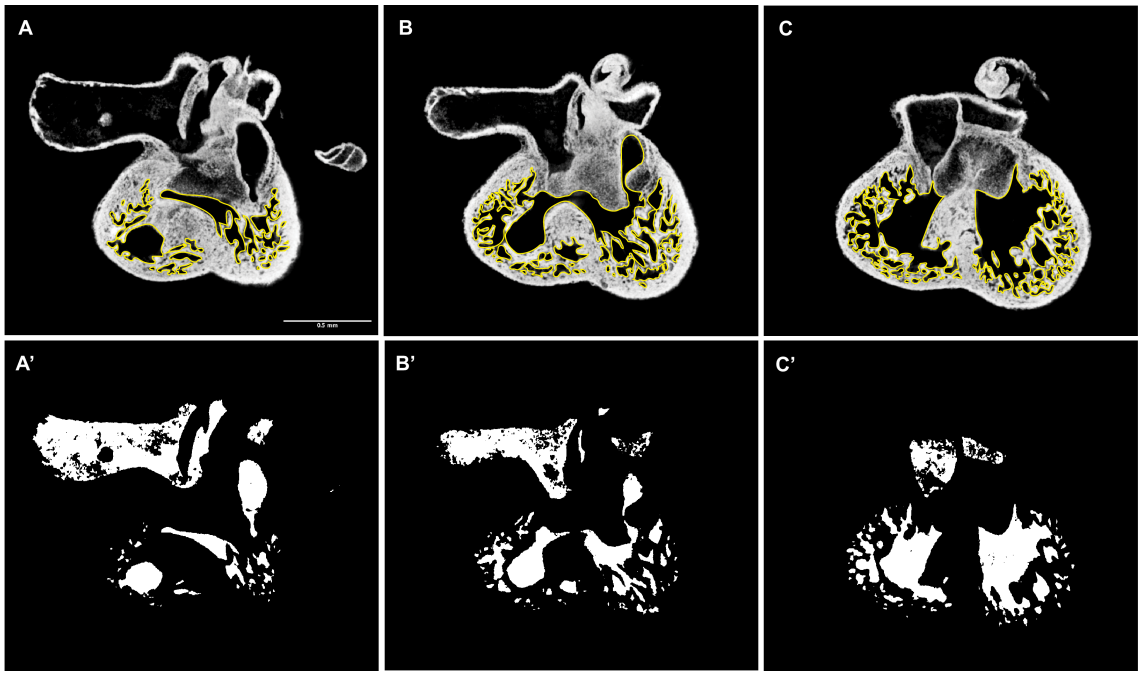

Figure 3.11 Outline and segmentation of the ventricular lumen space in E13.5 high-resolution episcopic microscopy data sets. (A) The frontal section of an E13.5 heart before the interventricular communication, the lumen is outlined in yellow. (A') The section from (A) with the custom binary segmentation Python script applied (B) Frontal section of the same heart is recessed until the interventricular communication is visible. Yellow outline shows the ventricular lumen. (B') The section from (B) with the custom binary segmentation Python script applied. (C) Frontal section of the same heart recessed further until past the interventricular septum. Yellow outline indicates the ventricular lumen space. (C') The section from (C) with the custom binary segmentation Python script applied.

The final script output was a binary image stack with the lumen highlighted, the image stack was then opened in the open-source molecular visualisation software, ChimeraX (Meng *et al.*, 2023). The software converted the image stack into a surface mesh that was saved as a cross-platform compatible .stl file. Following mesh construction, I imported the lumen meshes into MeshLab (Cignoni *et al.*, 2008) and removed the atrial lumen, leaving just the structure of the ventricles along with the spaces between the trabeculation (Figure 3.12A). The mesh was further processed by decimation to reduce file size and smoothened by creating an Alpha Complex of the mesh (Edelsbrunner and Mücke, 1994), which shrink-wrapped the surface to limit the noise from the trabecular space protrusions (Figure 3.12B). The mesh was

refined by removing the ventricular lumens, leaving only the IVC bridge between them. The morphology of the IVC varied widely between the samples, some IVCs had larger communications (Figure 3.12C) whereas some hearts had smaller and narrower IVCs (Figure 3.12D). Visualisation of the IVC in this process reinforced that these structures were complex three-dimensional morphologies and should be quantified in such a state as to reduce subjectivity in sectioning.

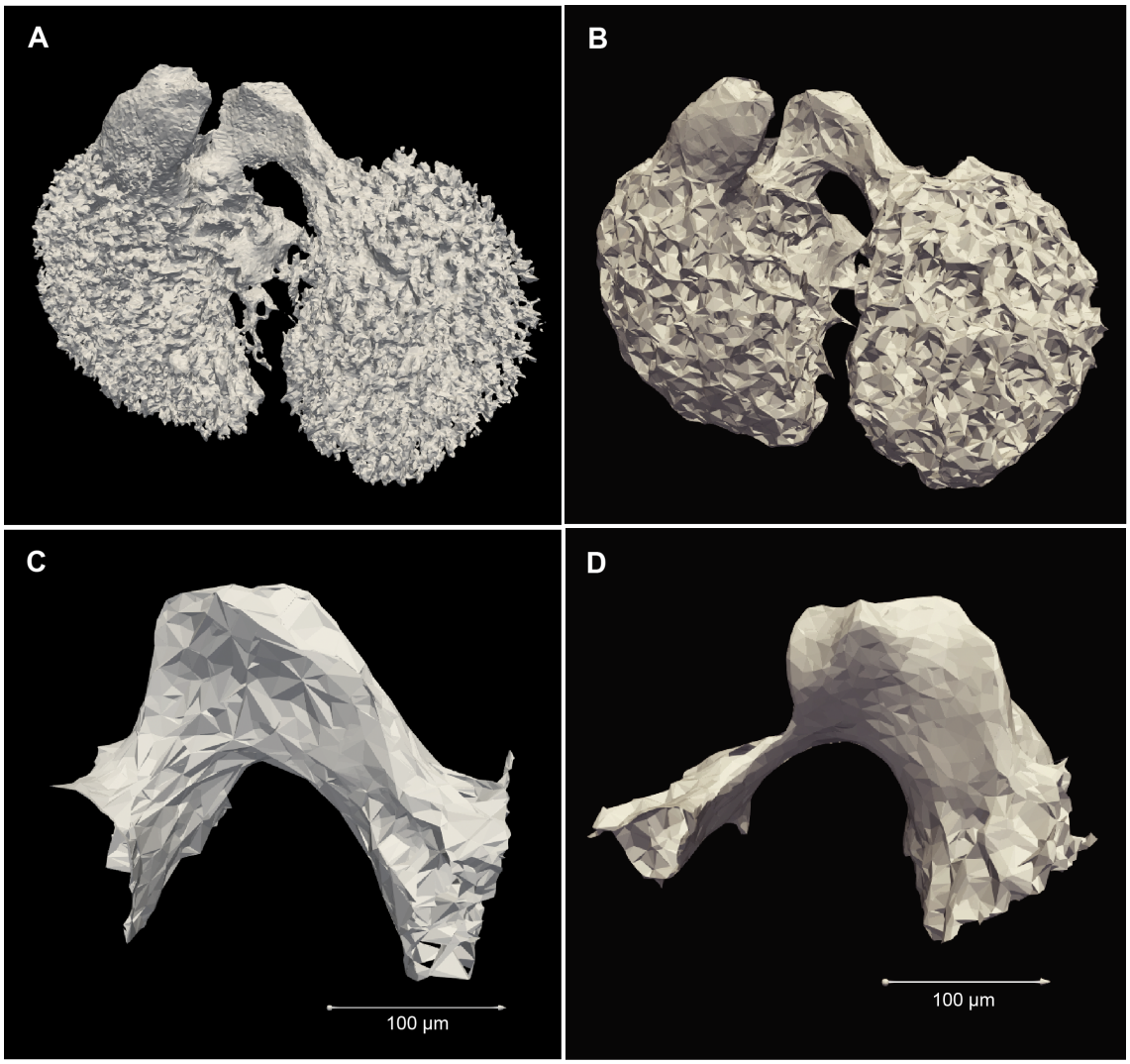

Figure 3.12 3D mesh object of an E13.5 ventricular lumen space isolated from the heart. (A) Mesh of the ventricular lumen space viewed from a frontal orientation. (B) The same lumen mesh as an alpha complex object to smoothen out trabeculation. (C) Interventricular communication bridge isolated from the lumen mesh. (D) An example of another interventricular lumen bridge where the communication is smaller.

Instead of measuring the lumen directly from the created meshes slice by slice, I wanted to find a way to take the entire morphology of the IVC into account. To this end, I imported the E13.5 lumen meshes obtained from the segmentation algorithm into the open-source software 3D Slicer (Fedorov *et al.*, 2012) to trim to the IVC "bridge" (Figure 3.13B) and applied a center-line extraction using the integrated extension for the Vascular Modelling Toolkit (VMTK) (Antiga *et al.*, 2008) to the shape (green line in Figure 3.13B). Selecting endpoints for the center-line at the left ventricle (endpoint-1 in Figure 3.13B) and right ventricle (endpoint-2 in Figure 3.13B), the algorithm finds a central line through the lumen of the space using the endpoints as guides. The VMTK module was then further used to extract the cross-sectional area and diameter of the sections perpendicular to the center-line (purple plane within structure, Figure 3.13B).

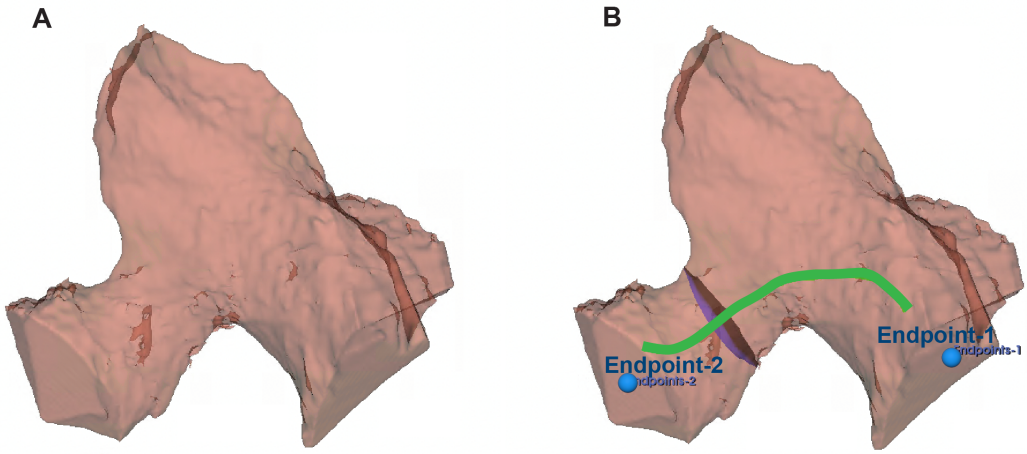

Figure 3.13 Measuring the minimum cross-sectional area of E13.5 interventricular communications. (A) Surface mesh of the interventricular bridge in an E13.5 embryonic heart using 3D Slicer. (B) The same surface mesh with a centerline through the shape (green line) as guided by two endpoints (blue labels), the minimum cross-sectional area perpendicular to the centerline is shown as a purple plane within the shape.

This analysis was performed on the E13.5 Dp1Tyb and wild-type hearts, with the minimum cross-sectional area recorded (Figure 3.14A) and along with 5 area measurements at either side of the minimum measurement (Figure 3.14B). The same was recorded for the diameter of the cross-section (Figures 3.14C-D) for wild-type and Dp1Tyb embryos. In both measurements, there was no difference found in the minimum area or diameter. Interestingly, while the minimum cross-sectional area

and diameter were similar in both genotypes, there was a large spread of what the surrounding area looked like (Figures 1.14B-D).

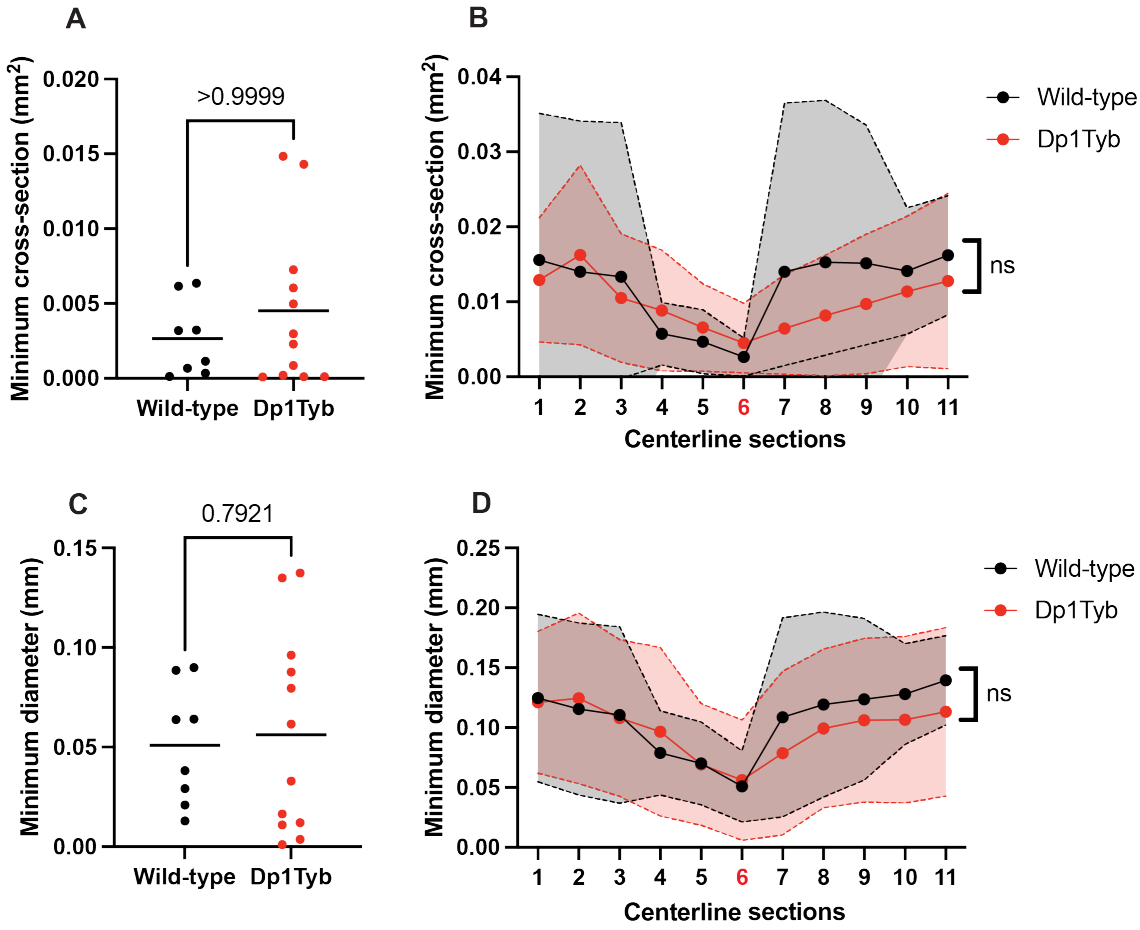

Figure 3.14 Minimum cross-sectional area and diameter of E13.5 interventricular communication for Dp1Tyb and wild-type embryos. (A) Minimum cross-sectional area for wild-type and Dp1Tyb embryos. (B) Cross-sectional areas of 5 planes before and after the minimum area (section 6) along the centerline. (C) Minimum diameter of cross-section for both genotypes. (D) Diameter of the cross-section 5 planes before and after the minimum diameter (section 6). (A, C) Show individual samples and mean, (B, D) shows mean and SD. Statistics: Mann Whitney-U (A, C), two-way ANOVA (B, D). Wild-type n = 8, Dp1tyb n = 12.

3.3 Discussion

This chapter has focused on morphometrics derived from 3D reconstructions of wild-type and Dp1Tyb embryos at the embryonic stages leading up to ventricular septation or the failure to do so properly in the Dp1Tyb embryos that go on to present CHD. The precision needed to detect very subtle changes in anatomy that lacks well-defined landmarks required a change in the normal methodology for measuring anatomical structures. The basis for this was the isotropic 3D image data sets, which could have the plane of section manipulated to any angle, and segmenting structures in the embryonic heart to assess the morphometric changes in 3D by different computational means.

3.3.1 Interventricular communication closure and muscular septum growth is not impacted in Dp1Tyb hearts

While HREM was a good technique for this project and provided the necessary image resolution to quantify small anatomical structures, the technique was time-consuming and destructive. As previously described in the chapter, the HREM imaging process cuts the resin block containing the embryos and images the cut surface of the block which for whole embryos could take up to 8 hours per sample. This also meant the samples were destroyed in the process. It is possible to collect the sections cut from the HREM for further staining, but with each embryo taking approximately 8 hours to section it would have been a difficult and arduous task to collect the relevant sections as they are cut. There is non-destructive alternative to this HREM: recent advances in soft-tissue micro-CT imaging have shown its capability for image resolution high enough to detect CHD and track developmental structures within the heart at earlier stages (Handschuh and Glösmann, 2022; Li-Villarreal *et al.*, 2023). With HREM, the maximum spatial resolution is 1 µm x 1 µm x 1 µm to 5 µm x 5 µm x 5 µm (Geyer *et al.*, 2017) (in this experiment the resolution was 2.55 µm x 2.55 µm x 2.55 µm), whereas the newer models of Micro CT have reported resolutions between 3 and 11 µm (Li-Villarreal *et al.*, 2023). Micro CT also allows for multiplexing embryos, reducing the time needed to obtain the data. As mentioned, micro-CT is not destructive and could allow for the embryos to be used for immunostaining afterwards (Hopkins *et al.*, 2015), thereby reducing animal usage

and adhering to the NC3Rs framework of aiming to reduce the number of animals needed in a project requiring both types of analysis (Hubrecht and Carter, 2019).

The main findings of this chapter were that there were no differences in the growth of the mVS or the closure of the IVC between wild-type and Dp1Tyb embryos at any of the stages investigated. While this was disappointing and unexpected, given that over half of Dp1Tyb embryos will go on to have CHD at E14.5, only a day later than the latest stage in the results of this chapter (Lana-Elola *et al.*, 2016). These defects were from failure of septation at some point prior to E14.5 but just not in what was measured in the experiments in this chapter. The results were particularly surprising given that the later stages analysed were microstaged as being closer to or actually at E14.0 than E13.5 (Figure 3.4). Microstaging of the embryos showed a surprising variability in the calculated ages of the embryos compared to when they were harvested, with some embryos limb-bud staged to a full embryonic stage earlier than when they were collected (Table 3.1). Even controlling for the difference between microstage and nominal harvesting stage ultimately did not show that there was a difference between the two genotypes at any stage in any of the quantifications.

This chapter focused on the mVS and overall closure of the IVC, but other structures such as the OFT wall and AVC contribute to the final stages of fusion once the mVS has already grown and so could be the locus of the Dp1Tyb VSD and show a pre-E14.5 morphological signature. Both sets of endocardial cushions have a large role to play in this completion of ventricular septation, with undeveloped AVC forming one of the hallmarks of AVSDs – the common atrioventricular valve or bridging leaflet (Ahmed and Anjum, 2023). In addition, the failure of proper OFTC development (and thus OFT septation) leads to defects in arterial vessel patterning alongside VSDs (Mostefa-Kara *et al.*, 2015).

The apparent lack of difference between Dp1Tyb and wild-type surface shapes described in this chapter points to sub-surface, i.e. histological differences, as likelier causes of the VSD phenotype. Unfortunately, HREM cannot resolve to cellular resolution. Failure in septation could result from abnormal cell processes in any of the structures associated with cardiac septation, which have been seen in other mouse models of CHD, such as aberrant proliferation, apoptosis, fusion, or differentiation (Snider and Conway, 2011).

3.3.2 Ventricular septation in Dp1Tyb hearts through 3D analyses reveals no differences

At E12.5, I had set out to characterise how the septal OFTC comes in contact with the surface of the mVS using the proximity of coordinates on the two 3D meshes of the structures segmented from the HREM data sets (Figure 3.9A). While the results from this did not show a phenotype in the Dp1Tyb embryos, it challenged me to find different ways to use the data set and to look at the project from a different angle.

This led to the solution on how to approach the E13.5 hearts, where I had struggled with finding the sectioning plane for the smallest IVC to measure, by inverting the problem and only looking at the lumen of the ventricles. The isolated lumen bridges (Figures 3.12C-D), which included the foramen I previously tried to measure, proved to be a complex geometry. This was solved by making use of vessel segmentation algorithms like VMTK by segmenting the IVC “bridge” as it were a vessel and applying an analysis to find the most stenotic point, i.e. the smallest IVC area. This methodology could lead to other interesting analyses such as using computational fluid dynamics to model blood flow.

Blood is flowing through this structure at E13.5 and if this was something that could be computationally modelled using the isolated bridge, this would not only further inform the patency of the structure but regions in which more or less pressure is exerted on the lumen wall by blood. It is also known that fluid shear stress within the embryonic heart is implicated many developmental processes such as in the OFT valvular remodelling through activation of mechanosensitive pathways such as YAP in both mice (Wang *et al.*, 2023) and zebrafish (Duchemin *et al.*, 2019). The force exerted on the inner heart lumen from blood flow is sensed through primary cilia (Hierck *et al.*, 2008; Hierck *et al.*, 2008), which are often implicated in the pathogenesis of CHDs (Klena *et al.*, 2017). Interestingly, the formation of primary cilia is found to be impacted in trisomy 21 through in vitro models of and in the Dp16Yey DS mouse model (Galati *et al.*, 2018; Jewett *et al.*, 2023). In the future, a combination of fluid dynamic modelling and these 3D lumen segmentations could be informative in identifying localised regions within the developing heart that experience higher mechanical stress and how this may impact cellular behaviours and signalling pathways implicated in DS CHDs.

To conclude, this chapter has demonstrated that there were no changes in the Dp1Tyb embryos in how the IVC closes through the stages leading to ventricular septation nor how the mVS grows cranially to the inner heart curvature. Further analysis in 3D did not find defective contact of the Dp1Tyb proximal septal OFTC to the apical mVS surface, and the patency of the E13.5 IVC was unchanged. As heart defects are found in Dp1Tyb hearts just a day later at E14.5, evidence of defective development may lie in the other structures involved in ventricular septation such as the OFTC. Furthermore, if there were no structural changes to the anatomy, it does not mean there were no changes to the cellular processes in the mutant which could also contribute to the defects observed at E14.5. Regardless, this chapter has comprehensively tracked the heart development from post-heart looping to just before ventricular septation in both wild-type and Dp1Tyb embryos using a 3D data set. Additionally, this chapter has also demonstrated how to apply more unconventional analyses to a 3D developmental dataset to thoroughly characterise anatomical structures.

Chapter 4. Outflow tract cushion morphology in Dp1Tyb mice

4.1 Introduction

The previous chapter has established that there was no marked difference in how the mVS grows in Dp1Tyb embryos compared to stage-matched to wild-type embryos. As established by the Tybulewicz lab (Lana-Elola *et al.*, 2016), Dp1Tyb-specific CHD are found at E14.5 which means that if there is no difference in how the IVC narrows with respect to the growth of the mVS in the stages prior to that, then changes might be found in the other structures associated with completing septation. These structures, which seal the remaining IVC through fusion with the mVS, are the endocardial cushions (Figure 4.1).

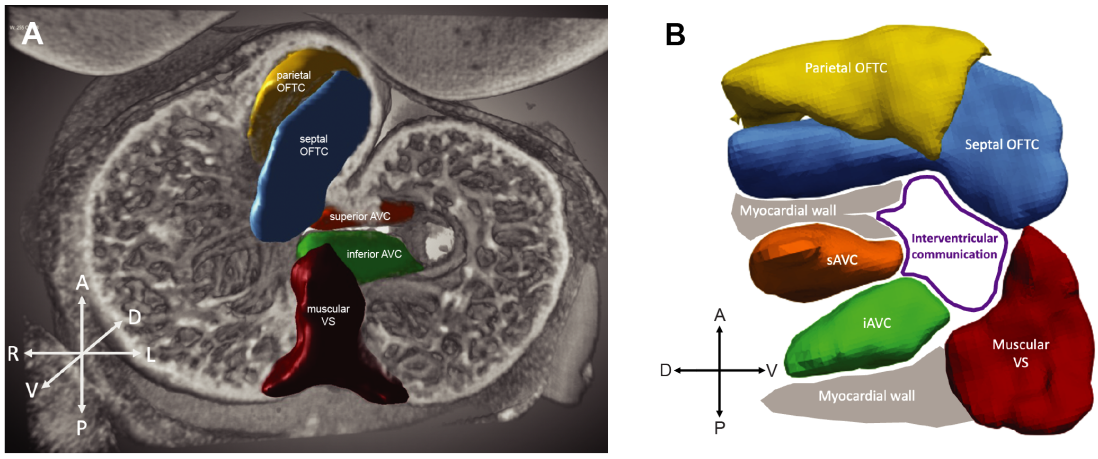

Figure 4.1 3D segmentation of structures in an E12.5 embryonic heart. (A) The following structures were segmented from 3D image data sets of an E12.5 embryonic heart: the muscular ventricular septum (VS) in red, superior atrioventricular cushions (sAVC) in orange, inferior atrioventricular cushions (iAVC) in green, parietal outflow tract cushions (OFTC) in yellow and septal OFTC in blue. (B) The segmented structures are rotated and viewed from the right, the presumed intervening regions of myocardial wall are highlighted in grey and the approximate shape of the interventricular communication is outlined in purple.

Both pairs of endocardial cushions, the AVCs and OFTCs, have important roles in proper chamber septation and valve formation. AVCs are implicated and are well-

characterised in the aetiology of AVSDs (Markwald *et al.*, 1981; Anderson *et al.*, 1998; Kim *et al.*, 2001), which are the most common CHD in DS, making up 29% of heart defects in humans (Benhaourech *et al.*, 2016) and appearing in around 25% of Dp1Tyb embryos at E14.5, albeit as a component in the latter of more complex defects (i.e. with VSD and OFT defects) (Lana-Elola et al. 2016). However, the OFTCs are less studied in the context of DS, despite DS patients presenting with OFT-related CHDs such as DORV, OA and ToF (Ghimire *et al.*, 2013; Morrison *et al.*, 2018). Moreover, OFTC defects were also identified in Dp1Tyb embryos in combination with VSDs (Figure 4.2) in nearly 30% of heart defects, suggesting that, in the Dp1Tyb model, where there is failure of proper OFT formation, there is also failure of complete ventricular septation.

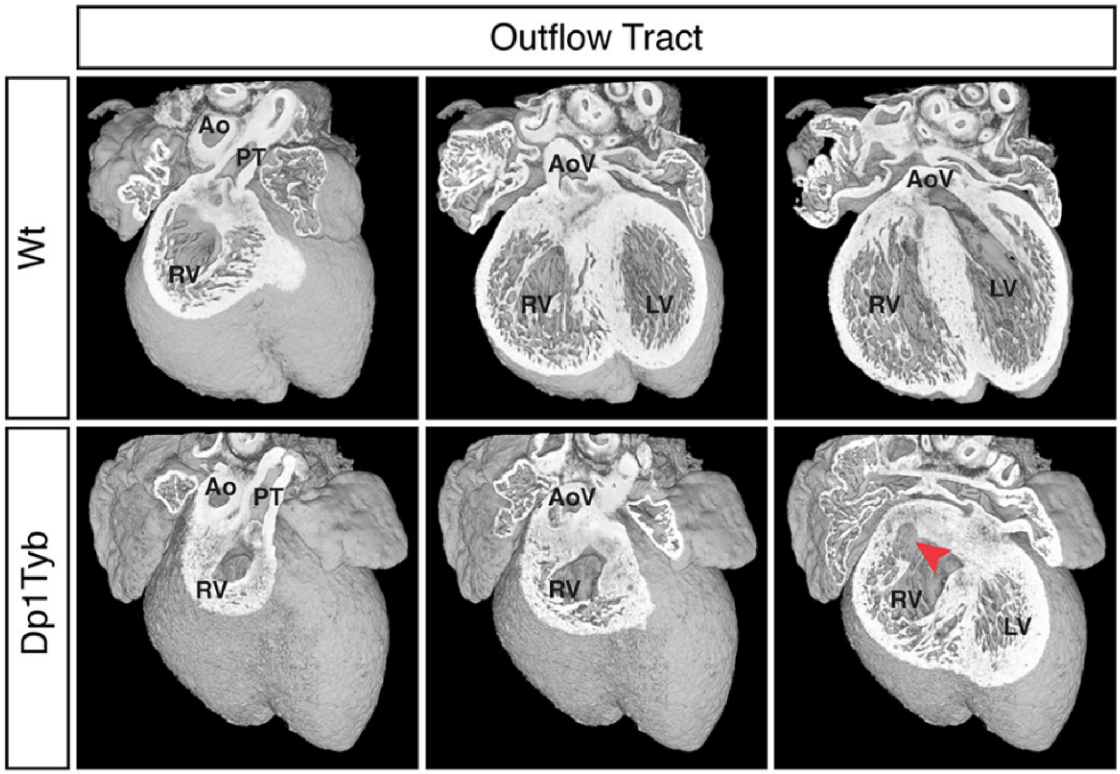

Figure 4.2 Double outlet right ventricular outflow tract defect in Dp1Tyb mouse heart. 3D reconstruction of a wild-type and a Dp1Tyb heart at E14.5 showing successive planes of the outflow tract vessels in the frontal orientation. The wild-type panels show normal arterial patterning with the aorta connected to the left ventricle. The Dp1Tyb panels show a double outlet right ventricle defect, with the red arrowhead illustrating the aorta emerging from the right ventricle. Adapted from Lana-Elola *et al.* 2016.

In the wider literature of heart development and defects, anomalies in the OFT are responsible for 30% of all CHD diagnosed (Neeb *et al.,* 2013). The OFT is a dynamic and transient structure that begins at the arterial pole of the heart and elongates into a heart tube by the arrival of cells from the mesoderm – the SHF cells – through migration and endothelial to mesenchymal transition; the CNCC add to the cushion population by migration through the carotid, aortic and pulmonary PAs (Kelly *et al.*, 2014). During heart elongation, the inner walls of the structure swell with cardiac jelly between the myocardium and the endocardial lining to accommodate the arriving cells. These form the OFTCs separated initially into two discrete structures, the septal and parietal OFTCs (Figure 4.1), which sit within the common arterial trunk. As embryogenesis progresses, the septal and parietal cushions "rotate" with the OFT and fuse at the distal end (furthest from the ventricle) which begins with progressive condensation of the mesenchyme in each cushion. This condensation in each cushion results in their joining to form a myocardial bridge that separates the OFT into the arterial vessels as well as contributing to the formation of the arterial valve leaflets at the distal OFT. This process proceeds downwards towards the ventricles to the proximal end to complete septation of the OFT into the pulmonary artery and aorta in a fully developed heart. Once the OFTCs are fused but there is still a common arterial trunk, the remaining proximal cushion fuses to the mVS to begin the final stages of ventricular septation. Absence of the septation and aplastic OFTC results in PTA, where the OFT remains unseptated and the common arterial trunk straddles both ventricles (Okishima *et al.*, 1986). Imbalanced septation where the mesenchymal condensation is not advancing proximally at the same rate in both parietal and septal cushions has been shown to lead to DORV, OA, VSDs and ToF (Stefanovic *et al.*, 2021). The OFTCs thus play an important role in not only proper OFT septation and arterial valve formation but the structural development of the heart as a whole.

The CHDs observed in Dp1Tyb embryos strongly suggest that the OFTCs are involved in the development of the phenotype. As they are transient structures that are not distinguishable at E14.5 when CHD are detected, I looked at earlier stages of development at E12.5 and E13.5 when they are actively remodelling to septate the OFT. In this chapter, I investigated the developing morphology of the OFTCs in wild-type and Dp1Tyb embryonic hearts using segmentation and morphometric analysis of 3D images.

4.2 Results

4.2.1 Outflow tract cushion septation is delayed in Dp1Tyb embryos

To analyse the development of the OFTCs in wild-type and Dp1Tyb embryos, I imaged them using HREM as described in the previous chapter and the methods (§§3.2.1 and §2.4). HREM provided not only the outlines of the developing heart tissue surfaces in accurate 3D, but also enabled some distinction to be made between tissues, with cushion tissue being less brightly stained than myocardial tissue. Cushion tissue was manually segmented and quantified, with randomisation and blinding to avoid subjective biases. Upon unblinding, in the segmentation of the E12.5 OFTCs, I observed morphological differences between wild-type and Dp1Tyb embryos. The distal regions of the cushions in wild-type embryonic hearts were more likely to have a myocardial bridge between the two cushions (Figure 4.3A), but in many of the Dp1Tyb cushions, instead of a myocardial bridge there would be areas of condensation with both cushion structures (Figure 4.3B). When the cushions are false-coloured, in wild-type hearts the distal septal and parietal cushions are separated by myocardial bridges (Figure 4.4A). More proximally, many of the wild-type OFTCs were in contact with each other (Figure 4.4B-C). In contrast, in many Dp1Tyb embryos, the septal and parietal cushions were abutting but the myocardial bridge was absent (Figure 4.4D). In the medial and proximal sections, Dp1Tyb cushions were spaced apart (Figures 4.4E-F) rather than abutting. Overall, this indicates that in Dp1Tyb hearts there is a lack of progression of OFT septation, as this bridge needs to form to separate the structure into the pulmonary artery and the aorta.

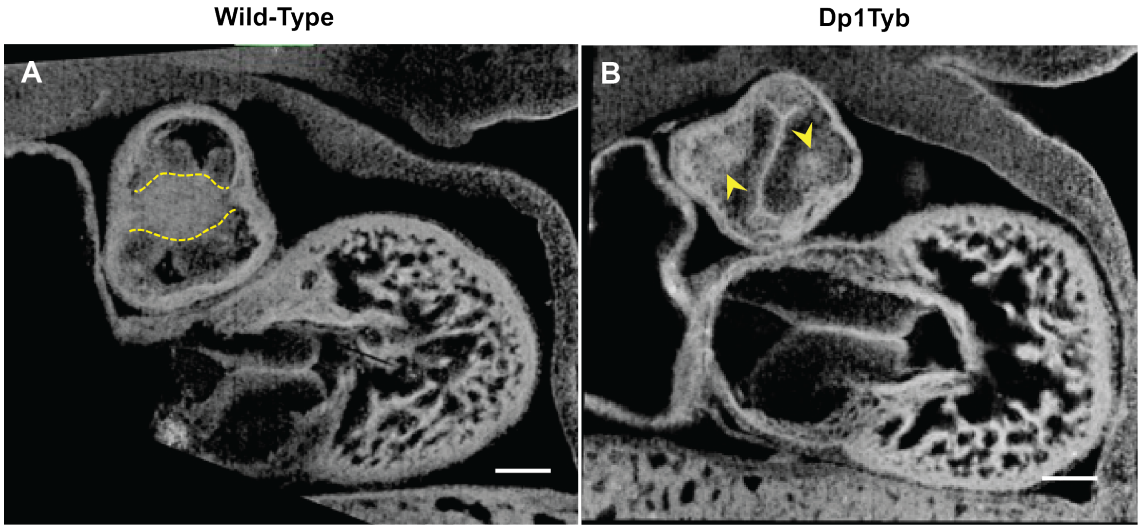

Figure 4.3 Formation of the myocardial bridge or mesenchymal condensation in the distal outflow tract at E12.5. (A) A transverse section of the distal outflow tract of a wild-type E12.5 heart with the myocardial bridge shown between the yellow dashed line. (B) Mesenchymal condensations but no myocardial bridge are shown in a transverse section of Dp1Tyb distal outflow tract at E12.5 (yellow arrowheads). Scale bars are 100 μm.

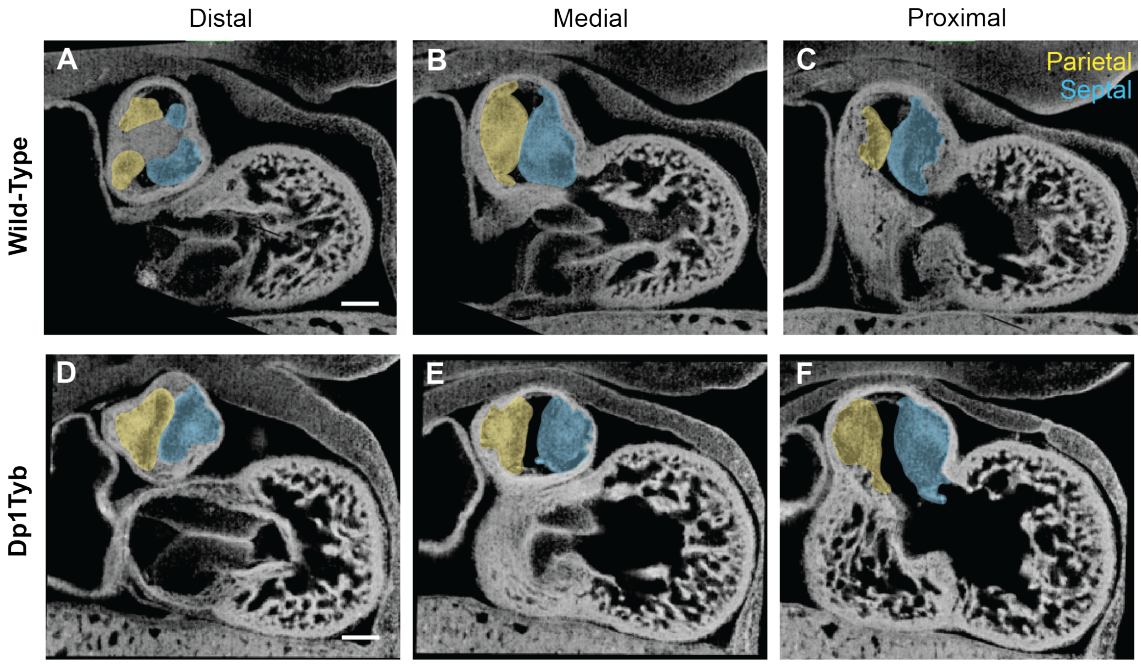

Figure 4.4 Successive planes of wild-type and Dp1Tyb outflow tract cushions at E12.5. High-resolution episcopic microscopy images show the distal, medial and proximal sections of embryonic hearts in a frontal orientation, where the parietal OFTC

is highlighted in yellow and the septal cushion is in blue. (A-C) The wild-type heart. (D-F) Dp1Typ heart. Scale bars are 100 μm.

Once images of the cushions had been segmented. their outlines were used to generate 3D meshes. This revealed that the two genotypes have different cushion morphologies in the distal region. Figure 4.5 shows 3D-renderings of the meshes derived from the segmentations of cushion tissue (containing mesenchymal cells and cardiac jelly) that had not differentiated into myocardial tissue. Most wild-type cushions had a “forked” distal anatomy (Figure 4.5A-C) due to the differentiation of tissue between the prongs of the “fork” into the myocardial bridge. Dp1Tyb cushions mostly had a rounded distal anatomy (Figure 4.5D-F). In unfused cushions, there was no myocardial bridge at the distal cushion anatomy but there was a condensation of mesenchyme within both septal and parietal OFTCs. These condensations are not visible in the renderings because they were surrounded by cardiac jelly and were not as “bright” in pixel value as the myocardial bridges, so were segmented as part of the cushion. Approximately half of all Dp1Tyb embryos collected had unfused cushions compared to ~17% in the wild-type. Despite this apparently clear-cut difference, Fischer’s exact test reports it as not significant ($p = 0.054$), presumably due to the low n-number of this analysis. To determine if this a real difference, a power calculation based off this data indicates that a minimum of 21 embryos per genotype should be used. This seemed to be specific to the heart as the limb-bud staging showed the same spread of embryonic age in all samples (Figure 4.6A) as well as in fused and unfused cushions in both genotypes (Figure 4.6B), ie. there was no correlation between limb age and heart phenotype.

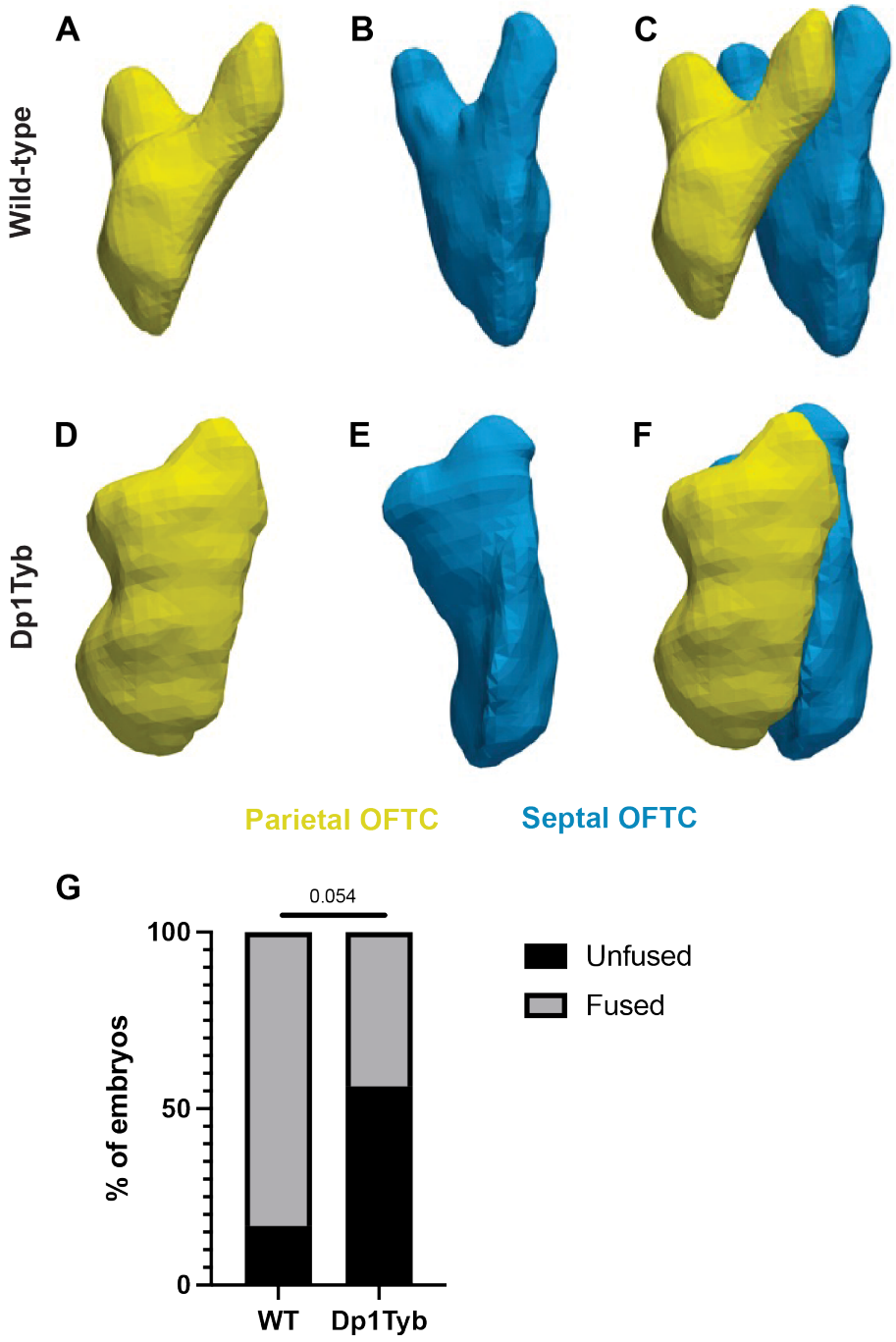

Figure 4.5 Fused and unfused outflow tract cushion morphologies at E12.5. (A-C) 3D segmentations of the remaining cushion mesenchyme showing cushions where fusion has begun in the distal OFTC. (D-F) Cushions that had yet to start fusing. The parietal cushions are false-coloured yellow and septal cushions blue. (G) Fused and unfused cushion morphologies are quantified and shown as a percentage of all embryos collected for wild-type and Dp1Tyb mice. Statistical test performed was Fischer's exact test; wild-type n=12, Dp1Tyb n=16.

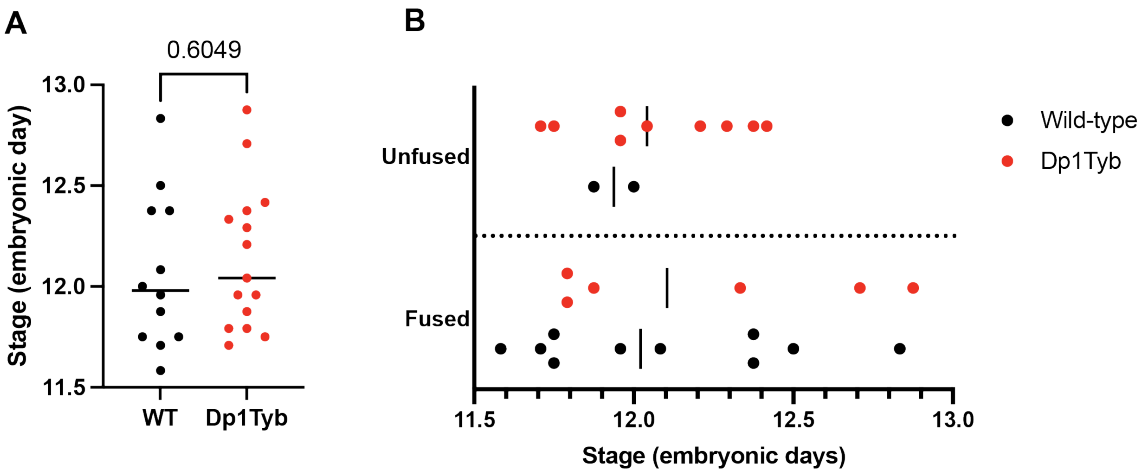

Figure 4.6 Microstaging of E12.5 wild-type and Dp1Tyb embryos. (A) A graph showing the spread of microstages for all wild-type and Dp1Tyb embryos. (B) Plot showing the microstage of embryos in each genotype separated into whether the outflow tract cushions had begun fusing or not in the sample. Statistics were performed with Mann-Whitney test, plots show the mean of each dataset; wild-type n=12, Dp1Tyb n=16.

4.2.2 Rotation of the outflow tract is unaffected

Proper rotation (helical morphology) of the OFT is implicated in the normal positioning of the great arteries (Stefanovic *et al.*, 2021) and inappropriate or incomplete rotation is found in some major CHD such as persistent truncus arteriosus, double outlet right ventricle and transposition of the great arteries (Bajolle *et al.*, 2006). PTA and DORV in particular have been identified in Dp1Tyb mutants at E14.5. With this in mind, I set out to determine whether there were any rotation defects in the hearts of E12.5 Dp1Tyb mice. I used E12.5 mice as the OFT has completed rotation but not septation at this stage and I used the relative positions of the OFTCs to assess the rotation between each analysed section and the cumulative rotation from distal to proximal OFT. Starting from comparable positions in the distal OFT, using the FIJI/ImageJ software package, I manually outlined the septal and parietal OFTCs at 25.5 µm z-intervals for 255 µm microns to the proximal OFT. The centroid coordinates of the parietal and septal cushions in a section were noted as x_1, y_1 and x_2, y_2 by measuring the ROIs. The coordinates were put into the following formula where θ is the angle between the two coordinates to the x-axis:

$$\theta = \arctan\left(\frac{y_2 - y_1}{x_2 - x_1}\right)$$

From this, I calculated the angle change from one section to the next with the 25.5 μm interval as well as the total change from a section to the first and distal-most section to capture the total rotation.

Figure 4.7A shows how the 3D mesh reconstructions of the OFTCs are looping into a left-handed helix when viewed from a frontal orientation, as described in the literature. Figures 4.7B-B'' shows representative sections in the original transverse orientation the embryos are embedded in for HREM imaging. Using this analysis described earlier, I found that there was no significant difference in how the cushions rotated from section to section in either genotype, with changes rarely exceeding 10 degrees from the previously analysed section in either rotational direction (Figure 4.7C). The cumulative angle changes were surprisingly very variable in both wild-type and Dp1Tyb embryos but were not statistically different (Figure 4.7D). These results may confirm the findings described in Bajolle *et al.*, 2006, as there is an overall negative trend in cumulative rotation of both genotypes, indicating that the parietal cushion is twisting leftwards around the septal cushion as the OFT rotates. However, the noise from this data set likely stems from the ages of the embryos used, with the E12.5 cohort having the largest spread of limb-bud stage and some embryos staging to a full embryonic day younger (§§3.2.1).

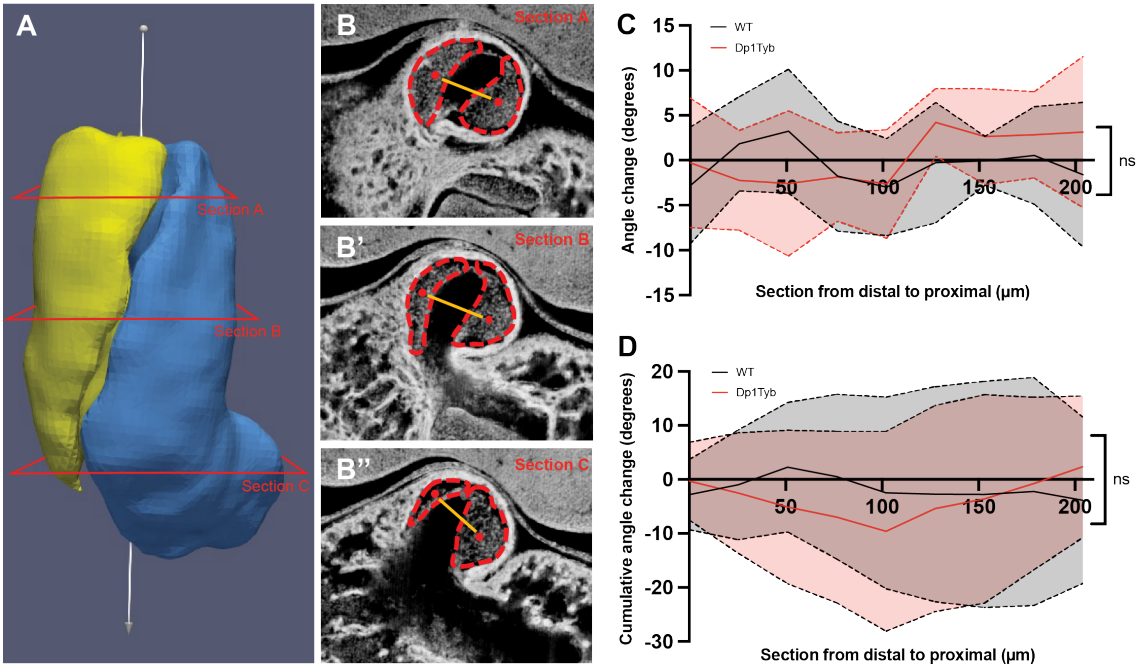

Figure 4.7 Rotation of the outflow tract at E12.5. (A) Segmented E12.5 outflow tract cushions with 3 section planes to illustrate where rotation measurements were obtained from. (B-B'') Sections from a transverse view of the outflow tract in (A), the outflow tract cushions are outlined with a dashed red line with the centroid of each cushion indicated with a red dot and the rotation line illustrated by the yellow line. (C) A graph tracking the angle change in degrees from one section to the previous. (D) A graph showing the cumulative angle change from each subsequent section to the starting section. The statistical test performed was Two-Way ANOVA, mean and standard deviation shown in C&D; wild-type n=10, Dp1Tyb n=14.

4.2.3 Dp1Tyb cushions are dysmorphic prior to septation

With some evidence of delayed OFT septation in the Dp1Tyb embryos at E12.5, I set out to assess whether the OFTCs were volumetrically and morphologically different. I imported the meshes to MeshLab, an open-source software, to calculate the volume using the "Compute Geometric Measures" function. This analysis includes all the OFTCs for this stage, regardless of whether they were fused or unfused. I found no significant change in the volumes of the septal cushions between Dp1Tyb and wild-type embryos (Figure 4.8A), nor any correlation between septal cushion volume and microstage in either genotype (Figure 4.8B). This was also the case when looking at the parietal OFTCs alone (Figure 4.8C-D) or when the septal

and corresponding parietal volumes were combined (Figure 4.8E-F). I found this result interesting as the results above in this chapter had shown delayed fusion of cushion development that one would expect to be correlated with more remaining (undifferentiated) cushion mesenchyme and therefore a larger cushion volume in the Dp1Tyb embryos. However, this could have been balanced by less gross cushion growth in Dp1Tyb embryonic hearts.

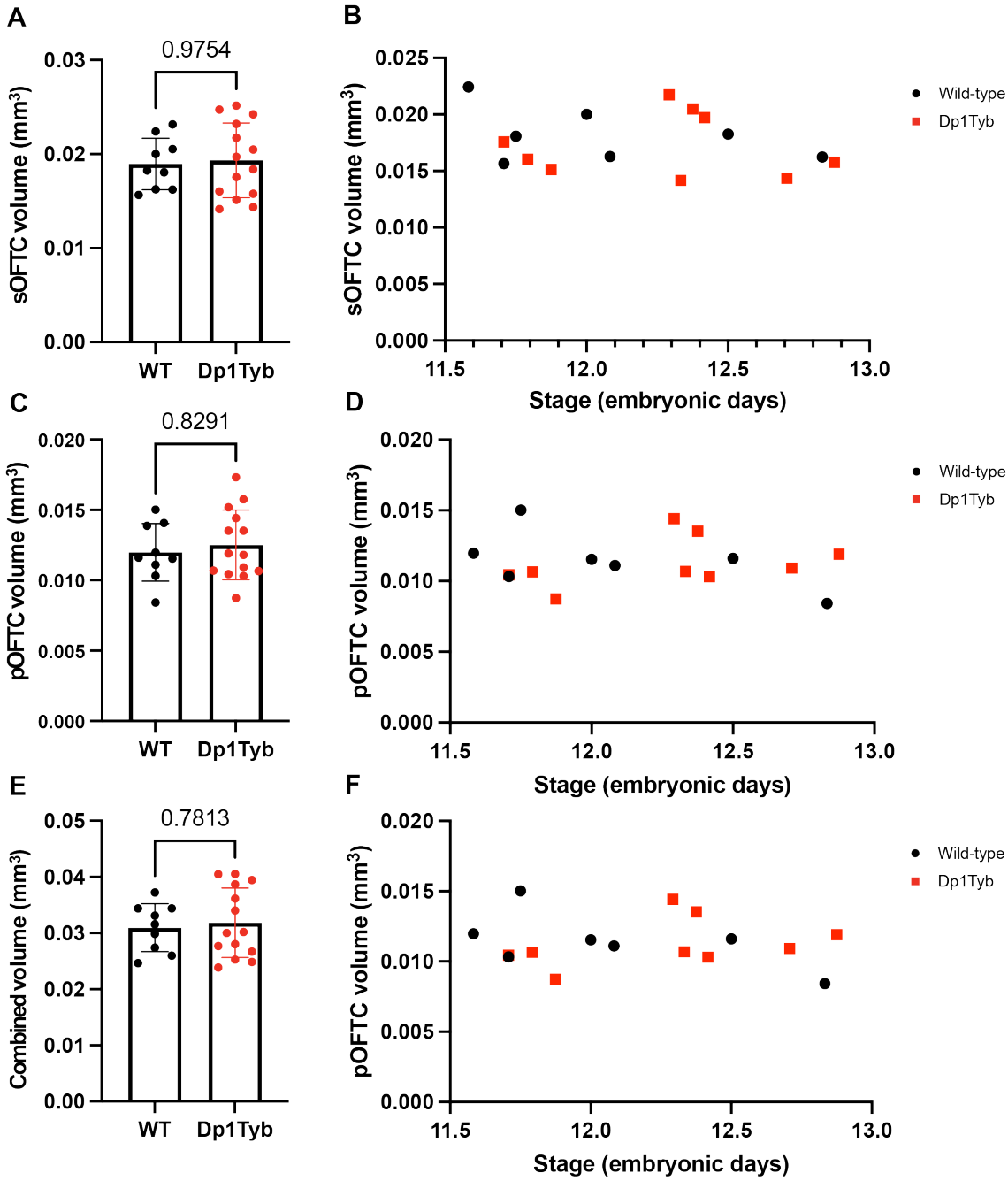

Figure 4.8 Septal and parietal cushion volumes in E12.5 wild-type and Dp1Tyb embryos. (A) Quantification of septal outflow tract cushion volume in both genotypes. (B) Plot of the microstage of each embryo sample against its septal cushion volume. (C) Parietal outflow tract cushion volume in both genotypes. (D) A plot of the microstage of each embryo sample against its parietal cushion volume. (E) The sum of the septal and parietal cushion volumes for each embryo in both genotypes. (F) A plot of the microstage of each embryo sample against the combined cushion volume. Statistics were performed using Mann-Whitney test, mean with standard deviation shown in A, C & E; wild-type n=9, Dp1Tyb n=14.

As a further quantification, using Dragonfly software, I measured the lengths of the cushions that had fused, thereby measuring the extent the distal region of the cushions had condensed and moved proximally towards the ventricles in preparation for OFT septation (Figure 4.9A-B). There was no significant change between the genotypes in the total cushion length in both fused and unfused morphologies (Figure 4.9C). The remaining cushion structure length below the fused distal area (in cushions where there was no fusion, this measurement is the same as the total cushion length) is not significantly changed between the wild-type and Dp1Tyb embryos (Figure 4.9D), or as a percentage of the whole cushion length (Figure 4.9E).

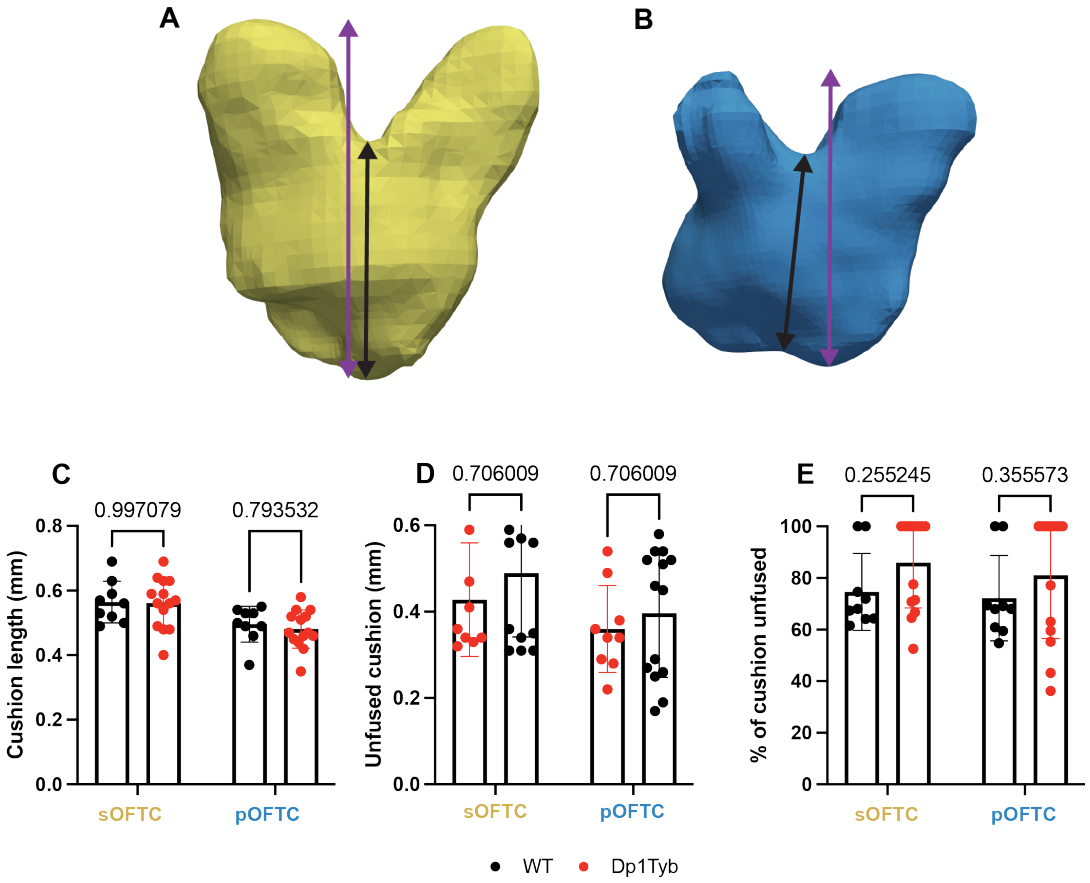

Figure 4.9 Quantification of parietal and septal cushion fusion and length at E12.5. (A-B) Segmentation of outflow tract cushions that had begun fusion, the parietal is shown in yellow (A) and the septal cushion in blue (B). (C) Total cushion length in the wild-type and Dp1Tyb cushions, indicated by the purple double-headed arrows. (D) Length of unfused cushion remaining, indicated by the double-headed arrows in A-B. (E) The length of the remaining unfused cushion is expressed as a percentage of the total cushion length for both genotypes. The statistics performed was a Mann-Whitney test, mean with standard deviation shown; wild-type n=6, Dp1Tyb n=6.

Following the E12.5 quantifications, I moved on to E13.5 OFTCs to continue tracking the developing anatomy of the OFT and the cushions. Cushions at this stage were much harder to segment from the HREM images due to the OFTCs appearing to have a higher tissue density than in earlier stages making the boundaries between myocardium and cushion mesenchyme harder to identify. This was overcome by digitally reslicing the image stack after the mesh boundaries had been interpolated from manual outlines to check that the boundaries were correct in every plane, if they were not I would add more manual segmentations to improve the software interpolation. Figure 4.10, shows an example cushion tissue outline in the transverse (XY), frontal (YZ) and sagittal (XZ) planes and 3D renderings of the structure segmented as the OFTC at E13.5. The cushion at E13.5 is no longer made of the septal and parietal components but is fused into a saddle-shaped structure with slight pronged protrusions in the ventral and dorsal areas of the cushion where the pulmonary and aortic valves are forming (Figure 4.10D-F).

In measuring the volumes of E13.5 OFTCs, I found that Dp1Tyb cushions had a decreased volume compared to wild-type cushions (Figure 4.11A). One might have expected that delayed myocardial differentiation would leave a greater volume of undifferentiated cushion tissue. This result therefore suggests that such an effect must be smaller than that of lower volume growth in Dp1Tyb compared to wild-type. To make sure that this difference was not due to a systematic stage difference between the sample sets, I plotted the individual cushion volumes against their microstages based on limb bud morphology. This showed no correlation between cushion volume and the age of the embryo (Figure 4.11B) and no significant difference between the average age and spread of the embryos between the genotypes (Figure 4.11C).

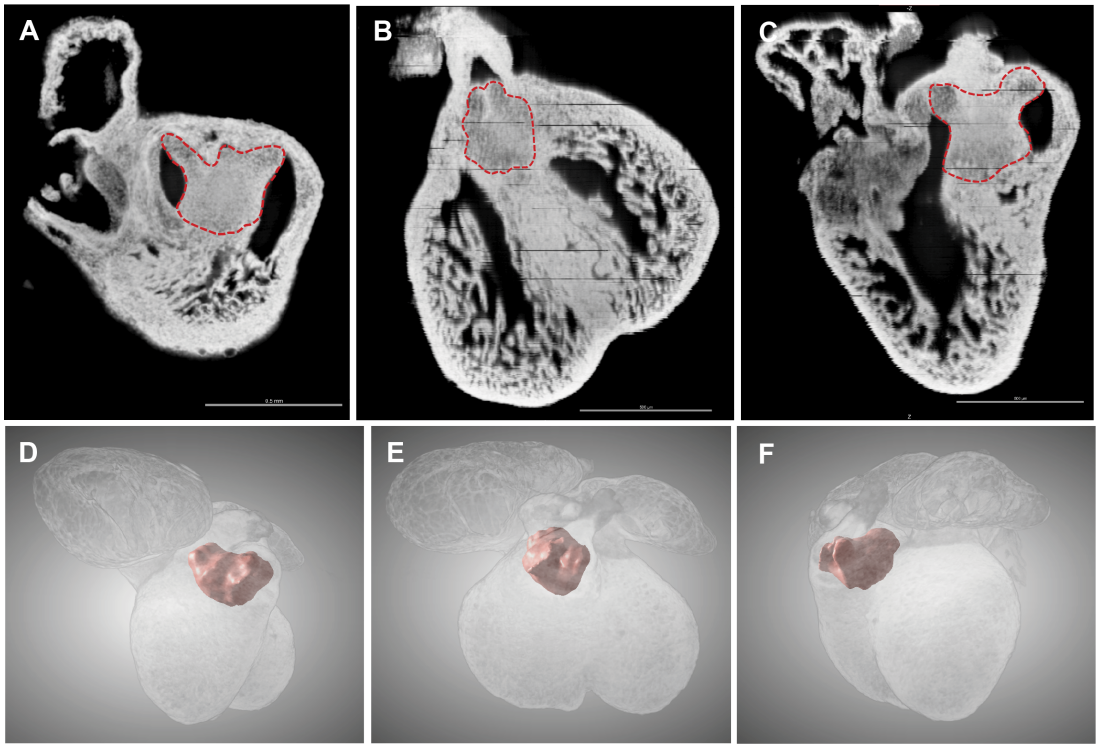

Figure 4.10 Segmentation of the now fused outflow tract cushion at E13.5. (A-C) The area of cushion mesenchyme in an E13.5 heart is encircled with a red dashed line, seen from transverse, frontal and sagittal orientations respectively. (D-F) 3D reconstruction of the segmented cushions within the heart, displayed from the right sagittal, frontal and left sagittal views respectively. Scale bars are 500 μm.

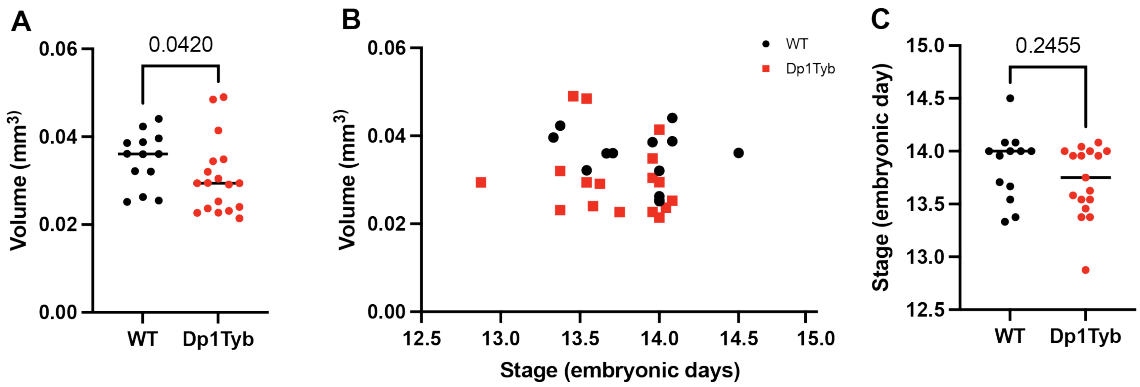

Figure 4.11 Corresponding the microstage of wild-type and Dp1Tyb embryos to the outflow tract cushion volume at E13.5. (A) Volumes of the outflow tract cushions of wild-type and Dp1Tyb hearts irrespective of microstage. (B) Plot showing the microstage of each embryo against the volume of its outflow tract cushion. (C) Comparison of the spread of microstages in the data set. Statistics used were Mann-Whitney tests, mean shown in A & C; wild-type n=13, Dp1Tyb n=18.

4.2.4 Morphometric analysis of outflow tract cushions

As there was a volumetric decrease in the Dp1Tyb OFTC at E13.5 compared to wild-type embryos, I set out to determine whether the volumetric changes were global for the cushions or if it was from specific regions of the cushion anatomy. In addition, during the segmentation of E13.5 OFTCs, I noticed there was a wide variation in cushion morphology. I questioned whether two observations could be related and how they might impact septation. The E13.5 OFTCs were broadly all saddle-shaped, with a pair of ridges on the ventral and dorsal sides of the cushion (a representation of this is illustrated in Figures 4.12B-C). However, the cushions tended to vary slightly in size, prominence of ridges, curvature of the saddle and flatness of the proximal cushion. I initially suspected that this may be due to the slight variations in embryonic age as a lot of morphological change happens immediately before ventricular septation is complete at E14.5.

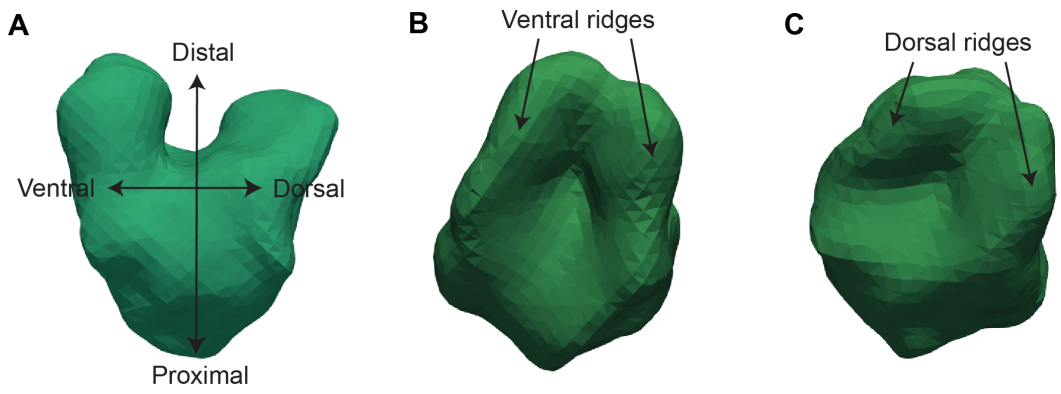

Figure 4.12 Anatomy of the outflow tract cushion at E13.5. (A) 3D segmentation of an outflow tract cushion viewed from the right sagittal, the horizontal arrows indicating the ventral-dorsal axis and vertical arrows indicating the distal-proximal axis. (B) The same cushion rotated to the ventral face, with the ventral ridges shown by the arrows. (C) The cushion rotated to show the dorsal ridges indicated by the arrows.

To test this hypothesis, I selected 9 cushions from each wild-type and Dp1Tyb group and arranged them from earlier to later stages based on limb-bud staging, which ranged from E13.5 to E14.1 in the wild-type and E13.4 to E14.1 in the Dp1Tyb embryos. Figure 4.13 shows the cushions in an anatomical sagittal orientation for visual assessment of the saddle curvature, Figure 4.14 displays the ventral ridge of

the cushions and Figure 4.15 shows the surface of the proximal cushion in the short-axis orientation. Arranging the cushions by microstage allows any phenotypes to be disaggregated temporally or due to genotype.

In the sagittal view (Figure 4.13), very few of the cushions have a more pronounced saddle shape at the distal end where there are bumps at both dorsal and ventral ends, created by the top of the ventral and dorsal ridges. This more pronounced morphology is seen in the wild-type embryos at E14.0 (Figure 4.13D) and E14.1 (Figure 4.13I), but in the Dp1Tyb at E13.6 (Figure 4.13M). I expected this phenotype to be from a more mature embryo, as this anatomy should coincide with the condensation of mesenchymal cells, formation of the valves and the septation of the OFT. The remainder of the cushions appear squarer in this orientation, but there is no apparent correlation in morphology between the genotypes or age.

Arranging the cushions by embryonic age revealed no obvious pattern in changing morphology and that anatomical variability happened regardless of genotype. However, these observations are qualitative descriptions that are prone to subjectivity, especially with such ambiguous and variable shapes. I, therefore, used an existing morphometric tool developed by the Green and Tybulewicz labs to apply a quantitative approach to assessing cushion morphology (Toussaint *et al.*, 2019). This process involved registration and atlasing the cushions to enable averaging and principal component analyses to quantify and map how different these shapes were from one another with respect to genotype.

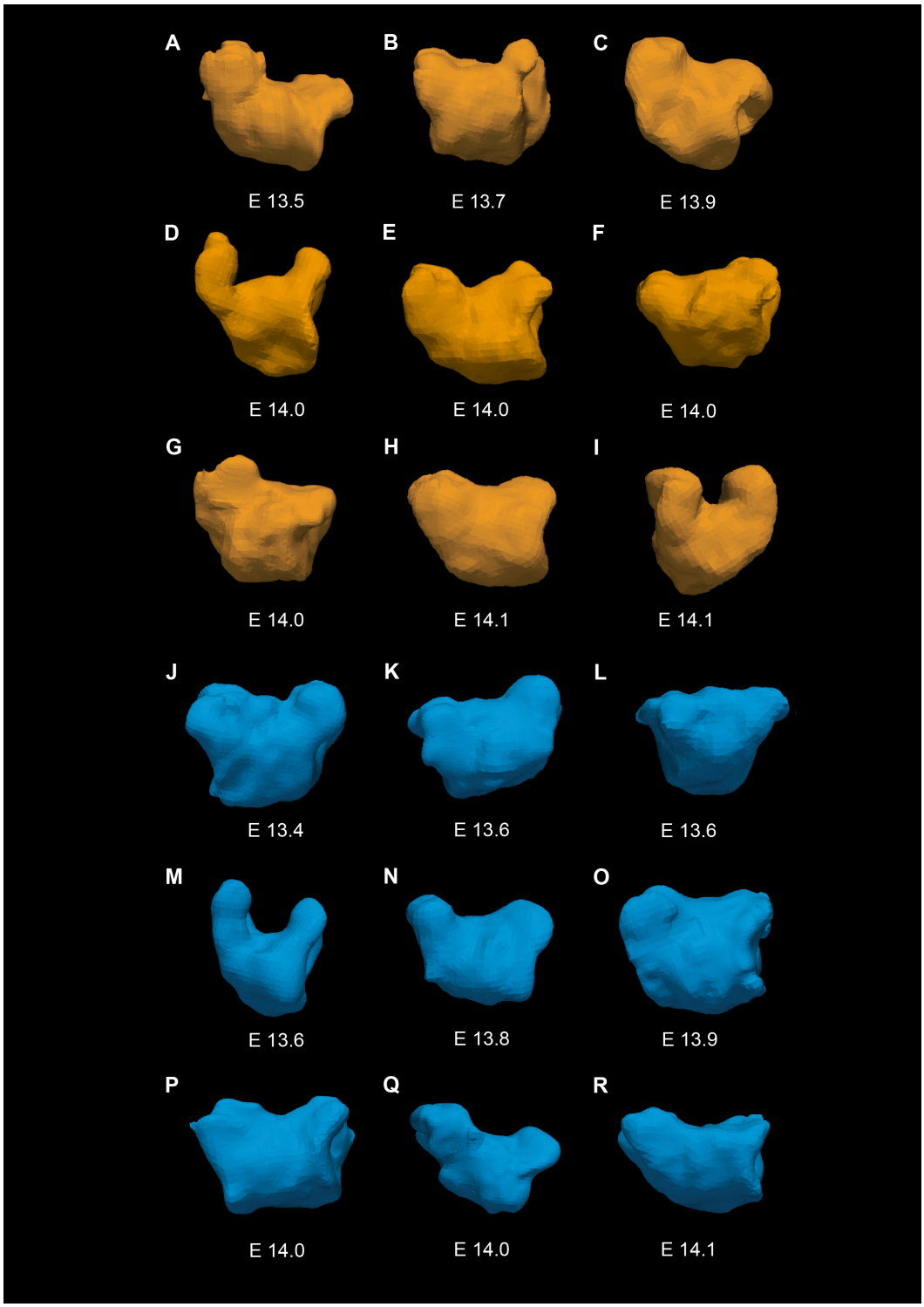

Figure 4.13 Sagittal view of selected samples of 3D segmentations of outflow tract cushions in E13.5 wild-type and Dp1Tyb hearts. Wild-type outflow tract cushions are false-coloured orange and are arranged by their microstaged ages, the Dp1Tyb cushions are similarly arranged by microstage and false-coloured blue.

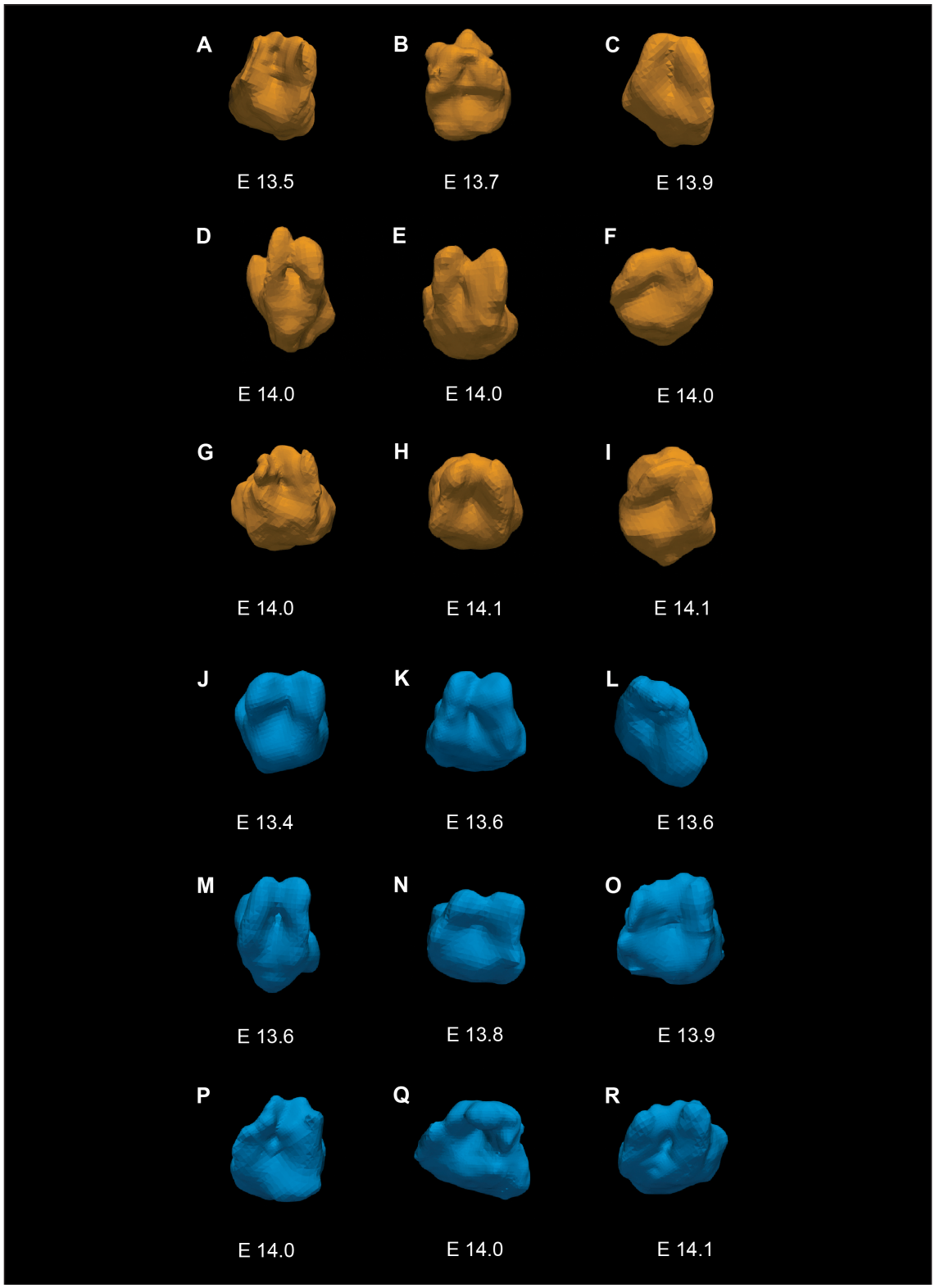

Figure 4.14 Ventral view of selected samples of 3D segmentations of outflow tract cushions in E13.5 wild-type and Dp1Tyb hearts. Wild-type outflow tract cushions are false-coloured orange and are arranged by their microstaged ages, the Dp1Tyb cushions are similarly arranged by microstage and false-coloured blue.

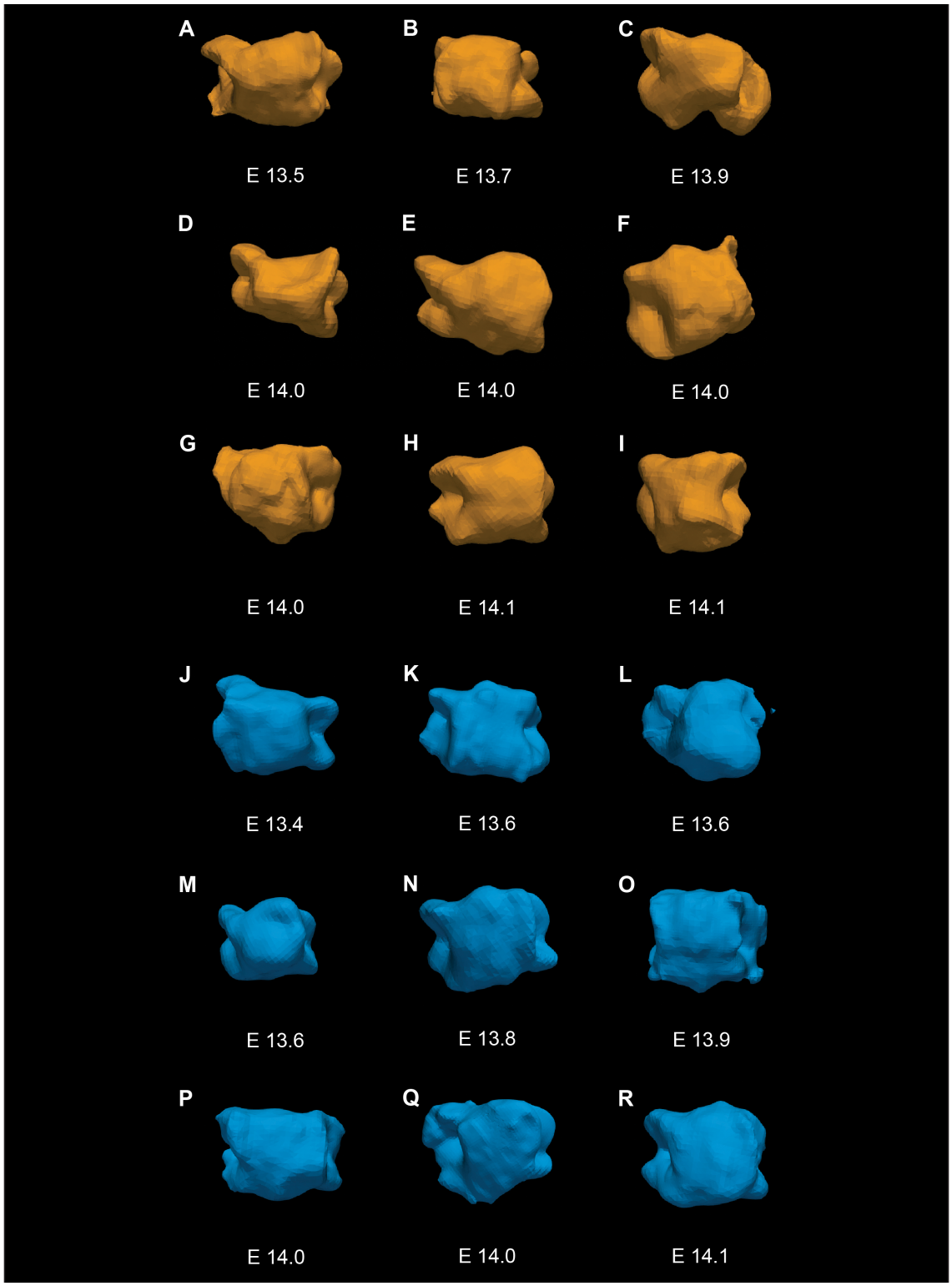

Figure 4.15 Short axis view of selected samples of 3D segmentations of outflow tract cushions in E13.5 wild-type and Dp1Tyb hearts. Wild-type outflow tract cushions are false-coloured orange and are arranged by their microstaged ages, the Dp1Tyb cushions are similarly arranged by microstage and false-coloured blue. This orientation displays the morphology of the proximal cushion.

Registration of the cushion shapes was not a trivial task given that there were no sharp and consistent landmarks. I approached this using two different software packages in series with help from Dr Saoirse O'Toole (King's College London). The first software I used to bring the OFTC meshes together was GeoMagic, a commercial package used for 3D CAD modelling. GeoMagic requires one shape from the dataset to be set as the "reference". For this, I selected the cushion I felt had the most obvious anatomy in terms of the placement of the ventral and dorsal ridges and the centre of the proximal cushion where there was a more pronounced bump. This is because the alignment to the reference could only be done one mesh at a time, so I had to be able to consistently choose the same landmarks on the reference cushion. This cushion is the same as seen in Figure 4.12. I then selected 9 "landmarks" on the reference cushion and their corresponding points on the mesh I wanted to align to the reference (Figure 4.16). The "landmarks" I chose were 4 on the upper and lower ventral ridges (Figures 4.16A-B), with the lower ridge defined as where the ridges meet the body of the cushion, the same 4 points on the dorsal ridge (Figures 4.16D-E) and finally one in the centre of the proximal cushion surface, where there is a ridge (Figures 4.16G-H). The software aligned the meshes in real time as I placed each landmark on the reference mesh and the corresponding one on the aligning mesh.

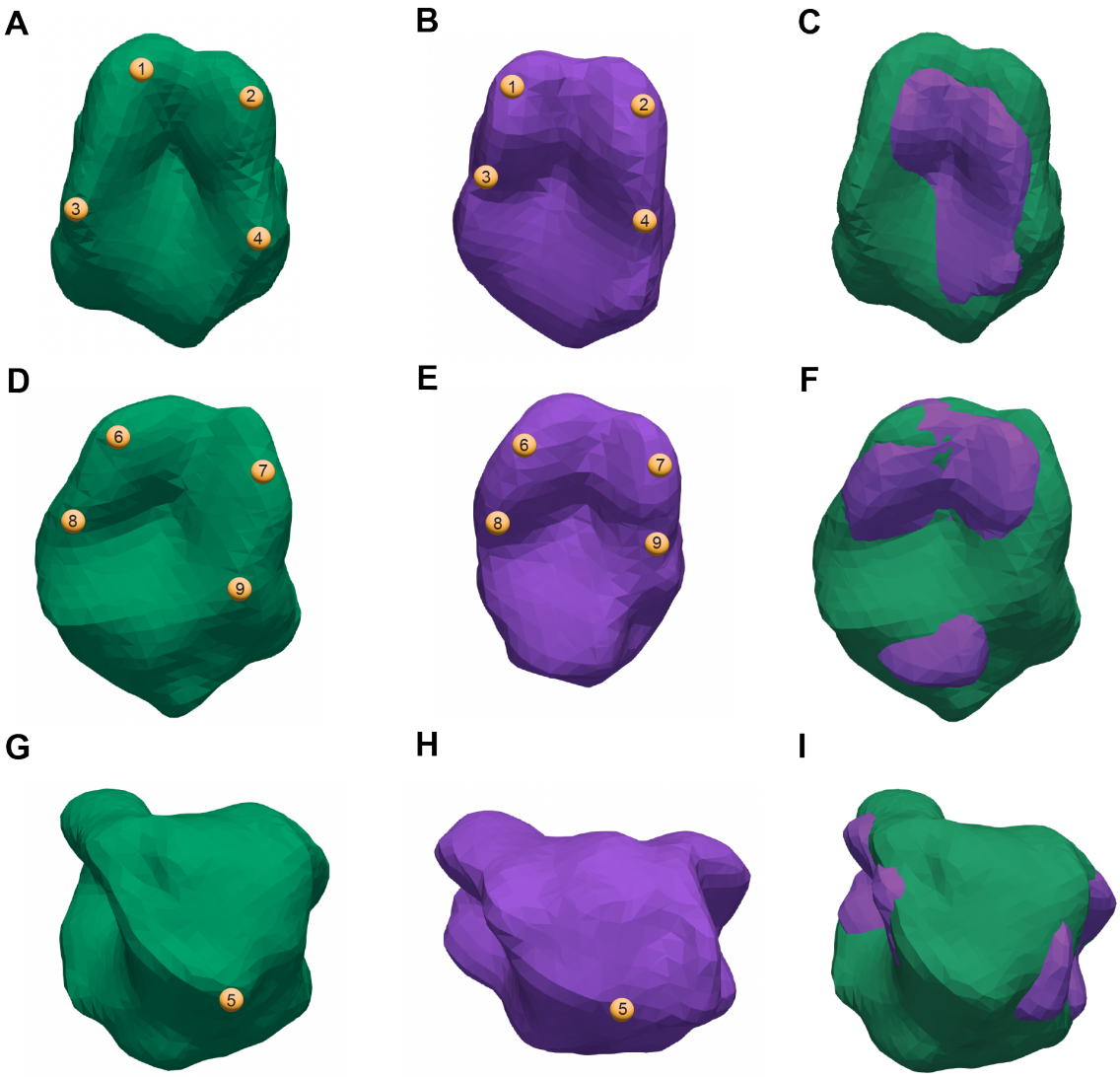

Figure 4.16 Locations of landmarks used for mesh registration for GeoMagic software. (A-C) 3D segmentation of E13.5 outflow tract cushions with the first 4 landmarks (orange spheres 1-4) placed on the ventral ridges of the wild-type reference mesh (green) and the corresponding landmarks on the aligning Dp1Tyb mesh (purple), panel C shows how the two meshes register when viewed together. (D-F) Location of the 5th landmark (orange sphere 5) in the centre of the proximal face of the wild-type reference and Dp1Tyb meshes, with the resulting registration in F. (G-I) Last 4 landmarks (orange spheres 6-9) placed on the dorsal ridges of the wild-type reference and the same points on the Dp1Tyb mesh, panel C shows the overlay of the meshes in this orientation after registration.

The second software I put the meshes through for alignment was WearCompare (O'Toole *et al.*, 2019). Initially developed by orthodontists to assess the wear on tooth surfaces by making 3D mesh renderings of a patient's teeth, I felt that the software could be applied to my project despite the difference in scale. WearCompare offered a similar strategy to alignment as GeoMagic, though instead of individual landmarks on the surface of the mesh for registration, it provided a paintbrush tool to select multiple regions on the mesh surface for the software to align the secondary mesh to (Figures 4.17A-C). Like GeoMagic, there needed to be a "reference mesh" to select the points on and the alignment could be seen in real-time so adjustments to areas selected could be made. The same reference mesh (Figure 4.12) was used for each alignment for consistency.

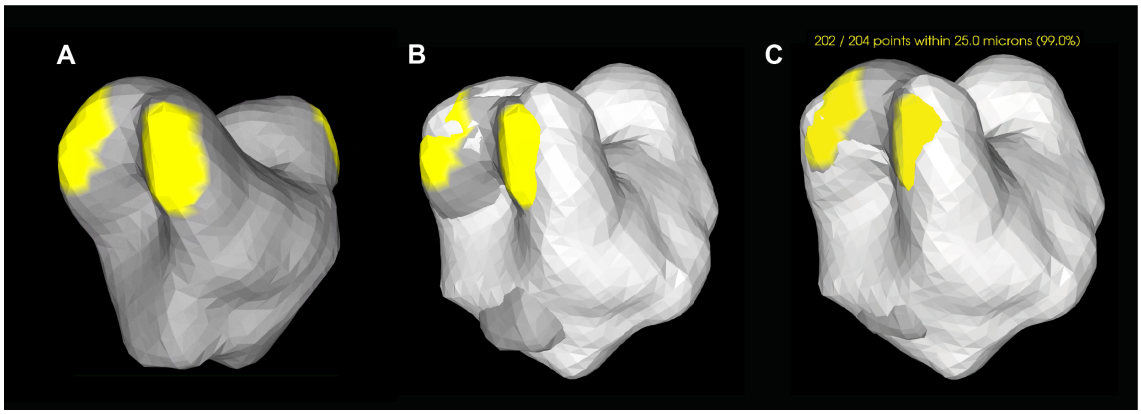

Figure 4.17 Secondary registration of E13.5 outflow tract cushion meshes with WearCompare. (A) Reference mesh (grey) viewed from an oblique ventral orientation, clusters of coordinates used for registration to the aligning meshes are highlighted in yellow. (B) Overlay of the aligning mesh (white). (C) Post-alignment in WearCompare based on 4 clusters of coordinates, 2 at each ventral and dorsal ridges. The yellow text indicates how many corresponding points on the aligning mesh are within 25 μm of the highlighted coordinates on the reference mesh.

GeoMagic had to be used first in this two-step alignment as some of the meshes were too far apart when opened together in the same 3D space which WearCompare struggled with but GeoMagic did not. After aligning in WearCompare, the software was used to visualise the distance between the surface of the reference mesh to the test meshes by creating a heatmap of the selected surface. Figure 4.18 shows an example Dp1Tyb cushion projected onto the wild-type reference cushion,

with the surface of the proximal face of the cushion and ventral ridges selected as areas to visualise morphological differences with a user-defined scale. From this randomly selected Dp1Tyb sample, the points on the Dp1Tyb proximal region of the cushion appear recessed by approximately 60 μm from the wild-type reference cushion. This is a visualisation of the observations I made with Figure 4.15 where the proximal cushion seemed to be flatter and squarer compared to the wild-types, but could not be quantified for statistical analyses. WearCompare can only do this for a pair of cushions at a time whereas the morphometric pipeline developed by (Toussaint *et al.,* 2021) will create 'average' morphologies using all supplied wild-type meshes and Dp1Tyb cushions and compare all the meshes. It will then produce a principal component analysis of the difference in shape and identify regions of change between the "average" wild-type and Dp1Tyb cushion.

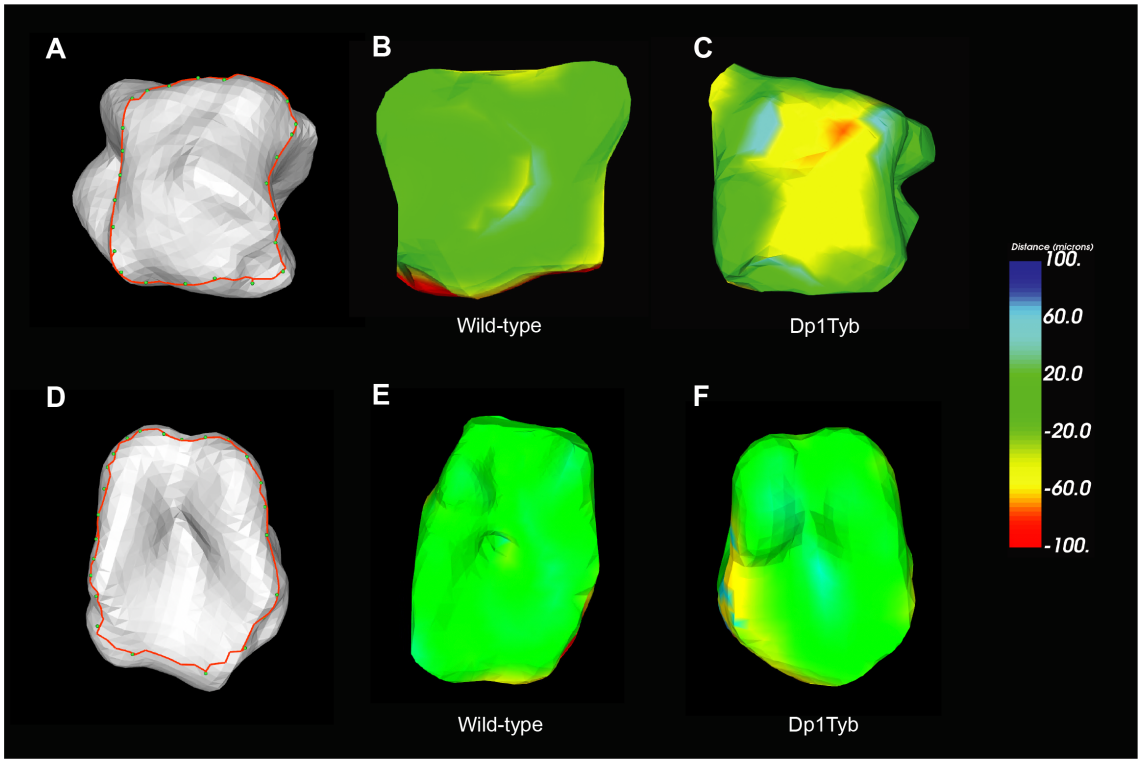

Figure 4.18 Heatmap of the deformation of surfaces from the reference wild-type outflow tract cushion to a representative Dp1Tyb cushion at E13.5 in WearCompare. (A) Outline of the proximal cushion anatomy in the wild-type reference mesh outlined in red. (B) Heat map of surface changes in another wild-type cushion to the reference. (C) Heat map of proximal surface changes from the wild-type reference to a Dp1Tyb cushion. (D) Outline of the ventral cushion anatomy including the ridges in red. (E) Surface change heat map of the ventral anatomy from the reference to a wild-type cushion. (F) Heat map of surface change in the ventral anatomy wild-type reference mesh to Dp1Tyb.

With the cushion meshes aligned based on the above landmarks in GeoMagic and further adjustment with WearCompare, I utilised the quantitative 3D morphometrics pipeline described in (Toussaint *et al.*, 2021). The pipeline was initially developed to compare the craniofacial morphology of Dp1Tyb mice to the wild-type but can be adapted for any 3D data set that can be aligned reliably. The pipeline uses a multi-part Python script that starts with binarizing and segmenting image stacks, creating the meshes, mesh alignment, atlas construction and finally shape statistics. As I already had the meshes created and aligned, I started with atlas construction. This script utilises Deformetrica, a software for the statistical analysis

of 2D and 3D shape data that computes the deformations of the objects given (Durrleman *et al.*, 2014; Bône *et al.*, 2018). Atlas construction outputs the mean shape of the populations, the moments of displacements from the meshes to the mean shape and the control points which define areas of the largest variability in the group. The number of control points is a parameter that can be adjusted, for this analysis I chose 62 control points for good coverage of my meshes considering their size, and I did not observe a change in the data output when the analysis was run with 180 points. These three data sets are used to calculate shape statistics, which is the last script in the pipeline.

The shape statistics script first computes a kernel principal component analysis (kPCA) (Schölkopf *et al.,* 1997), which allows the description of the data in reduced dimensional space to visualise how “different” the shapes of the meshes are as a whole. The kPCA did not show clustering of the wild-type and Dp1Tyb OFTC meshes (Figure 4.19). The kPCA analysis is described as not significant ($p = 0.57$) which suggests that despite the change in volume described above (§§4.2.3) the overall shapes are not different enough to be statistically described as such in the Dp1Tyb cushions.

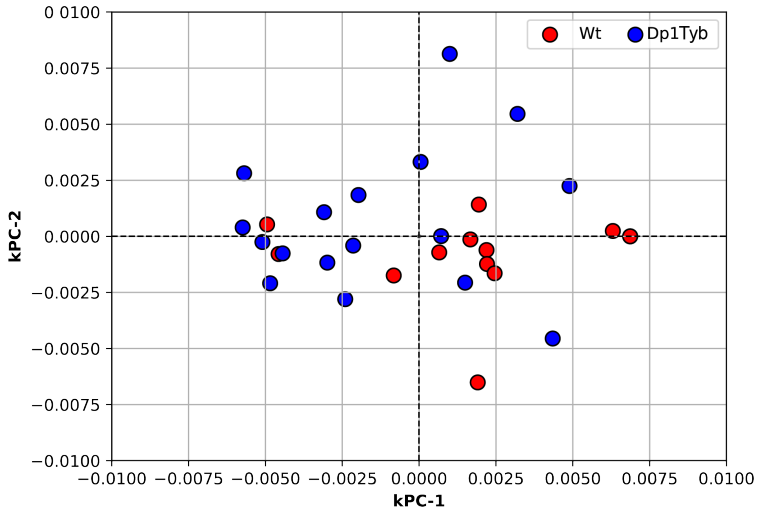

Figure 4.19 kPCA plot of wild-type and Dp1Tyb outflow tract cushion meshes. kPCA plots of the first two principal components determining the momenta of wild-type and Dp1Tyb outflow tract cushion meshes at E13.5 using a specified number of control points. Variance is determined by the areas of shape with the greatest change from one population to another.

The shape statistics Python script also used the “shooting” package from Deformetrica, which compares the mean shape of one group to the other, calculating the displacement of points on the meshes and localised volume change which can be projected back onto the meshes to visualise these changes. Figure 4.20A-D shows the average Dp1Tyb mesh and the displacement of points on the mesh relative to the average shape of the wild-type. The sagittal (Figure 4.20A) and short axis (Figure 4.20B) views show that the biggest displacement of points occurs in the proximal cushion according to heatmapping. There did not appear to be any changes as dramatic when looking at the ventral ridges (Figure 4.20C) or the dorsal ridges (Figure 4.20D). When the volume change is projected onto the same Dp1Tyb mean shape, the heat map colours flip as this visualisation shows the directionality of the shape change. The biggest changes are in the proximal cushion when viewed from the sagittal and short axis views (Figure 4.21A-B), where the average Dp1Tyb cushion shows a recession when compared to the wild-type mean. The ventral (Figure 4.21C) and dorsal ridges (Figure 4.21D) of the Dp1Tyb group show a change in volume which is perhaps reflective of point displacements described above.

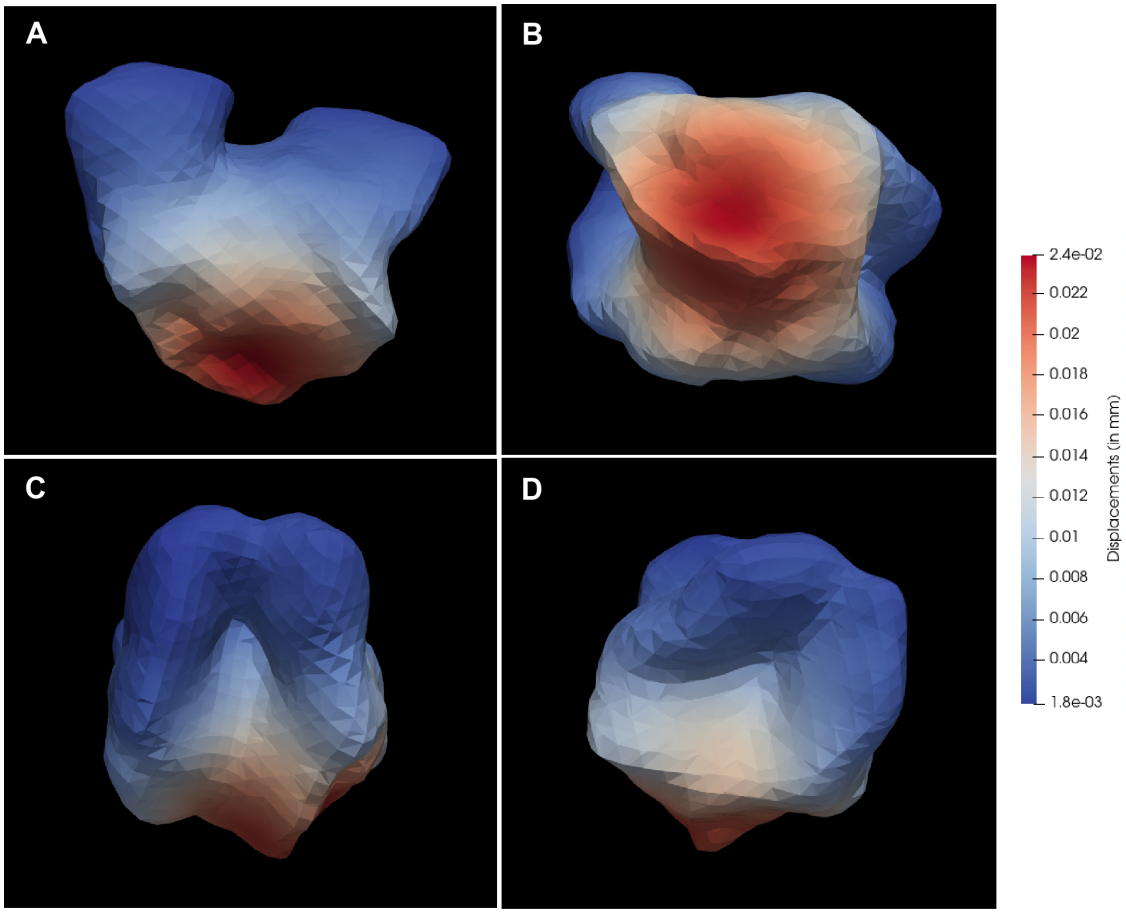

Figure 4.20 Heat maps of altered shape in Dp1Tyb outflow tract cushions compared to wild-type at E13.5. Displacement heat maps projected on the mean shape of a Dp1Tyb outflow tract cushion mesh at E13.5 when compared to the wild-type group average. (A) The sagittal view of the cushions from the right. (B) Short axis view of the cushion. (C) Frontal view of the cushion with the ventral ridges visible. (D) Posterior view of the cushion mesh with the dorsal ridges visible.

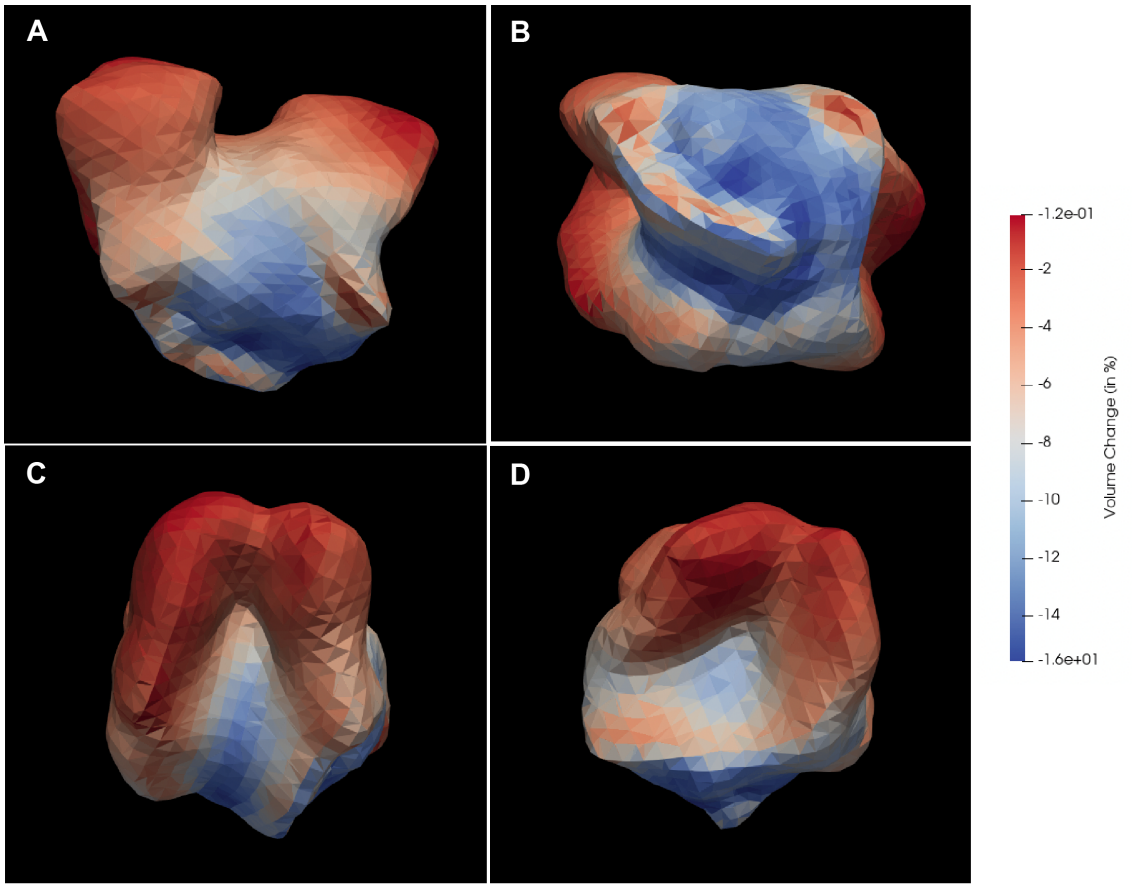

Figure 4.21 Heat map of localised volume changes in the Dp1Tyb outflow tract cushions compared to wild-type at E13.5. Volume change heat maps projected on the mean shape of a Dp1Tyb outflow tract cushion mesh at E13.5 when compared to the wild-type group average. (A) The sagittal view of the cushions from the right. (B) Short axis view of the cushion. (C) Frontal view of the cushion with the ventral ridges visible. (D) Posterior view of the cushion mesh with the dorsal ridges visible.

4.3 Discussion

In this results chapter, I tracked the developmental changes in OFTC morphology in the stages leading up to ventricular septation to assess whether the development of the OFT and fusion of the endocardial cushions are affected in the Dp1Tyb embryos. This was achieved by using the serially sectioned HREM images in combination with Dragonfly, the 3D image processing software, to segment the cushion structures from the images to create surface meshes of the structure. These meshes were then used to obtain volumetric and morphometric data to assess the developing structures.

4.3.1 Decreased fusion of Dp1Tyb outflow tract cushions at E12.5

The first observation of dysmorphic OFTCs in the Dp1Tyb embryos was made from the processed HREM images before segmentation, where, in contrast to wild-type OFTCs, Dp1Tyb cushions had not begun fusing and there was an absence of a myocardialised bridge forming the arterial roots (Figure 4.3A) in the distal cushions. Thus, the majority of Dp1Tyb hearts still shared a common arterial trunk. Instead of this bridge, there were swellings in both the parietal and septal cushions with areas of condensed mesenchyme (Figure 4.3B), which are presumably the progenitor pools for the myocardial bridge, characteristic of the previous developmental stage. The myocardial bridge forms from the condensed mesenchymal swelling within the individual OFTCs. These cells are derived from CNCC that have migrated in through the PAs at E8.5-E9.5 (Jiang *et al.*, 2000). The condensations of CNCC-derived mesenchyme split the distal ends of the cushions and then coalesce to form the myocardial bridge (Waldo *et al.*, 1998), which is the process I observed as delayed in the Dp1Tyb cushions.

Since by E13.5 Dp1Tyb cushions have fused and partitioned the arterial trunk, the difference at E12.5 suggests a developmental delay. This is specifically in the OFT of mutants exhibiting the unfused phenotype as there was no correlation between the microstage of the embryos (based on high-resolution limb morphology) and the progression of fusion. This suggested developmental delay could be caused by defective onset or progress of CNCC migration or could be a later delay, specifically in the timing of mesenchymal condensation, endocardial rupture or myocardial bridge-building itself. Ablation of CNCC has been shown in many studies to lead to defects in the alignment of arterial vessels and outflow septation (Kirby and Waldo, 1995). Although OFT defects with VSDs are rare in Dp1Tyb embryos compared to AVSDs and VSDs, the fact that there are occasional OFT defects in these mice suggests that CNCC may be involved in the phenotype and from CNCC ablation studies, timing of CNCC migration during development could be a factor. Another possibility is that the CNCC migrate into the OFT at the correct time, but are deficient in proliferation and that this leads to a delay in the start of septation. This has not been directly studied in DS models specifically looking at CNCCs. However, Dp1Tyb cranial (i.e. non-cardiac) neural crest cells were found to migrate normally but have a lower proliferation rate once at their destination leading to smaller neural

crest-derived craniofacial bones (Redhead *et al.*, 2023). In another DS mouse model, Ts65Dn, cranial neural crest cells were found to have deficits in delamination and migration in addition to mitosis in explant cultures of the neural tube (Roper *et al.*, 2009). It is possible that CNCC in the Dp1Tyb mice are also deficient in these processes. This could be explored using lineage labelling techniques by producing a Dp1Tyb.Wnt1-Cre transgenic mouse, unfortunately, this was beyond the time limitation of the project due to difficulties in mouse breeding.

It is also possible that the Dp1Tyb fusion delay was not due to abnormalities within the fusing CNCC-containing tissue itself. It was notable that the parietal and septal cushions sat further apart in the medial and distal cushion sections of the Dp1Tyb hearts that had been typed as “unfused” than the OFTCs in the wild-type embryos. In wild-type hearts, they abutted one another at the same levels of the OFT. As the Dp1Tyb cushions were not volumetrically larger at E12.5 nor were there consistent differences in shape at the distal ends, the gap between the cushions may be due to a bigger circumference of the OFT itself, or the cushion mesenchyme and cardiac jelly could be distributed differently throughout the structure without any difference in overall volume. With the latter hypothesis, more of the Dp1Tyb cushion mesenchyme may be distributed at the distal region of the cushion, leaving the medial and proximal regions of the cushions smaller and thus further apart. Smaller medial and proximal cushions may be responsible for the dysmorphology observed the next embryonic day at E13.5, as there is an indication of dysmorphic proximal anatomy of the Dp1Tyb OFTCs at this stage.

4.3.2 Dp1Tyb cushions are dysmorphic at E13.5

By the next embryonic day at E13.5, all the OFTC in Dp1Tyb embryos have completed fusion and the OFT has begun to form discrete arterial vessels. However, the remaining cushion tissue appears dysmorphic with Dp1Tyb cushions measuring smaller in volume, which is not correlated with microstaging of the embryos. Quantitative morphometrics of the E13.5 cushions using the previously described pipeline showed that there is no statistical change in the overall shape of the Dp1Tyb cushions compared to the wild-type. Mapping of volume change and mesh surface

displacement suggests there may be localised recession of the proximal cushion anatomy in the Dp1Tyb data set relative to the wild-type cushions.

Dysmorphic cushions have implications on ventricular septation, specifically the proximal cushion. The proximal region of the OFTC at E13.5 is partially fused to the crest of mVS but there remains a foramen between the ventricles which is termed the secondary IVC (Figure 4.22), to which the remaining mVS has to grow towards and completely fuse with. Once the OFTC has fully fused with the mVS the secondary IVC is remodelled and renamed the tertiary IVC. This is the space in which the AVCs must extrude to close the remaining foramen and complete ventricular septation (Anderson *et al.*, 2019). Once the proximal region of the OFTC fuses to the muscular septum it needs to muscularise. Failure to do so results in the connection becoming fibrous and leaving a persisting IVC that is not closed by the AVC i.e. a VSD. With the proximal cushions of the Dp1Tyb embryos, the “shelf” above the secondary IVC could be too dysmorphic to consistently allow fusion with the muscular septum, thus contributing to the development of the VSDs detected in the Dp1Tyb embryonic hearts at E14.5 (Lana-Elola *et al.*, 2016).

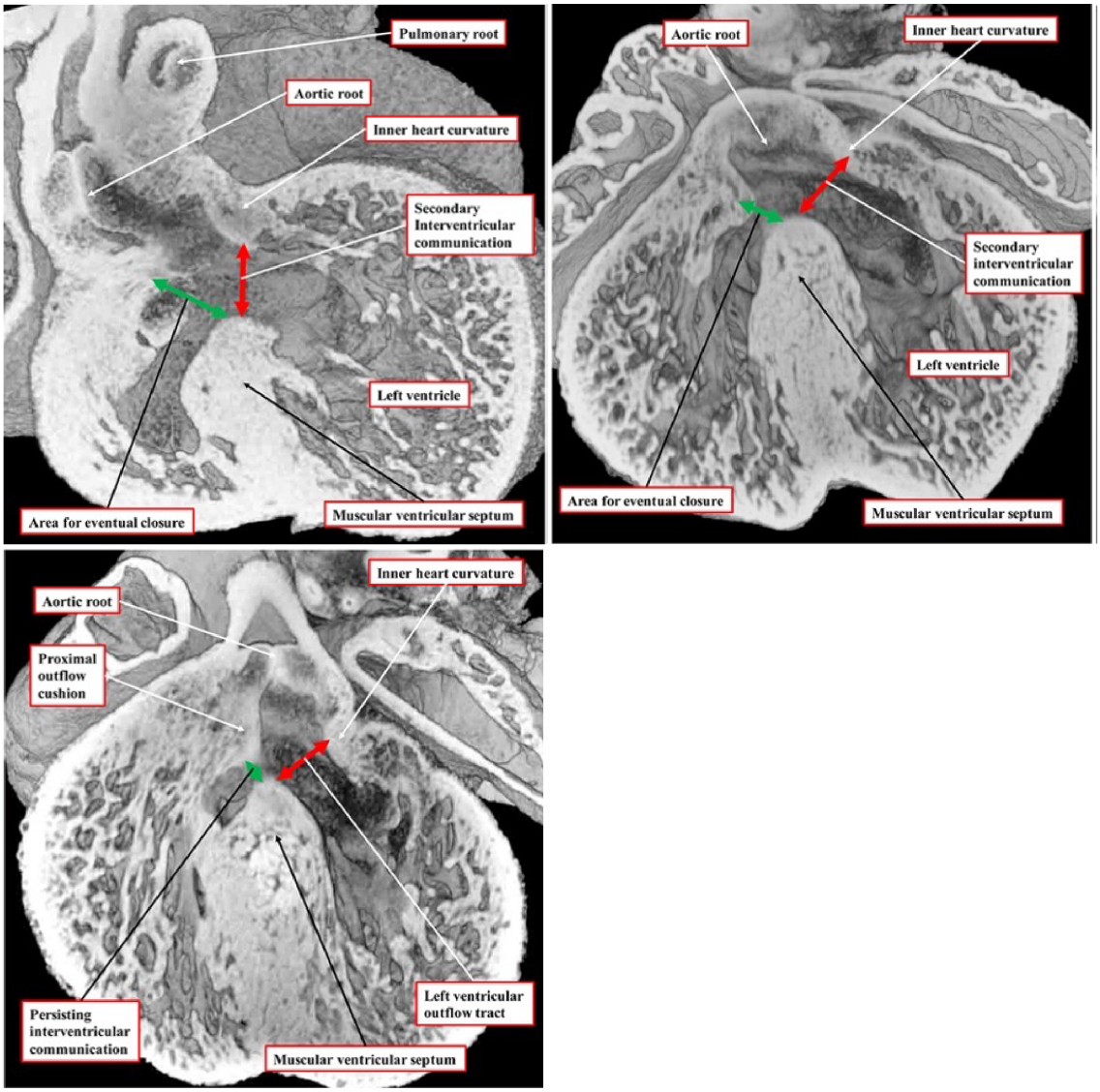

Figure 4.22 Episcopic images of E12.5-E13.5 embryonic mouse hearts with annotated anatomy. The secondary interventricular communication (shown with the red double-headed arrow) is remodelled to become the aorta arising from the left ventricle by complete outflow tract cushion fusion with the muscular ventricular septum. The remaining tertiary interventricular communication (green double-headed arrow) is closed by extrusion of the atrioventricular cushions to form a membranous septum, thereby completing ventricle septation. Top two panels are at E12.5, remaining panel is at E13.5. Adapted from Anderson *et al.*, 2019.

There are multiple points of potential failure if dysmorphic proximal cushions contribute to the lack of ventricular septation. Firstly, the proximal surface may not

extend proximally enough and simply fail to meet the muscular septum and fuse with it. Secondly, the delayed fusion of the cushions and reduced volume could be causing a misalignment of structures when fusing, such that, for example, a flat or blunt proximal OFTC is unable to flex and conform to the top of the muscular septum.

Disruption in the morphology of anatomical structures in development is due to disordered tissue morphogenesis, where altered cellular behaviour causes the cushion phenotype described in the Dp1Tyb embryos. The different proximal cushion morphology could be caused by a change in the number of mesenchymal cells occupying the cushions or a difference in the distribution of the cells throughout the structure, causing localised swelling or shrinking of the anatomy. If there is a change in cell number or distribution, it could arise from altered cellular processes like proliferation or apoptosis in different areas of the cushions. Expression of genes involved in proliferation has already been shown to be down-regulated in single-cell RNA-sequencing data of Dp1Tyb hearts at E13.5 (Lana-Elola *et al.*, 2023). Additionally, the OFTCs are matrix-rich structures, so there may be more or less extra-cellular matrix present within the cushions contributing to the change in volume. To identify if there are changed cellular processes, I used a framework described in Green (2022). This framework is used to characterise the elongation of mammalian tissues by individual or a combination of cellular behaviours, and therefore altered tissue morphology is likely caused by a disruption of one or more of these processes. These cellular behaviours are proliferation, orientation of cell division, cell rearrangement, directional matrix production/expansion, cell addition/subtraction, cell size and shape change. This framework is also referred to as PROMASS, for **p**roliferation, **r**earrangement, **o**rientation of division, **m**atrix, **a**ddition/**a**poptosis, **s**ize and **s**hape.

In the following Results chapter, I characterise some of the cellular behaviours from the framework, namely proliferation, apoptosis and ECM production, to ascertain which could be responsible for the altered morphology of the OFTC before ventricular septation and how these processes are affected in the Dp1Tyb embryos to result in the morphological phenotypes described in this chapter.

Chapter 5. Cellular characterisation of the outflow tract cushions

5.1 Introduction

In the previous chapter, I sought to characterise the morphology of the OFTCs at the developmental stages leading up to ventricular septation. Having characterised the morphology in 3D and deploying various morphometric methods, I was able to show delayed OFT development in Dp1Tyb embryos at E12.5 and variability in the shape of the cushions of E13.5 across both genotypes. Quantitative morphometric analysis of the E13.5 Dp1Tyb cushions showed no change in overall shape from the wild-type, but was suggestive of an altered proximal region. These results were derived from HREM images and made into 3D surfaces for morphometric analysis. Although this is a good technique for structural anatomy, it does not have single-cell resolution due to the staining used in the method. In the next step of the project, I sought to define the cellular basis of the changes between Dp1Tyb and wild-type embryonic hearts leading up to septation. As I had observed morphological differences at E12.5 and E13.5 in the mutants, I used these two times points for the next step of the study.

The OFTC is a complex structure in both how it morphologically develops and how it is established cellularly. Its development is contingent on the contributions and interactions of cells from different embryonic lineages. This process begins with the SHF-derived endocardium within the heart tube swelling with cardiac jelly and undergoing EndoMT at around E8.5-E9 (Kovacic *et al.*, 2019) followed closely by the migration of CNCC from the carotid, pulmonary and aortic PAs (Yamagishi, 2021). The structure reaches its maximal length at E10.5 and begins to twist anticlockwise as it remodels to begin septating into the aorta and pulmonary artery. This process was established in the previous chapter as normal in the Dp1Tyb embryos, where the lengths and rotation of the OFTCs in the mutant mice remained the same as wild-type littermates.

Once migration and EndoMT in the OFTCs have been completed, the cells have many different cellular behaviours. They begin to proliferate to expand the population within the cushions, secrete ECM to elongate and remodel the cushions, as well as undergo apoptosis or differentiate to begin myocardialisation for OFT and

ventricular septation. These developmental processes are essential for proper heart development and dysregulation of them has been shown to underlie different CHD. Examples of this include how hypoplasia of the OFTCs could be caused by fewer proliferating cells in the OFTC leading to defects such as double-outlet right ventricle and persistent truncus arteriosus (Nomura-Kitabayashi *et al.*, 2009), or how impairment of proliferation and increased apoptosis in the OFTCs of *Lrp1* mutant mice coincide with AVSDs (Lin *et al.*, 2020). Furthermore, there is evidence that a trisomy 16 mouse exhibits OFT abnormalities relating to cell patterning abnormalities that lead to dysmorphia and thus CHDs (Waller III *et al.*, 2000).

In this chapter, I sought to determine if any of these processes are disrupted in the Dp1Tyb mice at the key time points identified in the previous chapter (E12.5 and E13.5). I applied various immunohistochemistry techniques and immunofluorescence imaging in serial sections to conduct a comprehensive characterisation of cellular density, proliferation and apoptosis. I will describe how I developed methods to quantify the images, specifically by automating the analysis of the many images acquired per embryo and the results thereby obtained.

5.2 Results

5.2.1 Investigating cellular changes of septal OFTC and parietal OFTC at E12.5

Embryos at E12.5 were collected, prepared for paraffin embedding and then embedded for sagittal sectioning with the embryo on its left. This was so that sectioning would reveal the septal OFTC followed by the parietal OFTC in this orientation, allowing for separate analysis of the two cushions prior to their fusion. Embryos were sectioned on the microtome at 4 μm with every section kept and stained with haematoxylin and eosin. The slides were imaged at every 4th section, leaving a 16 μm space between each measurement thereby avoiding the possibility of counting the same nucleus twice. Although a few sections were lost during the sectioning and mounting process, I endeavoured to keep every section for each embryo for the most comprehensive quantification, with the aim to count every cell in each section.

As eosin does not stain the specific ECM proteins present in the OFTCs, the outline of the structures was demarcated from the surrounding myocardium by the absence of eosin staining (Figures 5.1A-B). Cells were counted in each imaged section by outlining the cushion boundary (Figure 5.1B, yellow outline). Initially, I counted some sections manually in FIJI (Figure 5.1C) to test the counts from a custom macro to manual counting. The macro deconvoluted the stain with the haematoxylin and eosin setting in “Colour Deconvolution”, thresholded, watershedded and particle counted (macro in Appendix §§8.3.1) (Figures 5.1D-E). The FIJI macro written for the cell counting automation was validated against manual counting, where the average percentage error remained lower than 5% (Figure 5.1F). The embryos were all analysed blind to genotype to avoid any possible biases.

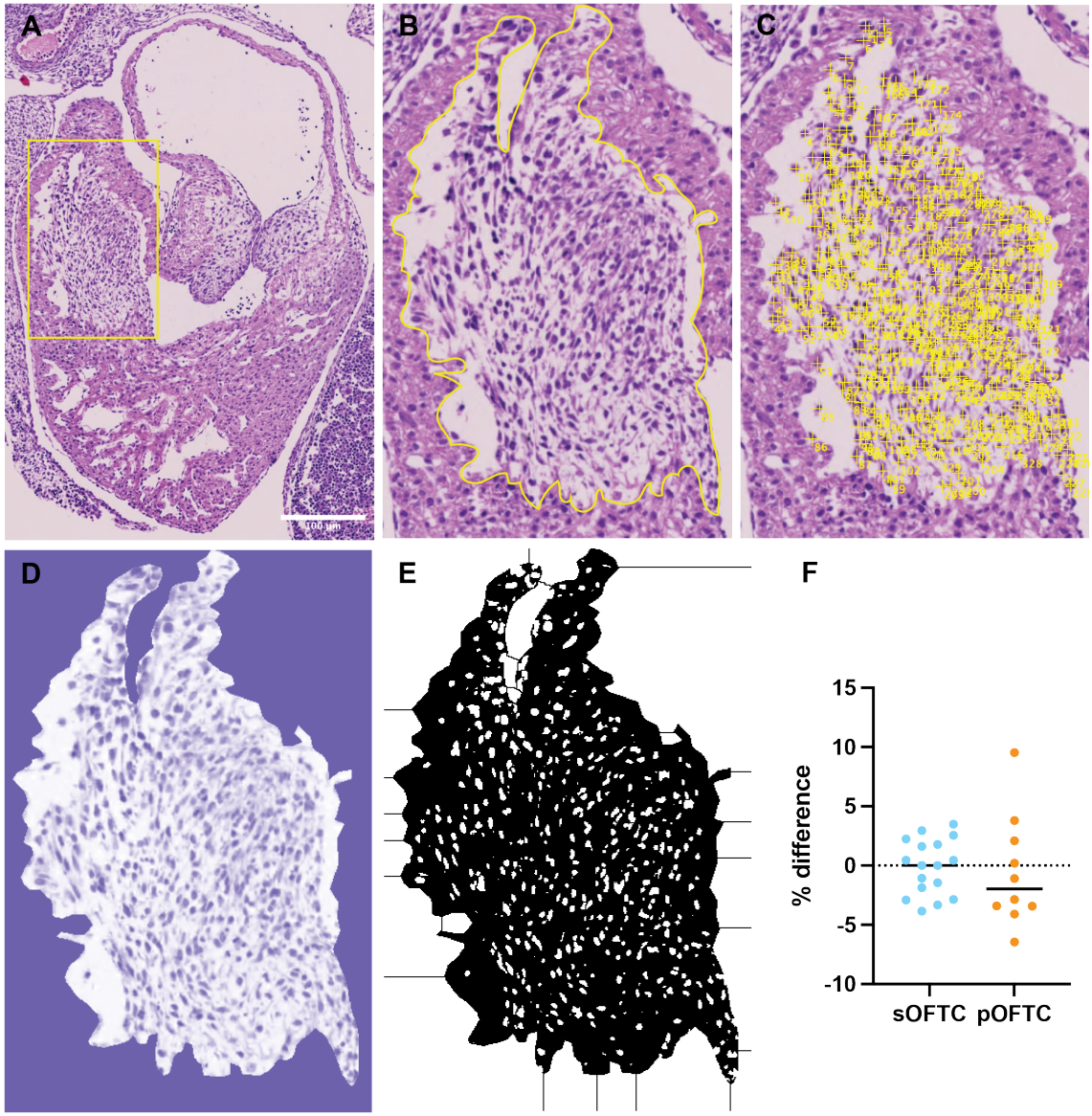

Figure 5.1 Comparison of counting cells manually and a FIJI thresholding macro in E12.5 OFTCs. (A) Haematoxylin and eosin-stained sections from E12.5 embryo containing a septal OFTC, yellow inset box shows location of the OFTC. (B) expanded image of the inset box from (A), here the border of the OFTC is outlined in yellow. (C) Manual counting of every haematoxylin-stained nuclei using the multi-point function in FIJI. (D) Region of interest containing the OFTC colour deconvoluted to show only haematoxylin stain. (E) Thresholded image for particle analysis. (F) Validation of the FIJI macro by plotting the percentage difference between manual counts and the FIJI macro, each point is a different section from either septal or parietal OFTCs. Line shows mean of percentages; septal OFTC n = 17, parietal OFTC n = 10. Scale bar is 100μm.

I observed that an area of condensed mesenchymal tissue was present in the mid-section of each cushion beginning at the distal edges, where cells were more densely packed and the condensed tissue boundaries were almost indistinguishable from the myocardium (Figures 5.2A-B'). This was present in all of the embryos analysed at this stage and likely corresponds to the beginning of the formation of the OFT septum and specification of the aortic and pulmonary valves.

Cells were counted within the drawn boundaries of the septal and parietal OFTCs (Figure 5.3A-C). The number of cells counted was not statistically significantly different between wild-type and Dp1Tyb embryos at this stage in either the septal OFTC (Figure 5.3D) or the parietal OFTC (Figure 5.3E) (p-values > 0.05, Mann-Whitney U-test). This also remains the same when the counts were combined to look at the cushions as a whole (Figure 5.3F). In addition, cell density was taken using the total cell counts divided by the combined area of all sections for the septal, parietal, and combined OFTCs (Figure 3G-I). This analysis also showed no statistical differences in the septal or parietal cushions, nor when the measurements from the two cushions were combined (Figure 5.3G-I).

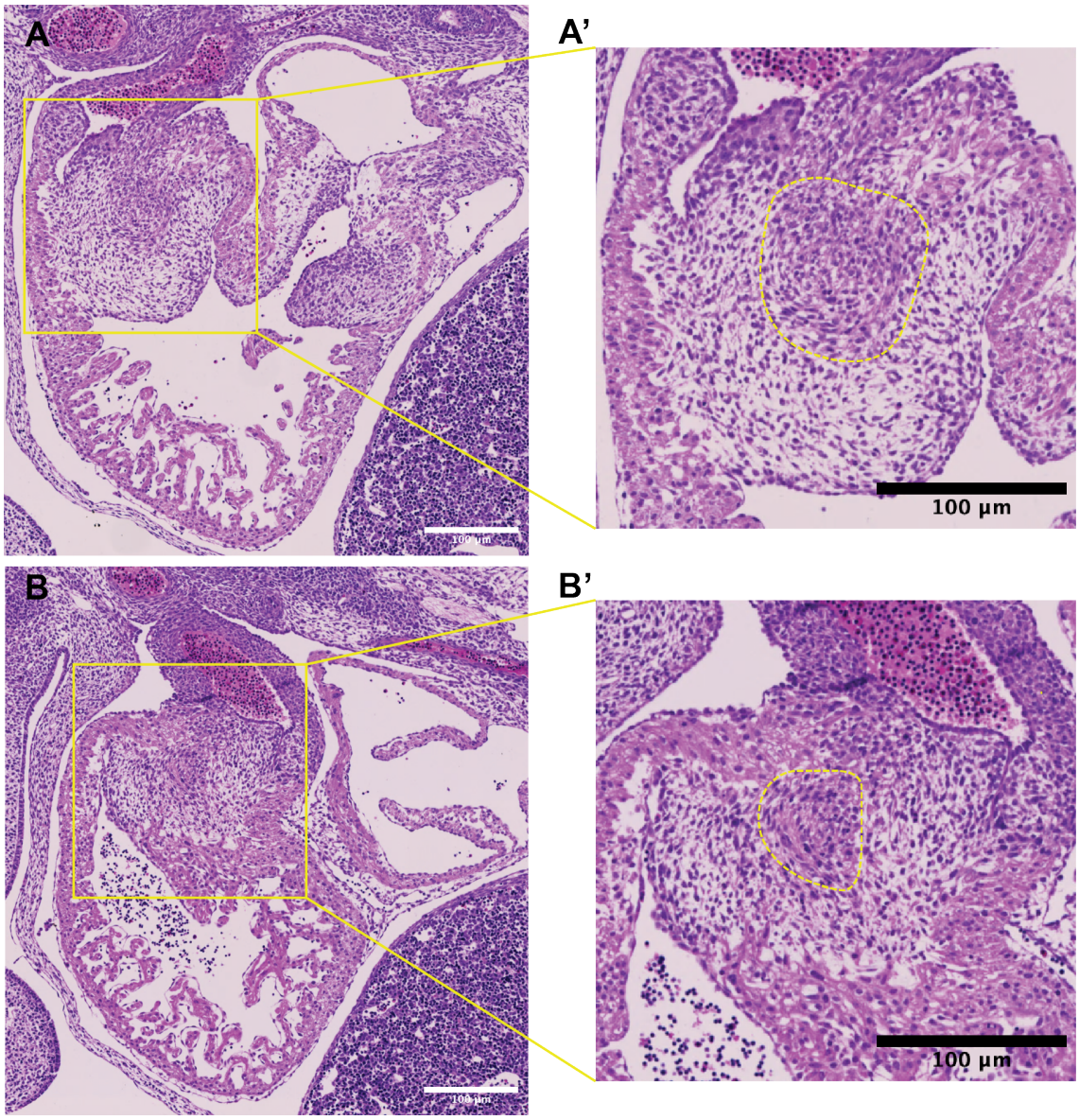

Figure 5.2 Condensed mesenchymal region within both OFTCs at E12.5. (A-A') Sagittal sections of E12.5 embryos where the area of condensed mesenchyme (outlined in dashed yellow line) is present in the septal OFTC. (B-B') Condensed mesenchyme in the parietal OFTC. Scale bars are 100 µm.

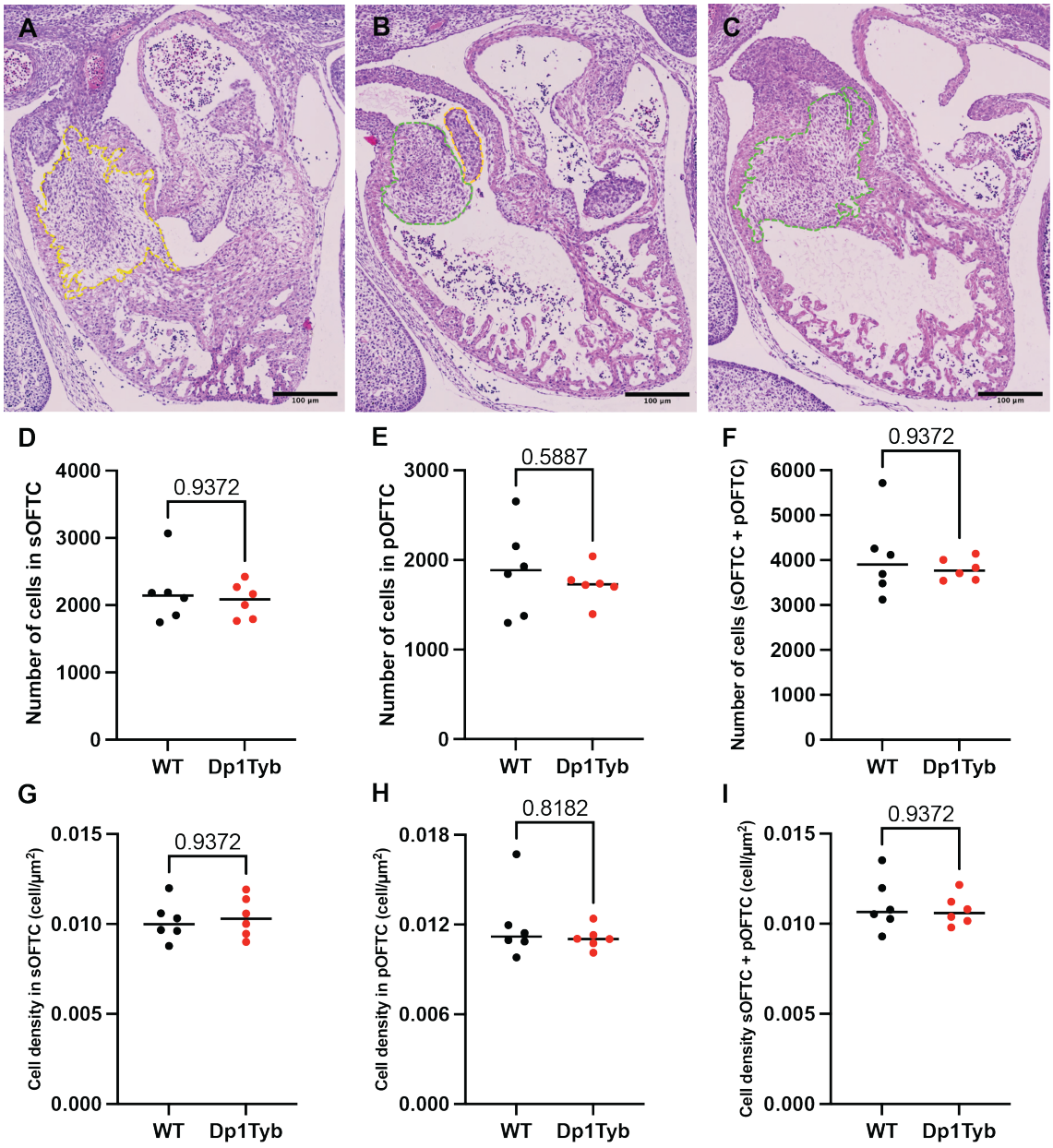

Figure 5.3 Quantification of cell count and cell density within the septal and parietal OFTCs of wild-type and Dp1Tyb embryos at E12.5. Haematoxylin and eosin stains of E12.5 embryo showing the septal OFTC outlined in yellow (A), a section with the end of the septal OFTC and start of the parietal OFTC outlined in green (B), and the parietal OFTC proper (C). Graphs of the total number of cells from all sections of wild type and Dp1Tyb in the septal OFTC (D), parietal OFTC (E), and with the cushions combined (F). Cell density plots of wild-type and Dp1Tyb in septal OFTC (G), parietal OFTC (H) and combined (I). Plots show mean of dataset. Wild type n = 6, Dp1Tyb n = 6; statistical analysis with Mann-Whitney U test.

5.2.2 Observing cellular changes in E13.5 OFTC utilising Alcian Blue staining

Having observed no OFTC cell number differences between Dp1Tyb and wild-type at E12.5, I moved on to the next embryonic day and collected embryos at E13.5. The embryos were dissected and prepared for paraffin embedding as previously described except for changing of the embryo orientation of embedding so that I would get transverse sections. This is due to the cushions becoming fused at E13.5 which meant that an easier orientation to identify the cushions would be transverse. Embryos were similarly sectioned at 4μm thickness with every section kept for staining and every 4th section imaged. However, haematoxylin and eosin staining proved no longer adequate for visually distinguishing cushion tissue from the myocardium, so the histological staining method was switched to Alcian blue counterstained with haematoxylin (Figure 5.4A-C). Alcian blue is a polyvalent basic dye and stains acidic glycosaminoglycans such as hyaluronic acid which is a major component of cardiac jelly and the cushion ECM environment (Tuckett and Morriss-Kay, 1988).

A similar strategy was deployed for cell counting as with E12.5 using an adapted version of the macro (Appendix §§8.3.2), where the “Colour Deconvolution” function was changed to Alcian blue and haematoxylin to match the stains. Figure 5.4D-G shows the same process as in E12.5 from deconvoluting, thresholding and particle counting. Due to the change in orientation, it was possible to track the change in the number of cells and cellular density from distal to proximal OFTC to locate if there were any changes spatially.

No difference was found in the total number of cells in the OFTCs at E13.5 (Figure 5.4H). There was a statistically insignificant trend towards lower cell density throughout the structure as a whole and along most of the distal-proximal axis of the OFT (Figure 5.4H-I). I also noted that the number of cells increased by more than two-fold from the combined counts of E12.5 septal and parietal OFTCs to the counts of the fused septum at E13.5 (Figures 5.3F & 5.4H). As similarly described at E12.5 in §§5.2.1, it was also observed that there was an area of condensed mesenchymal cells within the cushion, but with the addition of fragmented nuclei and cell debris (Figure 5.5A-B). This is consistent with apoptosis occurring within the cushion in preparation for OFT septation (Savolainen *et al.*, 2009). The appearance of cell

debris alongside the doubling of cells in number prompted a deeper investigation into characterising proliferation and apoptotic behaviours in these two stages using immunofluorescence staining.

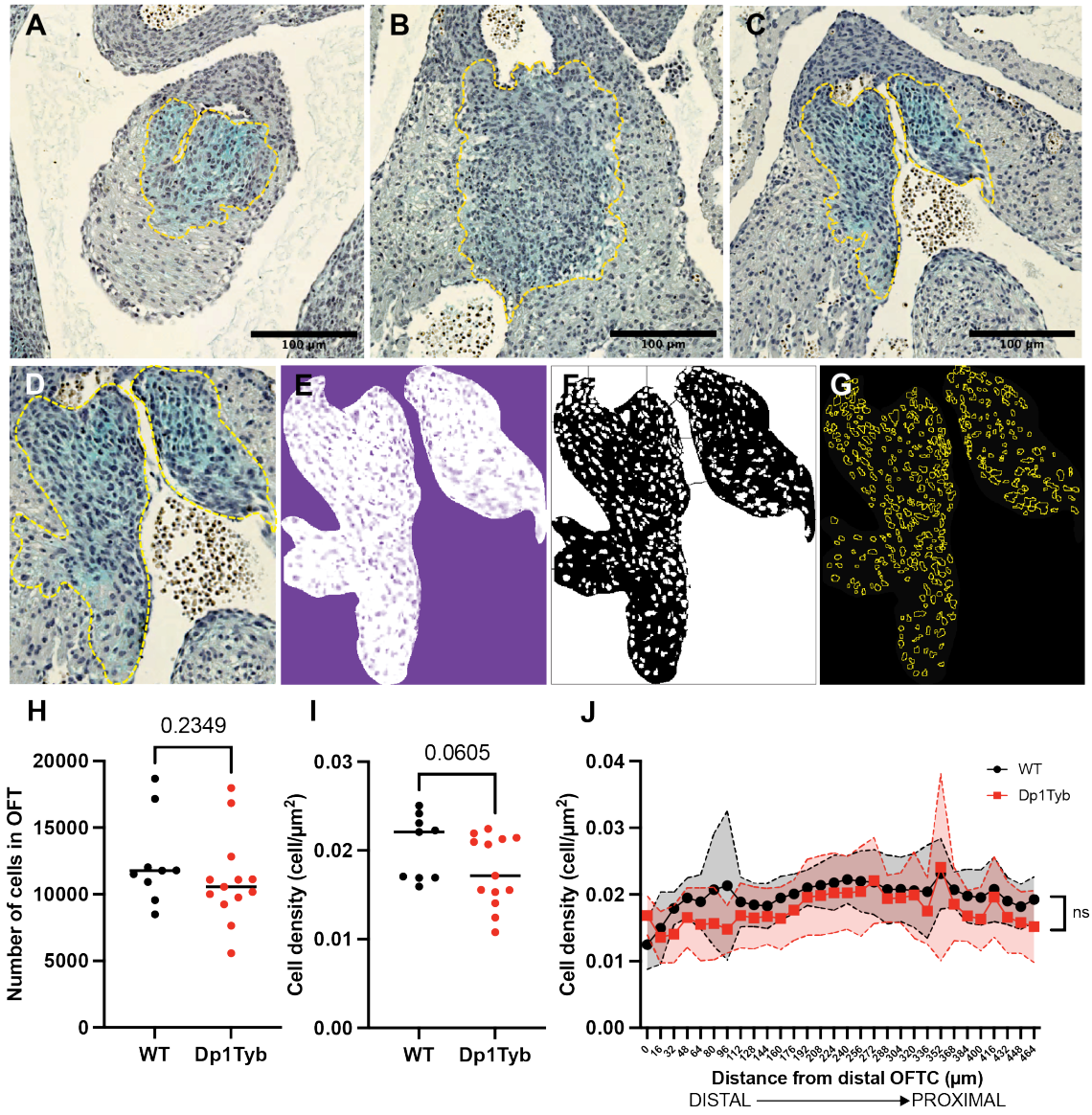

Figure 5.4 Cell counts and cell density in the OFTCs of E13.5 wild-type and Dp1Tyb hearts. (A) Distal, (B) medial, and (C) proximal OFTCs stained with Alcian blue and haematoxylin. Image processing steps within the cell counting FIJI macro: (D) ROI selection, (E) colour deconvolution for haematoxylin stains, (F) thresholding and (G) particle analysis. (H) Quantification of the total number of cells in wild-type and Dp1Tyb OFTCs. (I) Cell density across the entire cushion. (J) Cell density of each section in analysed in the cushion from a distal-proximal axis. Plots show mean and SD. Statistical

analysis with Mann-Whitney U test (H-I), two-way ANOVA (J); wild-type n = 9, Dp1Tyb n = 13. Scale bars are 100 μm.

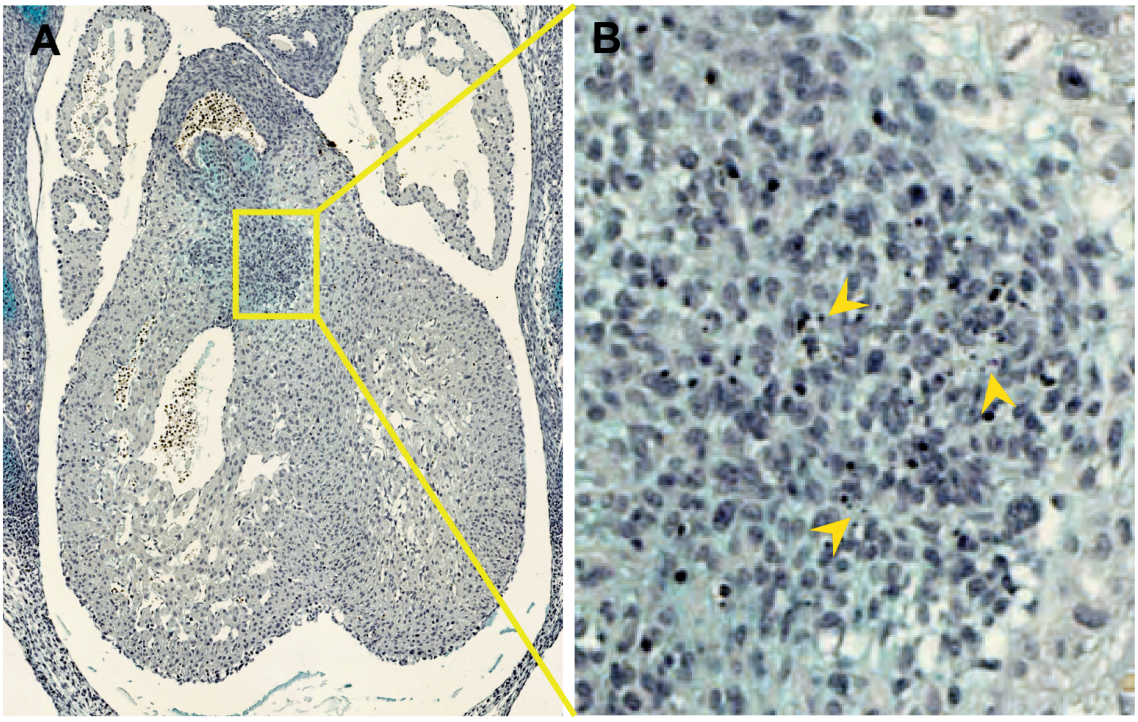

Figure 5.5 Area of condensed mesenchyme within E13.5 OFTC. A medial OFTC section stained with Alcian blue and haematoxylin (A) with yellow arrows indicating cell debris and fragmentation within the condensed mesenchyme (B).

5.2.3 Deploying a deep learning model for automated nuclear segmentation

To further investigate whether the trend of decreased cell density in Dp1Tyb embryos was due to a deficit in proliferation or an increase in apoptosis, I collected embryos at the same two stages (E12.5 and E13.5) for paraffin embedding of both stages in the transversal orientation and microtome sectioned them at 4μm for immunofluorescence staining. I selected to have both in the transverse orientation so the two developmental ages could be compared directly and to allow for spatial quantification. As the immunofluorescence staining was all done manually and individually imaged, rather than the more multiplexed method adopted for previous immunohistochemistry stains, I stained and imaged every 8th section leaving a 32μm gap between adjacent sections. Each section was stained for TUNEL to evaluate levels of apoptosis, Phosphohistone-3 (PHH3) (Dessauvagie *et al.*, 2015) to identify mitotic cells, and Sox9 to locate the mesenchymal cells (Akiyama *et al.*, 2004) and

therefore the location of the OFTCs before counterstaining with DAPI. Figures 5.6A-L and 5.7A-L are representative of the immunostaining in E12.5 and E13.5 respectively, where images were taken from the distal, medial and proximal cushions to demonstrate the changing cushion anatomy through the rostral-caudal axis. This orientation also meant that I would be able to track changes in apoptosis, proliferation, and cellular density at even intervals through the cushion, similar to Figure 5.4J.

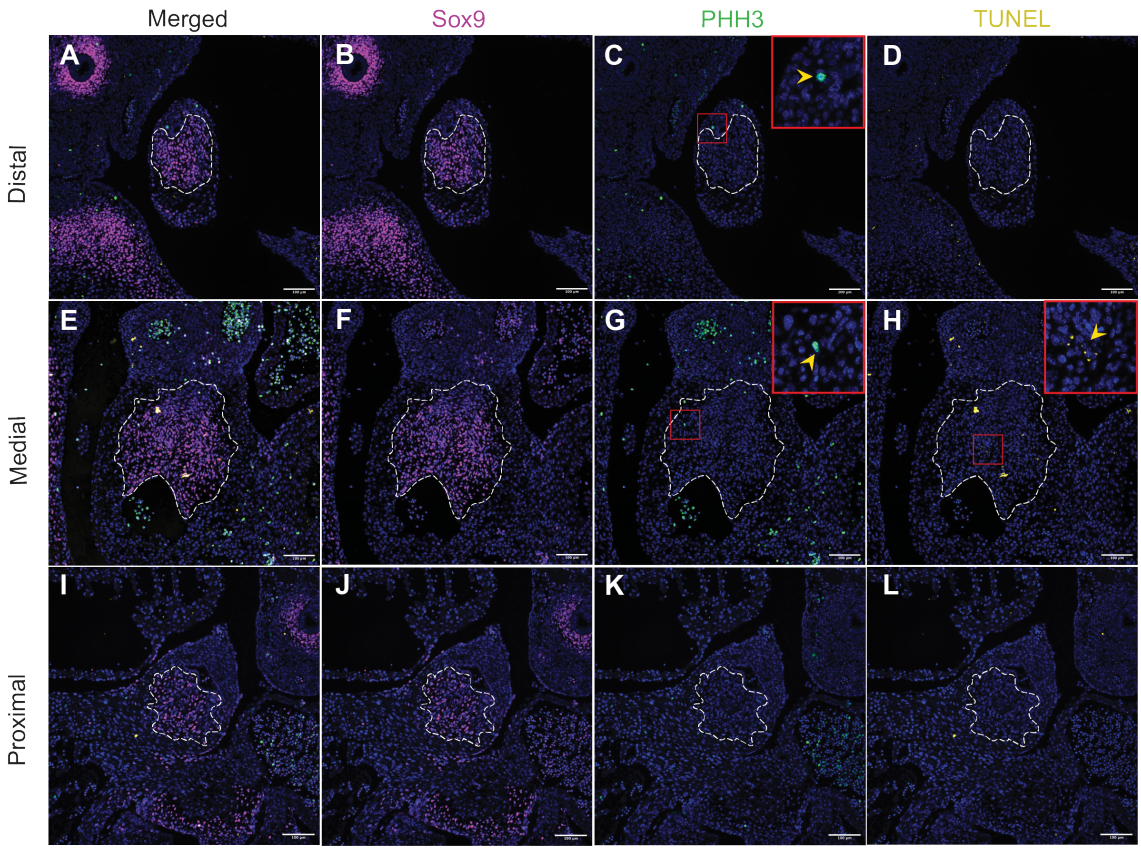

Figure 5.6 Transverse sections of E12.5 outflow tract cushion stained for a mesenchymal cell marker, proliferating cells and apoptosis. Sections were stained with Sox9 for mesenchymal cells, PHH3 for mitotic cells and TUNEL for cell death. The images selected show representative sections of the distal (A-D), medial (E-H) and proximal (I-L) cushions from a wild-type sample. The cushion area is outlined in the dashed white line. Cells undergoing mitosis and areas with apoptosis are indicated within the areas outlined in red box, which are enlarged in the inset with yellow arrowheads to indicate mitosis and apoptosis. Scale bars are 100μm.

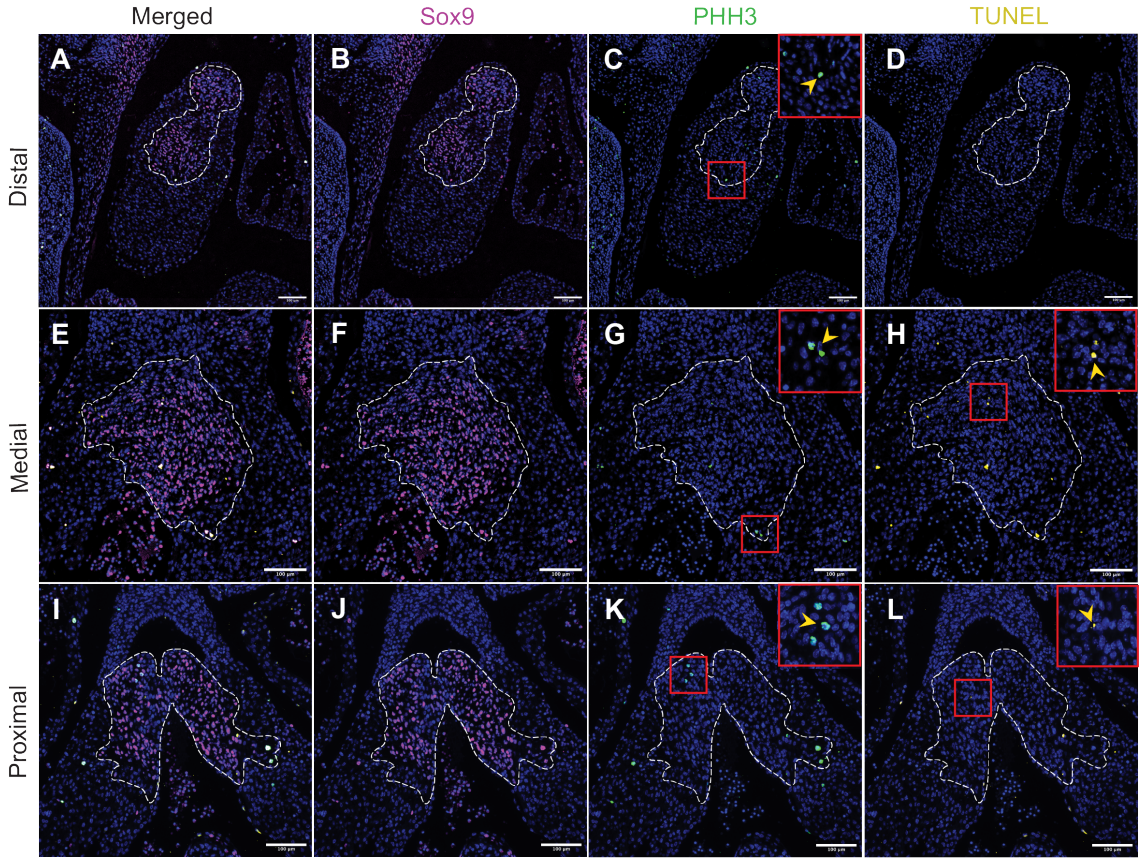

Figure 5.7 Transverse sections of E13.5 outflow tract cushion stained for a mesenchymal cell marker, proliferating cells and apoptosis. Sections were stained with Sox9 for mesenchymal cells, PHH3 for mitotic cells and TUNEL for cell death. The images selected show representative sections of the distal (A-D), medial (E-H) and proximal (I-L) cushions from a wild-type sample. The cushion area is outlined in the dashed white line. Cells undergoing mitosis and areas with apoptosis are indicated within the areas outlined in red box, which are enlarged in the inset with yellow arrowheads to indicate mitosis and apoptosis. Scale bars are 100μm.

Using DAPI as a nuclear counterstain allowed for clearer image segmentation of individual cells due to higher contrast in the DAPI channel (emission in the blue range at 461nm (Adler and Parmryd, 2013)) than between nuclear and non-nuclear colour in H&E staining. With sometimes thousands of nuclei per image, it was not feasible to manually count nor outline every nucleus within the Sox9 positive ROI of each serial section through all the embryos. Therefore, I chose to train a deep-learning nuclear detection network on my images using StarDist.

StarDist was built to segment nuclei through the recognition of non-convex objects in the training images (also known as star-convex shapes) (Schmidt *et al.*,

2018; Weigert *et al.*, 2020). Using its Python implementation through a Google Colaboratory notebook, I input sample training images selected from different areas of the DAPI channel and their corresponding manually annotated images (i.e. images with manually outlined nuclei) (Figure 5.8A-B) to train a personal model for the project. The annotated images were generated using the LabKit plug-in (Arzt *et al.*, 2022) in FIJI as recommended by the developers of StarDist. Each image contained 150-250 nuclei that were individually labelled with a paintbrush tool, a very time-consuming exercise as each nucleus needed to be as pixel-perfect as possible as well as accurate in its boundaries. As the samples were taken from different regions in the heart, the nuclei were quite densely packed and occasionally intersecting which meant there was a level of subjectivity to the boundaries of overlapping nuclei, but also judgement based on knowledge of what shapes nuclei tend to take.

The model was trained on 15 sample images, with 1 of the 15 reserved for validation of the model. The training set was then run through 400 epochs (cycles in which the entire training dataset is passed through the neural network), which was the recommended maximum for a full training. Data augmentation, which consists of random rotations, flips and changes in intensity of the training images, was also added to challenge the network and to thereby improve the training process, which is beneficial with smaller training sets of the kind I used.

I assessed the performance of the training by looking at training loss (blue line in Figure 5.8C-D) and validation loss (orange line in Figure 5.8C-D), where training loss assigns an error value after each epoch based on how much error there is of the model fitting the training data, and validation loss describes how much error there is when the model fits the validation dataset after each epoch. Continually decreasing training and validation losses are indicative of further training needed by increasing the number of epochs, however as seen in Figures 5.8C and D my loss curves quickly reach an asymptote which affirms that the model does not need further training. The model is also not overfitting the data as the curves remain levelled off, where a sudden increase of validation loss and simultaneous plummeting of training loss to zero would demonstrate this. Following the success of training a model on my images, I deployed the network through the StarDist plug-in in FIJI on unseen images and visually inspected the performance of the model (Figure 5.8E-G). I was satisfied with how well the nuclei in the unseen images were

segmented and went on to deploy the network on the larger ROIs that would encompass the OFTCs.

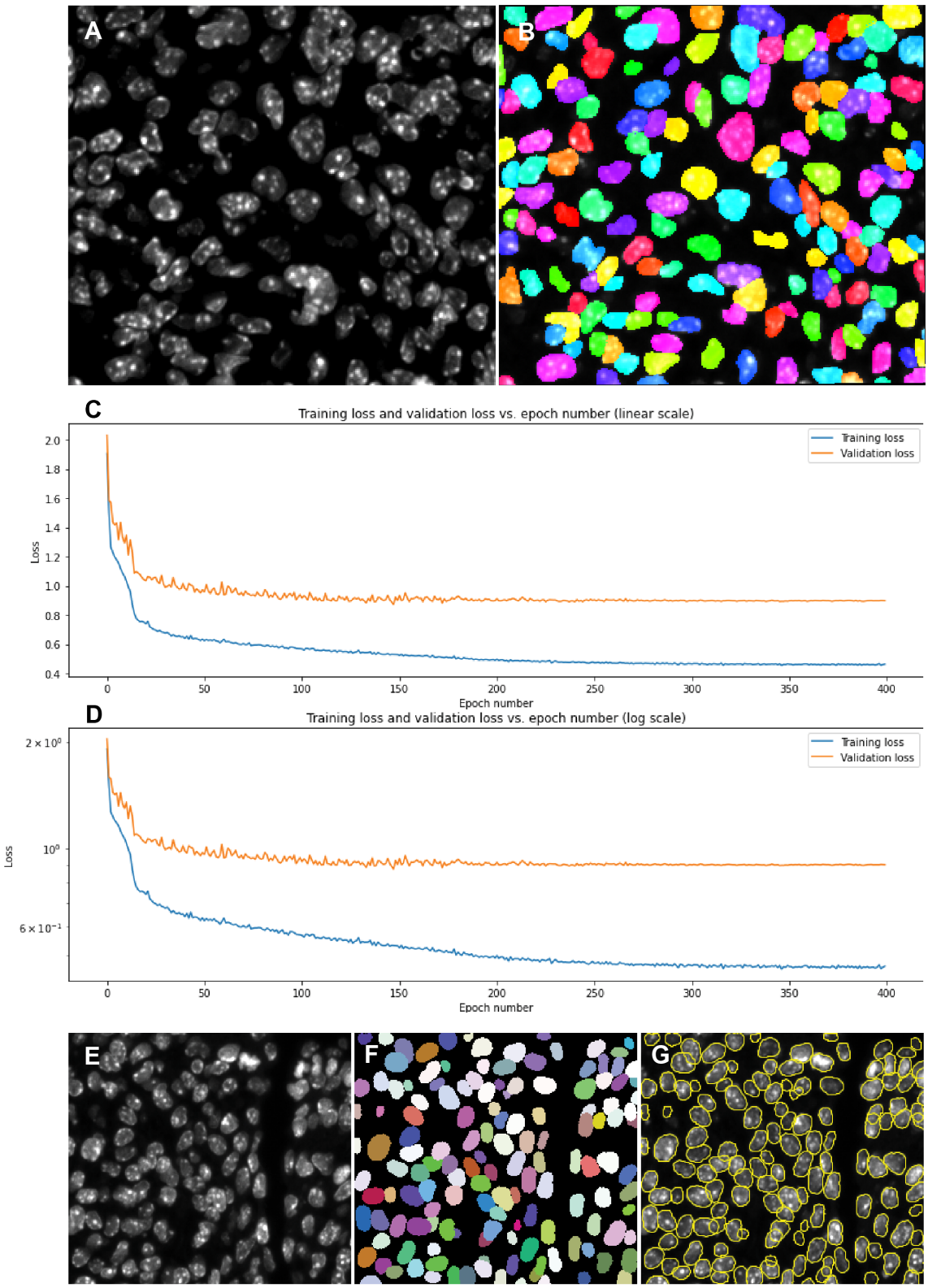

Figure 5.8 Training and validation of a StarDist nuclear segmentation deep-learning network. (A) A training image containing DAPI-stained cells. (B)

Corresponding manually painted nuclear mask. (C) Training loss plotted against the number of epochs (D) Validation loss plotted against the number of epochs (E) Unseen image. (F) Nuclear segmentation from the model. (G) Nuclear segmentation as ROIs overlayed on (E).

5.2.4 Cell density and packing are reduced in Dp1Tyb OFTCs

With my personally trained nuclear segmentation model, I could then accurately account for the number of cells within a given ROI and utilise the masks generated to catalogue the centroid coordinates of all the labelled cells. This method was deployed for better accuracy of cell number and to obtain nuclear masks for further analyses, which would be less accurate if using standard thresholding and particle analysis as conducted with earlier histological sections (§§5.2.1, §§5.2.2).

I identified the region containing OFTC by using Sox9 expression as a guide – I drew a border around the outermost Sox9 positive cells and defined this as the cushion ROI. While this is accurate from a cellular perspective, I felt that this was not entirely reflective of the true cushion region given that in Figure 5.1B it is clear that there is a region filled with ECM and no cells on the border of the cushions in many sections. This meant measuring cell density as a function of ROI area divided by the number of cells might not be as accurate as it could be. Therefore, to confirm any findings in cellular density more objectively, I deployed a spatial mapping script in R that was developed and written in the Green lab that generates internuclear spacing heatmaps using cell centroid coordinates to describe cell packing (Economou *et al.,* 2013; Brock *et al.,* 2016). By splitting the functions of the script, I extracted the value for the average distance from the centroid of a nucleus to its closest neighbours' centroids (obtained from StarDist) for every nucleus segmented out (Figure 5.9), this meant that I was able to get numerical values for packing to perform statistical analyses as well as follow through with the remainder of the script to generate heatmaps (Appendix §§8.4). The neighbours were identified using a function that incorporates Delaunay triangulation and the value of the average distance assigned a colour value on a user-defined scale. A further function uses Voronoi tessellation to create a tiled image with polygons assigned with the average of previous colour values for the area encompassed by the polygon.

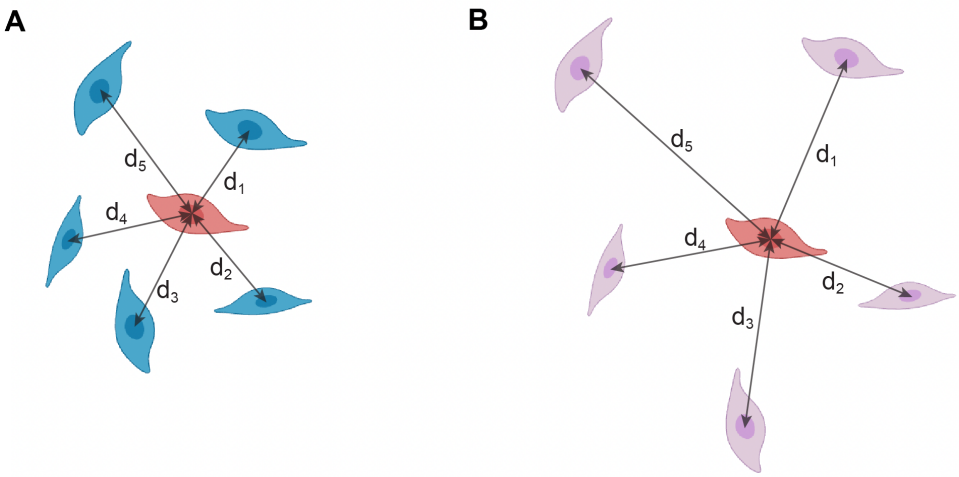

Figure 5.9 Internuclear spacing. A schematic of how internuclear spacing is calculated from the centroid of each nucleus to the centroids of its neighbours with the individual internuclear spaces labelled $d_{1\text{-}5}$ (A), a less densely packed region is also exhibited with larger internuclear distances (B).

At E12.5, the data showed that the total number of cells within the OFTC area of Dp1Tyb embryos was significantly decreased in the cushions as a whole and to the proximal end of the cushion (Figures 5.10A-B). Increased internuclear spacing would indicate that there was reduced cell packing, however, at this stage, there did not appear to be a statistically significant difference for the whole cushion (Figure 5.10C) or when analysing from a distal-proximal axis (Figure 5.10D). This was surprising as the trend in Figure 5.10D suggested increased spacing in the Dp1Tyb embryos in the proximal half of the cushion. However, with cell density measures, Dp1Tyb embryos have significantly reduced cell density when comparing the averages of the entire cushion (Figure 5.10E) as well as having consistently lower cell density in every section against the wild-type (Figures 5.10F). The discrepancy between internuclear spacing and the cell density at this stage could be from the cell-free edges of the cushion as evidenced in Figure 5.1B. Furthermore, these results are different from the findings in Figure 5.3, this is perhaps due to the increased accuracy of using a nuclear segmentation model like StarDist in combination with using a different boundary to mark where the cushion mesenchyme is. The ROI drawn for the H&E stains used the eosin-negative boundary to the myocardium, whereas the immunofluorescence stains use a cellular boundary with Sox9-positive cells.

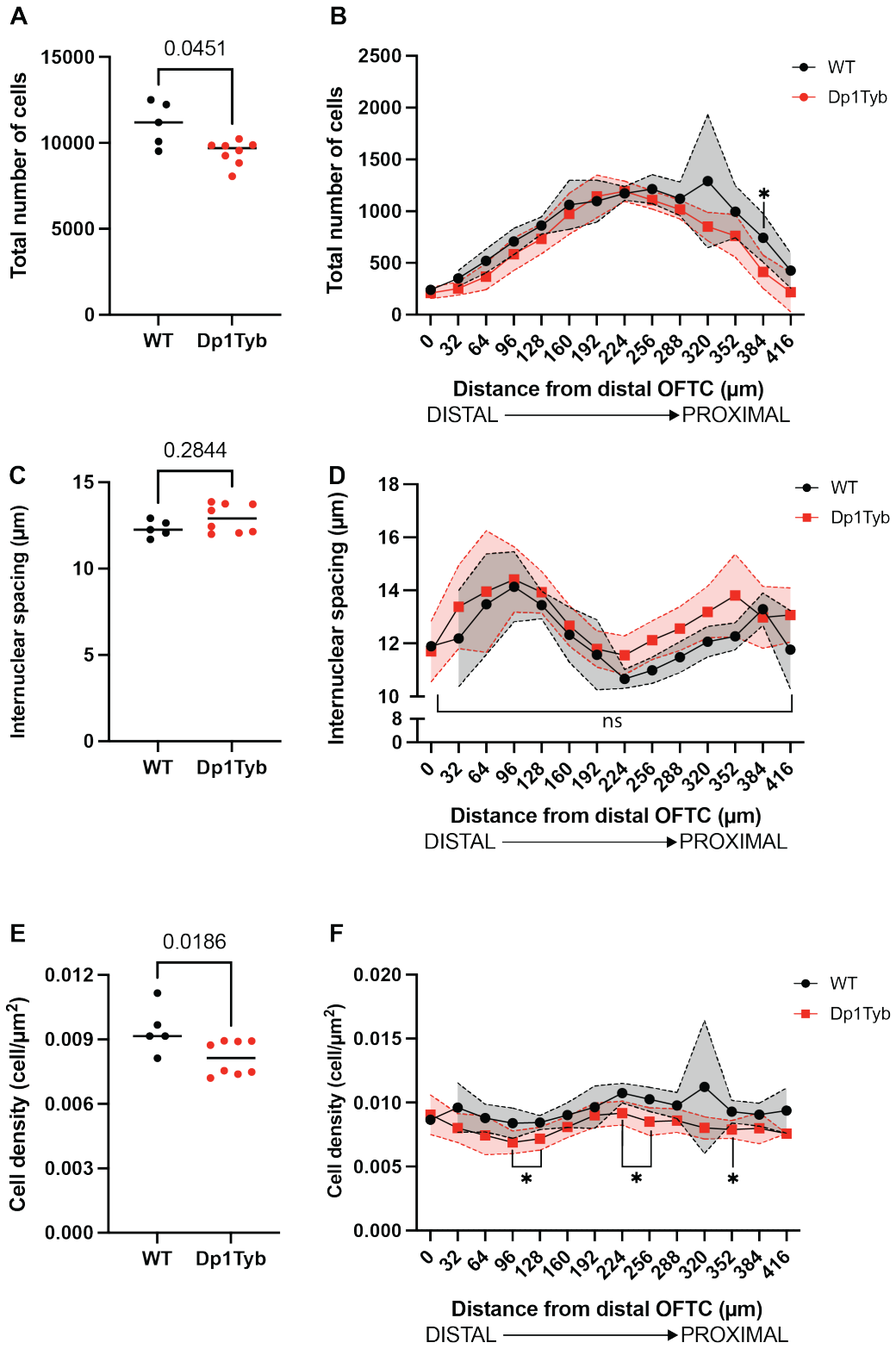

Figure 5.10 Total cell count, internuclear spacing and cell density at E12.5 for wild-type and Dp1Tyb OFTCs. (A) Total cell count of the entire cushion per embryo. (B) Cell count as a distal-proximal axis in each section. (C) Average internuclear spacing. (D) Internuclear spacing as a distal-proximal axis in each section. (E) Average cell density.

(F) Cell density as a distal-proximal axis in each section. Plots show mean (and SD for spatial plots). Statistical analysis for overall plots was Mann-Whitney U and for spatial plots a two-way ANOVA with multiple comparisons was used. Wild-type n = 5, Dp1Tyb n = 8. Where p-value is specified by asterisks: *p<0.05. Data without significance are noted by “ns”.

One embryonic day later at E13.5, the differences between wild-type and Dp1Tyb OFTCs shown in the E12.5 data became more pronounced. The overall cell count was not different between the two genotypes (Figure 5.11A) but the distribution of cells in Dp1Tyb was now more skewed to the proximal region of the cushion, with significantly more cells residing there (Figure 5.11B). I also noted that the number of cells counted in the cushion did not increase two-fold the same way that the haematoxylin & eosin stains at E12.5 and Alcian blue stains at E13.5 suggest. This perhaps suggests the underestimation of the cell population when using the macro to automate cell counting in the histology stainings, possibly due to overlapping or closely packed nuclei being counted as one. Internuclear spacing was increased throughout the Dp1Tyb cushions though not at every section (Figures 5.11C-D), this was reflected in the significantly decreased cell density measure in Dp1Tyb cushions (Figures 5.11E-F). This indicates that while there is a larger number of cells in the proximal cushion of the Dp1Tyb hearts, the area occupied by proximal cushion mesenchyme as marked by Sox9-positive cells has to be larger than that of the wild-type to result in both statistically significant increased nuclear spacing and reduced cell density values.

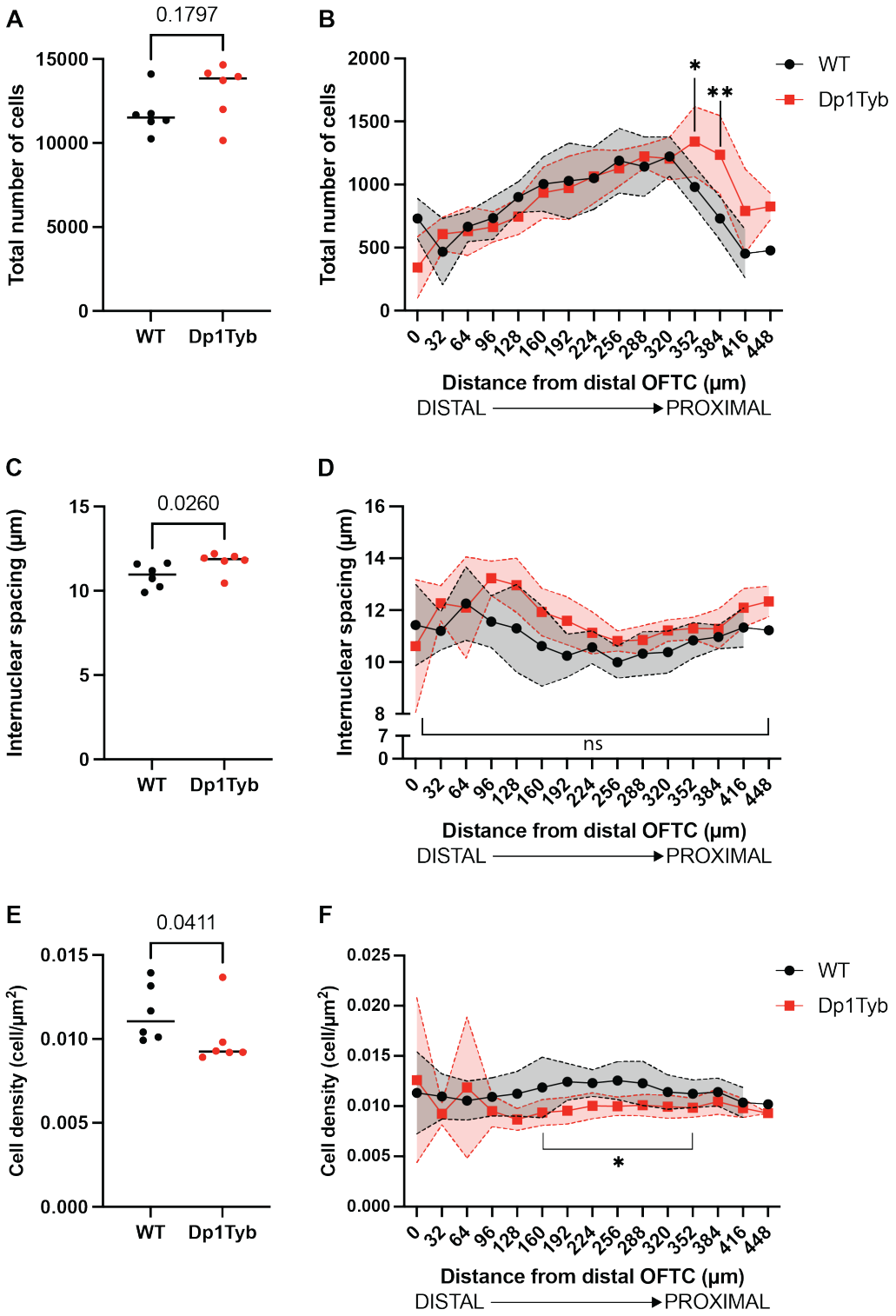

5.11 Total cell count, internuclear spacing and cell density at E13.5 for wild-type and Dp1Tyb OFTCs. (A) Total cell count of the entire cushion per embryo. (B) Cell count as a distal-proximal axis in each section. (C) Average internuclear spacing. (D) Internuclear spacing as a distal-proximal axis in each section. (E) Average cell density.

(F) Cell density as a distal-proximal axis in each section. Plots show mean (and SD for spatial plots). Statistical analysis for overall plots was Mann-Whitney U and for spatial plots a two-way ANOVA with multiple comparisons was used. Where p-value is specified by asterisks: *p<0.05, **p<0.01. Wild-type n = 6, Dp1Tyb n = 6.

Plotting the internuclear distances as heat maps for E12.5 and E13.5 showed the distribution of cell packing through the tissue for the sections and the morphology of each section that the data was extracted from. The heat maps show representative sections of wild-type and Dp1Tyb embryos at the distal, medial and proximal positions for E12.5 (Figures 5.12A-F) and E13.5 (Figure 5.13A-F). The darkest colours are indicative of smaller internuclear spacing (increased cell packing) in the region with a minimum value of 3 microns while lighter areas represent areas of higher nuclear spacing (reduced cell packing) with a maximum value of 18 microns. At E12.5 it visually appears as if the internuclear spacing was fairly uniform throughout the section, with perhaps a slightly darker area in the middle of the medial section compared to its periphery in the wild-type (Figure 5.12B). Overall, these plots show that internuclear spacing is very variable throughout different sections.

As could be inferred from the plots in Figures 5.10 and 5.11 and directly seen in Figure 5.12F compared to Figure 5.12C taken from a similar proximodistal level, the Dp1Tyb cushions were simply larger proximally in section than those in wild-type, which accounted for how cell density and packing were reduced while cell number was higher. A simply larger cushion was not an intuitive prelude to an ultimate septal deficit, suggesting that the Dp1Tyb phenotype might include a more complex cushion dysmorphology. This is further explored and quantified in the next section.

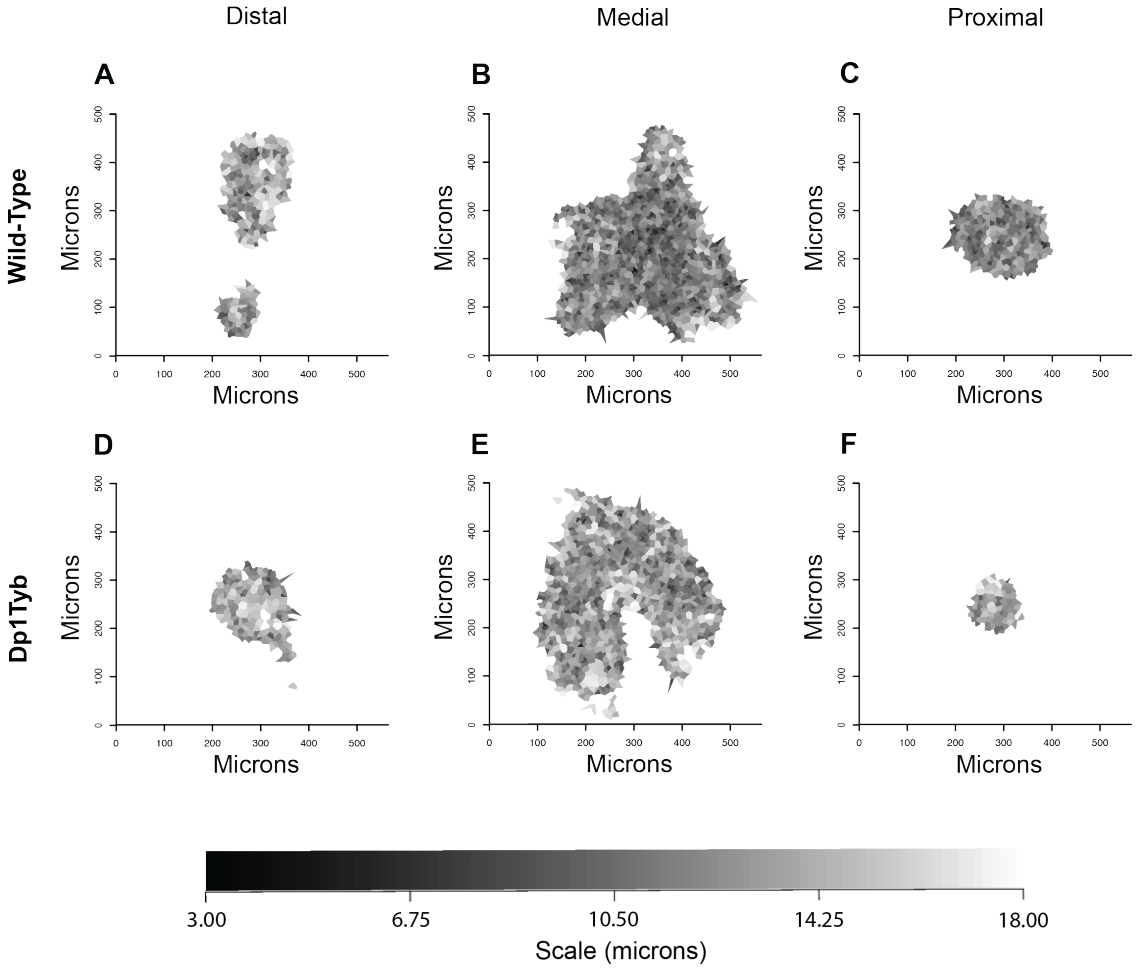

Figure 5.12 Heatmaps showing internuclear spacing throughout the OFTC of wild-type and Dp1Tyb hearts at E12.5. Representative heat maps of localised internuclear spacing in the distal (A, D), medial (B, E) and proximal (C, F) cushions of wild-type and Dp1Tyb embryos at E12.5 in transverse sections. The values of internuclear spacing are colour-coded in grayscale as per the scale bar, ranging between 3 and 18μm.

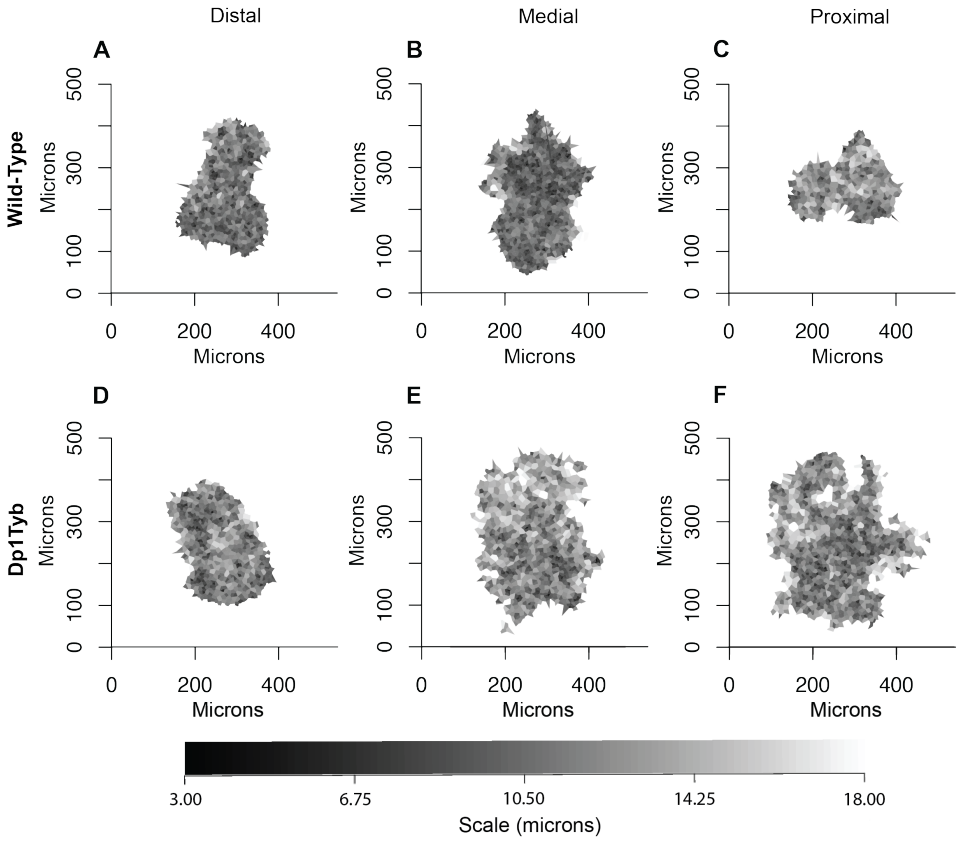

Figure 5.13 Heatmaps showing internuclear spacing throughout the OFTC of wild-type and Dp1Tyb hearts at E13.5. Representative heat maps of localised internuclear spacing in the distal (A, D), medial (B, E) and proximal (C, F) cushions of wild-type and Dp1Tyb embryos at E13.5 in transverse sections. The values of internuclear spacing are colour-coded in grayscale as per the scale bar, ranging between 3 and 18μm.

5.2.5 Dp1Tyb embryos have dysmorphic proximal cushions

To confirm that Dp1Tyb mice have dysmorphic proximal regions of the OFTCs due to the cell density decreasing but higher cell counts in the same sections, I used the metrics collected throughout the analysis for both stages to quantify the volume, length and section area in each genotype. The volume was approximated by multiplying the area of the section by the distance between measured sections (i.e., 32μm). This was an estimate of the actual cushion volume given that the z-step was coarse and the ROI was drawn around the boundaries of Sox9 positive cell areas which, as discussed above was not inclusive of any pockets of ECM surrounding the cushions that did not contain any cells. The lengths (heights) of the cushions were

taken as the number of sections that were imaged multiplied by 32μm, as the first section was the first containing the cushion mesenchyme the last was the final one showing cushion anatomy. For a more morphology-descriptive quantification, I plotted the area of each section ROI from the distal to proximal ends.

OFTCs of wild-type and Dp1Tyb cushions at E12.5 are not morphologically different when quantified with these metrics. Neither the volume (Figure 5.14A) nor the length (Figure 5.14B) had significant differences between genotypes and anatomically there was no difference in the ROI area of each section (Figure 5.14C). The plot of section areas of wild-type and Dp1Tyb formed an arc (Figure 5.14C) that was suggestive of an ellipsoidal domain of Sox9-positive mesenchymal cells are located. This would be a different anatomy from the 3D OFTC meshes constructed at this stage from HREM, although those were constructed from anatomical landmarks as opposed to cellular boundaries as it is here. The section areas in Dp1Tyb embryonic hearts remaining similar to wild-type hearts was consistent with the decrease in cell number in Figures 5.10A and B giving a reduced cell density (Figure 5.10E and F).

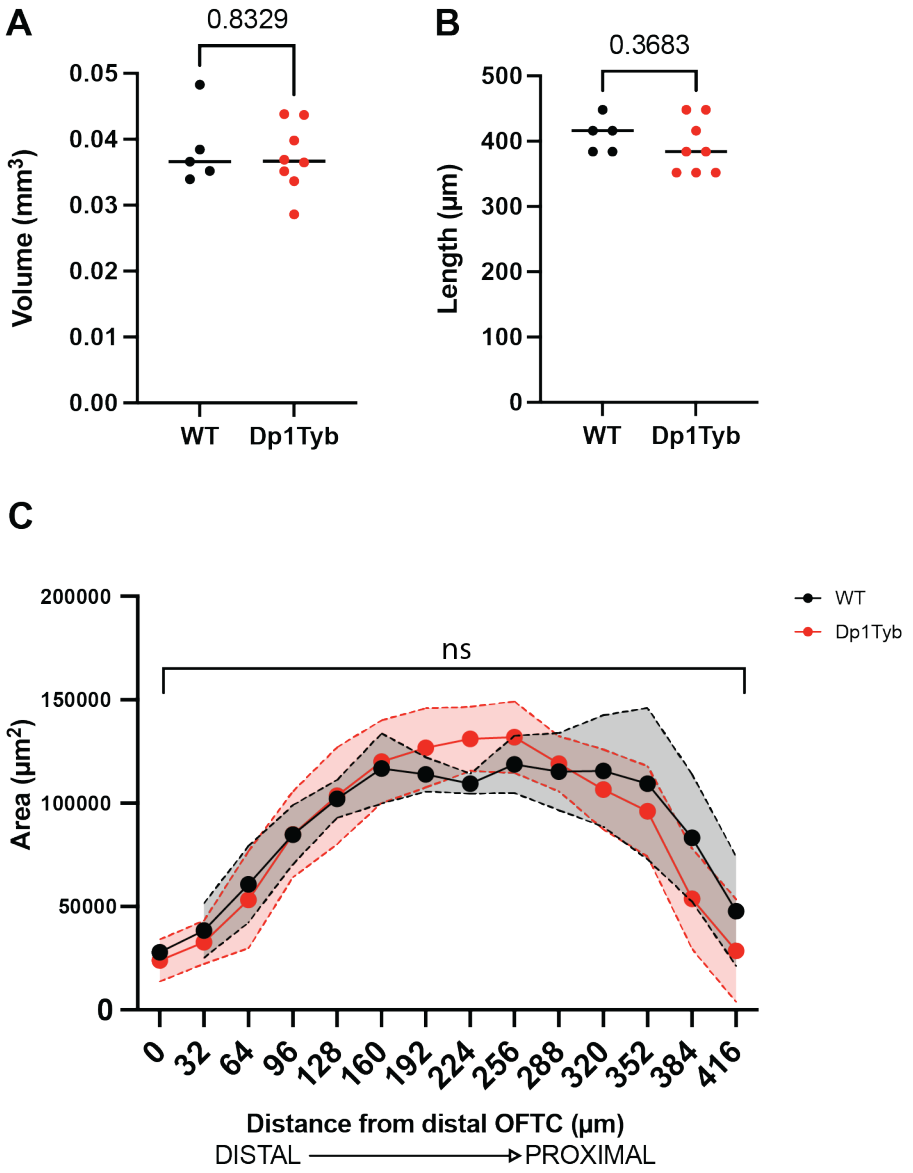

Figure 5.14 Morphological quantifications from serial sections of wild-type and Dp1Tyb OFTCs at E12.5. (A) Projected volume of the OFTCs from the cushion area. (B) Cushion length based on how many sections the OFTC spanned for each embryo. (C) The area of each section plotted against the distance from the distal/first section. Plots show mean (and SD for spatial plots). Statistical analysis was Mann-Whitney U (A-B) and two-way ANOVA (C). Wild-type n = 5, Dp1Tyb n = 8.

There was no statistically significant overall change in the volume or length of the cushion between genotypes, although there was perhaps a trend of larger cushion volume and longer cushion length in the Dp1Tyb embryos (Figure 5.15A-B). However, the section areas were significantly enlarged in the proximal region at E13.5 in the Dp1Tyb mice (Figure 5.15C). The plot showed that the areas were

similar between the wild-type and Dp1Tyb distal cushions, but begin to diverge from ~160μm below the distal end. I was surprised to find there was almost a doubling of ROI area in the last (i.e., most proximal) ~130μm of the cushion. This suggested that Dp1Tyb embryos have dysmorphic cushions specifically proximally, which is the area of the cushion that abuts and fuses to the mVS. I will further consider what this could mean in the context of the extracellular makeup of the dysmorphic cushions, its impact on ventricular septation and CHD in the chapter discussion below.

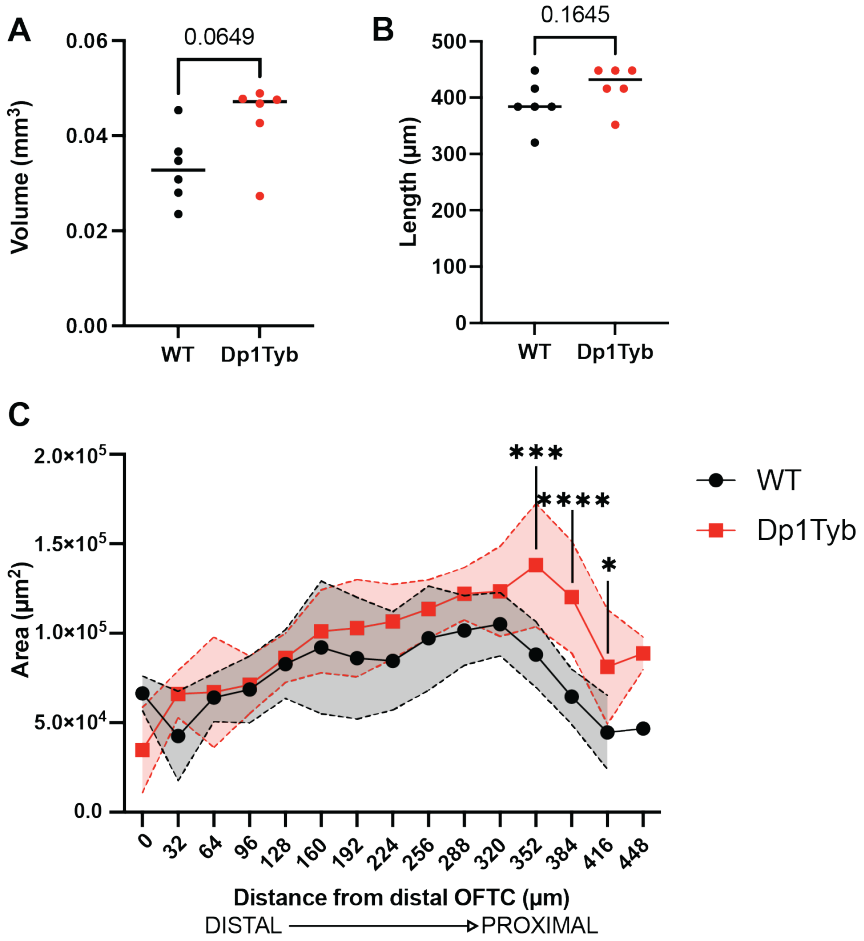

Figure 5.15 Morphological quantifications from serial sections of wild-type and Dp1Tyb OFTCs at E13.5. (A) Projected volume of the OFTCs from the cushion area. (B) Cushion length based on how many sections the OFTC spanned for each embryo. (C) The area of each section plotted against the distance from the distal/first section. Statistical analysis was Mann-Whitney U (A-B) and two-way ANOVA (C). Plots show mean (and SD for spatial plots). Statistical analyses were Mann-Whitney U (A-B) and two-way ANOVA (C). Where p-value is specified by asterisks: *p<0.05, **p<0.01, ***p<0.001, ****p<0.0001. Wild-type n = 5, Dp1Tyb n = 8.

5.2.6 Proportion of undifferentiated mesenchymal cells is unaffected

Though Sox9 was included as a marker to locate the OFTC boundaries, I observed that some of the cells that were detected by the StarDist nuclear segmentation were not Sox9 positive even though they were within the cushion boundaries. Sox9 is essential in the formation of the cardiac valves and septa, it is switched on when EndoMT occurs and cells migrate in the ECM (Akiyama *et al.*, 2004). Expression of Sox9 is maintained postnatally in mice, though the percentage of Sox9 cells in the endocardial cushions begins to decrease after E14.5 (Gallina and Lincoln, 2019). Tracking the expression of Sox9 at these two stages in the OFTC could indicate the proportion of cells in Dp1Tyb and wild-type hearts that are losing their mesenchymal identity in preparation for muscularisation to build part of the ventricular septum.

I took the nuclear mask generated for all cells in the DAPI channel and applied it to the cells in the Sox9 channel to query what percentage of the total cells were expressing Sox9 (defined as cells brighter than the average fluorescence intensity in Sox9-negative nuclear masks) and what the internuclear spacing and cell density of these cells were. It was also noticed that some Sox9 cells had a higher fluorescence intensity than others, so I quantified a “high expression” and “low expression” population based on their relative mean fluorescence intensity.

The Sox9 population in E12.5 embryos followed trends that were similar to those of the total cushion cell population with no differences between wild-type and Dp1Tyb embryos in cell density or internuclear spacing (Figures 5.16A-H) and there was no difference between the genotypes in the ratio of high and low expression Sox9 cells (Figures 5.16I-J). At E13.5, the quantifications of internuclear spacing, cell density and high-to-low expression ratios did not show any differences between wild-type and Dp1Tyb embryos (Figure 5.17A-H). The numbers of Sox9-positive cells (Figures 5.17A-B) mirrored that of the total cell number in Figure 5.11B for both genotypes where there were significantly more cells in the proximal cushion of Dp1Tyb embryos (Figure 5.17B). Overall, there was no trend in the proportion of cells that were Sox9-positive or their expression levels at either stage for wild-type and Dp1Tyb embryos. The same is said for the internuclear spacing and cell density.

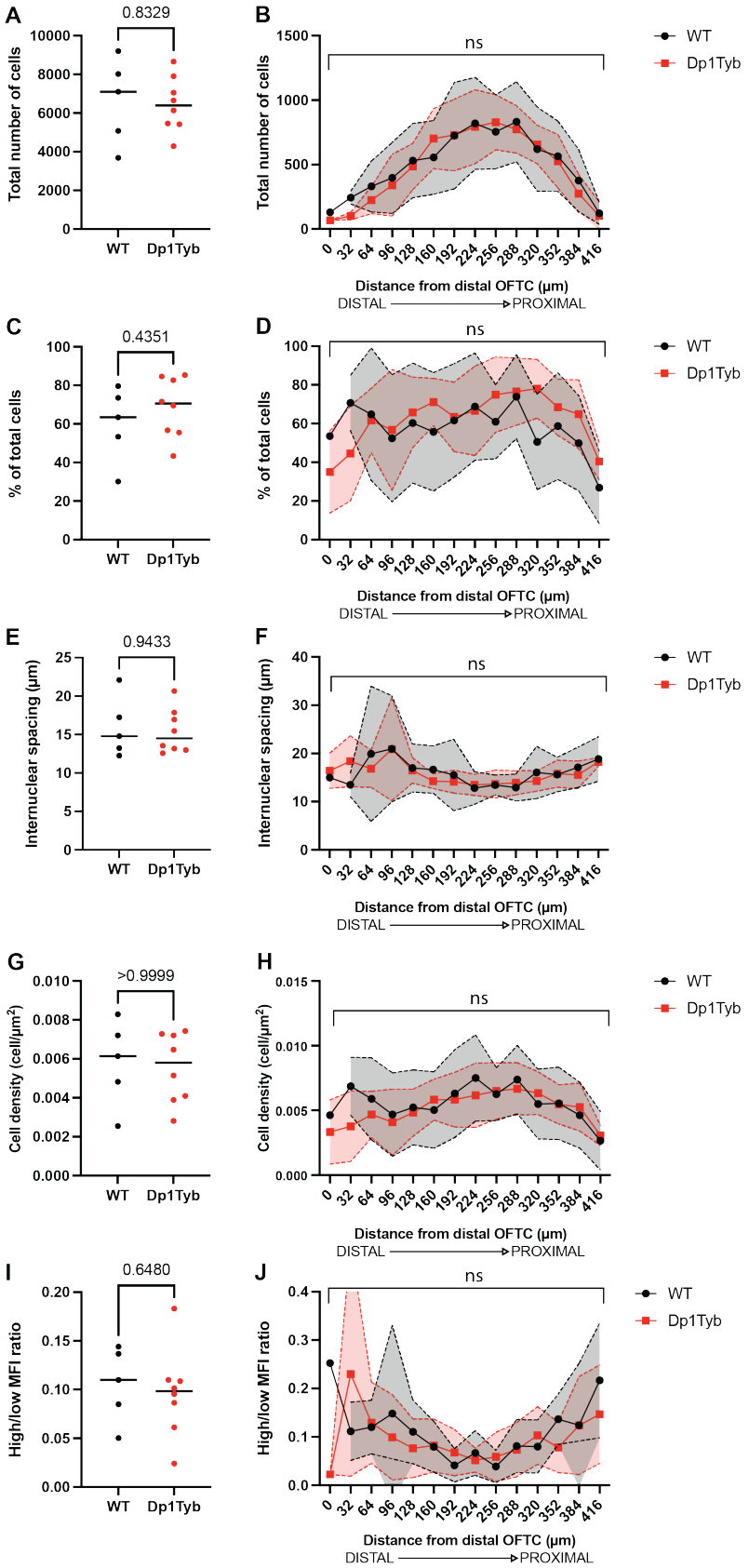

Figure 5.16 Sox9 positive cells in the OFTCs of E12.5 wild-type and Dp1Tyb hearts. Total number of Sox9 positive cells in the cushions (A) and spatially defined by plotting

cell count for each section from distal to proximal cushion (B). Percentage of total cells that are positive for Sox9 expression, plot as an average per embryo (C) and for each section (D). Internuclear spacing for Sox9 positive cells only plot as an average per embryo (E) and spatially (F). Average Sox9 positive cell density per embryo (G) and spatially defined (H). Plots showing the ratio of high to low fluorescence intensity Sox9 expression as an average per embryo (I) and for each section through the OFTC (J). Plots show mean (and SD for spatial plots). Statistical analyses were Mann-Whitney U (A, C, E, G, I) and two-way ANOVA (B, D, F, H, J).

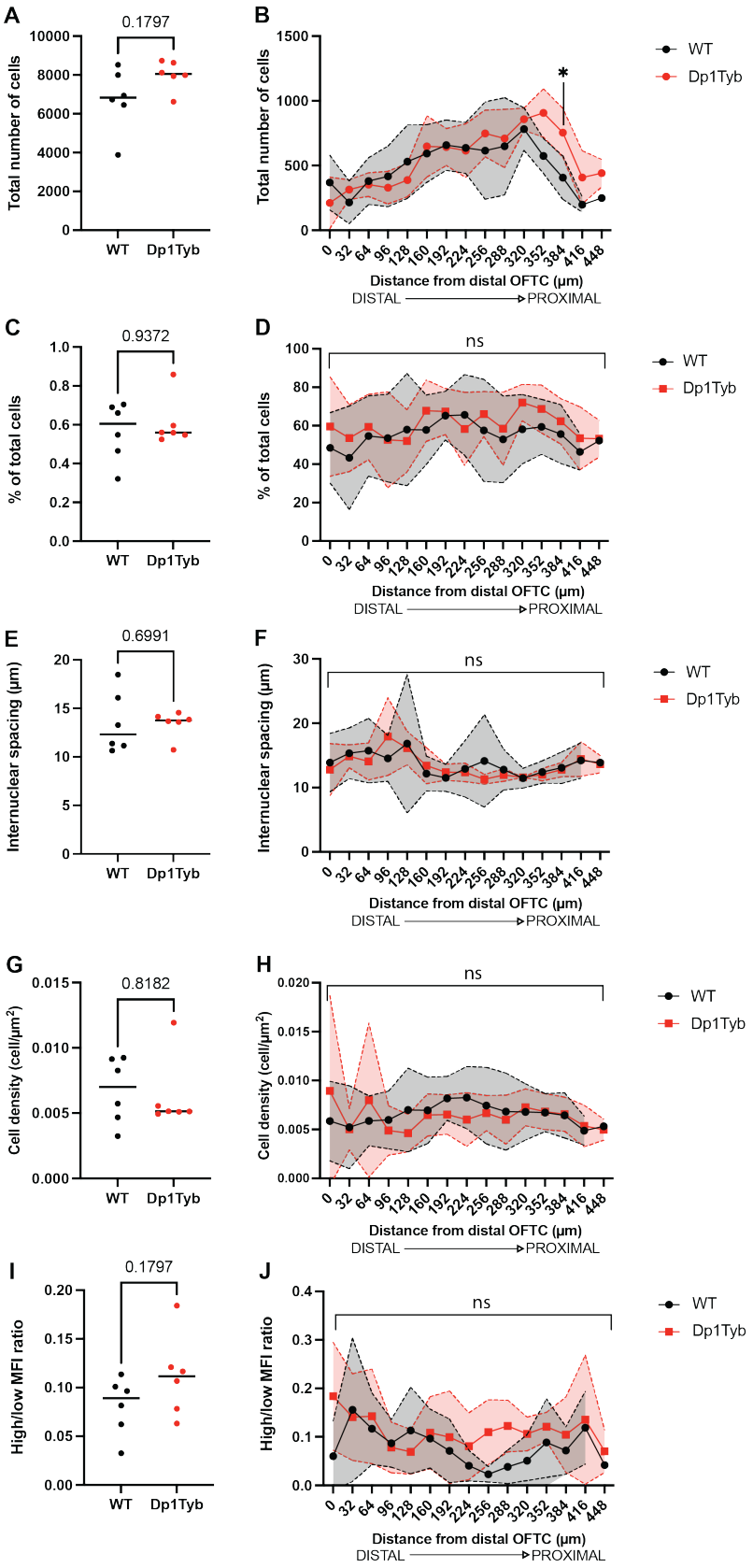

Figure 5.17 Sox9 positive cells in the OFTCs of E13.5 wild-type and Dp1Tyb hearts. Total number of Sox9 positive cells in the cushions (A) and spatially defined by plotting

cell count for each section from distal to proximal cushion (B). Percentage of total cells that are positive for Sox9 expression, plot as an average per embryo (C) and for each section (D). Internuclear spacing for Sox9 positive cells only plot as an average per embryo (E) and spatially (F). Average Sox9 positive cell density per embryo (G) and spatially defined (H). Plots showing the ratio of high to low fluorescence intensity Sox9 expression as an average per embryo (I) and for each section through the OFTC (J). Plots show mean (and SD for spatial plots). Statistical analyses were Mann-Whitney U (A, C, E, G, I) and two-way ANOVA (B, D, F, H, J). Where p-value is specified by asterisks: *p<0.05.

5.2.7 Apoptosis is unaffected in Dp1Tyb outflow tract cushions

I was interested in exploring apoptosis in the Dp1Tyb embryos as I had found a cell density and cell packing defect in the OFTC of the mutants and one of the possibilities that lead to a reduction in the number of cells (as seen at E12.5, Figure 5.10A-B) is an increase in cell death. Though there is an increase in cell number in the proximal region of the cushion at E13.5 (Figure 5.11B), it may be that more apoptosis is happening in the wild-type hearts compared to the Dp1Tyb hearts. Programmed cell death plays an important role in the development of the heart, where apoptosis is localised to regions of septation such as the OFTCs (Sharma *et al.*, 2004) and thus lead to changes in morphology. These regions are usually coincident with areas of condensed mesenchyme, as seen in the histological sections in Figures 2 and 5. Apoptosis is described as starting in the OFTCs at E10.5 and increasing in intensity in the distal OFTC as the pulmonary trunk and aorta emerge as separate vessels.

I assayed apoptosis using a TUNEL assay (Terminal deoxynucleotidyl transferase dUTP nick end labelling). TUNEL detects cell death by identifying DNA breakage in cells; the enzyme terminal deoxynucleotidyl transferase (TdT) catalyses the attachment of random nucleotides tagged with a fluorophore to DNA fragments that result from cell death or excessive damage (Fayzullina and Martin, 2014). The Click reaction I used for this assay allowed for a faster and more sensitive reaction than using a traditional antibody-mediated-staining: the Click-TUNEL assay utilises Alexa Fluor azides which have a smaller molecular weight than antibodies and therefore are more penetrative in the samples. I used Alexa-647 azide attachment

so the cell death could be imaged in the far-red channel (700-750nm) and there would be no risk of bleed-through excitation of other fluorophores, limiting the background noise on the image obtained.

For OFTCs in both stages, I measured the total number of TUNEL puncta, the average size of the puncta, the total area of TUNEL puncta and that metric as a percentage of the total cushion ROI area. For E12.5, there was no significant difference between wild-type and Dp1Tyb embryos in any of the measurements (Figures 5.18A-H). Although, interestingly, the number of puncta and total area taken up by the puncta were both higher in the middle of the cushion than the distal and proximal ends (Figures 5.18B & F), suggesting that cell death was occurring in the condensed mesenchyme, which follows a similar pattern observed in the histological sections (Figure 5.2). In the histological sections, this region did not seem to have any visible fragmentation of cells unlike at E13.5 where cell debris is obvious (Figure 5.5).

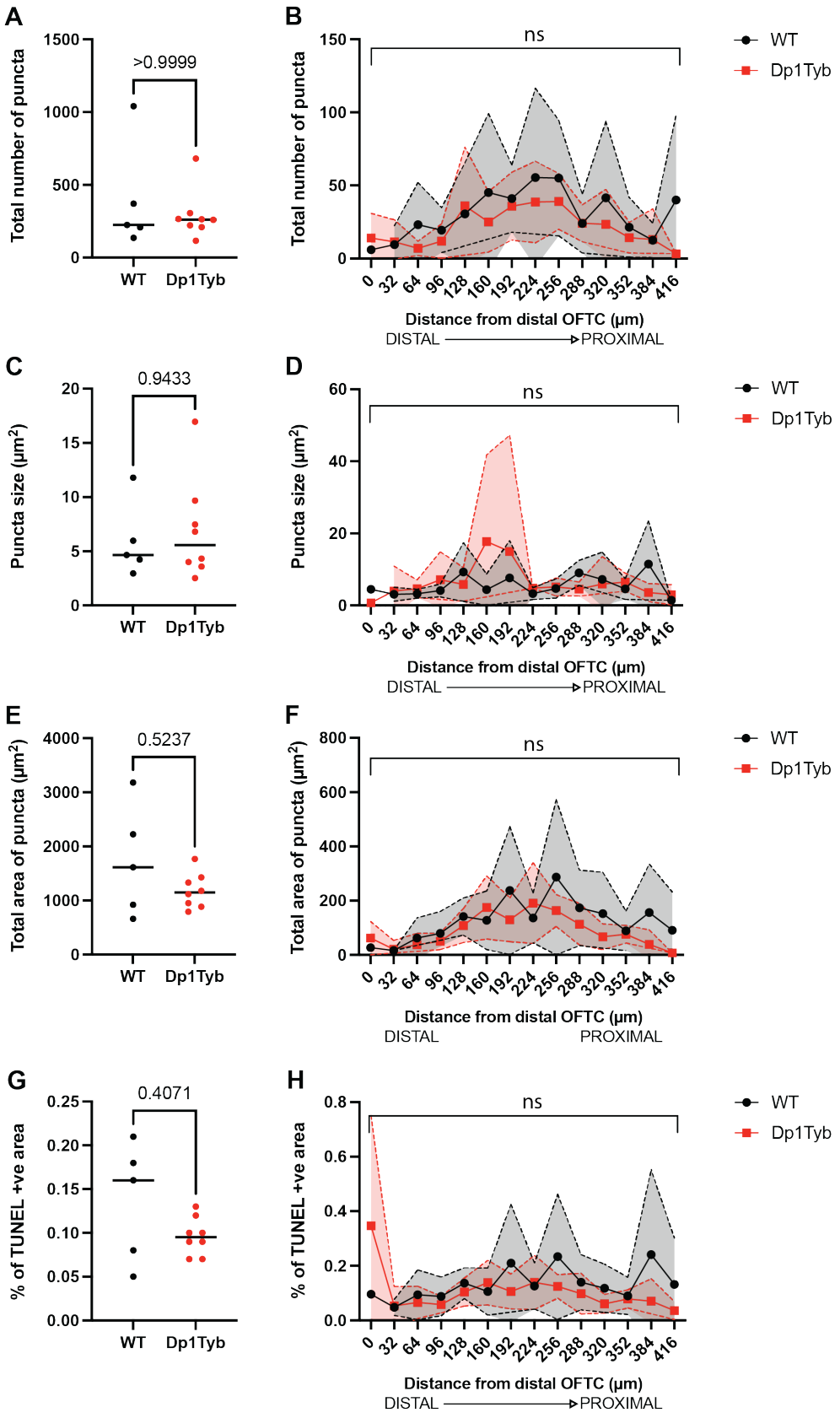

Figure 5.18 apoptosis in E12.5 OFTC of wild-type and Dp1Tyb hearts. Total number of TUNEL puncta in the cushions (A) and spatially defined by plotting puncta number for

each section from distal to proximal cushion (B). Puncta size plot as an average per embryo (B) and for each section (C). Total area of TUNEL puncta as a total of every section per embryo (E) and per section (F). Average percentage of the OFTC area that is occupied by TUNEL puncta in a section (G) and broken down per section (H). Plots show mean (and SD for spatial plots). Statistical analyses were Mann-Whitney U (A, C, E, G) and two-way ANOVA (B, D, F, H).

Sharma and colleagues (2004) described levels of cell death in the cardiac cushions as increasing significantly at E13.5. This was also seen in this dataset – the total number of puncta increased from an average of approximately 250 per section in both genotypes at E12.5 to 750-1000 puncta at E13.5 (Figure 5.19A). The spatial pattern of TUNEL-positive bodies followed a similar curve to that at E12.5 (Figure 5.19B), with more apoptosis occurring in the middle sections of the OFTCs. However, just like at E12.5, there was no significant difference in the number or size of puncta and the area of TUNEL-positive inclusions within the OFTC between the wild-type and the Dp1Tyb embryos (Figures 5.19C-H). Thus, overall, the Dp1Tyb tissue-level phenotypes could not be attributed to differences from the wild-type controls in the levels or distribution of apoptosis.

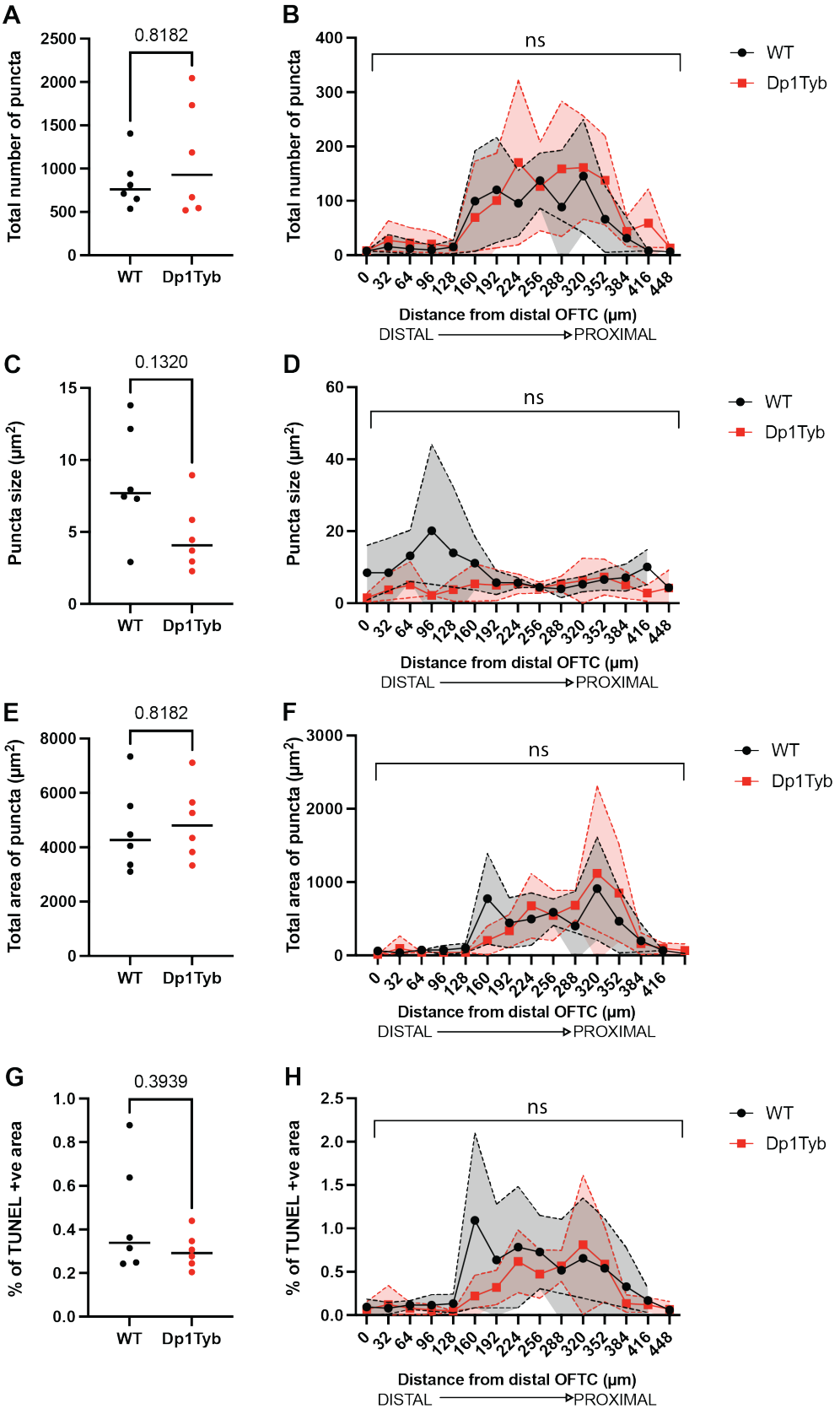

Figure 5.19 apoptosis in E13.5 OFTC of wild-type and Dp1Tyb hearts. Total number of TUNEL puncta in the cushions (A) and spatially defined by plotting puncta number for

each section from distal to proximal cushion (B). Puncta size plot as an average per embryo (B) and for each section (C). Total area of TUNEL puncta as a total of every section per embryo (E) and per section (F). Average percentage of the OFTC area that is occupied by TUNEL puncta in a section (G) and broken down per section (H). Plots show mean (and SD for spatial plots). Statistical analyses were Mann-Whitney U (A, C, E, G) and two-way ANOVA (B, D, F, H).

5.2.8 Proliferation is reduced in Dp1Tyb outflow tract cushions

Proliferation in the OFTC is not a well-characterised process, described in the literature as happening after EndoMT in the cushions in the process of OFT septation and vascularisation into smooth muscle. There has been evidence that indicates impaired proliferation specifically in the Dp1Tyb model, where this was shown in transcriptomic data (Lana-Elola *et al.*, 2023). Proliferation is also shown to be impacted in neural crest-derived structures in the craniofacial region of Dp1Tyb mice likely responsible for its dysmorphology (Redhead *et al.*, 2023). As data in the previous chapter suggested the cushions may be dysmorphic (§§4.2X), I hypothesised that proliferation may be affected in the OFTC too.

I used an anti-PHH3 antibody to identify any cells undergoing mitosis as this was a reliable immunostaining that would work alongside the TUNEL assay and Sox9 antibody. In this analysis, I quantified the absolute number of mitotic cells within the OFTC ROI, the percentage of the total cells that were mitotic/positive for PHH3 staining and within the population of mitotic cells what percentage was also Sox9 positive. This analysis was completed overall for each embryo and per section to allow for any regional or spatial patterns to emerge.

There was no statistical difference in proliferation through the OFTCs at E12.5 between wild-type and Dp1Tyb embryos overall or spatially (Figures 5.20A-B). Regardless of genotype there was more proliferation in the proximal half of the cushions in absolute numbers but this corresponded to higher cell number: the percentage of cells being mitotic was similar proximally versus distally for both wild-type and Dp1Tyb embryos, with hints of slightly higher mitotic index at each end (Figure 5.20B-C). There was no spatial pattern in the proliferation of mesenchymal Sox9-expressing cells at this stage in either group, with ranges of approximately 30% to 80% throughout the cushions and depending on the embryo.

By the next embryonic day at E13.5, a defective proliferation phenotype emerged in the Dp1Tyb OFTCs. While the total number of mitotic cells per embryo remained statistically insignificant between the wild-type and the mutants (Figure 5.21A-B), when separated by its midpoint 224μm into distal and proximal portions, the Dp1Tyb OFTCs showed a conspicuous and statistically significant decrease in the percentage of mitotic cells (using a Mann-Whitney U test) in a region proximal to the mid-point of the cushion (Figure 5.21D). Similarly to E12.5 results, the proportion of double-positive cells for Sox9 and PHH3 was highly variable and not significantly different between genotypes.

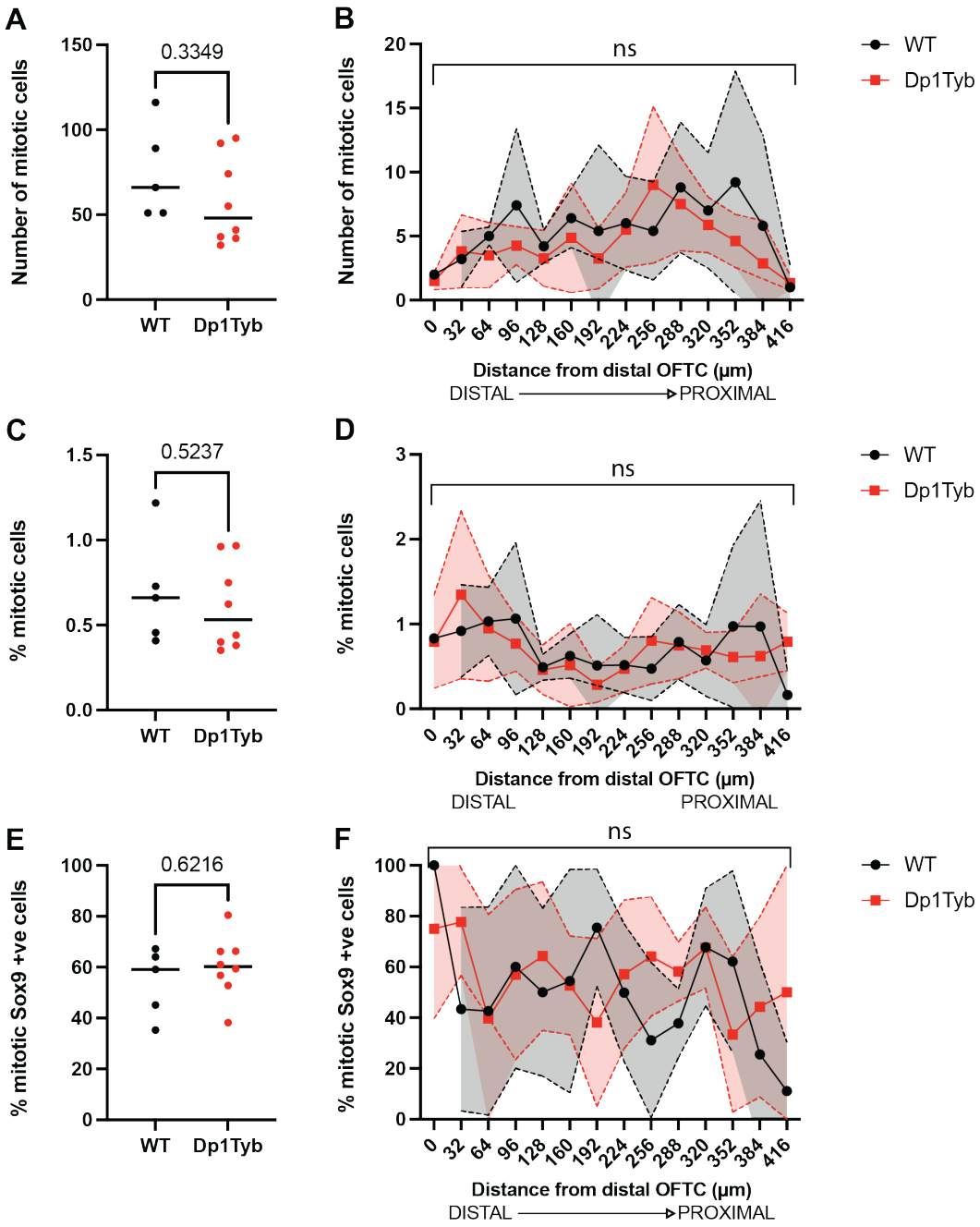

Figure 5.20 Population of mitotic cells in the OFTCs of wild-type and Dp1Tyb hearts at E12.5. A graph showing the overall count of proliferating (PHH3 positive) cells in both genotypes (A) and per each corresponding section analysed from distal to proximal cushion (B). Average count of proliferating cells in wild-type and Dp1Tyb as a percentage of the total cell population (C) and for each corresponding section (D). Quantification of the percentage of Sox9 expressing cells that are also mitotic as an average through all sections I and for each section through the cushion (F). Plots show mean (and SD for spatial plots). Statistical analysis performed: Mann-Whitney U test (A, C, E) and two-way ANOVA (B, D, F). Wild type n = 5, Dp1Tyb n = 8.

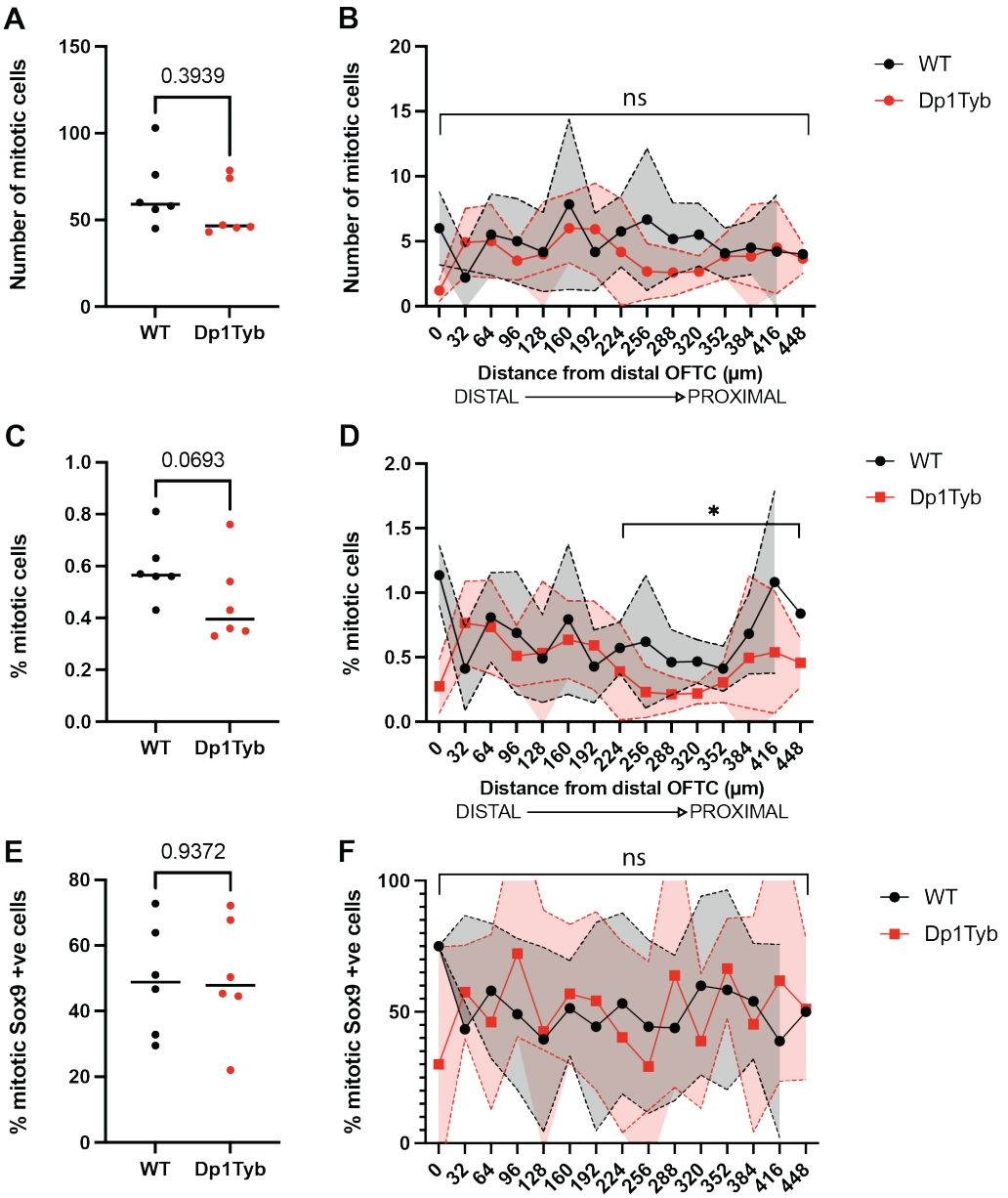

Figure 5.21 Population of mitotic cells in the OFTCs of wild-type and Dp1Tyb hearts at E13.5. A graph showing the overall count of proliferating (PHH3 positive) cells in both genotypes (A) and per each corresponding section analysed from distal to proximal cushion (B). Average count of proliferating cells in wild-type and Dp1Tyb as a percentage of the total cell population (C) and for each corresponding section (D). Quantification of the percentage of Sox9 expressing cells that are also mitotic as an average through all sections I and for each section through the cushion (F). Plots show mean (and SD for spatial plots). Statistical analysis performed: Mann-Whitney U test (A, C, E) and two-way ANOVA (B, D, F). Where p-value is specified by asterisks: **p<0.01. Wild type n = 6, Dp1Tyb n = 6.

5.3 Discussion

In this chapter, an in-depth cellular characterisation of the OFTC of wild-type and Dp1Tyb OFTCs revealed three phenotypes:

1. Reduced cellular density throughout the cushion at E12.5 and E13.5
2. Gross enlargement proximally at E13.5
3. Reduced proliferation proximally at E13.5

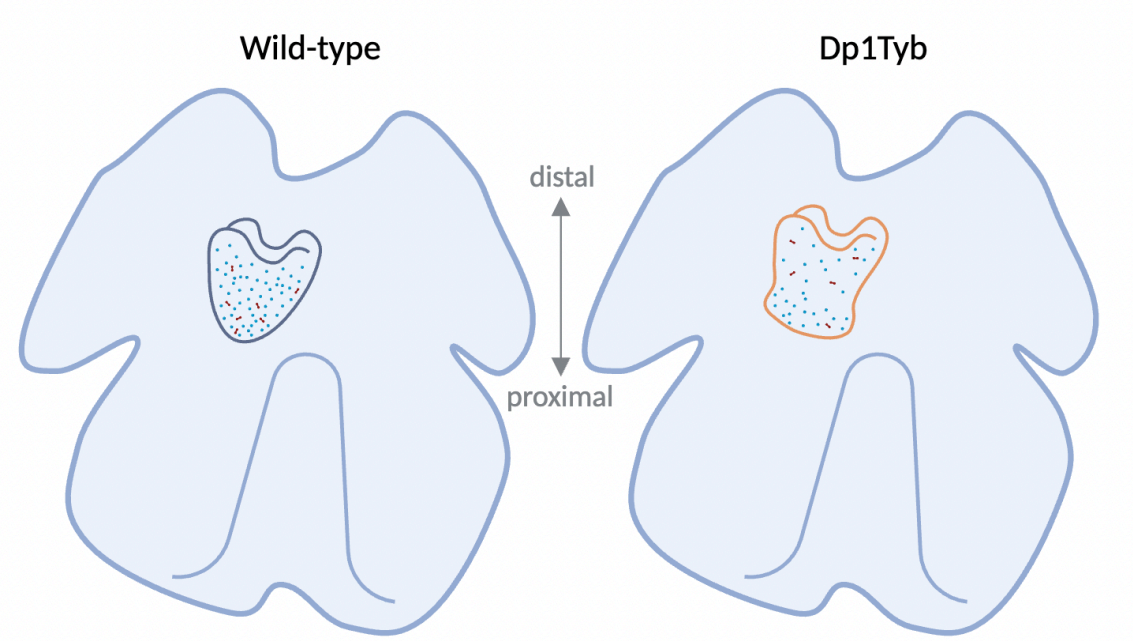

Figure 5.22 Outflow tract cushions at E13.5 in wild-type and Dp1Tyb hearts. A schematic demonstrating the changes in cushion morphology and cellular make-up of the OFTCs in wild-type and mutants at E13.5. The Dp1Tyb hearts are shown as having an enlarged proximal area with a less dense network of cells and fewer mitotic events.

5.3.1 Cell density defect

A consistent phenotype in both E12.5 and E13.5 in the Dp1Tyb hearts was reduced cell density (observed for both stages) and increased spacing in between individual nuclei (observed at E13.5). Interestingly the same phenotype arises for different reasons – at E12.5 the reduction in cell density was due to fewer cells (Figures 5.10A, B, E &F) compared to wild type while the area of each section did not differ between

the genotypes, whereas at E13.5 this reduction comes from an enlargement of the OFTC area per section. In fact, the total number of cells increases in the proximal tip of the cushion along with a two-fold increase in the area of the proximal cushion sections, with the biggest increase starting approximately 350μm from the start of the distal cushion. I will expand on the increase in area further in the discussion below. This finding suggested several reasons that could underlie the defect. The first cell density defect at E12.5 due to a lower cell count could stem from an earlier proliferation defect in the prior developmental stages, a migratory defect in the CNCC that colonise the OFT, or a partial failure of EndoMT of SHF-derived cells.

I was not able to investigate prior developmental stages as this thorough characterisation section by section was time-consuming as all immunofluorescence staining and imaging were done manually and not multiplexed. Ideally, this experiment would have extended back to E11.5 and perhaps E10.5 to continue chasing the phenotype to locate its temporal origins.

A migration defect could have been explored by using a neural crest lineage tracing transgenic mouse; this was attempted during my project by crossing the Dp1Tyb mice to Wnt1-Cre to create a double mutant, however due to poor breeders and sudden deaths from many male Wnt1-Cre mice I was not able to establish a line. These Dp1Tyb.Wnt1-Cre mice would have been crossed to an existing nuclear tracking Sun1-GFP mouse line to identify the proportions of CNCC in the OFT and whether there were different proportions of cell lineages in Dp1Tyb OFTCs. Furthermore, the same mice could have been used for migration studies, such as taking explants from the dorsal neural tube and performing migration assays at both a single-cell level and a collective migration. This would have been a particularly interesting experiment given that CNCC have long been considered implicated in many CHDs, with most neurocristopathies possessing a cardiac defect (Keyte and Hutson, 2012). Additionally, experiments from a previous member of the Green and Tybulewicz labs found a proliferation but not migration defect in the Dp1Tyb neural crest-derived craniofacial bones (Redhead *et al.*, 2023). The other population of cells contributing to the OFTC is SHF derived. Similarly to exploring CNCC, a SHF lineage tracing could be achieved through crossing Dp1Tyb mice with a Mef2c-Cre or Nkx2.5-Cre mouse (Peterson *et al.*, 2021) and determining what percentage of the OFT population is established from the SHF.

While the cell density defect in Dp1Tyb at E12.5 is caused by a smaller population of cells within the same-sized cushion, the phenotype observed at 13.5 is directly due to a larger area per section from the medial region to proximal regions. I hypothesise that this could be caused by an increase in ECM production, leading to such swelling of the cushion that though it allows for a larger population of cells locally it is not enough to retain wild-type levels of cell density.

5.3.2 Proximal cushion enlargement in the Dp1Tyb

This leads to the second finding: the proximal cushions of the Dp1Tyb are hyperplastic at E13.5. This is to such an extent that while cell numbers in the proximal cushion increase in proportion to the area enlargement, it is still not enough to recover cell density or internuclear spacing to wild-type levels. As the cushion area is much larger this could be the result of more localised ECM and its production in the cushion.

The cushions at E13.5 are still primarily made up of cardiac jelly, a mixture of different ECM proteins secreted by fibroblasts. ECM dysregulation has been linked to the development of CHDs in many cases with knockouts of ECM proteins found in the OFTC leading to different types of cellular abnormalities. Examples of this include perlecan-null mice exhibiting abnormally increased cell counts in the OFTC along with hyperplastic cushions leading to transposition of the pulmonary artery and aorta and dysmorphic valves (Costell *et al.*, 2002), versican haploinsufficiency resulting in VSDs (Kern *et al.*, 2010), and hyaluronan deficient mice exhibiting failure to undergo EndoMT in the OFTC (Camenisch *et al.*, 2000).

This specific result seems to indicate that the ECM is dysregulated somehow within the Dp1Tyb OFTCs, leading to larger proximal cross-section of the cushions. The results in the chapter seem to be at odds with the overall morphology of E13.5 cushions as characterised in the previous chapter (§§4.2.3), where segmentation of the cushions from HREM images revealed a significantly smaller cushion volume in the Dp1Tyb, whereas serial section analysis in this chapter shows the trend of the cushions to be larger in volume. I found this perplexing and believe that it is due to the two different techniques underlying the measurement – in the HREM images I segmented the cushions based on observed tissue density changes, i.e. the

appearance of histological condensation (§§4.2.1). Whereas the immunostaining areas are determined by the boundary of ECM space or Sox9-positive cells, which may be result in more area being counted as it is based on cellular boundaries and the HREM is not resolved to cellular level.

5.3.3 Defect in proliferation

The last finding from the chapter is a decrease in the proportion of proliferating cells in the cushion at E13.5 in Dp1Tyb embryos. This change was observed once the quantification was broken down into corresponding sections between the embryos (Figure 5.21D). I was surprised to discover that the reduction in proliferation occurs in the proximal half of the Dp1Tyb cushion, coinciding with the larger cross-sectional area described in Figure 5.15C and the increase in cell count in Figure 5.11A.

This result was not the first time that proliferation decrease has been associated with the Dp1Tyb mouse model. The Tybulewicz lab has described that the Dp1Tyb mice have a reduction in proliferation in the AVCs through Dp1Tyb mice crossed to a mouse with the cell-cycle reporter Fucci (unpublished, Dr Rifdat Aoidi), this is discussed further in the general discussion (§§7.4.8). Additionally, reduced expression of E2F target genes linked to proliferation in a Dp1Tyb single-cell transcriptomic experiment was shown in Dp1Tyb E13.5 hearts (Lana-Elola *et al.*, 2023). Furthermore, as briefly mentioned in discussion point §§5.3.1, decreased proliferation has also been observed in the craniofacial regions (Redhead *et al.*, 2023). Thus, it was exciting to also see that the OFTCs also display this phenotype immediately before septation. The transcriptomic signature and craniofacial proliferation phenotypes were both rescued in the Dp1Tyb*Dyrk1a*$^{+/+/-}$ transgenic mouse, where only Dyrk1a has been reduced back to 2 copies (Lana-Elola *et al.*, 2023; Redhead *et al.*, 2023). Unfortunately, it was beyond the scope of this current project to include the Dp1Tyb*Dyrk1a*$^{+/+/-}$ mouse in the study but it would be a pertinent and logical next step to see if Dyrk1a is one of the causative genes in the decrease in proliferation here as well.

To summarise the findings in this chapter, the OFTCs of Dp1Tyb embryos were found to be less cellularly dense compared to wild-type controls at both E12.5 and E13.5. At E13.5 this was paired with an enlarged proximal region which

coincided with lower rates of proliferation. These findings suggest that the proximal anatomy of the Dp1Tyb OFTC is dysmorphic and with more cardiac jelly at a stage where it should be fully fusing to the crest of the mVS. This phenotype could impact how this region of the cushion comes together with mVS before septation is completed, thereby potentially contributing to its failure. This is further discussed in the general discussion.

With this phenotype coinciding with a larger proximal cushion likely due to increased ECM, I was interested in finding out whether these two findings could be linked. While ECM changes can affect signalling pathways and cellular behaviours, it can also change the material properties of the heart such as stiffness of tissues. To investigate this further, I decided on two avenues - to investigate whether the dysmorphic Dp1Tyb cushions also had different material properties and to look at YAP expression in the OFTCs, as YAP not only responds to tissue stiffness and haemodynamic flow to localise to the nucleus (Wang *et al.*, 2023) but is also implicated in the correct development of OFTCs through proliferation via the Hippo pathway (Chen *et al.*, 2020) and EndoMT transitions (Zhang *et al.*, 2014a).

Chapter 6. Exploration of outflow tract cushion stiffness before septation

6.1 Introduction

6.1.1 Material stiffness in the embryonic heart

In my previous results chapter, I demonstrated that the Dp1Tyb OFT cushions have a reduced cell density throughout the cushion structure at both E12.5 and E13.5 compared to those in wild-type mice. This was found in combination with regional differences in the cross-sectional area of the cushions, specifically a larger area in Dp1Tyb OFT cushions at the proximal end nearest the ventricles. The implication was that lower cell density in this region as a result of a larger cushion mesenchymal area would mean more ECM. Increased deposition of ECM in the cushion may impact the regional stiffness of the structure and possibly impact tissue morphogenesis and the process of ventricular septation. The combination of subtle morphological changes but increased ECM in the Dp1Tyb OFTCs gave credence to the hypothesis that altered mechanical properties of the OFTC rather than just altered shape might factor in the VSD phenotype.

In the last decade, atomic force microscopy (AFM) has been adopted as one of the preferred techniques to measure the material properties of biological materials, namely the elastic modulus. Examples of tissues examined using AFM are the human brain (Fuhs *et al.,* 2023), mouse ovarian follicles (Hopkins *et al.,* 2021) and various disease model cell lines (Gautier *et al.,* 2015). AFM is capable of achieving nanoscale resolution (Benitez and Toca-Herrera, 2014). The AFM microscope incorporates a physical probe that contacts and indents the surface of the specimen. The probe, which can vary in size and shape depending on the sample material/tissue and the experimental scale, is glued to a cantilever. A laser beam is directed at the surface of the cantilever and is reflected onto a photodiode matrix. As the probe (under the control of fine motors) interacts with the sample, the cantilever bends resulting in the deflection of the laser beam. The deflection is captured by the photodiode to return a quantitative output (Peña *et al.,* 2022) (Figure 6.1). The deflection can be used either to test the material properties, such as elasticity or stiffness, since the spring-stiffness of the cantilever deflection can be calibrated, or

to probe the topology of a tissue by keeping the deflection constant and recording the motor-translation needed to maintain this.

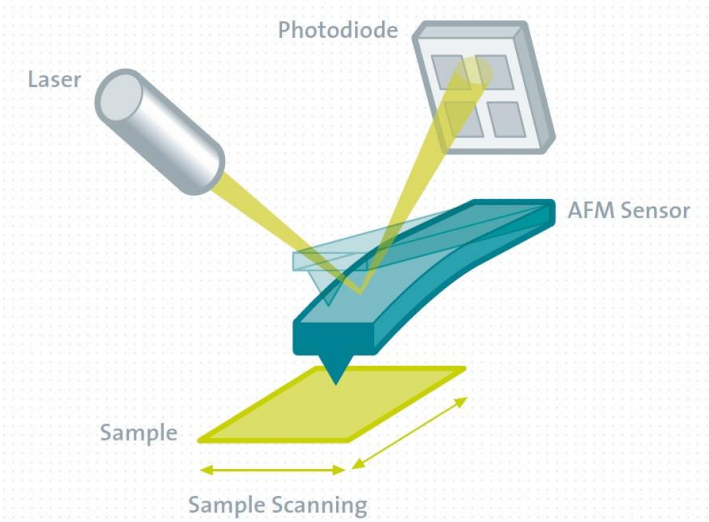

Figure 6.1 Atomic force microscopy. The schematic shows how data such as force spectroscopy is acquired. The AFM sensor consists of the cantilever and bead that probes the sample surface, typically scanning the sample surface as a grid. A laser is directed at the cantilever and its beam is deflected as the cantilever interacts with the sample. This deflection is captured by the photodiode. The image was obtained from "raman.oxinst.com/techniques/scanning-probe-microscopy".

Force spectroscopy AFM is the modality that returns values associated with the material properties of a given sample. This is typically returned as Young's Modulus, which is the unit of measurement of elasticity (Pa). Elasticity in this context refers to the ability of a substance to resist deformation (i.e. the opposite of the idiomatic meaning of the word "elasticity"). Therefore, Young's Modulus is considered the measure of inherent "material stiffness" in biological tissue through how likely it can deform based on its elastic properties, where high values indicate tissue that is more resistant to deformation ("stiffer") and low Young's modulus values suggest more easily deformed tissue (less "stiff"). Strictly speaking, the formal definition of the word "stiffness" in Engineering and Physics is the deformability of a structure rather than a material, but it is assumed for practical purposes that at the AFM probe scale the two are either equivalent or at least closely related.

The use of AFM on biological material is often referred to as 'bio-AFM', its increasing popularity and accessibility has resulted in the publication of a protocol for first-time users and explanations of how to interpret results (Hopkins *et al.*, 2021).

In the context of the heart AFM has primarily been used in the exploration of material properties of adult cardiac tissue and cultured cardiomyocytes, such as the contractility and biomechanical properties of isolated cardiomyocytes (Benech and Romanelli, 2022), mechanical changes in the cardiac tissue of young and old monkey aortas (Qiu *et al.*, 2010), and cardiac fibrosis from myocardial infarction injury models (Peña *et al.*, 2022). It has also been used to characterise the dynamic levels of ECM in a heart regeneration model in zebrafish where it was determined through AFM that areas of active regeneration were less stiff (Garcia-Puig *et al.*, 2019).

Despite its many different applications, there appears to be limited literature on the use of AFM in embryonic mouse hearts. I was able to find 2 studies that specifically used AFM on embryonic mouse hearts to test for stiffness, where the youngest embryonic age for both was E13.5 (van der Loo *et al.*, 2008; Jacot *et al.*, 2010). The results from the two studies both used a dissected sample from the left ventricle and had values in similar ranges (10-30 kPa) for the stage. The literature is more sparse on AFM in the endocardial cushions and even less so in the specific case of the OFTC. There are two AFM studies I could find on the stiffness of AVC explants (Tan *et al.*, 2013; Sewell-Loftin *et al.*, 2014), although these were cultured explants rather than fresh dissections performed here. It appears that the impact of the material stiffness of the OFTC on the process of ventricular septation is an unexplored area of research. The results below may be the first description of AFM on freshly dissected OFTC from normal embryonic mouse hearts, let alone in the context of DS. However, limited time and sample number meant that these represented a highly preliminary pilot study.

6.1.2 The role of Yap in outflow tract development

The YAP/Hippo pathway is a well-established integrator of a number of mechanical stimuli during growth and development in many systems and tissues (Boopathy and Hong, 2019; Zheng and Pan, 2019; Fu *et al.*, 2022) and therefore presented a potential additional target for investigation of the hypothesis that the Dp1Tyb VSD phenotype might have mechanical causes. This pathway has been implicated in the development of the heart and more specifically the growth of the endocardial

cushions through EndoMT and proliferation (Zhang *et al.*, 2014b) and the development of the OFTC. The latter was demonstrated by Wang and colleagues (2023), who found YAP to be regulated by fluid shear stress: blood flow increased YAP nuclear translocation and this led to increased levels of proliferation, consistent with the previous finding that there is increasing shear stress from blood flow exerted on OFTCs at E12.5 and E13.5 as blood pressure rises which affects the remodelling the cushions undergo between these two stages (Andrés-Delgado and Mercader, 2016). These effects suggested that YAP regulation could be relevant to the work in this thesis given the results above showing a decrease in the proliferation cells in the cushion mesenchyme of E13.5 Dp1Tyb OFTCs.

Furthermore, as I had demonstrated differential cell density in the Dp1Tyb cushions I hypothesised that if there were any changes in stiffness due to more ECM in the Dp1Tyb cushions, this might be reflected in YAP nuclear translocation as YAP has been shown to translocate to the nucleus on stiff substrates (Scott *et al.*, 2021).

6.2 Results

6.2.1 Setting up atomic force microscopy of embryonic hearts

A detailed explanation of the tissue preparation and AFM parameters will be described in the Materials and Methods (§§2.11). In brief, for this investigation, embryos were collected at E12.5 and E13.5 and microdissected, unfixed, with fine-tipped forceps and a micro-scalpel for the heart (Figure 6.2A). Once the heart was isolated, I used the scalpel to free the distal OFTC from the aortic sac and cut the proximal OFT where the arterial trunk joins the right ventricle, using the inner heart curvature as guidance (Figure 6.2B). The OFT was then transversely bisected into the distal and proximal halves of the OFTC (Figure 6.2C) and placed on glass-bottom dishes previously coated with Cell-Tak. I took care to ensure that the plane at which the two halves were separated was the surface making contact with and sticking to the dish (Figure 6.2D). This meant that the exposed surfaces for each half were the most distal and proximal cushion surfaces of the dissected OFT. The samples were then allowed to rest, covered, at 4°C for 2 hours to ensure good adhesion to the dish. This dissection was difficult to carry out as the OFT at E12.5 and E13.5 are approximately 500 μm in length or less and then to bisect it while ensuring that the

tissue was not crushed in the cutting process and that the cut surfaces were as even as possible for the AFM. Before beginning force mapping, the dishes containing the samples were flooded with PBS (a delicate step that resulted in the loss of a few of the samples due to the explant detaching from the dish bottom). Explants were prepared blind to genotype.

Force mapping was performed in a 10 x 10 grid of points over a 10 μm x 10 μm area (i.e at 1 μm intervals) by Oliva Courbot (Elosegui Artola Lab, the Francis Crick Institute). For the experiment, a pre-calibrated rectangular cantilever attached with a spherical 5 μm bead with a spring constant of k = 0.152N (Bruker, SAA-SPH-5UM). The sensitivity of the cantilever was measured with contact-free calibration in the JPK SPM (v7.0) software, using thermal noise measurements and fitting the results according to Sader and colleagues (1999). It is noted that this calibration method is only valid for rectangular cantilevers, as was used here.

The bead and cantilever can be seen with the dissected distal and proximal cushions tissues of E12.5 and E13.5 samples in Figure 6.2E-H. The experiment aimed to test 4 areas for stiffness, two on the distal and two on the proximal tissues for both E12.5 and E13.5. Care was taken to ensure that the areas being sampled was in the centre of the tissue as much as possible to avoid measuring the myocardium that surrounds the cushion. For each 10 x 10 sampling grid 100 force curves were generated and a Hertz model was fitted, from which a mean Young's Modulus value was calculated. The Hertz model assumes there is linear elastic relationship between the beaded cantilever and the tissue, where surface interactions such as tissue adhesion to the bead can be neglected (Kontomaris and Malamou, 2020). An example of a force curve is shown in Figure 6.2I. Some measurements were discarded based on the approach and deflection of the cantilever. An example of a discarded curve is shown in Figure 6.2J, where the approach (light blue) and deflection (dark blue) curves do not form a clear baseline and there is a constant deflection suggesting that the cantilever tip was in contact with the tissue the entire time. The processing of force curves was completed by Olivia Courbot to produce Young's Moduli for each sample and the resulting data was prepared as per a recently published AFM protocol (Norman *et al.*, 2021).

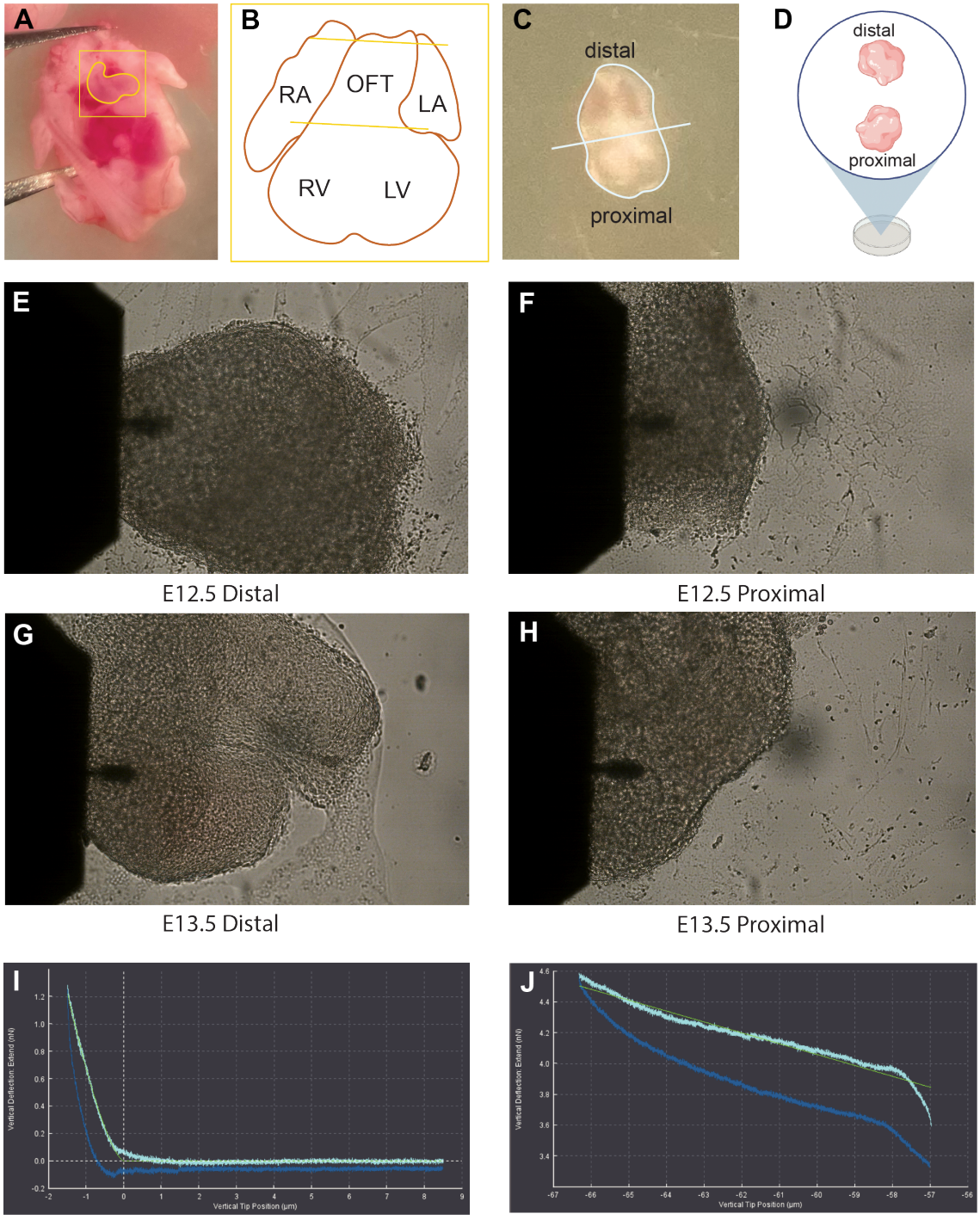

Figure 6.2 Dissection of the outflor tract cushions and subsequent atomic force microscopy (AFM) set up. (A) Dissection of an embryo with the outflow tract and ventricles outlined in yellow. (B) Cartoon demonstrating the extraction of the outflow tract (yellow lines). (C) Subsequent bisection of the outflow tract into distal and proximal samples (white line). (D) cartoon showing the placement and adherence of the samples to a dish. (E) E12.5 distal outflow tract cushion and AFM cantilever and bead. (F) E12.5 proximal outflow tract cushion and AFM cantilever and bead. (G) E13.5 distal outflow

tract cushion and AFM cantilever and bead. (H) E13.5 proximal outflow tract cushion and AFM cantilever and bead. (I) A kept force-curve. (J) An example of a discarded force curve.

The percentage of force curves kept for each OFT (combining the distal and proximal sampling areas) can be seen in Table 6.1 for the seven embryos (labelled S1-7) used at E12.5. The portion of force curves kept remained above 80% in all samples for E12.5 except for S7, this is likely indicative of the sample topology being especially uneven and therefore difficult to measure.

Sample	% of force curves kept
S1	96.3
S2	96.3
S3	83.7
S4	82.7
S5	87.8
S6	91.8
S7	56.0

Table 4 Percentage of force curves kept for analysis in all E12.5 samples. A table showing the percentage of force curves kept for further analysis in the 7 embryos used in the experiment, this includes the force curves generated for every sampling region in each embryo.

For eight E13.5 embryos (S1-8), the numbers were similarly consistent with the majority of force curves used for further analysis (Table 6.2). This was an important metric to consider, as the number of force curves kept affects the frequency distribution of Young's Moduli for each genotype, which will be discussed in further detail below.

Sample	% of force curves kept
S1	78.5
S2	80.3
S3	82.5
S4	95.5
S5	77.8
S6	80.0
S7	89.5
S8	96.0

Table 5 Percentage of force curves kept for analysis in all E13.5 samples. A table showing the percentage of force curves kept for further analysis in the 8 embryos used in the experiment, this includes the force curves generated for every sampling region in each embryo.

6.2.2 Stiffness in outflow tract cushions at E12.5

Young's Moduli for each sampling region were plotted as a histogram to assess the frequency distribution of the values (Figure 6.3A-B). In the proximal region, the histogram shows most values for Dp1Tyb and wild-type samples clustering around 100-200 Pascals (Figure 6.3B). Interestingly, the Dp1Tyb sample distribution is slightly shifted to higher values of Young's Modulus, which could be suggestive of small regions of increased stiffness of the Dp1Tyb proximal cushion sample. However, the frequency distribution of the distal OFTC region is completely skewed by one Dp1Tyb sample (Figure 6.3A). One sampling region was found to have Young's Modulus values at a median of 3511 pascals, compared to the rest of the values in both genotypes which clustered around 50-200 pascals.

I plotted all of Young's Moduli for the distal region of the OFTC (Figure 6.3C) and the proximal region of the OFTC (Figure 6.3D) for both genotypes. The spread of data can be further split into individual samples according to genotype, represented with box and whisker plots where the maximum and minimum values are denoted by the whiskers and the bounding values for the box represent the 1st and 3rd quartiles with the median shown as the horizontal line. In Figure 6.3E, the

spread of Young's Moduli in individual samples again demonstrates that the higher values originate from one sample, S1. Figure 6.3F shows the individual proximal cushion samples, where there is a wider distribution of values in S1 but not in S6. With all the distributions taken together, the data suggests that there could be areas of increased stiffness in the proximal region of the Dp1Tyb OFTC.

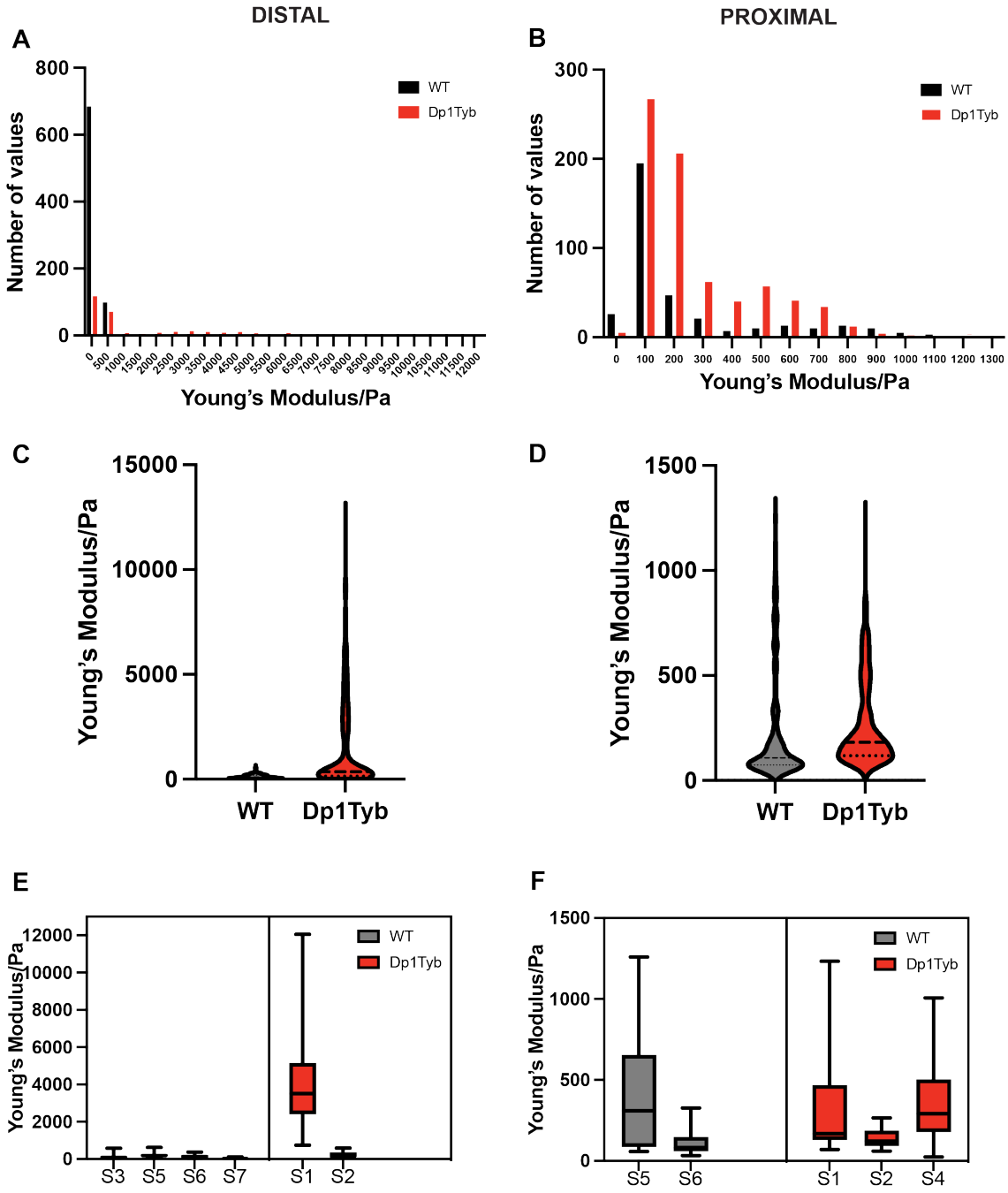

Figure 6.3 Distributions of Young's Moduli in the outflow tract cushions of E12.5 Dp1Tyb and wild-type embryos. (A-B) Histograms showing the distribution of Young's

Modulus in the proximal and distal outflow tract cushions of both genotypes. (C-D) Violin plot of the distribution of Young's Modulus in all distal (C) and proximal (D) OFT samples separated into Dp1Tyb and wild-type. Dotted lines indicate the 1st and 3rd quartiles, the dashed line is the median. (E-F) Young's modulus for distal (E) and proximal (F) samples shown as box and whisker plots, the minimum and maximum values are indicated by the limits of the 'whiskers', the 1st and 3rd quartiles by the bounding box and the median by the line within the box. Wild-type n = 4, Dp1Tyb n = 3.

For statistical quantitation, I calculated the mean for each sample by averaging the Young's Moduli. However, due to the low sample number in the wild-type of the proximal cushions and Dp1Tyb distal cushions, it was not possible to run any meaningful statistical analyses on the values. Nevertheless, the mean values for Young's Moduli in the distal regions of the cushions are shown in Figure 6.4A proximal cushions are represented in Figure 6.4B. In combining the distal and proximal averages for each sample, it was possible to run a statistical analysis (Figure 6.4C), which did not show a significant change between the Dp1Tyb and wild-type.

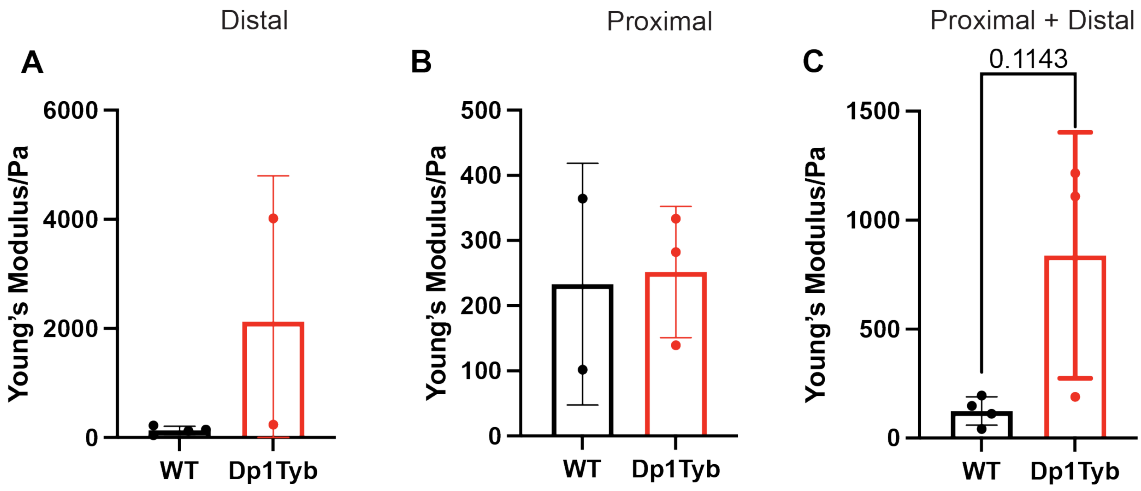

Figure 6.4 Mean stiffness values in the outflow tract cushions of E12.5 Dp1Tyb and wild-type embryos. (A) Mean of Young's Modulus in distal outflow tract cushions. (B) Mean of Young's Modulus in proximal outflow tract cushions. (C) Combined mean of Young's Modulus in the proximal and distal cushions. Data is shown as mean ± SD and statistics calculated with Mann Whitney-U test. Proximal: wild-type n = 2, Dp1Tyb n = 3; distal: wild-type n = 4, Dp1Tyb n = 2; combined: wild-type n = 4, Dp1Tyb n = 3.

6.2.3 Stiffness in outflow tract cushions at E13.5

As with the E12.5 Young's Moduli in both regions of Dp1Tyb and wild-type cushions, I plotted the values for the distal and proximal regions of the cushions as a frequency distribution (Figure 6.5A-B). The distribution of data here looks similar for both regions of the cushion between the genotype. With all of the individual values plotted with the median values, the distal and proximal regions of the cushions in Dp1Tyb embryos look similar to that of the wild-type (Figures 6.5C-D). As with the E12.5 samples, the values were highly variable. For the distal samples, the box and whisker plots (Figure 6.5E) show which sample the aforementioned spread originates from. S3 and S5 in the wild-type embryos both have much higher maximum Young's Moduli than all of the other samples regardless of genotype. In the proximal Dp1Tyb OFTC (Figure 6.5E), 2 out of the 3 samples had a large spread of data and the remainder had a small range restricted to values below 500 pascals.

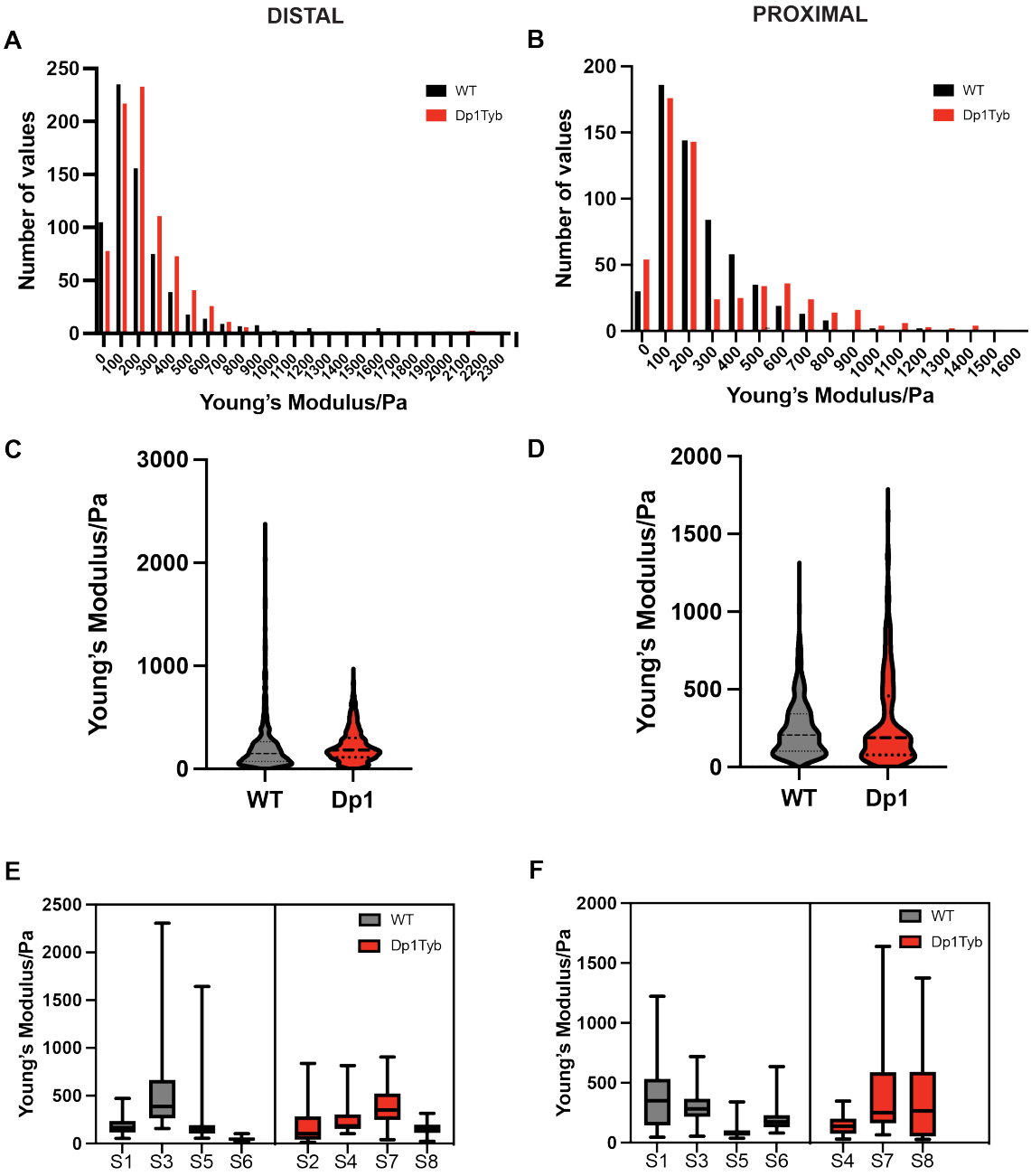

Figure 6.5 Distributions of Young's Moduli in the outflow tract cushions of E13.5 Dp1Tyb and wild-type embryos. (A-B) Histograms showing the distribution of Young's Modulus in the proximal and distal outflow tract cushions of both genotypes. (C-D) Violin plot of the distribution of Young's Modulus in all distal (C) and proximal (D) OFT samples separated into Dp1Tyb and wild-type. Dotted lines indicate the 1st and 3rd quartiles, the dashed line is the median. (E-F) Young's modulus for distal (E) and proximal (F) samples shown as box and whisker plots, the minimum and maximum values are indicated by the limits of the 'whiskers', the 1st and 3rd quartiles by the bounding box and the median by the line within the box. Wild-type n = 4, Dp1Tyb n = 4.

The means of proximal and distal OFTCs of the two genotypes were then compared and tested to determine if there were any statistical differences. Unlike the dataset obtained for E12.5, there were enough samples in both proximal and distal regions at E13.5 for statistical analyses. Both distal and proximal regions of the cushions did not have a statistical difference in the means of Young's Moduli between wild-type and Dp1Tyb (Figure 6.6A-B). The combined means of proximal and distal regions for each genotype were also insignificant (Figure 6.6C), suggesting that there are no regional or overall areas of differential stiffness in the mutant OFTCs.

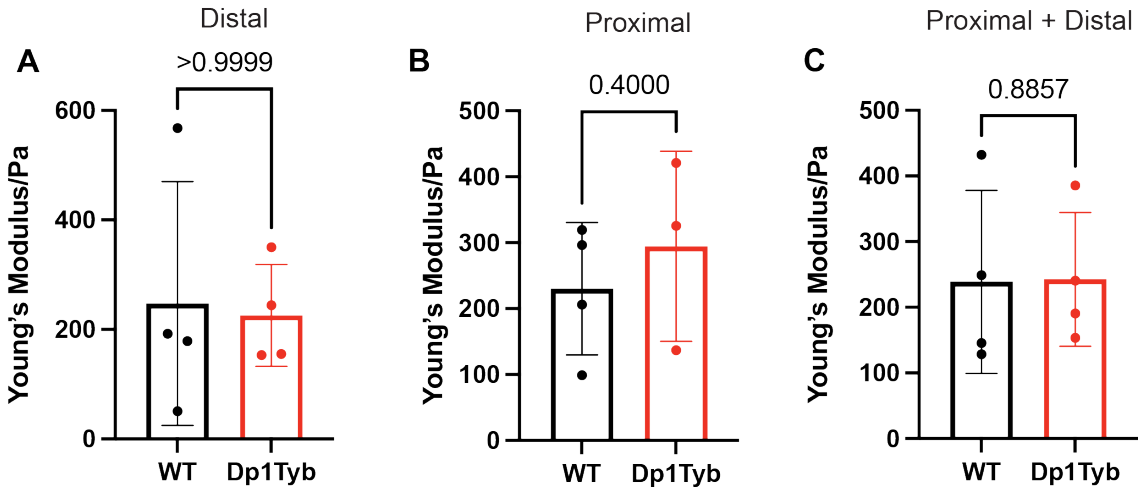

Figure 6.6 Mean stiffness values in the outflow tract cushions of E13.5 Dp1Tyb and wild-type embryos. (A) Mean of Young's Modulus in distal outflow tract cushions. (B) Mean of Young's Modulus in proximal outflow tract cushions. (C) Combined mean of Young's Modulus in the proximal and distal cushions. Data is shown as mean ± SD and statistics calculated with Mann Whitney-U test. Proximal: wild-type n = 4, Dp1Tyb n = 3; distal: wild-type n = 4, Dp1Tyb n = 4; combined: wild-type n = 4, Dp1Tyb n = 4.

6.2.4 YAP expression in outflow tract cushions and experimental set up

Concurrent with my investigation into whether there were regional changes in the material properties of the OFTC at E12 and E13.5 in the Dp1Tyb embryos, I investigated YAP expression in the cushions at the same two stages. I selected comparable distal, medial and proximal sections for wild-type and Dp1Tyb cushions at E12.5 and E13.5, making sure that the intervals between the 3 section levels

remained similar. To reduce variability from manual staining, the sections were processed in the same run on the Leica BOND RX automated stainer with antibodies against Sox9 and YAP, then counterstained with DAPI (performed by Experimental Histopathology, the Francis Crick Institute). I imaged the immunostained sections on a Zeiss Apotome 2 semi-confocal microscope. A representative staining from this experiment is shown in Figure 6.7A-D. The staining within the OFTC can be seen in the inset box and panels E-H where an example YAP nuclear localisation is indicated by the yellow arrowhead. As seen in these images, the expression of YAP was apparently ubiquitous in the heart (Figure 6.7B) with clear areas of increased intensity in the nucleus or cytoplasm.

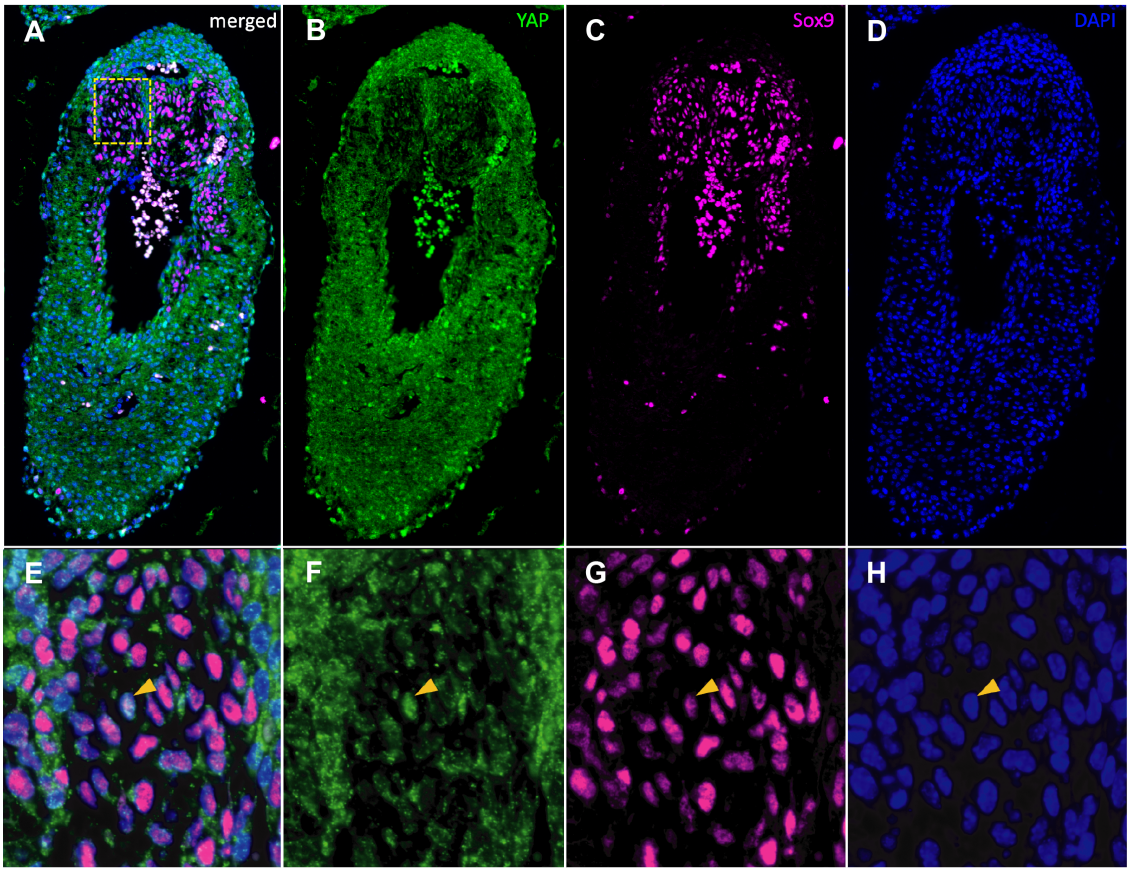

Figure 6.7 Immunofluorescence staining of YAP and Sox9 in the outflow tract cushions. (A-D) Immunofluorescence staining of YAP and Sox9 with a DAPI counterstain. (E-H) The Inset box of dashed yellow outline in (A) is shown in greater detail. Yellow arrowhead points to a cell with yap nuclear localisation.

To quantify the nuclear/cytoplasmic ratio, I followed the strategy outlined in Figure 6.8. Using the Sox9 mesenchymal staining as guidance to where the cushion

was (based on the knowledge that Sox9 is initially expressed in a subpopulation of the whole cushion), I manually drew an ROI around the region of high relatively uniform (albeit mosaic) Sox9-positive nuclei. With the ROI extracted, I deployed my StarDist deep-learning model (as detailed in §§5.2.3 above) on the DAPI channel to obtain a nuclear mask (Figure 6.8A). With the mask selected in the YAP channel, I calculated the MFI of the YAP intensity within all the nuclei (Figure 6.8B). To quantify the cytoplasmic YAP signal, I developed the following procedure. I thresholded the YAP channel for the whole image (using the built-in local contrast filter “Otsu” in Fiji) (Figure 6.8C) and used the result to segment the image for all the YAP fluorescence in the ROI (Figure 6.8D) from which the nuclear mask areas were subtracted. MFI of the (Total YAP-positive areal)-(nuclear YAP-positive area) was then taken as the cytoplasmic signal. This procedure took into account that the cushion structure is filled with cardiac jelly between the mesenchymal cells and such cell-free tissue had to be excluded.

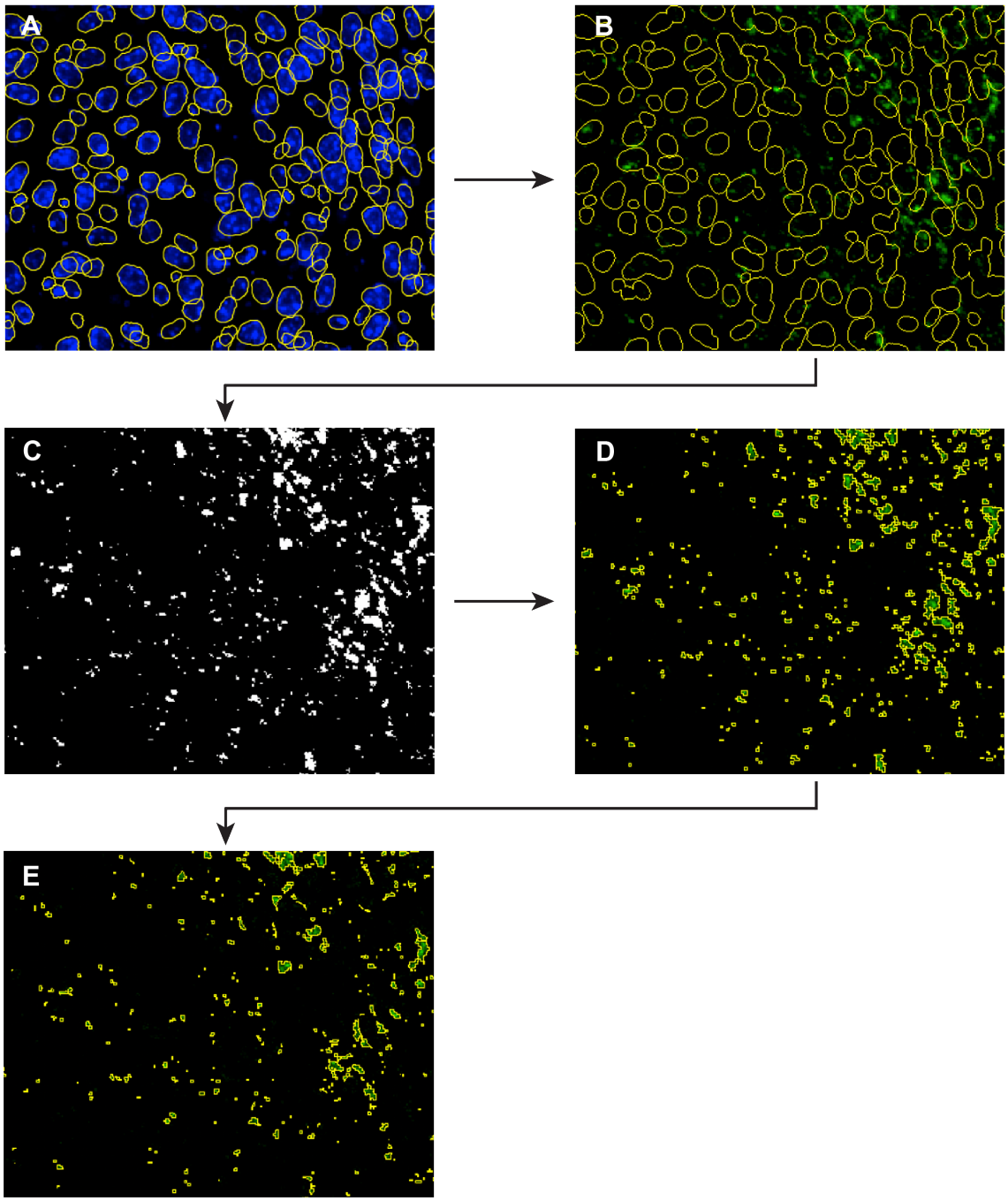

Figure 6.8 Pipeline of YAP nuclear/cytoplasmic ratio analysis in immunofluorescence images in FIJI. (A) DAPI nuclear masks applied after using Sox9 to outline tissue and StarDist for nuclear segmentation. (B) Nuclear mask on the YAP channel. (C) Thresholded YAP channel. (D) Combination of all YAP signals as a mask (yellow outline). (E) Subtraction of nuclear mask from YAP signal mask.

6.2.5 YAP expression in Dp1Tyb outflow tract cushions

The nuclear/cytoplasmic ratio of YAP fluorescence intensity was found to be significantly lower in the distal OFTC of the Dp1Tyb embryos (Figure 6.9A) using the image analysis pipeline described above. This result indicated that there is less nuclear localisation specifically in the distal Dp1Tyb OFTC compared to the wild-type. In the medial (Figure 6.9B) and the proximal (Figure 6.9C) OFTCs, there was no differential nuclear/cytoplasmic YAP MFI between the two genotypes. When the 3 section levels were averaged for each sample (Figure 6.9D) there were no statistical differences in either analysis.

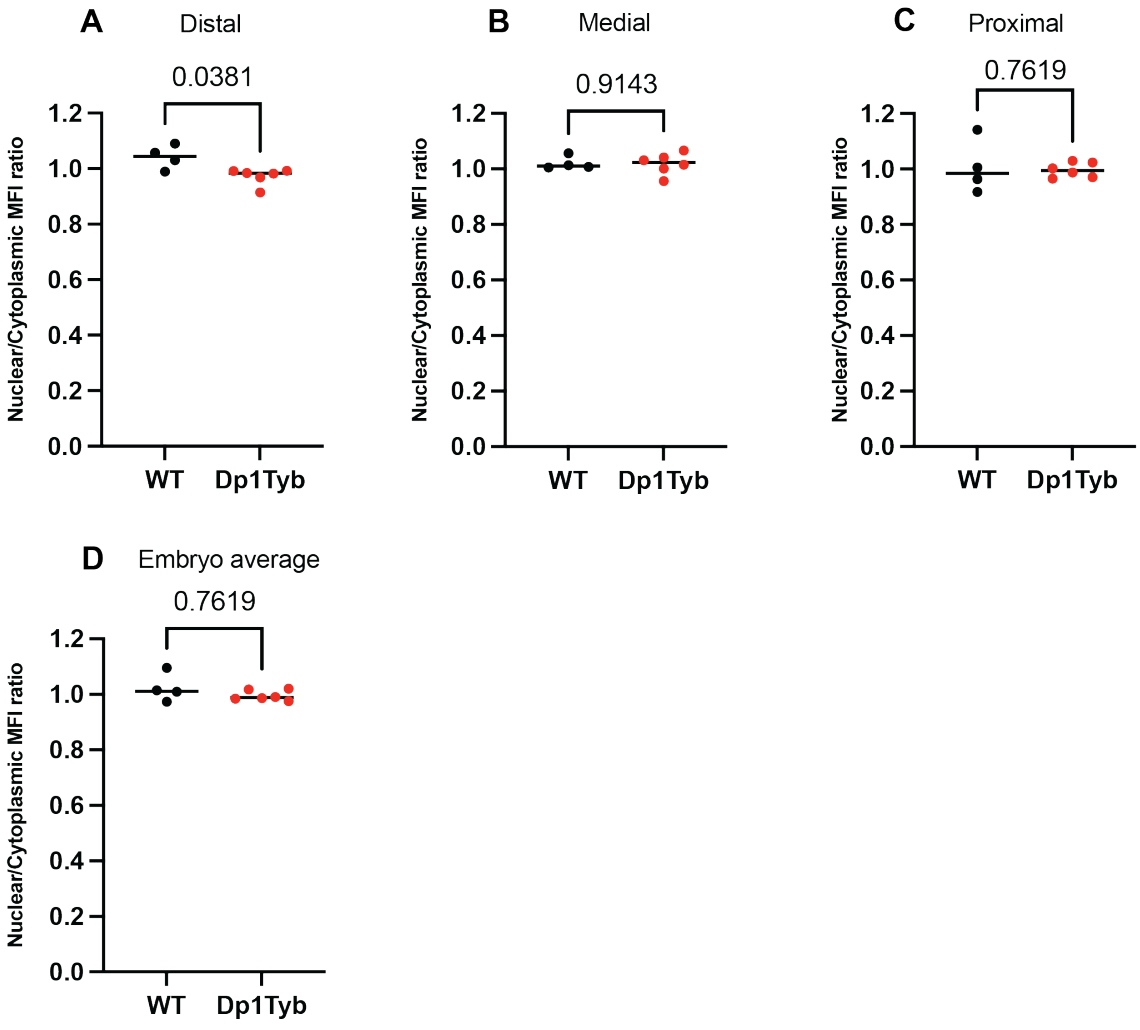

Figure 6.9 Nuclear to cytoplasmic ratio of YAP signal in the outflow tract cushions of E12.5 Dp1Tyb and wild-type embryos. (A) Distal outflow tract cushion nuclear/cytoplasmic ratio. (B) Medial outflow tract cushion nuclear/cytoplasmic ratio. (C) Proximal outflow tract cushion nuclear/cytoplasmic ratio. (D) Average of the distal, medial and proximal outflow tract cushion nuclear/cytoplasmic ratios in for each embryo.

Line in data shows mean; statistical analysis: Mann Whitney-U test. Distal: wild-type n = 4, Dp1Tyb n = 5; medial: wild-type n = 4, Dp1Tyb n = 6; proximal: wild-type n = 4, Dp1Tyb = 6; combined: wild-type n = 4, Dp1Tyb n = 6.

The same analysis was repeated for the next stage (E13.5). Here, the reduced YAP nuclear translocation seen in Dp1Tyb hearts from the previous day is no longer present in the same region at E13.5 (Figure 6.10A). Similarly, there were no changes in the intensity of YAP intensity ratios in either cellular compartment in the medial (figure 6.10B) and proximal (Figure 6.10C) sections. There were no significant differences found in the analysis of the combined average across each sample (Figure 6.10D). These results were somewhat surprising given the well-distributed proliferative differences (with Dp1Tyb samples consistently lower) identified in E13.5 cushions (§§5.2.8). This suggests that YAP may not be the pathway implicated in the proliferation defect identified in the Dp1Tyb OFTCs.

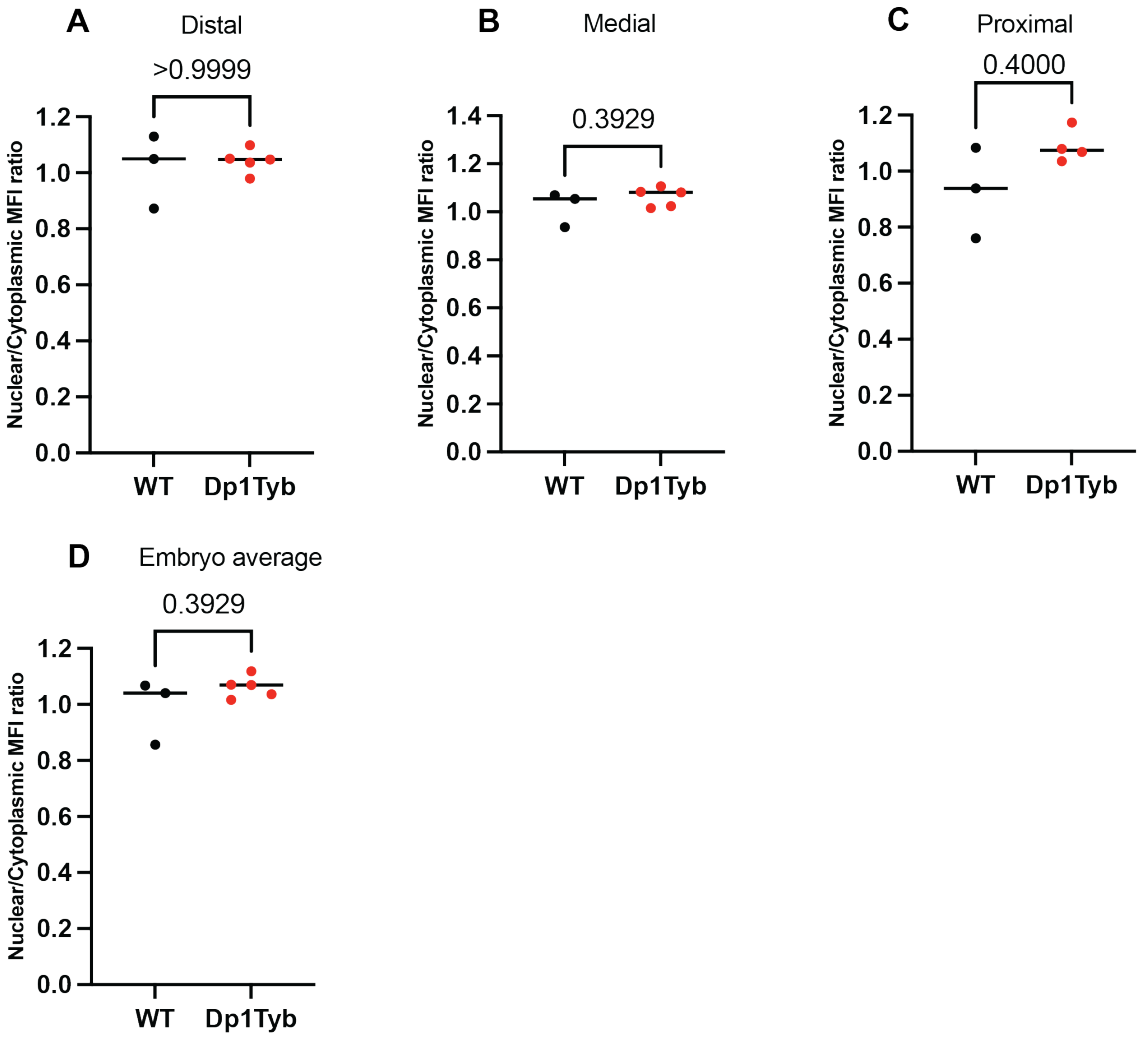

Figure 6.10 Nuclear to cytoplasmic ratio of YAP signal in the outflow tract cushions of E13.5 Dp1Tyb and wild-type embryos. (A) Distal outflow tract cushion nuclear/cytoplasmic ratio. (B) Medial outflow tract cushion nuclear/cytoplasmic ratio. (C) Proximal outflow tract cushion nuclear/cytoplasmic ratio. (D) Average of the distal, medial and proximal outflow tract cushion nuclear/cytoplasmic ratios in each embryo. Line in data shows mean; statistical analysis: Mann Whitney-U test. Distal: wild-type n = 3, Dp1Tyb n = 5; medial: wild-type n = 3, Dp1Tyb n = 5; proximal: wild-type n = 3, Dp1Tyb = 4 combined: wild-type n = 3, Dp1Tyb n = 5.

6.3 Discussion

In this chapter, I investigated two aspects of mechanics the OFTCs of Dp1Tyb embryonic hearts at E12.5 and E13.5, measuring material stiffness using AFM and nuclear localisation of YAP using immunofluorescence microscopy.

6.3.1 Outflow tract cushion stiffness

Here I attempted to characterise the material stiffness of Dp1Tyb and wild-type OFTCs at two embryonic stages, E12.5 and E13.5. Due to the need to develop the protocol for this work and the limited time available for this study, it was possible to examine only a very small number of specimens with what was likely a sub-optimal selection of test parameters. I therefore take the results to be highly preliminary and purely exploratory, but as potentially providing a useful pilot for a more thorough and convincing set of future experiments.

The data indicated that there was no change in the material stiffness of the mutant samples at either stage in both the proximal and distal cushions or when the data was combined. As this was an unexplored territory with very little literature on the material stiffness of embryonic mouse OFTCs, there were no expectations of what the results would look like other than the broad expected range of Young's Modulus. This was based on the two previously mentioned AFM studies of the stiffness in the embryonic left ventricles at E13.5, where there were two expectations: firstly, that cushion tissue that is filled with ECM will be less stiff than the myocardium of the left ventricle at the same stage (reported between 10-30 kPa) and secondly, the embryo will likely be stiffer at E13.5 than E12.5.

At E12.5, the distribution of Young's moduli initially indicated that there was possibly a small shift to higher (i.e. stiffer) values in the proximal cushions, but this may be the result of a highly spread set of data that varied from sample to sample. In the distal cushion, there was one potentially anomalous sample from the Dp1Tyb. This particular sample had maximum Young's Modulus of over 12 kPa which departed from the ranges seen in all other samples across genotype and stage. I hypothesise that instead of the cushion being tested here, the grid was placed on the myocardium (i.e. the OFT wall) instead of the cushion mesenchyme as the values were similar to the reported stiffness (10-30 kPa) of the left ventricle at E13.5 (van

der Loo *et al.*, 2008; Jacot *et al.*, 2010). During the acquisition of data, we endeavoured to pick areas within the middle of the tissue, but this was occasionally difficult for the probe to access as some samples did not have an even surface from the dissection. Additionally, the E12.5 data set struggled with a low number of samples in either genotype, this was in part due to time constraints for the actual experiment and loss of samples due to low adhesion to the dish. This prevented any meaningful statistics from being performed on the proximal and distal data sets.

AFM of the E13.5 OFTC was performed after the E12.5 samples, where there was better adhesion of the cushion samples to the Cell-Tak coated dishes during tissue preparation. More successful adhesion of the tissue was a result of aspirating any excess PBS around the tissue once placed on the Cell-Tak. This translated to the loss of only one tissue sample (a Dp1Tyb proximal cushion, S2) and a more consistent acquisition of data. Ultimately, the data did not show any significant changes in either proximal or distal cushions or when combined. Interestingly, when comparing the two embryonic stages it appeared that the median of E12.5 Young's Moduli is lower than at E13.5 in both genotypes which perhaps confirms that the cushions also become progressively more stiff as the embryo develops and the structures mature.

An additional caveat to the AFM data is that both E12.5 and E13.5 samples were derived from one litter each.

Given that this was the first foray into the material properties of the cushion, other parameters should be trialled to improve consistency and yield results more relevant to the length-scales likely to affect septation. Perhaps most obvious key parameters are the size of the AFM bead and that of sampling grid. The bead was 5 μm in diameter, which means an indentation of roughly 1 μm. The sampling grid was 10 μm x 10 μm, which is likely too small to capture the broader stiffness of a region and runs into the possibility of measuring the stiffness of specific cells instead of regions of the sample tissue. The size of the sampling grid was chosen due to the size of the tissue, as it would have been difficult to find two non-overlapping regions of OFTC that did not include the myocardial border within the grid. In comparison, Jacot and colleagues (2010), who performed one of the embryonic left ventricle AFM studies, indented 7 regions spaced 10 μm apart and obtained 7 force-curves as a result. While the spacing in that study is likely to be more representative of the whole tissue, far fewer force curves were generated.

Further optimisations could include trialling frozen sections of embryonic tissue for a more consistent topology for the AFM probe and control of where the sampling grid is placed on the anatomy. The usage of frozen tissue is well documented in AFM (Shen *et al.*, 2020; Peña *et al.*, 2022) and would allow for the acquisition of larger numbers of samples as cryosectioned OFTCs could be kept and stored until needed. On the other hand, however careful the freezing procedure, there is always a risk that a freeze-thaw cycle could alter the material stiffness and so would have to be carefully validated/controlled by making measurements before and after freeze-thaw on at least some of the same samples.

The mechanical properties of cardiac tissue and structures during heart morphogenesis have been shown to the important for processes like cardiac differentiation, which mesenchymal cells in the OFTC are undergoing during the septation process. For example, the stiffening of the cardiac matrix during heart tube formation has been suggested as the origin of coordinated cardiac myocyte beating (Wei *et al.*, 2001; Majkut *et al.,* 2014). Additionally, it has also been shown that the hardening of the cardiac matrix modifies the morphology and growth of myocytes in vitro (Pandey *et al.*, 2018). The cardiac matrix consists of many differing types of ECM where their relative abundances and arrangements can inform the stiffness of a structure. ECM architecture and its impact on the material properties of the OFTC in the Dp1Tyb is currently unknown, how this can be further explored will be detailed in the general discussion. The technical limitations of AFM in this will also be touched upon in the general discussion, as well as alternative methods for investigating the material properties of the OFTC.

6.3.2 YAP nuclear localisation

Generally, the data showed that there was no statistical change in the nuclear to cytoplasmic ratio of YAP in the OFTC of the Dp1Tyb embryonic hearts except for in the distal Dp1Tyb embryo OFTC at E12.5 where there was more YAP in the nucleus than in the wild-type embryos. This was consistent with my findings that this part of the anatomy was morphologically different in the Dp1Tyb embryos, having delayed distal OFTC fusion and OFT septation (§§ 4.2.1). The possible impacts of this result will be discussed further in the chapter. Though there were no statistically significant

differences in the nuclear localisation of YAP in the medial and proximal Dp1Tyb OFTCs compared to wild-type, both the embryo average and pooled sections showed a trend of lower nuclear/cytoplasmic YAP concentration ratios. More samples would be needed to be assessed to determine whether this is experimental noise or not. A power calculation indicates that a minimum of 11 samples per genotype should be used to reveal any real differences.

In the E13.5 Dp1Tyb cushions, there were no significant changes in any of the anatomical regions of the OFTC or when the data was pooled. This data set also had fewer embryos in each genotype for comparison and had a larger spread of ratios in the wild-type, so any patterns or trends would not be discernible here and the data set would benefit from more embryos added.

Condensation of the cushion mesenchyme in the distal OFTCs of the septal and parietal OFTC involves apoptosis among other cell behaviours. This was noted in §§5.2.2 where I had seen cell debris in areas of condensed mesenchyme in the OFTC as had Sharma and colleagues (2004) who noted programmed cell death in regions of septation in the mouse heart. YAP is a known regulator of apoptosis through the Hippo pathway during development where it is a downstream effector in the pathway, although it has more been associated with the control of organ size (Cheng *et al.*, 2022). Additionally, YAP is implicated in cellular differentiation through Hippo, a process that is essential in the distal OFTC during OFT septation to form a myocardial bridge to separate the arterial trunk. In particular, YAP and its co-effector TAZ have been shown to influence the cell fate of mesenchymal stem cells through mechanotransduction, for example, cells on a stiffer matrix induced YAP/TAZ nuclear localisation and drive differentiation into osteoblasts but mesenchymal stem cells on a softer matrix encourages differentiation into adipocytes (Dupont *et al.*, 2011). Thus, given the versatility of YAP, even a clear-cut difference in its localisation in Dp1Tyb embryos compared to that in wild-type embryos would have required further experiments to distinguish apoptotic from mechanotransducing roles.

Overall, due to the limited sample numbers and the absence of dramatic genotype-dependent differences in either material properties or in YAP localisation, the studies in this chapter must be taken, more than anything else, as feasibility studies for the approaches taken. Potential routes for follow-up will be discussed in more detail in the General Discussion in the next chapter.

Chapter 7. General discussion

7.1 Overview of key findings

This project was an investigation into the failure of ventricular septation in DS using the DS mouse model Dp1Tyb, initially focusing on the closure of the IVC and muscular septum growth which was initially intended to be followed by characterising these cellular processes using the PROMASS framework (Green, 2022). With this outline of the project, my first step was to characterise the embryonic stages between the start and the end of ventricular septation. This time frame is often described as E11.5 to E14.5, where at E14.5 septation should be complete (Krishnan *et al.,* 2014). E14.5 was also the stage at which the Tybulewicz lab had established that 62% of Dp1Tyb embryos had a type of CHD (Lana-Elola *et al.*, 2016).

Initially hypothesising that some embryos may fail ventricular septation due to defective growth of the mVS, I collected wild-type and Dp1Tyb embryos from E10.5 to E13.5 to ensure I captured all the stages leading up to ventricular septation to characterise the changing morphology of the mVS during this period. As so many changes occur during a relatively short period, I created a temporally resolved developmental timeline of this process by assigning a more precise embryonic age using limb-bud morphogenesis. This not only provided a comprehensive timeline of ventricular septation but also ensured any differences between the two groups could be attributed to genotype rather than the natural variation in developmental ages within a litter. Additionally, staging the embryos this way meant that dysmorphology phenotypes could be distinguished from a developmental delay phenotype. Embryos between the stages E10.5 to E13.5 were sectioned for HREM and reconstructed in 3D to measure the size and closure of the IVC and the length of the mVS (Chapter 3). Surprisingly, no differences were found in the size and shape of the IVC or length of the muscular septum of the Dp1Tyb embryos and controls at any age investigated. This suggested that failure of ventricular septation was likely not due to deficits in the overall growth of the mVS towards the ventricular septation junction.

Following on from this finding, I turned to look at the other components crucial to ventricular septation: the endocardial cushions. There are two sets of cushions, the OFTCs and the AVCs, and I decided to focus on the OFTCs as they are the first set of endocardial cushions to contact and fuse to the muscular septum at E12.5

(Mohun and Anderson, 2020; Anderson *et al.*, 2023). In addition to this, some of the CHDs identified in the Dp1Tyb at E14.5 are OFT defects which suggested that the development of the OFT is affected in the mutant. Using the HREM dataset I had collected, I began characterising the morphology of the OFTCs of Dp1Tyb and wild-type hearts at E12.5 and E13.5 (Chapter 4). I selected these two stages as the ones immediately preceding the previously reported septal phenotype. During these stages the OFTCs undergo complex remodelling of their shapes. They begin to fuse to achieve septation of the distal OFT into the two arterial vessels at E12.5. Concurrent with that process, part of the proximal septal OFTC is fusing with mVS to narrow the IVC and restrict it to the posterior of the heart. I segmented the cushions (defined as less bright regions) from the HREM data sets at these two stages and measured their dimensions and volumes. At E13.5, I found that the fused OFTC of the Dp1Tyb embryos were significantly smaller than those in wild-type controls (Figure 4.11A). To determine if this was an overall shrinkage of the structure or if volume reduction was localised to specific regions of the Dp1Tyb cushion, I adapted a land-mark free morphometrics pipeline previously developed and used for Dp1Tyb crania (Toussaint *et al.*, 2021). My analysis showed that the proximal region of the Dp1Tyb OFTC was the most affected, with most of the volume changes taking place in that specific anatomy (Figure 4.20).

To understand which cellular processes were driving changes in morphology at E12.5 and E13.5, I used two elements of the PROMASS framework to begin my investigation – proliferation and apoptosis (Chapter 5). Dp1Tyb hearts had shown a proliferation defect (reduction) through both a scRNA-sequencing cell cycle signature and flow cytometry of cell cycle stages (Lana-Elola *et al.*, 2023). Apoptosis is also a key process in the development of the OFT, with programmed cell death occurring in the fusion of the OFTC and the septation of the OFT (Sharma *et al.*, 2004). I carried out a thorough characterisation of these processes through immunofluorescence staining for apoptosis and proliferation in serial sections of Dp1Tyb and wild-type embryos through the entire cushion, distinguishing the distal, medial and proximal regions. I took advantage of new and improved computational methods of nuclear image segmentation in these experiments, deploying a neural network trained on my own manually-generated dataset using StarDist to automate the process. This showed that Dp1Tyb OFTCs at both E12.5 and E13.5 had reduced cell density throughout. Surprisingly, and in apparent contradiction to the HREM data,

the proximal region of the Dp1Tyb OFTC occupied a significantly larger cross-sectional area than that in the wild-type controls at comparable proximodistal locations. Despite more cells in this region of the Dp1Tyb sections, the cell density remained lower, suggesting there was more ECM in the proximal regions of the Dp1Tyb cushions. Lastly, there were fewer proliferating cells (as measured by the number of PHH3-positive cells) in the OFTC of Dp1Tyb embryos at E13.5. The reduced-proliferation phenotype also appeared restricted to the proximal half of the cushion. Together, this data suggests Dp1Tyb OFTC are not only dysmorphic but have a reduced cell density and lower rates of proliferation, with the proximal region of the structure being specifically impacted. As these phenotypes are found in the OFTC structure in the stages during OFT septation and prior to ventricular septation, it is likely that these defects contribute to the failure of these processes to occur properly in the majority of Dp1Tyb hearts.

Finally, I explored what the above phenotypes could mean for the material properties of the Dp1Tyb cushions and if signalling of YAP, a mechanosensitive protein linked to proliferation and remodelling of the OFTC in valvulogenesis (Wang *et al.*, 2023), was affected (Chapter 6). To investigate the material properties in the Dp1Tyb cushions at E12.5 and E13.5, I trialled the use of AFM on my samples, which may be the first example of AFM on fresh dissections of OFTCs. Despite considerable technical difficulties in setting up the experiments and the limitations of the technique, I was able to acquire very preliminary data on the stiffness of the distal and proximal regions of the OFTCs in both genotypes but found no statistically significant stiffness differences between Dp1Tyb and wild-type embryo tissue. In my investigation of YAP nuclear translocation in Dp1Tyb OFTCs at the same two stages, I used immunofluorescence staining and StarDist nuclear segmentation to measure the ratio of nuclear-to-cytoplasmic YAP fluorescence. I found that the distal region of E12.5 Dp1Tyb OFTCs showed a reduction of YAP nuclear-to-cytoplasmic ratio. Despite the low sample number, these experiments served as a potentially useful pilot from which more thorough investigations can be launched. Potential routes for follow-up experiments will be discussed in the Future Directions section of this chapter.

7.2 Interpretation of the Dp1Tyb outflow tract cushion phenotypes

This thesis presents three key findings regarding the OFTC phenotype which will be discussed in detail separately below in the context of wider research and its implications for our understanding of complete cardiogenesis. The key findings are as follows:

1. The OFTCs of Dp1Tyb embryos are dysmorphic at key time points of ventricular septation.
2. Dp1Tyb OFTCs show a defect in the number of proliferating cells that appear to be restricted to the proximal regions of the structure.
3. Cell density is reduced in the OFTCs.

Broadly, these findings paint a picture of the Dp1Tyb embryos possessing atypical OFTC structure and cellularisation. Here I hypothesise that this OFTC cushion phenotype in the mutant impacts both the proper ventricular septation process and OFT septation resulting in the VSDs and OFT defects identified in the Dp1Tyb embryos at E14.5 (Lana-Elola *et al.*, 2016).

7.2.1 Dysmorphology of the Dp1Tyb outflow tract cushions

In this thesis, the OFTCs of Dp1Tyb embryos were found to be dysmorphic in two different measurements. First, in Chapter 4, the Dp1Tyb OFTCs were seemingly delayed in fusing to one another at E12.5 which may delay the septation of the OFT into the pulmonary artery and the aorta, where a common arterial trunk was still present at the distal OFT. At the next stage at E13.5, the now-fused OFTC of Dp1Tyb embryos were volumetrically smaller than their wild-type littermates. Quantitative morphometrics of these OFTC shapes indicated that volumetric decrease in the Dp1Tyb embryos was mostly localised to the proximal region of the cushion with a recessed surface compared to controls. This was a particularly interesting finding, as the proximal cushions forms a part of the membranous ventricular septum. Secondly, in the cellular characterisation of the OFTCs in Chapter 5, it was discovered that the proximal cross-sections of E13.5 OFTCs were significantly larger than comparable sections of wild-type embryos. Taken together, these findings present the Dp1Tyb

OFTC cushions as atypical in morphology which is likely to impact the ventricular and OFT septation process, therefore likely contributing to CHD phenotypes in the mutant.

My HREM-based analysis of Dp1Tyb OFTC showing it to be smaller in Dp1Tyb embryos than in controls at E13.5 (Chapter 4, Figure 4.11) would seem to be at odds with the Sox9-staining-based larger cross-sectional area of the proximal region of Dp1Tyb cushion at the same stage (Chapter 5, Figure 5.15). This discrepancy is presumably to do with the different measurement methods. The HREM data were based on pixel values of differential penetration of fluorescent embedding resin. At the stage, the cushion is still ECM-rich and less dense than the surrounding myocardium, so the cushion stained less brightly than condensed myocardium. The area of Sox9-positive cells, marks where the mesenchymal cellular population of the cushion ends and the myocardium starts.

The Sox9 staining enabled visualisation of the clear boundary of the mesenchymal cells of the cushion which probably extends further than the areas of cushion registered in the HREM. As this discrepancy is in the proximal regions of the Dp1Tyb cushions, the Sox9 staining could show an area of mesenchymal cells in the proximal cushion that on the HREM does not appear to have the same density as the rest of the OFTC. Therefore in the Dp1Tyb hearts, it was not segmented out in 3D as it appeared brighter like the myocardium. This translated to a smaller volume with a recessed proximal area in the Dp1Tyb mice, but not the wild-type. It is tempting to speculate that perhaps how this region of tissue stains for HREM (yet is clearly mesenchymal cushion in the Sox9-staining) may be reflective of different material properties in the region. It should also be considered that perhaps the morphological differences seen in the Dp1Tyb cushions do not impact septation and therefore not causal to the identified CHDs, but the material properties of the structure may prevent proper septation from taking place. This is discussed further below in the chapter after the consideration of morphological phenotype.

Nevertheless, if the proximal OFTCs are dysmorphic as shown they could contribute to the failure of VSDs in multiple ways. As the data in §§4.2.4 shows that the proximal cushions were recessed in the Dp1Tyb, the OFTC may not extend proximal enough into IVC to make full contact with the mVS, which at this point will have grown cranially to meet the OFTC. Alternatively, instead of the OFTC of the Dp1Tyb embryos not extending proximally enough to fully fuse with the mVS, it could

be that the positioning of the cushion is causing a misalignment of the structures resulting in the failure of proper septation. For instance, if the Dp1Tyb cushions were to sit more posterior in relation to the top of the mVS, the fusion of the mVS with the proximal OFT may fail to form a continuous septal structure. While there does not appear to be any literature on the positioning of the OFTCs in relation to the muscular septum for ventricular septation, there is evidence to suggest that the positioning of the OFT cushions is required for correct OFT septation (Henderson, Eley and Chaudhry, 2020). At a more granular scale, several pathways are involved in the positioning of the OFTC, for example, BMP signalling and the interaction between several Tbx transcription factors and Notch signalling (O'Donnell and Yutzey, 2020). Disruption of BMP signalling has been shown to result in CHDs such as VSDs and DORV, the latter of which is a structural outflow positioning defect (Wang *et al.*, 2011).

It may be that the positioning of the OFTCs in the Dp1Tyb is not only affected by its morphology but perhaps the implication of the CNCCs that contribute to its development. Aside from being involved in the positioning of the OFTCs, the CNCC are an important progenitor population for the proper development of the OFT. It is well documented that the CNCC are essential for the remodelling of the OFTC and septating the OFT, as evidenced by many neurocristopathies sharing a common phenotype of OFT defects (Keyte and Hutson, 2008). It has also been suggested that DS should be counted as a neurocristopathy due to the localisation of some DS phenotypes, notably the CHDs and craniofacial dysmorphology which is also found among other neurocristopathies. There is some evidence to suggest that the neural crest are important in the pathogenesis of DS phenotypes through studies conducted in two different mouse models of DS. First, Roper and colleagues (2009) showed that neural crest in the Ts65Dn mice was deficient in delamination, migration and mitosis, likely through an altered response to Shh. However, a caveat of this study is the presence of extra Hs21-non-syntenic genes in the Ts65Dn mouse (discussed in detail in §§1.1.4 above). More recently, Redhead and colleagues (2023) demonstrated in the Dp1Tyb mice that cranial neural crest cells were not deficient in migration to the cranial region, but were proliferatively defective once at their destination, resulting in hypoplastic neural crest-derived craniofacial bones. In addition to this, in vitro studies of human induced pluripotent stem cells with trisomy 21 showed a migratory but not proliferation defect when the cells were differentiated

in to neural crest (Liu *et al.*, 2022). It is plausible that a similar phenotype may be found in the CNCC of Dp1Tyb mice, I have outlined some follow-up experiments for CNCC in §§7.4.6 of the future directions of this project.

On the other hand, while the CNCC may be involved in some of the cardiac defects observed in the Dp1Tyb mice, it cannot be the basis for all the cardiac phenotypes. The Dp1Tyb mice also form AVSDs with a common atrioventricular valve, which are not derived from CNCCs. As I will discuss in §§7.4.8 of this chapter, the AVCs of Dp1Tyb embryos also have the same phenotypes as described in this thesis in the OFTC. It may be that there are indeed deficits in migration and/or proliferation of the CNCC as was observed in the cranial neural crest, but only in addition to defects in other progenitor populations and/or dysregulated pathways from increased gene dosage in trisomy 21.

7.2.2 Reduced proliferation in the Dp1Tyb outflow tract cushions

The second key finding of my thesis is a reduction in the number and proportion of mitotic cells in the Dp1Tyb OFTCs in the proximal half of the structure (Chapter 5, Figure 5.21). This was a particularly interesting find as it mirrors work carried out by other members of the lab in other tissues in this model. As mentioned above, a proliferation defect was identified in the neural crest-derived craniofacial regions of the Dp1Tyb mice (Redhead *et al.*, 2023). scRNA-sequencing of E13.5 Dp1Tyb hearts revealed downregulation of genes implicated in proliferation compared to wild-type levels (Lana-Elola *et al.*, 2023). The same study also showed this defect through flow cytometry, where an increased proportion of cardiomyocytes and endocardial cells from Dp1Tyb hearts were found to be in G1 and decreased in S-phase, indicating a reduced proliferation. This was also shown to be partially regulated through Dyrk1a, where the reduction of *Dyrk1a* back to 2 copies partially rescued these proliferation deficits. It is not yet known whether the proliferation defect in the OFTCs identified in this thesis is also Dyrk1a-dependent and if so how Dyrk1a would reduce proliferation.

It is unclear how the reduction in proliferating cells in the OFTC of Dp1Tyb hearts could affect ventricular or OFT septation. One possibility is that reduced proliferation within the OFTC results in a change in the morphology of the structure.

This may fit with this data as the proximal region of Dp1Tyb cushions have lower rates of proliferation which coincides with where I identified localised reduction of cell density (see next section below) and dysmorphology of the OFTC. However, this would be more likely if the proliferation defect were found in the proximal region of the OFTC in Dp1Tyb hearts in the stage prior (at E12.5) to influence a morphological change in the shape of the cushion, but there was no identifiable proliferation phenotype at E12.5. Alternatively, the proliferation could be independent of or incidental to the difference in morphology between the genotypes, with the morphological difference being caused by changes in ECM production, cell movement/condensation. It is also not unlikely that dividing cells are less able to make ECM, differentiate, or move and condense, than non-proliferating ones.

Multiple pathways have been associated with proliferation within the cushion mesenchyme. For example, VEGF and FGF4 play important roles in driving the proliferation of the cushion mesenchyme (Dor *et al.*, 2001; Sugi *et al.*, 2003), whereas EGF and Jag1, a Notch ligand, are negative regulators of proliferation (Chen *et al.*, 2000; MacGrogan *et al.*, 2016). Interestingly, mice that are hypomorphic for the EGF receptor show increased numbers of cushion mesenchymal cells and enlarged cushions, which is similar to the observations of the increased section area and cell number made in Chapter 5 (Chen *et al.,* 2000). A further consequence of the reduction in cell proliferation within the cushion is a reduction in cellular density of the structure, which was observed at both E13.5 and E12.5, this is further discussed below.

7.2.3 Lower cell packing density in Dp1Tyb outflow tract cushions

Finally, the last key finding of this research showed that there was a reduction in cell density at both E12.5 and E13.5. As shown in §§5.2.4 (Figures 5.10-11), there is a reduction in cell packing density of the Dp1Tyb cushion at both stages throughout the entire structure. This was further confirmed in the E13.5 Dp1Tyb embryos where there was significantly increased nuclear spacing between the individual nuclei. This metric indicated that the reduced cell density phenotype is not an artefact of pockets of acellular areas in the cushion, but that the cells are consistently spaced further apart within the cushions in the mutant. This phenotype implies that if in the Dp1Tyb

hearts there are fewer cells in the structure occupying a similar area, or, in the case of the E13.5 Dp1Tyb cushions, there is a much larger proximal area and more cells but still less cellularly dense, then there is more ECM.

ECM is an important component of both sets of endocardial cushions, where they begin as acellular swellings of the inner heart tube. These spaces become progressively cellularised by EndoMT and migratory populations, where the cushion mesenchyme grows in number through the proliferation of these populations, but remaining an ECM-rich structure until myocardialisation and differentiation of these populations during septation (van den Hoff and Wessels, 2020). The cardiac ECM within the cushions are made up of both fibrillary and non-fibrillary ECM proteins, examples of fibrillary ECM proteins are certain types of collagens and fibronectin whereas non-fibrillary ECM proteins found in the cushions are hyaluronic acid (HA) and proteoglycans such as versicans (Silva *et al.*, 2021). While there are a myriad of different ECM proteins that could be explored and discussed, two particular ECM proteins seem likely to be particularly pertinent to this project: versican and collagen type VI.

Versican is an ECM protein that is abundant in all four of its variants (V_0-V_3) throughout cardiogenesis in different structures, it is particularly highly expressed in the endocardial cushions. It has been shown that the proteolysis of versican through ADAMTS and matrix metalloproteinases is needed for proper remodelling of the proximal OFT into the arterial vessels, a process which determines proper OFT patterning and is implicated in ventricular septation (Kern *et al.,* 2006). Perhaps more interestingly, versican deposition was found to be affected by increased expression of RUNX1, which maps to Hsa21, in trisomic foetal fibroblasts (Mollo *et al.*, 2022). It is possible that in the Dp1Tyb, the increased gene dosage of RUNX1 leads to more versican in the OFTCs, leading to decreased cell density and affecting OFT remodelling.

In the same study of foetal fibroblasts trisomy 21, RUNX1 was also found to dose-dependently upregulate different types of collagens, amongst which was collagen VI, where 2 of its 3 subunits are encoded on Hsa21 (Mollo *et al.*, 2022). Additionally, DSCAM (also located on Hsa21 and Mmu16) interacts with COL6A2 (on Hsa21 but Mmu10), a gene encoding one of the subunits (Grossman *et al.*, 2011). DSCAM and COL6A2 are both important to proper heart formation and chamber septation, with transgenic mice that overexpress both genes found to have a litany

of CHDS including AVSDs, VSDs and TOF (Grossman *et al.*, 2011). More specifically, more collagen VI was found in the endocardial cushions of human foetal hearts with DS compared to foetal hearts at the same stage (Gittenberger-De Groot *et al.*, 2003). Fibrillar collagens are also found to be upregulated in transcriptomic data of human DS foetal hearts, these include collagen types I, III, V, XIII (Conti *et al.*, 2007). Fibrillar collagens provide the framework for three-dimensional tissue structure, some collagens (e.g. collagen type XIII) are also able to cross-link and modulate the stiffness of tissue structure.

So far, there has been no thorough investigation into the different types of ECM within the Dp1Tyb OFTCs and the relative deposition of different ECM proteins compared to wild-type mice. As mentioned above, multiple types of ECM proteins are found to be upregulated in human DS foetal hearts (Conti *et al.*, 2007), with some fibrillar ECM proteins that are implicated in modulating the material stiffness of a tissue. This provides some evidence that further exploration of the material properties of the OFTCs, beyond the preliminary AFM work conducted in this thesis, is warranted in the Dp1Tyb. I will outline some future experiments that could be conducted to start characterising this aspect of cushion development.

Another consideration is that since there is a reduction in cell density at both E12.5 and E13.5 Dp1Tyb OFTCs, the OFTCs may have been deficient in cellularisation of the cushions, which begins earlier in development (around E9.5). As described previously, the OFTCs are populated primarily by cells from two progenitor populations: the SHF and the CNCC. However, it has not yet been described in the Dp1Tyb mice the percentage of cells within the OFTC that can be traced to a CNCC origin or SHF. Both progenitor populations are essential in the septation of the OFT and the ventricular septation, where it has long been shown that loss or deficiency in CNCC is associated with failure of OFT septation (Kirby *et al.*, 1983) and SHF field cells are also needed for septation of the OFT (Xu *et al.*, 2004). Further work is needed to identify the contributions of each progenitor population to the OFTC mesenchyme and whether this is affected in the Dp1Tyb mice. To add to this, a lineage tracing experiment would give answers on whether the reduction in cell density in the mutant is arising from one of the two lineages or if it is a global reduction in the structure. Such an experiment should also be linked to the proliferation defect discussed above, where the proliferation defect may be within

distinct cell lineages as suggested in the neural crest-derived craniofacial regions of the Dp1Tyb mice (Redhead *et al.*, 2023).

7.3 Limitations and caveats

Throughout this thesis, there were some techniques where I felt there were limitations to their use that should be considered alongside the interpretation of the data. Here I will discuss these concerns and, where appropriate, discuss alternatives.

7.3.1 Limb bud morphology and embryonic staging

As many morphological changes are happening in the heart at the stages of interest in this thesis, it was important to try and break down the traditional embryonic staging further for a thorough characterisation of these processes. While the limb bud morphology was undoubtedly a useful tool in achieving a finer temporal resolution for each embryonic stage than the nominal embryonic day, the technique does have some limitations. These are primarily to do with the user input, as the orientation of the image of the limb bud and the user-defined points can impact the outcome of the stage. Additionally, for older stages the $\chi^2\nu$ value, which describes the reliability of the age estimation, is expected to increase due to the higher variability of samples one's limb outline is compared to. This was a trend that I had noticed in the limbs I had staged, where the $\chi^2\nu$ value increased after E11.5, suggesting the reliability of the age estimate was decreased.

There are some alternatives to limb bud staging that could be used instead of it or in addition. As the majority of the HREM data sets that were used in this project included the embryo, the somites are visible in the images and could be counted for staging. Somite counting is commonly used from E7.5 when the somites appear and continue to increase until a final total of 60 somites at E14.0, but it is predominantly used between E8.0 and E10.5 as the 22 somites are added within that span so staging can be broken down to approximately 2.7-hour intervals during this period (Michos *et al.*, 2004). I did not use this method because the limitation of counting somites to stage embryos is that the number of stages decreases in later embryogenesis (Wong *et al.*, 2015).

Theiler staging could also be used as the whole embryo is captured with HREM. Theiler staging is a classical staging system that defines its time scale based on multiple morphological features (Theiler, 1972). To stage with Theiler's system, the morphology of multiple anatomical areas needs to be defined, these include the eyes, whiskers, epidermis and limbs. These characterisations are not only time-consuming to make, but are also mostly qualitative and prone to variation between individual researchers. In addition to this, there is evidence that the development of the mouse embryos is not synchronous across all tissues and organs, for example there is asynchronicity of left and right limb bud development (Boehm *et al.*, 2011).

There have been some developments in the creation of a 4D atlas of mouse embryo development for morphological staging. The creation of such an atlas was achieved by tracking the 3D trajectories of multiple anatomical points in E11.5 to E14.5 embryos, resulting in a resolution of 72 minutes (Wong *et al.*, 2015). As yet, there is no machine-learning staging system for mouse embryos using 3D data, but this has recently been developed for zebrafish embryos to astonishing accuracy (Pond *et al.*, 2021). This may one day be feasible for mouse embryos as advances in deep-learning image segmentation of multiple organs was described by Rolfe and colleagues (2023). Such a system could be used to compare the development of multiple organs within an embryo and between samples to ascertain if specific organs have a developmental delay as a phenotype.

7.3.2 Muscular septum and interventricular communication measurements

In the characterisation of the muscular septum length and the aperture of the IVC in Chapter 3, there were some limitations of the measurement technique, touched on in the chapter discussion. All of these measurements were conducted using the 3D reconstruction of each heart, digitally slicing through the anatomy and changing the oblique of the plane for the optimum section that could be used for measuring the anatomy. I attempted to maintain consistency by only taking measurements in planes where the mVS was at its most "solid" i.e. where there was the least amount of trabeculation. Though this technique is likely still more accurate than measuring from histological sections, where orientations cannot be changed. However, another researcher using the same data set may not choose the exact sample plane and

angle at which to take the same measurements. A more objective approach could be to further take advantage of the 3D aspect of the data set and segment the muscular septum from the bulboventricular groove to the crest of the mVS structure and measure its length by applying a bounding box to the mesh so there is no risk of an oblique measurement by place points on the 3D shapes.

The limitations of measuring the patency of the IVC were addressed in Chapter 3 (Figure 3.11-12) for E13.5 embryos where a single plane was inadequate to capture the foramen morphology. This was resolved through segmentation of the IVC and applying a centerline through the shape, then using a cross-sectional area analysis perpendicular to the centerline.

7.3.3 3D landmarking

After OFTC cushion segmentation for E13.5, the meshes generated needed to be registered to one another to be analysed in the land-mark free morphometrics pipeline described in Toussaint *et al.* (2021). As described in Chapter 4, the morphologies of the E13.5 OFTCs were very variable with few consistent landmarks in either genotype. While I was able to identify areas of the anatomy that I felt were consistent when looking through all the meshes to input into GeoMagic for the initial alignment, this may not be the same from user to user. After each alignment, I was careful to check in different orientations to confirm the alignment, but it was impossible to ensure perfect alignment with very inconsistently shaped structures. This was in part why I opted to add a second registration with WearCompare, where instead of single points for land-marking I could select regions with a paint-brush tool for alignment.

7.3.4 Atomic force microscopy

Using AFM to measure the material stiffness of embryonic tissue is a relatively new application of the technique. Very few embryonic organs and tissues have been tested for stiffness and as a result, there is no atlas of the ranges of stiffness for various embryonic tissues. For the heart, as discussed in Chapter 6, there was extremely limited literature on bio-AFM in embryonic heart tissue. While the results

obtained in Chapter 6 may be the first AFM measurements on freshly dissected OFTCs, this was an exploratory section of the project with multiple technical limitations and caveats to the results.

There are a few limitations to consider in the initial set-up of the tissue prior to AFM. The dissection of the OFTC and then bisecting it was a delicate process involving a very small structure; there was no guarantee that every embryo was dissected from the same area to free the OFT from the aortic sac and ventricles thereby ensuring that the exact same region of tissue was being measured, just that it was broadly the distal region and the proximal region. Additionally, once the distal and proximal regions were separated, there was some difficulty in getting them to remain adhered to the dish on the face at which they were bisected. This was a particular problem in the E12.5 data set in §§6.2.2 and resulted in the loss of many samples. There was better adherence of the tissue to the dish if it was allowed to rest on the Cell-Tak for longer, but despite being covered during this period there is a risk that the tissue would dry out which could impact its material properties.

In the acquisition of the data, some samples were challenging to find suitable regions to set the sampling grid, selecting from an already small area of the tissue (within the middle of the structure) to ensure that the mesenchyme was being sampled and not the myocardium. This was likely done once in the data set at E12.5. Due to it being manually dissected tissue, the cut surfaces varied in topology. Uneven surfaces made it harder to find suitable regions because the approaching cantilever had to be able to clear the surface of the tissue, if the cantilever was in contact with the tissue the force curve generated would not be accurate. Additionally, I believe that the experiment would have benefitted from using a larger bead and sampling grid to probe the tissue. The bead and sampling grid used in this thesis measured stiffness in very small (10 μm x 10 μm) regions, a larger bead and sampling grid would give a better measure of overall stiffness of the sample.

Finally, the process from harvesting the embryo to taking the measurements on the AFM took several hours, with the bulk of the time being waiting for the tissue to adhere to the Cell-Tak. It is possible that some of the tissue may have begun degenerating, but this was not apparent under the microscope. Regardless, it remains that the conditions in which the OFTC samples were probed were far removed from biological conditions.

Overall, the data obtained from performing AFM on Dp1Tyb and wild-type OFTCs was an interesting exploration of the material properties of the structure which has not been described in detail before, if at all. The data suffered from a low sample number and therefore could not provide meaningful conclusive data, but is a worthwhile avenue to pursue in the continuation of this project, as long as one is mindful of the caveats and can optimise the protocol to reduce issues such as variability in dissection or shortening the time from harvesting to probing. The future directions for measuring the material stiffness of the OFTCs, including AFM optimisation and alternative techniques will be discussed under “Future Directions” below.

7.4 Future directions

Many questions remain following the work presented in this thesis. Here I will present further experiments for the future of the project and what questions they could answer.

7.4.1 Typing heart defects at later embryonic stages

In the first characterisation of the CHDs found in the Dp1Tyb mouse hearts (Lana-Elola *et al.*, 2016), the defects were typed from embryos harvested at E14.5. While the literature indicates that chamber septation should be completed at this stage (Krishnan *et al.*, 2014), this thesis has shown and discussed that harvesting age is presumptive of conception at midnight and is not reflective of the embryo’s age when staged by other means. The data from Lana-Elola and colleagues (2016) shows that while there is a significantly larger proportion of Dp1Tyb embryos at E14.5 have CHDs compared to the control, the wild-type embryos also have a surprisingly high number of defects (Figure 7.1A). Possibly with a later stage harvest, this background level of CHDs would have been eliminated since many of the defects in the wild-type are perimembranous VSDs, which are typically very small foramen remaining at the posterior of the heart near the cardiac outlets. There is a possibility that the foramen would close and complete septation of the ventricles given an extra few hours of development. It is likely that this may eliminate some of the defects observed in the

Dp1Tyb model, as many “CHDs” observed such as VSDs and DORV could be incomplete septation and/or incomplete OFT rotation.

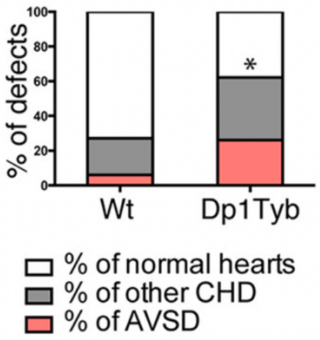

Figure 7.1 Percentages of Dp1Tyb and wild-type embryos found to have congenital heart defects. Adapted from Lana-Elola et al., 2016.

It should therefore be a priority to repeat the typing of heart defects in both the Dp1Tyb and wild-type littermate controls at a later stage, for example at E15.5. It would also be interesting to collect the “microstage” of the data whether by limb bud morphology or other modalities (as described above in §§7.3.1) to correlate any defects to finer staging.

7.4.2 Further characterisation of cellular processes

While this project attempted to characterise the tissue morphogenesis of structures such as the mVS and the OFTCs in the Dp1Tyb, it was not possible in the time available to conduct the intended characterisation of all the cellular processes underlying heart morphogenesis. A framework for exploring these cellular behaviours is PROMASS (Green, 2022), which was used to an extent within this thesis. In Chapter 5, I characterised the proliferation and apoptosis of cells within the Dp1Tyb OFTC at E12.5 and E13.5 during a period of tissue remodelling. Indeed, the results did show a proliferative defect in the E13.5 Dp1Tyb OFTC which may be linked to the morphological changes observed in the proximal region of the cushion, however, this was not conclusively proven here.

Using PROMASS as guidance, the next logical experiment would be to investigate the orientation of division in the OFTC of the Dp1Tyb, to ascertain if oriented division is perhaps leading to the morphology change. An ideal modality for this experiment would be Light Sheet microscopy, where established protocols for clearing embryonic heart tissue have been extensively published and resolved to

single-cell resolution (Ding *et al.*, 2018; Ren *et al.*, 2022). If combined with immunostaining for mitotic spindle fibres, such as Aurora-B, it would be possible to note the orientation of cell division in 3D in the embryonic heart. Clonal analysis in the embryonic hearts has indicated that the myocardial cells undergo oriented cell division from as early as the primitive heart tube at E8.5 and is maintained in various regions, including the ventricular septum, after E14.5 (Meilhac *et al.*, 2004).

Characterisation of the size and shape of cells would also be an important avenue for future work. There are several ways in which this could be investigated, from assessing nuclear deformation within existing data to utilising different immunostainings to look at size and shape of individual cells. Firstly, using existing data, it would be possible to use the immunofluorescence images I gathered for cellular characterisation of the Dp1Tyb OFTCs at E12.5 and E13.5 to assess nuclear aspect ratio, also known as nuclear deformation (Li *et al.*, 2016), using the StarDist nuclear segmentation. This would be informative of whether force is applied to the cells within the cushion structure as it remodels and undergoes morphogenesis, since nuclei in the absence of applied force are generally spherical. All elements of this experiment are available for the OFTC, where the images used in the cellular characterisation in Chapter 5 could be used along with the same StarDist nuclear segmentation model and the nuclear deformation analysis is accessible as a MATLAB script through the Green Lab. However, this was not undertaken due to time constraints. This is likely a better route for the OFTC cells, given that cells within the cushion structure are mesenchymal and the outline of the cell membrane would be difficult to ascertain through staining. Cell shape captured by membrane labelling, for example as a by-product of lineage labelling, would enable measurement of changes in cell size and this could be compared to cell spacing to quantify intercellular, i.e. ECM volume.

The application of PROMASS could be applied to other structures in the heart that undergo morphogenesis as well. I propose that the mVS should be reinvestigated from a cellular standpoint, in part due to the mVS only being characterised by its length in 3D reconstructions of Dp1Tyb and wild-type embryos at E10.5-E13.5, but also that unpublished observations of Dp1Tyb E14.5 hearts show a more pyramidal morphology than their wild-type littermates (Figure 7.2, orange dashed lines). To confirm these observations, the morphology of the mVS could be assessed first by the width of the structure at the base and its crest. Then

embryonic hearts of both genotypes between E10.5 to E14.5 would be sectioned in the frontal orientation and immunostained. Outlines of cells within the muscular septum could be visualised for F-Actin (such as phalloidin) and analysed based on their size and shape, similar to a study by Francou and colleagues (2017) earlier in cardiogenesis. Additionally, proliferation within the mVS could be assessed using an anti-PHH3 antibody similar to experiments in this thesis. This would be informative in characterising the growth of the muscular septum, to determine if there are zones of proliferation in the structure that drives morphogenesis. Alternatively, the morphogenesis of the mVS may be achieved through other means such as compaction of the surrounding trabeculation (Contreras-Ramos *et al.*, 2008, 2009), this is discussed in §§7.4.8 below. This is an area of debate within the field and thus would be a valuable observation to make.

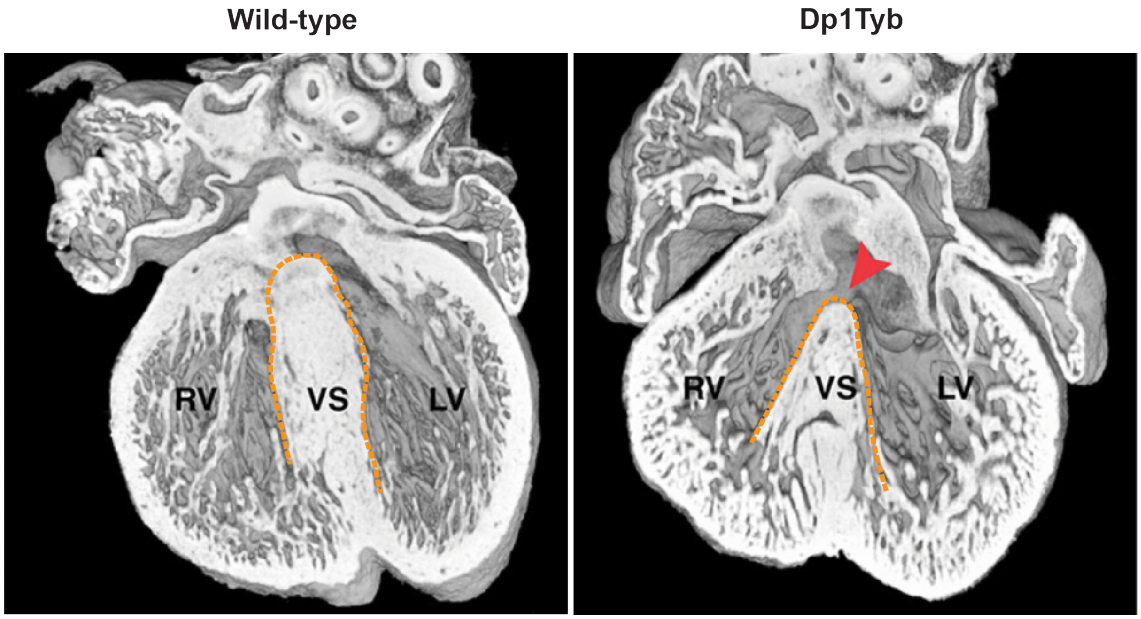

Figure 7.2 3D reconstructions of E14.5 wild-type and Dp1Tyb hearts. The ventricular septum (VS) outlined in dashed orange. The red arrowhead indicates a ventricular septal defect. RV: right ventricle, LV: left ventricle. Adapted from Lana-Elola et al. 2016.

7.4.3 Characterising extracellular matrix proteins

The ECM plays a large role in heart morphogenesis and has been indicated to be dysregulated in the DS and CHDs. As discussed above, the endocardial cushions are rich with many different types of ECM proteins. There are several different ways

to approach the characterisation of the ECM in the Dp1Tyb hearts. First, there should be an identification of the most abundant types of ECM within the OFTC. This could be gleaned from scRNA-Seq data of E13.5 Dp1Tyb and wild-type hearts along with immunostaining for the most abundant according to literature such as versican, collagens and hyaluronan. The immunostaining of these ECM components could be made quantitative or semi-quantitative by measuring the MFI of immunofluorescence and comparing signals between genotypes.

For more specific characterisation of collagen, where immunolabelling the fibrils can be challenging, second harmonic generation (SHG) imaging could be utilised. SHG is a non-linear optical microscopy method and does not rely on any labelling of collagen with reagents. Briefly, the technique captures the structure of collagen fibrils through the interaction of two gamma-photons of equal frequency with a non-linear material (such as collagen fibrils). The two gamma-photons may then combine and produce a new photon with double the frequency and half the wavelength of the original (Campagnola and Dong, 2011; Chen *et al.*, 2012). This is registered as a signal from the non-linear material the original photons interact with. Appropriate photon pairs are generated in two-photon microscopes and because it has the right spatial scale, an image of collagen fibrillar assemblies can be produced. The use of SHG has been extended to the developing heart, where regional differences in the organisation of collagen fibrils have been identified in early embryonic mouse heart (Figure 7.3A) (Lopez and Larina, 2019). Furthermore, images generated from SHG can be further analysed to quantify the length, directionality and organisation of the collagen fibrils (Figure 7.3B). This would be an exciting direction to take the project, as there does not seem to be a characterisation of collagen fibrils within the endocardial cushions yet, especially in the context of DS. SHG does have some limitations (e.g. fibrils not in the XY plane cannot be captured) and recently a method using conventional confocal microscopy and a Fast Green stain has been reported that could be a good alternative (Timin and Milinkovitch, 2023).

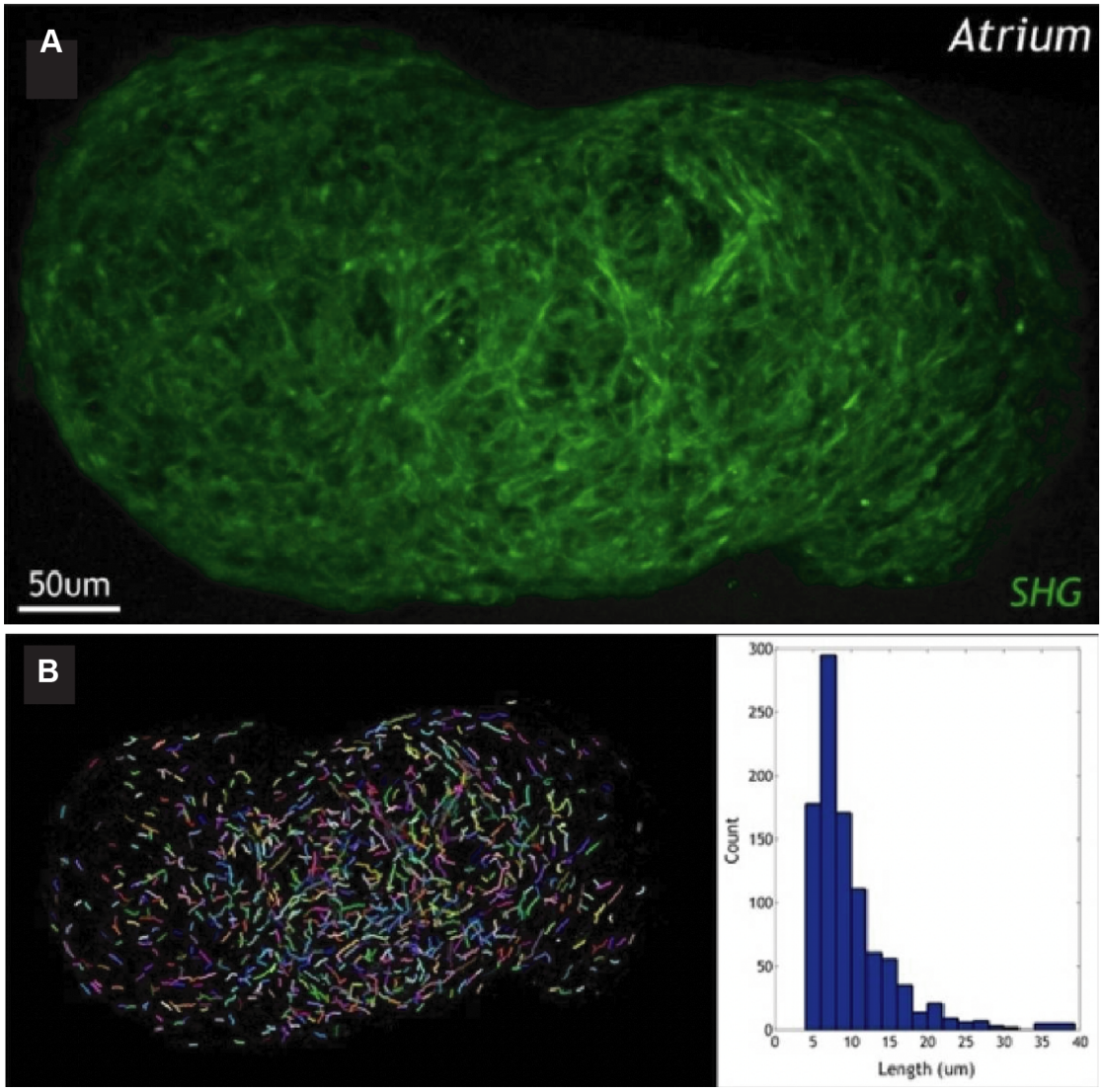

Figure 7.3 Second harmonic imaging and analysis in the embryonic heart. (A) Second harmonic imaging of collagen fibrils in an E8.5 heart. (B) Visualisation of the directionality of the collagen fibrils in (A) and the histogram plot of collagen fibril lengths. Adapted from Lopez and Larina, 2019.

A second technique that could be trialled in relation to ECM within the cushions is Raman Spectroscopy. Raman microscopy is a relatively new label-free vibrational technique that allows for the probing of ECM structure and composition in biological tissue (Bergholt *et al.,* 2019). It relies on the principles of Raman scattering, where lasers interact with a material and cause the energy of the laser photons to shift. The directionality of the shift is interpreted as the vibrational mode of the sample and therefore its biochemical and structural characteristics (Cialla-May *et al.*, 2019). Raman microscopy has previously been applied to adult cardiac tissue, where it was

able to differentiate between different collagen subtypes in human aortas (You *et al.*, 2017). This could be used to further probe what different components of the ECM are in the developing OFTC and whether this differs in the Dp1Tyb embryos. Investigation of the ECM would link to further exploration of the material stiffness of tissues beyond the preliminary AFM experiments in this thesis, which is impacted by components of ECM proteins.

7.4.4 Improving material stiffness measurement

Although the limitations of the AFM experiments performed in this thesis are outlined above (§§7.3.4), further characterisation of the material stiffness of endocardial cushions would be informative and important in developing our understanding of septation. The cushions are rich with ECM and, as discussed above, this impacts the material properties of the anatomy.

While the AFM data discussed in Chapter 6 of this thesis is preliminary and exploratory, it provides a blueprint for future work in this area and indications of where optimisations and changes should be made. To obtain a measurement of the tissue stiffness at longer length-scales, it would be pertinent to increase the size of the bead used to probe the sample surface. The precise size of the bead should be a point of optimisation, since larger beads are recommended for softer materials (~1 kPA or softer) to avoid penetrating the tissue rather than indenting it (Norman *et al.*, 2021). Larger beads are also recommended when testing the stiffness of regions of tissue, where smaller beads used for this purpose may run the risk of probing single cells. This should be paired with a larger sampling grid which can be defined in the JPK AFM software, in doing so it may be possible to cover the majority of the cushion mesenchyme with one grid. Further optimisations should also extend to the tissue preparation, such as using cryosections of the cushion tissue rather than fresh dissections and the optimal period at which the tissue is well adhered to the Cell-Tak but its material properties are not affected by the time spent outside of PBS.

Larger beads (up to 75μm) can be glued to the AFM cantilever but this can impact the cantilever balance which can result in calibration and deflection issues (Norman *et al.*, 2021). AFM may be more appropriately suited to the nano-scale for which it was developed, to the extent that AFM has been used to probe protein-DNA interactions (Lyubchenko *et al.*, 2014). Given this limitation, it might be preferable to

use other techniques to measure the elasticity and material stiffness of a tissue. One such technique is nanoindentation. Nanoindentation operates under parallel principles to AFM, it is similarly based on scanning probe microscopy with probe on a deformable mount controlled by motorized positioners (Griepentrog *et al.*, 2013). The primary difference is that purpose-built mounts are more robust so that the probe can be several tens of microns in diameter, making it more suitable for the probing of larger tissue structures. With increasing commercial availability of nanoindentation, future work in this aspect of the project may be more suited to the technique.

Another technique to consider is micropipette aspiration which has been used in probing the elasticity of cells and tissues. The major advantage of this technique is its simplicity and the relatively low-tech equipment needed. Micropipette aspiration is set up using a microscope and a glass capillary pipette of a known inner radius attached to an aspirator capable of applying small incremental amounts of negative pressure. Under the microscope, a constant negative pressure is applied to the tissue sample through the micropipette which induces a deformation in the tissue (Petridou and Heisenberg, 2019), this deformation is captured by the microscope. The elasticity is then calculated by the extent of tissue deformation in relation to the applied negative pressure. This technique has been applied to some structures in the embryonic heart already, for example in chick embryonic AA (Lashkarinia *et al.*, 2023) and even embryonic mouse OFTC explants (Wang *et al.*, 2023).

7.4.5 Determining CHD effects of Dyrk1a and other unidentified causative genes

Dyrk1a was recently shown as one of the dosage-sensitive causative genes in the development of CHDs and craniofacial dysmorphology of Dp1Tyb through a genetic mapping panel of Mmu16 (Lana-Elola *et al.*, 2023; Redhead *et al.*, 2023). Outside of the Dp1Tyb mouse model, Dyrk1a has also been implicated in the neurological deficits of DS, which is the most penetrant phenotype in the condition (Duchon and Herault, 2016; Brault *et al.*, 2021). Dyrk1a was also found to be partially responsible for reduced mitochondrial potential, mitochondrial dysmorphology and defects in proliferation in the heart.

Dyrk1a has not yet been explored in the OFTC of Dp1Tyb embryos. This thesis provides the necessary initial characterisation of OFTC in the Dp1Tyb mice at a morphological and cellular level needed for comparative studies with the Dp1Tyb.*Dyrk1a*$^{+/+/-}$ mouse strain. The same analyses and quantifications laid out in this thesis could be applied to the Dp1Tyb.*Dyrk1a*$^{+/+/-}$ strain to ascertain if restoring *Dyrk1a* back to 2 copies would rescue OFTC dysmorphology, proliferation and/or cell density defects described in the Dp1Tyb mice at the same stages to find out whether any or all correlate with the CHD rescue.

As outlined by Lana-Elola *et al.* (2023), there are likely to be other causative genes other than Dyrk1a. This is currently under investigation at the Tybulewicz lab using a systematic genetic mapping panel and subsequent individual gene knockouts. At the time of writing this thesis, the second causative gene is unidentified and referred to as Gene X. There are six coding genes that are under interrogation based on the mapping panel: *Mx2, Tmprss2, Ripk4, Prdm15, C2cd2* and *Zbtb21*. Currently, none of these genes are known to be associated with CHDs. When Gene X is revealed, the same experimental steps should be undertaken to explore whether it is also implicated in the OFTC phenotypes observed in the Dp1Tyb mice. The identification of *Dyrk1a* and eventually Gene X will help to pinpoint cellular mechanisms and pathways that could explain these phenotypes in the OFTC as well as for CHDs in DS as a whole.

7.4.6 Testing the role of cardiac neural crest cells

CNCC are essential to heart morphogenesis and in particular, the development of the OFT and formation of the pulmonary artery and aorta. Deficiencies in CNCC have been shown numerous times to impair heart development to some degree. The neural crest itself is implicated in DS, with some evidence of NC impairment in the condition as discussed in this thesis.

As the CNCC delaminate and migrate into the heart from the neural tube, this may be the first potential point of failure in the Dp1Tyb mice. To assess migration, it would be easiest to study the explants of CNCC. This can be achieved through the dissection of the neural tube between the otic pit and the 3rd somite at E8.5 (Epstein *et al.*, 2000). Explant cultures can then be time-lapse imaged over 24-48 hours to

quantify the migration of the CNCC. The migration of CNCC can be quantified in two methods: collectively or as singular cells. Collective migration can be quantified by measuring the spread of the cells away from the original explant, as was done by Roper *et al.* (2009) in the cranial neural crest of the DS model Ts65Dn. Single cells can also be tracked, as was shown in (Redhead *et al.*, 2023), where the average speed cells migrating away from the explant culture can be calculated alongside the directionality of migration.

A major limitation of this project is the lack of lineage tracing for CNCC derivatives and SHF cells (this will be discussed below in §§7.4.7). There were numerous attempts to set up a colony of a Dp1Tyb.*Wnt1*-Cre mouse strain, which would have allowed for the tracking of CNCC derivatives in the OFTC and more widely in the heart. However, the generation of this strain was unexpectedly difficult with the combination of the Dp1Tyb mice being bad breeders and the low frequency of obtaining a double mutant male mouse (Dp1Tyb.*Wnt1*-Cre) that could be used in matings with standard C57BL6 females. In addition to this, I noticed that many of the mice generated carrying *Wnt1*-Cre were prone to developing seizures and dying before they could be put into mating. This may be due to the strain of *Wnt1*-Cre mice being used to generate these lines deriving from the original transgenic *Wnt1*-Cre mouse presented in Danielian *et al.* (1998), which was later found to be expressing ectopic activation of Wnt signalling (Lewis *et al.*, 2013). As a response to this, a new transgenic line for neural crest lineage labelling was created, the *Wnt1*-Cre2, which does not ectopically express *Wnt* (Dinsmore, Ke and Soriano, 2022). This mouse strain has been imported by the Tybulewicz lab and a new mouse colony is being established; in time, the *Wnt1*-Cre2 will be used to create a Dp1Tyb.*Wnt1*-Cre2 mouse strain. An alternative to the *Wnt1*-Cre2 mouse for lineage labelling the neural crest would be to use a Sox10-Cre instead, which is also a widely used reporter for neural crest lineages (Simon *et al.*, 2012).

A CNCC lineage reporter such as the *Wnt1*-Cre2 could be used for multiple experiments in the context of CHD in DS. With a Dp1Tyb.*Wnt1*-Cre2 crossed to a nuclear reporter, the first experiment should be to characterise the number of CNCC-derived cells in the heart to wild-type littermates at the same stage. This would establish the baseline of what the correct numbers of CNCC-derived cells are in OFTC at each stage and whether there are changes in these numbers in Dp1Tyb embryos. Additionally, there would be observations of cell numbers in the different

regions of the OFTC, to see if the distribution changes in the mutant hearts. This should extend to earlier time points than in this project, as the CNCC migrate into the heart before E10.5 (Jiang *et al.*, 2002).

Proliferation can be quantified alongside the initial cellular characterisation of the CNCC in Dp1Tyb.Wnt1-Cre2 using an anti-PHH3 antibody and counting the CNCC-derived cells that are mitotic. This would reveal whether the CNCC in the Dp1Tyb are specifically deficient in proliferation; if so, this would echo the findings of Redhead and colleagues (2023), where there was a proliferative but not migratory defect in the cranial neural crest of Dp1Tyb mice.

Lastly, the creation of a Dp1Tyb.*Wnt1*-Cre2 allows for neural crest-specific knockout of causative genes. For example, the Dp1Tyb.*Dyrk1a*KO mouse strain that is currently maintained as a colony at the Francis Crick Institute could be crossed to the Dp1Tyb.*Wnt1*-Cre2 and assayed for any changes to the relative rate of CHDs and which types. This could continue to similar experiments described throughout this thesis. When Gene X is found, the experiments could be repeated with Gene X depleted from the CNCC as well as with both *Dyrk1a* and Gene X to assess if there is recovery of some phenotypes found thus far. However, as previously mentioned it is unlikely to be a full recovery of phenotypes, as some affected structures such as the AVCs are not CNCC-derived.

7.4.7 Second heart field-derived cells

A similar genetic approach can be taken to investigate the SHF-derived cells in the heart, which is the second essential population in the formation of the OFTC. Aside from contributing to the formation of the OFT and cushions, SHF-derived cells are found to contribute to the right ventricular wall and the ventricular septum. The Dp1Tyb mouse stain can be crossed to a SHF lineage marker such as *Mef2c*-Cre or *Nkx2-5*-Cre (Harmon and Nakano, 2013) to gain a double mutant strain that can be crossed to a fluorescent nuclear reporter line. Following a similar strategy to the CNCC lineage tracing experiments described above, SHF-labelled cells can be counted at the same stages of CNCC lineage labelling. This would allow a comparison of the percentages of SHF-derived and CNCC-derived cells and their localisation within the OFTC structure, how this changes through heart

morphogenesis and during OFT septation but most importantly, whether these ratios change with the Dp1Tyb samples.

The endocardium of the OFT which lines the OFTCs are derived from the SHF and undergoes EndoMT to populate the cushion mesenchyme (Verzi *et al.*, 2005). Another role of these SHF-derived cells is thought to be in the muscularisation of the cardiac outlet septum during ventricular septation. This has been speculated to occur through the differentiation of the proximal cushion mesenchyme of the OFT, which is likely to be endocardial derived and hence from the SHF (van den Hoff and Wessels, 2020). It may be interesting to investigate this as some defects in the Dp1Tyb hearts are found in this region, where perhaps there is a deficiency in the differentiation of these SHF-derived cells which fails to form this region of the septum and the cardiac outlets.

Creating a Dp1Tyb.*Mef2c*-Cre or a Dp1Tyb.*Nkx2-5*-Cre would also allow for the deletion of causative genes from the duplicated region and restore to 2 copies. Embryos generated from these crosses should be similarly screened for the occurrence of heart defects and type of defects. Additional characterisation of proliferation within the SHF-derived cells would also be of importance, as the defect in proliferation within the OFTCs could be due to either CNCC or SHF-derived cells, or in both populations equally.

7.4.8 Other structures in cardiac development

Much of this thesis has focused on the OFTCs due to them being interesting transient structures of heterogenous origins, which have thus far gone relatively unstudied in the context of the DS CHDs. However, there are other structures involved in proper heart septation that merit thorough investigations as well. This subsection will touch on some aspects of these as starting points for deeper exploration.

Firstly, the AVCs should be further characterised in the Dp1Tyb. There have been some unpublished observations that the AVCs of Dp1Tyb cushions do not fuse with one another as they should in normal atrioventricular valve formation, which may be the basis of the common atrioventricular valve (or bridging leaflet) that is the hallmark of AVSDs. However, it has not yet been elucidated what mechanisms drive fusion of the cushions and how they are disrupted in the Dp1Tyb embryos. Some

preliminary work carried out by Rifdat Aoidi in the Tybulewicz Lab at the Francis Crick Institute has shown that the AVCs have a reduced cell density defect similar to the OFTCs. Additionally, proliferation defects are also seen in the AVCs, with Dp1Tyb mice crossed to a Fucci reporter line (cells in G1 express mCherry, cells in S-G2-M express GFP) showed a lower ratio of cells in S-G2-M to G1, consistent with rates of proliferation (Figure 7.4A-C). It is not yet known whether the defects in the AVC of Dp1Tyb embryos are Dyrk1a-dependent.

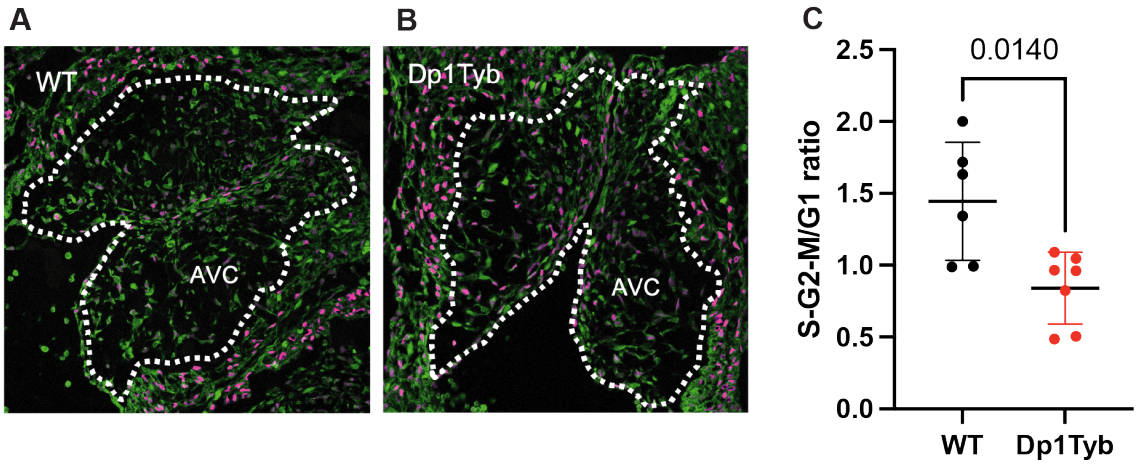

Figure 7.4 Reduced proliferation in the atrioventricular cushions of Dp1Tyb embryos at E11.5. Preliminary unpublished data provided by Rifdat Aoidi, Francis Crick Institute. (A) Wild-type fucci reporter mouse heart with the atrioventricular cushions outlined. (B) Dp1Tyb.Fucci reporter mouse heart with the atrioventricular cushions outlined. (C) Quantification of the S-G2-M/G1 ratio of wild-type and Dp1Tyb embryos. Statistics performed was Mann Whitney-U; the graph shows mean + SD . Wild-type n = 6, Dp1Tyb n = 7.

The trabeculation of the heart in the Dp1Tyb embryos has also gone relatively unstudied. The trabeculae are a meshwork of finger-like protrusions of the inner ventricular wall, consisting of trabecular cardiomyocytes and lined by endocardium. Trabeculation aids the embryo in increasing cardiac output and permits nutrient and oxygen uptake in the embryonic myocardium prior to coronary vascularisation (Samsa *et al.*, 2013). While the Dp1Tyb mouse model does not show dramatic trabecular-related defects such as Left Ventricular Noncompaction cardiomyopathy, there has been no quantitative characterisation to determine whether the trabeculae structure differs more subtly in the Dp1Tyb hearts to the wild-type. This could be analysed using existing HREM data sets of embryonic hearts for Dp1Tyb and wild-

type embryos. Using the lumen segmentation pipeline described in §§3.2.3, the inverse of (i.e. void volume around) the trabeculation is also segmented. Fractal analysis can be applied to these images to calculate the "complexity" of the trabeculation as a quantitative output. Fractal dimension analysis uses the geometry of a given object to give a statistical index of complexity, although initially used to describe objects that are self-similar at infinite scales, it has been used to describe complexity in biology and applied to the medical imaging field (Sandu *et al.*, 2008). It is also commonly used to describe the level of trabeculation within the heart in many studies of human hearts from cardiac MRIs (Captur *et al.*, 2013; Cai *et al.*, 2017; Zhang *et al.*, 2023). Furthermore, it has been thought that the mVS is partially formed through the coalescence of surrounding trabecular branches in the left and right ventricles, which has been observed in chick embryos (Contreras-Ramos *et al.*, 2008). As we do not yet know if the muscular septum plays a role in the pathogenesis of CHDs in DS, it is important to consider all aspects of its morphogenesis, including the role of trabeculation.

As heart development progresses, the trabecular myocardium collapses and forms part of the myocardial wall; this process is termed compaction and helps the formation of a thick, compact ventricular wall. In mouse embryos, this process occurs in the mouse after E14.5 (Risebro and Riley, 2006). Failure of compaction results in CHDs like Left Ventricular Noncompaction cardiomyopathy (Choquet *et al.*, 2019). It is not known if this process is impacted in the Dp1Tyb mouse hearts, as this has not been studied at all.

7.5 Conclusions

This project began as an investigation into the developmental process leading up the ventricular septation and how this is impacted in the Dp1Tyb mouse model of DS to lead to CHDs. What followed was the exploration of different aspects of heart morphogenesis and the development of sometimes unconventional analyses to objectively and quantitatively measure aspects of heart anatomy and ventricular septation.

To better understand the anatomical changes happening within the heart during ventricular septation, I sought to create detailed developmental anatomical

time series of 3D images starting from the formation of the muscular septum at E10.5 in the mouse to the final stage immediately before full septation of the left and right ventricles at E14.5. Each embryo collected for this endeavour was further staged according to its limb morphology to record a more accurate embryonic age. In doing so, I was able to characterise the morphogenesis of the mVS and closure of the IVC in normal septation and compare this process to the Dp1Tyb embryos to determine if any changes in this timeline could suggest aberrant septation. While this aspect of the project was interesting in forming a comprehensive timeline of ventricular septation, there were no differing mVS or obvious IVC metrics in the Dp1Tyb. This prompted me to explore other aspects of ventricular septation.

The OFTC emerged as an exciting direction of study as it is the first structure to fuse to the mVS, initiating the final steps of septation and formation of the membranous septum. From the same dataset that was used to develop a comprehensive timeline for ventricular septation in both genotypes, I segmented out the 3D morphology of the initially separate septal and parietal OFTCs. This revealed that the Dp1Tyb OFTC were likely to be more delayed in its fusion at the distal OFTC, a timely process necessary for separating the OFT into the pulmonary artery and the aorta. By the next day at E13.5, the development of the OFTC is matched in both Dp1Tyb and wild-type embryos but here a morphological difference emerged. The Dp1Tyb OFTCs were found to be smaller in volume, where quantitative morphometrics of the cushion shape revealed that the shape changes were localised to the proximal regions of the cushion.

As tissue morphogenesis is usually driven by a combination of cellular behaviours, so in dysmorphic tissues, these cellular behaviours must be affected. I serially sectioned the OFTCs of E12.5 and E13.5 Dp1Tyb and wild-type embryos, enabling the application of various immunostaining techniques at consistent intervals between each section. This approach was taken to evaluate the levels of proliferation and apoptosis in the cushions as well as the cellularisation of the tissue. Here, several phenotypes emerged in the Dp1Tyb samples; the OFTC at both stages were found to have lower cell density than their wild-type counterparts and there was a reduction in proliferating cells in the proximal region at E13.5 which coincided with an enlargement of section area occupied by mesenchymal cells. These findings suggested that the OFTC were dysmorphic in areas of its structure that are involved in the ventricular septation process.

In particular, I hypothesised that if there is a reduction in cell density within the OFTCs at both E12.5 and E13.5 in Dp1Tyb embryos there must be more ECM between the cells as the cushion is primarily a matrix-rich tissue. With more ECM proteins in the cushions, I thought that there may be a change in the material properties of the OFTC which was perhaps impacting its ability to complete fusion to the mVS or maintain contact as blood flows between the ventricles. I embarked on a preliminary investigation into how this could be explored, I collaborated with Oliva Courbot (Elosegui-Artola lab, Francis Crick Institute) to test the regional stiffness of the OFTCs. While there were no conclusive answers that could be drawn from these experiments due to the low sample number and need for optimisation, it is likely the first example of successful AFM on freshly dissected OFTC tissue. These final experiments of my thesis represent an exploration of techniques that should be considered in the future directions of this project.

The wide scope for future experiments is discussed at length earlier in this chapter. These future directions broadly fall into four categories:

1. Further characterisation of other structures involved in heart morphogenesis and if these are affected in the Dp1Tyb.
2. Exploration of ECM proteins in the development of the OFTC and ventricular septation and how this may impact the material properties of the structure.
3. Lineage tracing of the progenitor cells that contribute to the OFTCs and ventricular septation.
4. How CHD causative genes in DS such as Dyrk1a affect the ventricular septation process.

Overall, the work presented in this thesis begins to characterise the cellular behaviours underpinning OFTC development and its contribution to the ventricular septum and how these behaviours are altered in the context of CHD formation in DS. While the research in this project raises many more questions about the impact of the identified phenotypes, it serves as a starting point for further exploration in elucidating the developmental aetiology of CHDs in DS. Perhaps with a better understanding of how CHDs arise in chromosomal disorders like DS, there will be more informed targets for therapeutics aimed at improving clinical outcomes for those born with heart defects.

Chapter 8. Appendix

8.1 Lumen segmentation from HREM images

```
import argparse
import os
import sys

import cc3d
import numpy
import pyvista

from scipy.interpolate import interpn
from scipy.ndimage import binary_fill_holes, binary_erosion,
distance_transform_edt
from skimage import measure
from skimage.io import imread, imsave
from skimage.morphology import binary_dilation, selem

HOLE_FILLING = 2


#
https://github.com/lforet/CoinVision/blob/master/build/mahotas/mahotas
/bwperim.py
def bwperim(bw, n=4):
    """
    perim = bwperim(bw, n=4)
    Find the perimeter of objects in binary images.
    A pixel is part of an object perimeter if its value is one and
there
    is at least one zero-valued pixel in its neighborhood.
    By default the neighborhood of a pixel is 4 nearest pixels, but
    if `n` is set to 8 the 8 nearest pixels will be considered.
    Parameters
    ----------
      bw : A black-and-white image
      n : Connectivity. Must be 4 or 8 (default: 8)
    Returns
```

```
-------
  perim : A boolean image
"""

if n not in (4, 8):
    raise ValueError('mahotas.bwperim: n must be 4 or 8')
rows, cols = bw.shape

# Translate image by one pixel in all directions
north = numpy.zeros((rows, cols))
south = numpy.zeros((rows, cols))
west = numpy.zeros((rows, cols))
east = numpy.zeros((rows, cols))

north[:-1, :] = bw[1:, :]
south[1:, :] = bw[:-1, :]
west[:, :-1] = bw[:, 1:]
east[:, 1:] = bw[:, :-1]
idx = (north == bw) & \
      (south == bw) & \
      (west == bw) & \
      (east == bw)
if n == 8:
    north_east = numpy.zeros((rows, cols))
    north_west = numpy.zeros((rows, cols))
    south_east = numpy.zeros((rows, cols))
    south_west = numpy.zeros((rows, cols))
    north_east[:-1, 1:] = bw[1:, :-1]
    north_west[:-1, :-1] = bw[1:, 1:]
    south_east[1:, 1:] = bw[:-1, :-1]
    south_west[1:, :-1] = bw[:-1, 1:]
    idx &= (north_east == bw) & \
           (south_east == bw) & \
           (south_west == bw) & \
           (north_west == bw)
return ~idx * bw
```

```
# https://stackoverflow.com/questions/48818373/interpolate-between-two-images
def signed_bwdist(im):
    '''
    Find perim and return masked image (signed/reversed)
    '''
    im = -bwdist(bwperim(im)) * numpy.logical_not(im) + bwdist(bwperim(im)) * im
    return im


def bwdist(im):
    '''
    Find distance map of image
    '''
    dist_im = distance_transform_edt(1 - im)
    return dist_im


def interp_shape(top, bottom, precision):
    '''
    Interpolate between two contours

    Inumpyut: top
            [X,Y] - Image of top contour (mask)
           bottom
            [X,Y] - Image of bottom contour (mask)
           precision
             float  - % between the images to interpolate
                Ex: num=0.5 - Interpolate the middle image between top and bottom image
    Output: out
            [X,Y] - Interpolated image at num (%) between top and bottom

    '''
    if precision > 2:
        print("Error: Precision must be between 0 and 1 (float)")
```

```
    # plot = plt.imshow(top, cmap='gray', vmin=0, vmax=255)
    # plt.show()
    # plot = plt.imshow(bottom, cmap='gray', vmin=0, vmax=255)
    # plt.show()

    top = signed_bwdist(top)
    bottom = signed_bwdist(bottom)

    # row,cols definition
    r, c = top.shape

    # Reverse % indexing
    precision = 1 + precision

    # rejoin top, bottom into a single array of shape (2, r, c)
    top_and_bottom = numpy.stack((top, bottom))

    # create ndgrids
    points = (numpy.r_[0, 2], numpy.arange(r), numpy.arange(c))
    xi = numpy.rollaxis(numpy.mgrid[:r, :c], 0, 3).reshape((r * c, 2))
    xi = numpy.c_[numpy.full((r * c), precision), xi]

    # Interpolate for new plane
    out = interpn(points, top_and_bottom, xi)
    out = out.reshape((r, c))

    # Threshold distmap to values above 0
    out = out > 0

    # plot = plt.imshow(out, cmap='gray', vmin=0, vmax=255)
    # plt.show()

    return out


def process_image(binary_images, closed_images, masked_images, image):
    # Our signal is actually 0s
    thresholded = image == 0
    binary_images.append(thresholded)
```

```
    # Closing in order to identify background
    inverted = thresholded != 1
    closed_image = inverted
    closed_image = binary_dilation(closed_image, selem.disk(5))
    closed_image = binary_dilation(closed_image, selem.disk(3))
    closed_image = binary_fill_holes(closed_image)
    closed_image = binary_erosion(closed_image, iterations=12)
    closed_images.append(closed_image)

    # Use closed_image to subtract from signal (i.e. mask the heart to
remove background)
    masked = numpy.logical_and(closed_image, thresholded)
    masked_images.append(masked)


def process_htunm_data(source, target, xy=1.0, z=1.0,
reduction_fraction=0.5):
    files = os.listdir(source)
    files = sorted(files)

    counter = 0
    name = ""
    old_signal_pixels_count = 0
    interpolate_start = None
    last_viable_image_index = None
    raw_images = list()
    binary_images = list()
    closed_images = list()
    masked_images = list()
    for idx, file in enumerate(files):
        if not file.endswith(".tif") or file.endswith(".tiff"):
            continue

        # Get a good name
        if counter == 0:
            name = file.replace(".tif", "").replace(".tiff", "")

        # Load the image
```

```
        im_filepath = os.path.join(source, file)
        image = imread(im_filepath)
        raw_images.append(image)

        # Count
        signal_pixels_count = numpy.count_nonzero(image)

        # Eliminate if it's a big change
        if counter != 0 and (signal_pixels_count <= 500 or
abs(signal_pixels_count - old_signal_pixels_count) > 10000):
            print("Bad Image at: " + str(idx))
            if interpolate_start is None and last_viable_image_index
is not None:
                interpolate_start = last_viable_image_index
            continue

        # Handle interpolation for previously skipped images
        if interpolate_start is not None:
            # Load the bottom interpolation
            bottom_image = imread(os.path.join(source,
files[interpolate_start]))

            # Calculate the missing images and the interpolation level
            steps = idx - interpolate_start
            amount_step = 1 / steps

            # Loop through our missing images
            for interpolation_steps in range(steps):
                amount = amount_step * (interpolation_steps + 1)
                interpolated_image = interp_shape(image, bottom_image,
amount)

                # Process the image and add it to our stacks
                process_image(binary_images, closed_images,
masked_images, interpolated_image)

            interpolate_start = None

        # Process this image
```

```
            process_image(binary_images, closed_images, masked_images,
image)

            # Save and update loop vars
            counter += 1
            old_signal_pixels_count = signal_pixels_count
            last_viable_image_index = idx

    # Save as tiff stack
    if not os.path.isdir(target):
        os.mkdir(target)

    # Combine our filtered binary images and save
    combined_images = numpy.stack(raw_images, axis=0)
    imsave(os.path.join(target, name + "_raw.tiff"), combined_images)

    # Combine our filtered binary images and save
    combined_images = numpy.stack(binary_images, axis=0)
    imsave(os.path.join(target, name + "_binary.tiff"),
combined_images)

    # Combine our closed images and save
    combined_images = numpy.stack(closed_images, axis=0)
    imsave(os.path.join(target, name + "_closed.tiff"),
combined_images)

    # Combine our masked images and save
    combined_images = numpy.stack(masked_images, axis=0)
    imsave(os.path.join(target, name + "_masked.tiff"),
combined_images)

    # 3d connected components
    labelled = cc3d.connected_components(combined_images)
    imsave(os.path.join(target, name + "_labelled.tiff"), labelled)

    # Largest label extraction
    labels_out, N = cc3d.largest_k(
        labelled, k=1,
        connectivity=26, delta=0,
```

```
            return_N=True,
        )

        # Selection
        highlighted = labels_out == 1
        imsave(os.path.join(target, name + "_highlighted.tiff"),
highlighted)

        # Mesh generation
        verts, faces, norm, val = measure.marching_cubes(highlighted,
spacing=(xy, xy, z))
        faces = faces + 1  # Apparently a fix
https://stackoverflow.com/questions/48844778/create-a-obj-file-from-
3d-array-in-python

        # Save as obj
        obj_path = os.path.join(target, name + ".obj")
        with open(obj_path, 'w') as obj_file:
            for item in verts:
                obj_file.write("v {0} {1} {2}\n".format(item[0], item[1],
item[2]))
            for item in norm:
                obj_file.write("vn {0} {1} {2}\n".format(item[0], item[1],
item[2]))
            for item in faces:
                obj_file.write("f {0} {1} {2}\n".format(item[0], item[1],
item[2]))

        # Force memory clean up
        del verts, faces, norm, val, highlighted, labelled,
combined_images

        # Use pymesh to load it into memory
        reader = pyvista.get_reader(obj_path)
        mesh = reader.read()
        decimated = mesh.decimate(reduction_fraction,
volume_preservation=True)
        mesh.plot(color='tan')
        decimated.plot(color='tan')
```

```
    decimated.save(os.path.join(target, name + "_simplified_" +
str(reduction_fraction) + ".stl"))

    # Mesh simplification
    # model = class_mesh_simplify.mesh_simplify(verts, faces, 0,
simplification_ratio)
    # model.generate_valid_pairs()
    # model.calculate_optimal_contraction_pairs_and_cost()
    # model.iteratively_remove_least_cost_valid_pairs()
    # model.generate_new_3d_model()
    # model.output(os.path.join(target, name + "_simplified_" +
str(simplification_ratio) + ".obj"))


if __name__ == '__main__':
    parser = argparse.ArgumentParser("Heart Lumen Mesh Generation")
    parser.add_argument("-i", type=str, default=None, help="Please
provide the input path to the folder containing your images.",
required=True)
    parser.add_argument("-o", type=str, default=None, help="Please
provide the output path to the folder where you wish to save the
data", required=True)
    parser.add_argument("-vsxy", type=float, default=1.0, help="Please
provide the voxel spacing in the xy direction", required=False)
    parser.add_argument("-vsz", type=float, default=1.0, help="Please
provide the voxel spacing in the z direction", required=False)
    parser.add_argument("-rf", type=float, default=0.95, help="Please
provide the reduction fraction (e.g. 0.5 would be a 50% reduction in
complexity) you wish to apply.", required=False)
    args = parser.parse_args()

    process_htunm_data(args.i, args.o, xy=args.vsxy, z=args.vsz,
reduction_fraction=args.rf)
```

8.2 Approximation analysis

```
# # Visualising the distance between two mesh objects
```

```
# The script imports 2 meshes (.stl) format and calculates the
distance from points on the second mesh to its closest neighbouring
point on the first mesh. These values can then be mapped on to the
second mesh as a heat map with the option to restrict the heatmap
values to the fusion interface of the two meshes. The distances are
then plotted as frequncy distribution plots for a graphical
representation of the information.

# In[17]:


import pyvista as pv
pv.global_theme.background = 'black'
pv.BasePlotter.center = [0, 0, 0]

#Import meshes - septal outflow tract cushions (softc) and muscular
septum (septum)
softc = '~/Desktop/Mesh_data/meshes/SID9088_sOFTC.stl'
septum = '~/Desktop/Mesh_data/meshes/SID9088_septum.stl'

#Conversion in to pyvista mesh - these will be used for the remainder
of the script
mesh1 = pv.read(softc)
mesh2 = pv.read(septum)

#Plot to check the location of the meshes in relation to one another
plotter = pv.Plotter(notebook=True)
plotter.add_mesh(mesh1, smooth_shading=True)
plotter.add_mesh(mesh2, smooth_shading=True)
plotter.show()


# In[18]:


#Uses a 3D KD-Tree to find the closest neighbour of each
coordinate/point on mesh2 to mesh1
#The distances are saved in array 'd' and can be queried for mean,
minimum & maximum
from scipy.spatial import KDTree
import numpy as np
tree = KDTree(mesh1.points)
d, idx = tree.query(mesh2.points )
mesh2["distances"] = d
print("mean", np.mean(d))
print("minimum", np.min(d))
print("maximum", np.max(d))


# In[7]:


#Distances from the KDTree are projected on to mesh2 as a heatmap
p = pv.Plotter(notebook=False)
p.add_mesh(mesh2, scalars="distances", smooth_shading=True,
flip_scalars=True)
p.add_mesh(mesh1, color=True, opacity=0.25, smooth_shading=True)
p.show()
```

```
# In[8]:


#Restriction of heatmap distances to just the interface of mesh2-mesh1
p = pv.Plotter(notebook=False)
p.add_mesh(mesh2, clim=[0, 0.075], above_color='white',
scalars="distances", smooth_shading=True, flip_scalars=True)
p.add_mesh(mesh1, color=True, opacity=0.25, smooth_shading=True)
p.show()


# Using the information from KD-Tree and neighbour analysis, the array
containing the distances is filtered to contain only values between 0-
0.075mm. These values are used to plot histograms to visualise the
distribution of distances for the entire mesh, then finally just for
the interface where the two anatomical structures will fuse.

# In[19]:


import os
import matplotlib.pyplot as plt
data = d
#The following returns a frequency distribution plot for all values
plt.style.use('seaborn-pastel')
plt.xlabel("distance to closest neighbour (mm)")
plt.ylabel("frequency")
plt.hist(data, bins=50)
plt.savefig('histograms/SID9088_histplot_full.png', transparent=True,
dpi=300)
plt.show()


# In[20]:


#The following returns a frequency distribution plot for values less
than 0.075mm (i.e. fusion interface)
import pandas as pd
interface_data = pd.DataFrame(data, columns=['Distance'])
interface_data = interface_data[interface_data.Distance < 0.075]
data2 = interface_data.to_numpy()
#Check to see conversion from pd.DataFrame to np array
np.save("distances/SID9088.npy", data2)
data2
print("mean", np.mean(data2))
print("minimum", np.min(data2))
print("maximum", np.max(data2))


# In[21]:


#Plotting frequency distribution plot for the narrowed values
plt.style.use('seaborn-pastel')
plt.xlabel("distance to closest neighbour (mm)")
plt.ylabel("frequency")
histinfo = plt.hist(data2, bins=20)
```

```
plt.show()

bincount = histinfo[0]
np.save('distances/SID9088_counts_10.npy', bincount)

bins = np.savetxt('distances/bins.csv', histinfo[1], delimiter=',')


# In[22]:


#Density plot instead of a frequency with added KDE for visualisation
import seaborn as sns
sns.distplot(data2, kde=True, bins=20, hist=True, axlabel='distance to
closest neighbour (mm)')
plt.xlim(0.00,0.075)
plt.ylabel('density')
plt.savefig('histograms/SID9088_histplot_interface.png',
transparent=True, dpi=300)


# Numpy arrays from each data set can now be grouped in to two
genotypes: wild-type (wt) and Dp1Tyb. Data from each set can now be
averaged and then plotted in the same frequency distribution plot.

# In[47]:


#plot two arrays in to density plot - data from each wild type needs
to be averaged
wt = np.load('distances/SID9085.npy')
plt.style.use('seaborn-muted')
sns.distplot(data2, kde=True, bins=10, hist=True, axlabel='distance to
closest neighbour (mm)')
sns.distplot(wt, kde=True, bins=10, hist=True, axlabel='distance to
closest neighbour (mm)')


# In[19]:


#method 1: extract count information for each bin from histograms of
each data set, average count per bin and plot
# test to see if this is basically the same as just collating all the
data together and plotting a freq. density hist.

bins = np.genfromtxt('distances/bins.csv', delimiter=",")
bins = bins[:,0]
sid9090= np.load('distances/SID9090_counts_20.npy')
sid9085= np.load('distances/SID9085_counts_20.npy')
sid9088= np.load('distances/SID9088_counts_20.npy')


wt_count= np.column_stack((sid9090, sid9085, sid9088))
wt_mean = np.mean(wt_count, axis=1)
wt_mean = np.column_stack((bins, wt_mean))

df = pd.DataFrame(data=wt_mean)
df.columns = ['Distance', 'Frequency']
```

```
fig = df.plot.bar(x='Distance', y='Frequency', stacked = True, width =
1.0)


# In[23]:


#method 2: all data sets of saved range of distances are concatenated
and plot as a density histogram
#vs a average bin count plot

#Load in WT data sets
sid9083= pd.DataFrame(data = np.load('distances/SID9083.npy'))
sid9085= pd.DataFrame(data = np.load('distances/SID9085.npy'))
sid9088= pd.DataFrame(data = np.load('distances/SID9088.npy'))
sid9090= pd.DataFrame(data = np.load('distances/SID9090.npy'))
sid9094= pd.DataFrame(data = np.load('distances/SID9094.npy'))
sid9095= pd.DataFrame(data = np.load('distances/SID9095.npy'))
sid9096= pd.DataFrame(data = np.load('distances/SID9096.npy'))
sid9100= pd.DataFrame(data = np.load('distances/SID9100.npy'))

wt_concat = pd.concat([sid9083, sid9085, sid9088, sid9090, sid9094,
sid9095, sid9096, sid9100])
wt_concat = wt_concat.to_numpy()

#Load in Dp1Tyb data sets
sid9084= pd.DataFrame(data = np.load('distances/SID9084.npy'))
sid9086= pd.DataFrame(data = np.load('distances/SID9086.npy'))
sid9087= pd.DataFrame(data = np.load('distances/SID9087.npy'))
sid9089= pd.DataFrame(data = np.load('distances/SID9089.npy'))
sid9091= pd.DataFrame(data = np.load('distances/SID9091.npy'))
sid9092= pd.DataFrame(data = np.load('distances/SID9092.npy'))
sid9093= pd.DataFrame(data = np.load('distances/SID9093.npy'))
sid9097= pd.DataFrame(data = np.load('distances/SID9097.npy'))
sid9098= pd.DataFrame(data = np.load('distances/SID9098.npy'))
sid9099= pd.DataFrame(data = np.load('distances/SID9099.npy'))
sid9346= pd.DataFrame(data = np.load('distances/SID9346.npy'))
sid9347= pd.DataFrame(data = np.load('distances/SID9347.npy'))
sid9349= pd.DataFrame(data = np.load('distances/SID9349.npy'))
sid9350= pd.DataFrame(data = np.load('distances/SID9350.npy'))

dp1_concat = pd.concat([sid9084, sid9086, sid9087, sid9089, sid9091,
sid9092, sid9093, sid9097, sid9098, sid9099,
                        sid9346, sid9347, sid9349, sid9350])
dp1_concat = dp1_concat.to_numpy()

plt.style.use('seaborn-muted')
plt.xlim(0, 0.075)
sns.distplot(wt_concat, kde=True, bins=20, hist=True,
axlabel='distance to closest neighbour (mm)')
sns.distplot(dp1_concat, kde=True, bins=20, hist=True,
axlabel='distance to closest neighbour (mm)')
plt.ylabel("density")
plt.legend(labels=["WT", "Dp1Tyb"], loc="upper left")

plt.savefig('histograms/combined_hist_plot.png', transparent=True,
dpi=300)
```

```
# In[24]:


np.savetxt("distances/wt_concat.csv", wt_concat, delimiter=",")
np.savetxt("distances/dp1_concat.csv", dp1_concat, delimiter=",")
```

8.3 Cell counting macro for FIJI

8.3.1 E12.5 H&E sections

```
run("RGB Color");
roiManager("Select", 1);
setBackgroundColor(8, 8, 8);
run("Clear Outside");
run("Colour Deconvolution2", "vectors=[H&E 2]
output=8bit_Transmittance simulated cross hide");
close();
close();
//run("Brightness/Contrast...");
run("Enhance Contrast", "saturated=0.35");
setAutoThreshold("Moments");
//run("Threshold...");
//setThreshold(0, 100);
setOption("BlackBackground", false);
run("Convert to Mask");
run("Watershed");
run("Analyze Particles...", "size=3-25 display");
```

8.3.2 E13.5 Alcian blue and haematoxylin sections

```
run("RGB Color");
//run("Brightness/Contrast...");
run("Enhance Contrast", "saturated=0.35");
run("Colour Deconvolution", "vectors=[H DAB]");
close();
close();
roiManager("Select", 0);
run("Crop");
setBackgroundColor(8, 8, 8);
run("Clear Outside");
setAutoThreshold("Default");
setAutoThreshold("MaxEntropy");
setOption("BlackBackground", false);
run("Convert to Mask");
run("Watershed");
run("Analyze Particles...", "size=13-300 show=[Overlay Masks]
display");
```

8.4 Internuclear spacing, Sox9 and TUNEL data analysis

```
#Set up tab file first
#tab <- data.frame("embryo", "sox9+", "sox9+hi", "sox9+lo",
"sox9cd", "sox9stdev", "DAPI+", "DAPIcd", "DAPIstdev", "TUNEL",
"TUNELarea", "TUNELmax", "TUNELmin", "TUNELavg")

#DAPI, Sox9 and TUNEL tables must be save in the same folder for
each section
embryo <- "2842_8_8" #edit when moving to next embryo/slide
bg <- 262     #maximum background value of nuclear masks in Sox9
channel from Sox9 negative area in that section
data.files <-
list.files("/Users/htunm/Desktop/Data/E12.5/2842_8/8", pattern =
"*.csv", full.names=TRUE)
data <- lapply(data.files, read.csv)
dapi <- data[[1]]
sox9 <- data[[2]]
tunel <- data[[3]]

#read cell count in dapi file and calculate average cell
displacement
XY <- dapi
E <- XY[, 7:8]
CD<-centroid.displacement(E,0)
CS<-centroid.spacing(CD)
dapiSpacing <- centroid.spacing(CD)
#dapiSpacing <- unique(rapply(list(dapiSpacing), function(x)
head(x, 1)))
dapiSpacing <- na.omit(dapiSpacing)

dapi.count <- length(dapi[, 1])
dapi.cd <- mean(dapiSpacing)
dapi.stdev <- sd(dapiSpacing)

#read cell count in sox9 file and calculate average cell
displacement
XY <- sox9
  #average of upper half intensity and threshold based on BG value
and do hi/low split
XY$Q4intensity = rowMeans(XY[ , c(4,6)], na.rm=TRUE)
  #drop values below threshold, CHANGE THIS FOR EACH NEW SECTION
XY <- XY[! XY['Q4intensity'] <= bg,]
  #normalise values between 0 and 1 for Q4 intensity
process <- preProcess(as.data.frame(XY$Q4intensity),
method=c("range"))
norm_scale <- predict(process, as.data.frame(XY$Q4intensity))
XY <- cbind(XY, norm_scale)
colnames(XY)[10] ="norm"
sox9.hi =  sum(XY$norm >= 0.5)
sox9.low = sum(XY$norm < 0.5)

E <- XY[, 7:8]
CD<-centroid.displacement(E,0)
CS<-centroid.spacing(CD)

sox9Spacing <- centroid.spacing(CD)
```

```
#sox9Spacing <- unique(rapply(sox9Spacing, function(x) head(x,
1)))
sox9Spacing <- na.omit(sox9Spacing)

sox9.count <- length(XY[, 1])
sox9.cd <- mean(sox9Spacing)
sox9.stdev <- sd(sox9Spacing)

#tunel area and puncta count
puncta.count <- length(tunel[, 1])   #number of puncta
puncta.area <- (sum(tunel[, 3]))    #total area of TUNEL positive
puncta
puncta.min <- min(tunel$Area)
puncta.max <- max(tunel$Area)
puncta.avg <- mean(tunel$Area)

#add data as new row
# "embryo", "sox9+", "sox9+hi", "sox9+lo", "sox9cd", "sox9stdev",
"DAPI+", "DAPIcd", "DAPIstdev", "TUNEL", "TUNELarea", "TUNELmax",
"TUNELmin", "TUNELavg"
df <- c(embryo, sox9.count, sox9.hi, sox9.low, sox9.cd,
sox9.stdev, dapi.count, dapi.cd, dapi.stdev, puncta.count,
puncta.area, puncta.max, puncta.min, puncta.avg)
tab <- rbind(tab, df)
write.csv(tab, "~/Dropbox (The Francis
Crick)/Data/OFTC_IF/Data/OFTC_IF_E12.5_added.csv",
row.names=FALSE)
```

Reference List

Adler, J. and Parmryd, I. (2013) 'Colocalization analysis in fluorescence microscopy', *Methods in Molecular Biology (Clifton, N.J.)*, 931, pp. 97–109. Available at: https://doi.org/10.1007/978-1-62703-056-4_5.

Ahmed, I. and Anjum, F. (2023) 'Atrioventricular Septal Defect', in *StatPearls*. Treasure Island (FL): StatPearls Publishing. Available at: http://www.ncbi.nlm.nih.gov/books/NBK562194/ (Accessed: 27 November 2023).

Aït Yahya-Graison, E. *et al.* (2007) 'Classification of Human Chromosome 21 Gene-Expression Variations in Down Syndrome: Impact on Disease Phenotypes', *American Journal of Human Genetics*, 81(3), pp. 475–491.

Akiyama, H. *et al.* (2004) 'Essential role of Sox9 in the pathway that controls formation of cardiac valves and septa', *Proceedings of the National Academy of Sciences of the United States of America*, 101(17), pp. 6502–6507. Available at: https://doi.org/10.1073/pnas.0401711101.

Al-Dairy, A. *et al.* (2022) 'Repair of double orifice mitral valve with an atrioventricular septal defect in a girl with Ellis-Van Creveld syndrome', *Clinical Case Reports*, 10(5), p. e05888. Available at: https://doi.org/10.1002/ccr3.5888.

Altuna, M., Giménez, S. and Fortea, J. (2021) 'Epilepsy in Down Syndrome: A Highly Prevalent Comorbidity', *Journal of Clinical Medicine*, 10(13), p. 2776. Available at: https://doi.org/10.3390/jcm10132776.

Amr, N.H. (2018) 'Thyroid disorders in subjects with Down syndrome: an update', *Acta Bio Medica : Atenei Parmensis*, 89(1), pp. 132–139. Available at: https://doi.org/10.23750/abm.v89i1.7120.

Anderson, R.H. *et al.* (1998) 'The diagnostic features of atrioventricular septal defect with common atrioventricular junction', *Cardiology in the Young*, 8(1), pp. 33–49. Available at: https://doi.org/10.1017/S1047951100004613.

Anderson, R.H. *et al.* (2012) 'Normal and abnormal development of the intrapericardial arterial trunks in humans and mice', *Cardiovascular Research*, 95(1), pp. 108–115. Available at: https://doi.org/10.1093/cvr/cvs147.

Anderson, R.H. *et al.* (2014) 'The development of septation in the four-chambered heart', *Anatomical Record*, 297(8), pp. 1414–1429. Available at: https://doi.org/10.1002/ar.22949.

Anderson, R.H. *et al.* (2019) 'Remodeling of the Embryonic Interventricular Communication in Regard to the Description and Classification of Ventricular Septal Defects', *Anatomical Record*, 302(1), pp. 19–31. Available at: https://doi.org/10.1002/ar.24020.

Anderson, R.H. *et al.* (2023) 'Development of the arterial roots and ventricular outflow tracts', *Journal of Anatomy* [Preprint]. Available at: https://doi.org/10.1111/joa.13973.

Anderson, R.H. and Bamforth, S.D. (2022) 'Morphogenesis of the Mammalian Aortic Arch Arteries', *Frontiers in Cell and Developmental Biology*, 10. Available at: https://doi.org/10.3389/fcell.2022.892900.

Anderson, R.H., Brown, N.A. and Webb, S. (2002) 'Development and structure of the atrial septum', *Heart*, 88(1), pp. 104–110.

Andrés-Delgado, L. and Mercader, N. (2016) 'Interplay between cardiac function and heart development', *Biochimica et Biophysica Acta (BBA) - Molecular Cell Research*, 1863(7, Part B), pp. 1707–1716. Available at: https://doi.org/10.1016/j.bbamcr.2016.03.004.

Annabi, M.R., Kerndt, C.C. and Makaryus, A.N. (2023) 'Embryology, Atrioventricular Septum', in *StatPearls*. Treasure Island (FL): StatPearls Publishing. Available at: http://www.ncbi.nlm.nih.gov/books/NBK482372/ (Accessed: 2 December 2023).

Antiga, L. *et al.* (2008) 'An image-based modeling framework for patient-specific computational hemodynamics', *Medical & Biological Engineering & Computing*, 46(11), pp. 1097–1112. Available at: https://doi.org/10.1007/s11517-008-0420-1.

Antonarakis, S.E. (2017) 'Down syndrome and the complexity of genome dosage imbalance', *Nature Reviews Genetics*, 18(3), pp. 147–163. Available at: https://doi.org/10.1038/nrg.2016.154.

Arron, J.R. *et al.* (2006) 'NFAT dysregulation by increased dosage of DSCR1 and DYRK1A on chromosome 21', *Nature*, 441(7093), pp. 595–600. Available at: https://doi.org/10.1038/nature04678.

Arzt, M. *et al.* (2022) 'LABKIT: Labeling and Segmentation Toolkit for Big Image Data', *Frontiers in Computer Science*, 4. Available at: https://www.frontiersin.org/articles/10.3389/fcomp.2022.777728 (Accessed: 31 October 2023).

Bai, Y. *et al.* (2013) 'Bmp signaling represses Vegfa to promote outflow tract cushion development', *Development (Cambridge, England)*, 140(16), pp. 3395–3402. Available at: https://doi.org/10.1242/dev.097360.

Bajolle, F. *et al.* (2006) 'Rotation of the myocardial wall of the outflow tract is implicated in the normal positioning of the great arteries', *Circulation Research*, 98(3), pp. 421–428. Available at: https://doi.org/10.1161/01.RES.0000202800.85341.6e.

Barlow, G.M. *et al.* (2001) 'Down syndrome congenital heart disease: a narrowed region and a candidate gene', *Genetics in Medicine: Official Journal of the American College of Medical Genetics*, 3(2), pp. 91–101. Available at: https://doi.org/10.1097/00125817-200103000-00002.

Benech, J.C. and Romanelli, G. (2022) 'Atomic force microscopy indentation for nanomechanical characterization of live pathological cardiovascular/heart tissue

and cells', *Micron*, 158, p. 103287. Available at: https://doi.org/10.1016/j.micron.2022.103287.

Benhaourech, S., Drighil, A. and El Hammiri, A. (2016) 'Congenital heart disease and down syndrome: Various aspects of a confirmed association', *Cardiovascular Journal of Africa*, 27(5), pp. 287–290. Available at: https://doi.org/10.5830/CVJA-2016-019.

Benitez, R. and Toca-Herrera, J.L. (2014) 'Looking at cell mechanics with atomic force microscopy: experiment and theory', *Microscopy Research and Technique*, 77(11), pp. 947–958. Available at: https://doi.org/10.1002/jemt.22419.

van den Berg, G. *et al.* (2009) 'A caudal proliferating growth center contributes to both poles of the forming heart tube', *Circulation research*, 104(2), pp. 179–188. Available at: https://doi.org/10.1161/CIRCRESAHA.108.185843.

Bergholt, M., Serio, A. and Albro, M. (2019) 'Raman Spectroscopy: Guiding Light for the Extracellular Matrix', *Frontiers in Bioengineering and Biotechnology*, 7. Available at: https://www.frontiersin.org/articles/10.3389/fbioe.2019.00303 (Accessed: 17 December 2023).

Bergström, S. *et al.* (2016) 'Trends in Congenital Heart Defects in Infants With Down Syndrome', *Pediatrics*, 138(1), p. e20160123. Available at: https://doi.org/10.1542/peds.2016-0123.

Bittles, A.H. and Glasson, E.J. (2004) 'Clinical, social, and ethical implications of changing life expectancy in Down syndrome', *Developmental Medicine & Child Neurology*, 46(4), pp. 282–286. Available at: https://doi.org/10.1111/j.1469-8749.2004.tb00483.x.

Boehm, B. *et al.* (2011) 'A landmark-free morphometric staging system for the mouse limb bud', *Development*, 138(6), pp. 1227–1234. Available at: https://doi.org/10.1242/dev.057547.

Bolunduț, A.C., Lazea, C. and Mihu, C.M. (2023) 'Genetic Alterations of Transcription Factors and Signaling Molecules Involved in the Development of Congenital Heart Defects—A Narrative Review', *Children*, 10(5), p. 812. Available at: https://doi.org/10.3390/children10050812.

Bône, A. *et al.* (2018) 'Deformetrica 4: An Open-Source Software for Statistical Shape Analysis', in M. Reuter et al. (eds) *Shape in Medical Imaging*. Cham: Springer International Publishing (Lecture Notes in Computer Science), pp. 3–13. Available at: https://doi.org/10.1007/978-3-030-04747-4_1.

Boopathy, G.T.K. and Hong, W. (2019) 'Role of Hippo Pathway-YAP/TAZ Signaling in Angiogenesis', *Frontiers in Cell and Developmental Biology*, 7. Available at: https://www.frontiersin.org/articles/10.3389/fcell.2019.00049 (Accessed: 19 December 2023).

Brault, V. *et al.* (2021) 'Dyrk1a gene dosage in glutamatergic neurons has key effects in cognitive deficits observed in mouse models of MRD7 and Down

syndrome', *PLOS Genetics*, 17(9), p. e1009777. Available at: https://doi.org/10.1371/journal.pgen.1009777.

Briggs, L.E., Kakarla, J. and Wessels, A. (2012) 'The pathogenesis of atrial and atrioventricular septal defects with special emphasis on the role of the dorsal mesenchymal protrusion', *Differentiation; Research in Biological Diversity*, 84(1), pp. 117–130. Available at: https://doi.org/10.1016/j.diff.2012.05.006.

Brock, L.J. *et al.* (2016) 'Mapping cellular processes in the mesenchyme during palatal development in the absence of Tbx1 reveals complex proliferation changes and perturbed cell packing and polarity', *Journal of Anatomy*, 228(3), pp. 464–473. Available at: https://doi.org/10.1111/joa.12425.

Bruns, D.A. and Martinez, A. (2016) 'An analysis of cardiac defects and surgical interventions in 84 cases with full trisomy 18', *American Journal of Medical Genetics. Part A*, 170A(2), pp. 337–343. Available at: https://doi.org/10.1002/ajmg.a.37427.

Buijtendijk, M.F.J., Barnett, P. and van den Hoff, M.J.B. (2020) 'Development of the human heart', *American Journal of Medical Genetics. Part C, Seminars in Medical Genetics*, 184(1), pp. 7–22. Available at: https://doi.org/10.1002/ajmg.c.31778.

Burns, T. *et al.* (2016) 'The Dorsal Mesenchymal Protrusion and the Pathogenesis of Atrioventricular Septal Defects', *Journal of Cardiovascular Development and Disease*, 3(4), p. 29. Available at: https://doi.org/10.3390/jcdd3040029.

Bushdid, P.B. *et al.* (2003) 'NFATc3 and NFATc4 are required for cardiac development and mitochondrial function', *Circulation Research*, 92(12), pp. 1305–1313. Available at: https://doi.org/10.1161/01.RES.0000077045.84609.9F.

Cai, C.-L. *et al.* (2003) 'Isl1 identifies a cardiac progenitor population that proliferates prior to differentiation and contributes a majority of cells to the heart', *Developmental Cell*, 5(6), pp. 877–889. Available at: https://doi.org/10.1016/s1534-5807(03)00363-0.

Cai, J. *et al.* (2017) 'Fractal analysis of left ventricular trabeculations is associated with impaired myocardial deformation in healthy Chinese', *Journal of Cardiovascular Magnetic Resonance*, 19(1), p. 102. Available at: https://doi.org/10.1186/s12968-017-0413-z.

Camenisch, T.D. *et al.* (2000) 'Disruption of hyaluronan synthase-2 abrogates normal cardiac morphogenesis and hyaluronan-mediated transformation of epithelium to mesenchyme', *The Journal of Clinical Investigation*, 106(3), pp. 349–360. Available at: https://doi.org/10.1172/JCI10272.

Camenisch, T.D. *et al.* (2001) 'Regulation of cardiac cushion development by hyaluronan', *Experimental & Clinical Cardiology*, 6(1), pp. 4–10.

Campagnola, P. j. and Dong, C.-Y. (2011) 'Second harmonic generation microscopy: principles and applications to disease diagnosis', *Laser & Photonics Reviews*, 5(1), pp. 13–26. Available at: https://doi.org/10.1002/lpor.200910024.

Captur, G. *et al.* (2013) 'Quantification of left ventricular trabeculae using fractal analysis', *Journal of Cardiovascular Magnetic Resonance*, 15(1), p. 36. Available at: https://doi.org/10.1186/1532-429X-15-36.

Chen, B. *et al.* (2000) 'Mice mutant for Egfr and Shp2 have defective cardiac semilunar valvulogenesis', *Nature Genetics*, 24(3), pp. 296–299. Available at: https://doi.org/10.1038/73528.

Chen, X. *et al.* (2012) 'Second harmonic generation microscopy for quantitative analysis of collagen fibrillar structure', *Nature Protocols*, 7(4), pp. 654–669. Available at: https://doi.org/10.1038/nprot.2012.009.

Chen, X. *et al.* (2020) 'Molecular Mechanism of Hippo–YAP1/TAZ Pathway in Heart Development, Disease, and Regeneration', *Frontiers in Physiology*, 11. Available at: https://www.frontiersin.org/articles/10.3389/fphys.2020.00389 (Accessed: 31 October 2023).

Cheng, Y., Mao, M. and Lu, Y. (2022) 'The biology of YAP in programmed cell death', *Biomarker Research*, 10(1), p. 34. Available at: https://doi.org/10.1186/s40364-022-00365-5.

Choquet, C., Kelly, R.G. and Miquerol, L. (2019) 'Defects in Trabecular Development Contribute to Left Ventricular Noncompaction', *Pediatric Cardiology*, 40(7), pp. 1331–1338. Available at: https://doi.org/10.1007/s00246-019-02161-9.

Christoffels, V.M. *et al.* (2000) 'Chamber formation and morphogenesis in the developing mammalian heart', *Developmental Biology*, 223(2), pp. 266–278. Available at: https://doi.org/10.1006/dbio.2000.9753.

Cialla-May, D., Schmitt, M. and Popp, J. (2019) 'Theoretical principles of Raman spectroscopy', *Physical Sciences Reviews*, 4(6). Available at: https://doi.org/10.1515/psr-2017-0040.

Cignoni, P. *et al.* (2008) *MeshLab: an Open-Source Mesh Processing Tool*. The Eurographics Association. Available at: https://doi.org/10.2312/LocalChapterEvents/ItalChap/ItalianChapConf2008/129-136.

Conti, A. *et al.* (2007) 'Altered expression of mitochondrial and extracellular matrix genes in the heart of human fetuses with chromosome 21 trisomy', *BMC Genomics*, 8, p. 268. Available at: https://doi.org/10.1186/1471-2164-8-268.

Contreras-Ramos, A. *et al.* (2008) 'Normal Development of the Muscular Region of the Interventricular Septum – I. The Significance of the Ventricular Trabeculations', *Anatomia, Histologia, Embryologia*, 37(5), pp. 344–351. Available at: https://doi.org/10.1111/j.1439-0264.2008.00852.x.

Contreras-Ramos, A. *et al.* (2009) 'Normal Development of the Muscular Region of the Interventricular Septum. II. The Importance of Myocardial Proliferation', *Anatomia, Histologia, Embryologia*, 38(3), pp. 219–228. Available at: https://doi.org/10.1111/j.1439-0264.2008.00926.x.

Costell, M. *et al.* (2002) 'Hyperplastic Conotruncal Endocardial Cushions and Transposition of Great Arteries in Perlecan-Null Mice', *Circulation Research*, 91(2), pp. 158–164. Available at: https://doi.org/10.1161/01.RES.0000026056.81424.DA.

Dakkak, W. and Oliver, T.I. (2023) 'Ventricular Septal Defect', in *StatPearls*. Treasure Island (FL): StatPearls Publishing. Available at: http://www.ncbi.nlm.nih.gov/books/NBK470330/ (Accessed: 5 December 2023).

Danielian, P.S. *et al.* (1998) 'Modification of gene activity in mouse embryos in utero by a tamoxifen-inducible form of Cre recombinase', *Current Biology*, 8(24), pp. S1–S2. Available at: https://doi.org/10.1016/S0960-9822(07)00562-3.

Darrigrand, J.F. *et al.* (2020) 'Dullard-mediated smad1/5/8 inhibition controls mouse cardiac neural crest cells condensation and outflow tract septation', *eLife*, 9. Available at: https://doi.org/10.7554/eLife.50325.

Davisson, M., Schmidt, C. and Akeson, E. (1990) 'Segmental trisomy of murine chromosome 16: a new model system for studying Down syndrome - PubMed', *Prog Clin Biol Res*, (360), pp. 263–80.

De Bono, C. *et al.* (2018) 'T-box genes and retinoic acid signaling regulate the segregation of arterial and venous pole progenitor cells in the murine second heart field', *Human Molecular Genetics*, 27(21), pp. 3747–3760. Available at: https://doi.org/10.1093/hmg/ddy266.

Delabar, J.M. *et al.* (1993) 'Molecular mapping of twenty-four features of Down syndrome on chromosome 21', *European journal of human genetics: EJHG*, 1(2), pp. 114–124. Available at: https://doi.org/10.1159/000472398.

Délot, E.C. *et al.* (2003) 'BMP signaling is required for septation of the outflow tract of the mammalian heart', *Development (Cambridge, England)*, 130(1), pp. 209–220. Available at: https://doi.org/10.1242/dev.00181.

Dessauvagie, B.F. *et al.* (2015) 'Validation of mitosis counting by automated phosphohistone H3 (PHH3) digital image analysis in a breast carcinoma tissue microarray', *Pathology*, 47(4), pp. 329–334. Available at: https://doi.org/10.1097/PAT.0000000000000248.

Dice, J.E. and Bhatia, J. (2007) 'Patent Ductus Arteriosus: An Overview', *The Journal of Pediatric Pharmacology and Therapeutics : JPPT*, 12(3), pp. 138–146. Available at: https://doi.org/10.5863/1551-6776-12.3.138.

Dimopoulos, K. *et al.* (2023) 'Cardiovascular Complications of Down Syndrome: Scoping Review and Expert Consensus', *Circulation*, 147(5), pp. 425–441. Available at: https://doi.org/10.1161/CIRCULATIONAHA.122.059706.

Ding, Y. *et al.* (2018) 'Light-sheet Fluorescence Microscopy for the Study of the Murine Heart', *JoVE (Journal of Visualized Experiments)*, (139), p. e57769. Available at: https://doi.org/10.3791/57769.

Dinsmore, C.J., Ke, C.-Y. and Soriano, P. (2022) 'The Wnt1-Cre2 transgene is active in the male germline', *Genesis (New York, N.Y.: 2000)*, 60(3), p. e23468. Available at: https://doi.org/10.1002/dvg.23468.

Dodou, E. *et al.* (2004) 'Mef2c is a direct transcriptional target of ISL1 and GATA factors in the anterior heart field during mouse embryonic development', *Development (Cambridge, England)*, 131(16), pp. 3931–3942. Available at: https://doi.org/10.1242/dev.01256.

Dor, Y. *et al.* (2001) 'A novel role for VEGF in endocardial cushion formation and its potential contribution to congenital heart defects', *Development (Cambridge, England)*, 128(9), pp. 1531–1538. Available at: https://doi.org/10.1242/dev.128.9.1531.

Duchemin, A.-L., Vignes, H. and Vermot, J. (2019) 'Mechanically activated piezo channels modulate outflow tract valve development through the Yap1 and Klf2-Notch signaling axis', *eLife*, 8, p. e44706. Available at: https://doi.org/10.7554/eLife.44706.

Duchon, A. *et al.* (2011) 'Identification of the translocation breakpoints in the Ts65Dn and Ts1Cje mouse lines: Relevance for modeling down syndrome', *Mammalian Genome*, 22(11–12), pp. 674–684. Available at: https://doi.org/10.1007/s00335-011-9356-0.

Duchon, A. and Herault, Y. (2016) 'DYRK1A, a Dosage-Sensitive Gene Involved in Neurodevelopmental Disorders, Is a Target for Drug Development in Down Syndrome', *Frontiers in Behavioral Neuroscience*, 10. Available at: https://www.frontiersin.org/articles/10.3389/fnbeh.2016.00104 (Accessed: 17 December 2023).

Dunlevy, L. *et al.* (2010) 'Down's syndrome-like cardiac developmental defects in embryos of the transchromosomic Tc1 mouse', *Cardiovascular Research*, 88(2), pp. 287–295. Available at: https://doi.org/10.1093/cvr/cvq193.

Dupont, S. *et al.* (2011) 'Role of YAP/TAZ in mechanotransduction', *Nature*, 474(7350), pp. 179–183. Available at: https://doi.org/10.1038/nature10137.

Durrleman, S. *et al.* (2014) 'Morphometry of anatomical shape complexes with dense deformations and sparse parameters', *NeuroImage*, 101, pp. 35–49. Available at: https://doi.org/10.1016/j.neuroimage.2014.06.043.

Dyer, L.A. and Kirby, M.L. (2009) 'The Role of Secondary Heart Field in Cardiac Development', *Developmental biology*, 336(2), pp. 137–144. Available at: https://doi.org/10.1016/j.ydbio.2009.10.009.

Economou, A.D. *et al.* (2013) 'Whole population cell analysis of a landmark-rich mammalian epithelium reveals multiple elongation mechanisms', *Development (Cambridge)*, 140(23), pp. 4740–4750. Available at: https://doi.org/10.1242/dev.096545.

Edelsbrunner, H. and Mücke, E.P. (1994) 'Three-dimensional alpha shapes', *ACM Transactions on Graphics*, 13(1), pp. 43–72. Available at: https://doi.org/10.1145/174462.156635.

Epstein, J.A. *et al.* (2000) 'Migration of cardiac neural crest cells in Splotch embryos', *Development*, 127(9), pp. 1869–1878. Available at: https://doi.org/10.1242/dev.127.9.1869.

Evans, J.M. *et al.* (2014) 'Association Between Down Syndrome and In-Hospital Death Among Children Undergoing Surgery for Congenital Heart Disease', *Circulation: Cardiovascular Quality and Outcomes*, 7(3), pp. 445–452. Available at: https://doi.org/10.1161/CIRCOUTCOMES.113.000764.

Fayzullina, S. and Martin, L.J. (2014) 'Detection and Analysis of DNA Damage in Mouse Skeletal Muscle In Situ Using the TUNEL Method', *Journal of Visualized Experiments : JoVE*, (94), p. 52211. Available at: https://doi.org/10.3791/52211.

Federici, F. *et al.* (2012) 'Integrated genetic and computation methods for in planta cytometry', *Nature Methods*, 9(5), pp. 483–485. Available at: https://doi.org/10.1038/nmeth.1940.

Fedorov, A. *et al.* (2012) '3D Slicer as an image computing platform for the Quantitative Imaging Network', *Magnetic Resonance Imaging*, 30(9), pp. 1323–1341. Available at: https://doi.org/10.1016/j.mri.2012.05.001.

Ferrés, M.A. *et al.* (2016) 'Perinatal Natural History of the Ts1Cje Mouse Model of Down Syndrome: Growth Restriction, Early Mortality, Heart Defects, and Delayed Development', *PLOS ONE*, 11(12), p. e0168009. Available at: https://doi.org/10.1371/journal.pone.0168009.

Fischer, M. *et al.* (2022) 'Coordinating gene expression during the cell cycle', *Trends in Biochemical Sciences*, 47(12), pp. 1009–1022. Available at: https://doi.org/10.1016/j.tibs.2022.06.007.

Francou, A., De Bono, C. and Kelly, R.G. (2017) 'Epithelial tension in the second heart field promotes mouse heart tube elongation', *Nature Communications*, 8(1), p. 14770. Available at: https://doi.org/10.1038/ncomms14770.

Fu, M. *et al.* (2022) 'The Hippo signalling pathway and its implications in human health and diseases', *Signal Transduction and Targeted Therapy*, 7(1), pp. 1–20. Available at: https://doi.org/10.1038/s41392-022-01191-9.

Fuhs, T. *et al.* (2023) 'Combining atomic force microscopy and fluorescence-based techniques to explore mechanical properties of naive and ischemia-affected brain regions in mice', *Scientific Reports*, 13(1), p. 12774. Available at: https://doi.org/10.1038/s41598-023-39277-1.

Furlong-Dillard, J. *et al.* (2018) 'Resource Use and Morbidities in Pediatric Cardiac Surgery Patients with Genetic Conditions', *The Journal of Pediatrics*, 193, pp. 139-146.e1. Available at: https://doi.org/10.1016/j.jpeds.2017.09.085.

Galati, D.F. *et al.* (2018) 'Trisomy 21 Represses Cilia Formation and Function', *Developmental cell*, 46(5), pp. 641-650.e6. Available at: https://doi.org/10.1016/j.devcel.2018.07.008.

Gallina, D. and Lincoln, J. (2019) 'Dynamic Expression Profiles of Sox9 in Embryonic, Post Natal, and Adult Heart Valve Cell Populations', *The Anatomical Record*, 302(1), pp. 108–116. Available at: https://doi.org/10.1002/ar.23913.

Gao, S., Li, X. and Amendt, B.A. (2013) 'Understanding the Role of Tbx1 as a Candidate Gene for 22q11.2 Deletion Syndrome', *Current allergy and asthma reports*, 13(6), p. 10.1007/s11882-013-0384–6. Available at: https://doi.org/10.1007/s11882-013-0384-6.

Garcia-Puig, A. *et al.* (2019) 'Proteomics Analysis of Extracellular Matrix Remodeling During Zebrafish Heart Regeneration', *Molecular & Cellular Proteomics : MCP*, 18(9), pp. 1745–1755. Available at: https://doi.org/10.1074/mcp.RA118.001193.

Gardiner, J.D., Behnsen, J. and Brassey, C.A. (2018) 'Alpha shapes: determining 3D shape complexity across morphologically diverse structures', *BMC evolutionary biology*, 18(1), p. 184. Available at: https://doi.org/10.1186/s12862-018-1305-z.

Gautier, H.O.B. *et al.* (2015) 'Atomic force microscopy-based force measurements on animal cells and tissues', *Methods in Cell Biology*, 125, pp. 211–235. Available at: https://doi.org/10.1016/bs.mcb.2014.10.005.

George, R.M., Maldonado-Velez, G. and Firulli, A.B. (2020) 'The heart of the neural crest: cardiac neural crest cells in development and regeneration', *Development*, 147(20), p. dev188706. Available at: https://doi.org/10.1242/dev.188706.

Geyer, S.H. *et al.* (2017) 'High-resolution Episcopic Microscopy (HREM) - Simple and Robust Protocols for Processing and Visualizing Organic Materials', *Journal of Visualized Experiments : JoVE*, (125), p. 56071. Available at: https://doi.org/10.3791/56071.

Ghimire, L., Tawffik, O. and Schroeder, V.A. (2013) 'Combined obstructive hypertrophic cardiomyopathy and double outlet right ventricle in an infant with Down syndrome', *The American Journal of Case Reports*, 14, pp. 453–458. Available at: https://doi.org/10.12659/AJCR.889581.

Gittenberger-De Groot, A.C. *et al.* (2003) 'Collagen type VI expression during cardiac development and in human fetuses with trisomy 21', *The Anatomical Record Part A: Discoveries in Molecular, Cellular, and Evolutionary Biology*, 275A(2), pp. 1109–1116. Available at: https://doi.org/10.1002/ar.a.10126.

Goddeeris, M.M. *et al.* (2008) 'Intracardiac septation requires hedgehog-dependent cellular contributions from outside the heart', *Development*, 135(10), pp. 1887–1895. Available at: https://doi.org/10.1242/dev.016147.

Graham, A. *et al.* (2023) ‘A revised terminology for the pharyngeal arches and the arch arteries’, *Journal of Anatomy*, 243(4), pp. 564–569. Available at: https://doi.org/10.1111/joa.13890.

Graham, A., Okabe, M. and Quinlan, R. (2005) ‘The role of the endoderm in the development and evolution of the pharyngeal arches’, *Journal of Anatomy*, 207(5), pp. 479–487. Available at: https://doi.org/10.1111/j.1469-7580.2005.00472.x.

Granados-Riveron, J.T. and Brook, J.D. (2012) ‘The Impact of Mechanical Forces in Heart Morphogenesis’, *Circulation: Cardiovascular Genetics*, 5(1), pp. 132–142. Available at: https://doi.org/10.1161/CIRCGENETICS.111.961086.

Green, J.B.A. (2022) ‘Resolving morphogenesis into quantifiable cell behaviours’, *Development*, 149(21), p. dev199794. Available at: https://doi.org/10.1242/dev.199794.

Gribble, S.M. *et al.* (2013) ‘Massively Parallel Sequencing Reveals the Complex Structure of an Irradiated Human Chromosome on a Mouse Background in the Tc1 Model of Down Syndrome’, *PLoS ONE*. Edited by T. Thomas, 8(4), p. e60482. Available at: https://doi.org/10.1371/journal.pone.0060482.

Griepentrog, M., Krämer, G. and Cappella, B. (2013) ‘Comparison of nanoindentation and AFM methods for the determination of mechanical properties of polymers’, *Polymer Testing*, 32(3), pp. 455–460. Available at: https://doi.org/10.1016/j.polymertesting.2013.01.011.

Grossman, T.R. *et al.* (2011) ‘Over-Expression of DSCAM and COL6A2 Cooperatively Generates Congenital Heart Defects’, *PLoS Genet*, 7(11), p. 1002344. Available at: https://doi.org/10.1371/journal.pgen.1002344.

Gupta, M., Dhanasekaran, A.R. and Gardiner, K.J. (2016) ‘Mouse models of Down syndrome: gene content and consequences’, *Mammalian Genome*, 27(11–12), pp. 538–555. Available at: https://doi.org/10.1007/s00335-016-9661-8.

Handschuh, S. and Glösmann, M. (2022) ‘Mouse embryo phenotyping using X-ray microCT’, *Frontiers in Cell and Developmental Biology*, 10. Available at: https://www.frontiersin.org/articles/10.3389/fcell.2022.949184 (Accessed: 27 November 2023).

Harmon, A.W. and Nakano, A. (2013) ‘Nkx2-5 Lineage Tracing Visualizes the Distribution of Second Heart Field-Derived Aortic Smooth Muscle’, *Genesis (New York, N.Y. : 2000)*, 51(12), pp. 862–869. Available at: https://doi.org/10.1002/dvg.22721.

Head, E. *et al.* (2012) ‘Alzheimer’s Disease in Down Syndrome’, *European journal of neurodegenerative disease*, 1(3), pp. 353–364.

Henderson, D.J. *et al.* (2022) ‘Development of the Human Arterial Valves: Understanding Bicuspid Aortic Valve’, *Frontiers in Cardiovascular Medicine*, 8. Available at: https://www.frontiersin.org/articles/10.3389/fcvm.2021.802930 (Accessed: 7 December 2023).

Henderson, D.J., Eley, L. and Chaudhry, B. (2020) 'New Concepts in the Development and Malformation of the Arterial Valves', *Journal of Cardiovascular Development and Disease*, 7(4), p. 38. Available at: https://doi.org/10.3390/jcdd7040038.

Hernandez, D. and Fisher, E.M.C. (1996) 'Down syndrome genetics: unravelling a multifactorial disorder', *Human Molecular Genetics*, 5(Supplement_1), pp. 1411–1416. Available at: https://doi.org/10.1093/hmg/5.Supplement_1.1411.

Hierck, B.P., Van der Heiden, K., Poelma, C., *et al.* (2008) 'Fluid Shear Stress and Inner Curvature Remodeling of the Embryonic Heart. Choosing the Right Lane!', *The Scientific World Journal*, 8, pp. 212–222. Available at: https://doi.org/10.1100/tsw.2008.42.

Hierck, B.P., Van der Heiden, K., Alkemade, F.E., *et al.* (2008) 'Primary cilia sensitize endothelial cells for fluid shear stress', *Developmental Dynamics: An Official Publication of the American Association of Anatomists*, 237(3), pp. 725–735. Available at: https://doi.org/10.1002/dvdy.21472.

High, F.A. *et al.* (2007) 'An essential role for Notch in neural crest during cardiovascular development and smooth muscle differentiation', *The Journal of Clinical Investigation*, 117(2), pp. 353–363. Available at: https://doi.org/10.1172/JCI30070.

van den Hoff, M.J.B. and Wessels, A. (2020) 'Musculariza tion of the Mesenchymal Outlet Septum during Cardiac Development', *Journal of Cardiovascular Development and Disease*, 7(4), p. 51. Available at: https://doi.org/10.3390/jcdd7040051.

Holmes, G. (2014) 'Gastrointestinal disorders in Down syndrome', *Gastroenterology and Hepatology From Bed to Bench*, 7(1), pp. 6–8.

Hopkins, T.I.R. *et al.* (2021) 'Micromechanical mapping of the intact ovary interior reveals contrasting mechanical roles for follicles and stroma', *Biomaterials*, 277, p. 121099. Available at: https://doi.org/10.1016/j.biomaterials.2021.121099.

Hopkins, T.M. *et al.* (2015) 'Combining Micro-Computed Tomography with Histology to Analyze Biomedical Implants for Peripheral Nerve Repair', *Journal of neuroscience methods*, 255, pp. 122–130. Available at: https://doi.org/10.1016/j.jneumeth.2015.08.016.

Hubrecht, R.C. and Carter, E. (2019) 'The 3Rs and Humane Experimental Technique: Implementing Change', *Animals : an Open Access Journal from MDPI*, 9(10), p. 754. Available at: https://doi.org/10.3390/ani9100754.

Ivanovitch, K., Esteban, I. and Torres, M. (2017) 'Growth and Morphogenesis during Early Heart Development in Amniotes', *Journal of Cardiovascular Development and Disease*, 4(4), p. 20. Available at: https://doi.org/10.3390/jcdd4040020.

Ivanovitch, K., Temiño, S. and Torres, M. (2017) 'Live imaging of heart tube development in mouse reveals alternating phases of cardiac differentiation and morphogenesis', *eLife*, 6, pp. 1–30. Available at: https://doi.org/10.7554/eLife.30668.

Jacot, J.G., Martin, J.C. and Hunt, D.L. (2010) 'Mechanobiology of cardiomyocyte development', *Journal of Biomechanics*, 43(1), pp. 93–98. Available at: https://doi.org/10.1016/j.jbiomech.2009.09.014.

Jain, R. *et al.* (2011) 'Cardiac neural crest orchestrates remodeling and functional maturation of mouse semilunar valves', *The Journal of Clinical Investigation*, 121(1), p. 422. Available at: https://doi.org/10.1172/JCI44244.

Jewett, C.E. *et al.* (2023) 'Trisomy 21 induces pericentrosomal crowding delaying primary ciliogenesis and mouse cerebellar development', *eLife*. Edited by J.F. Reiter, A. Akhmanova, and J.F. Reiter, 12, p. e78202. Available at: https://doi.org/10.7554/eLife.78202.

Jiang, X. *et al.* (2000) 'Fate of the mammalian cardiac neural crest', *Development*, 127(8), pp. 1607–1616. Available at: https://doi.org/10.1242/dev.127.8.1607.

Jiang, X. *et al.* (2002) 'Normal fate and altered function of the cardiac neural crest cell lineage in retinoic acid receptor mutant embryos', *Mechanisms of Development*, 117(1), pp. 115–122. Available at: https://doi.org/10.1016/S0925-4773(02)00206-X.

Kelly, R.G., Buckingham, M.E. and Moorman, A.F. (2014) 'Heart Fields and Cardiac Morphogenesis', *Cold Spring Harbor Perspectives in Medicine*, 4(10), p. a015750. Available at: https://doi.org/10.1101/cshperspect.a015750.

Kern, C.B. *et al.* (2006) 'Proteolytic Cleavage of Versican During Cardiac Cushion Morphogenesis', *Developmental dynamics : an official publication of the American Association of Anatomists*, 235(8), pp. 2238–2247. Available at: https://doi.org/10.1002/dvdy.20838.

Kern, C.B. *et al.* (2010) 'Reduced versican cleavage due to Adamts9 haploinsufficiency is associated with cardiac and aortic anomalies', *Matrix biology : journal of the International Society for Matrix Biology*, 29(4), pp. 304–316. Available at: https://doi.org/10.1016/j.matbio.2010.01.005.

Keyte, A. and Hutson, M.R. (2008) 'The Neural Crest in Cardiac Congenital Anomalies', *Bone*, 23(1), pp. 1–7. Available at: https://doi.org/10.1038/jid.2014.371.

Keyte, A. and Hutson, M.R. (2012) 'The Neural Crest in Cardiac Congenital Anomalies', *Differentiation; Research in Biological Diversity*, 84(1), pp. 25–40. Available at: https://doi.org/10.1016/j.diff.2012.04.005.

Kim, J.-S. *et al.* (2001) 'Development of the Myocardium of the Atrioventricular Canal and the Vestibular Spine in the Human Heart', *Circulation Research*, 88(4), pp. 395–402. Available at: https://doi.org/10.1161/01.RES.88.4.395.

Kirby, Margaret L., Gale, T.F. and Stewart, D.E. (1983) 'Neural crest cells contribute to normal aorticopulmonary septation', *Science*, 220(4601), pp. 1059–1061. Available at: https://doi.org/10.1126/SCIENCE.6844926.

Kirby, M. L., Gale, T.F. and Stewart, D.E. (1983) 'Neural crest cells contribute to normal aorticopulmonary septation', *Science (New York, N.Y.)*, 220(4601), pp. 1059–1061. Available at: https://doi.org/10.1126/science.6844926.

Kirby, M.L. and Waldo, K.L. (1990) 'Role of neural crest in congenital heart disease', *Circulation*, 82(2), pp. 332–340. Available at: https://doi.org/10.1161/01.cir.82.2.332.

Kirby, M.L. and Waldo, K.L. (1995) 'Neural Crest and Cardiovascular Patterning', *Circulation Research*, 77(2), pp. 211–215. Available at: https://doi.org/10.1161/01.RES.77.2.211.

Klena, N.T., Gibbs, B.C. and Lo, C.W. (2017) 'Cilia and Ciliopathies in Congenital Heart Disease', *Cold Spring Harbor Perspectives in Biology*, 9(8), p. a028266. Available at: https://doi.org/10.1101/cshperspect.a028266.

Kontomaris, S.V. and Malamou, A. (2020) 'Hertz model or Oliver & Pharr analysis? Tutorial regarding AFM nanoindentation experiments on biological samples', *Materials Research Express*, 7(3), p. 033001. Available at: https://doi.org/10.1088/2053-1591/ab79ce.

Korbel, J.O. *et al.* (2009) 'The genetic architecture of Down syndrome phenotypes revealed by high-resolution analysis of human segmental trisomies', *Proceedings of the National Academy of Sciences*, 106(29), pp. 12031–12036. Available at: https://doi.org/10.1073/pnas.0813248106.

Kovacic, J.C. *et al.* (2019) 'Endothelial to Mesenchymal Transition in Cardiovascular Disease', *Journal of the American College of Cardiology*, 73(2), pp. 190–209. Available at: https://doi.org/10.1016/j.jacc.2018.09.089.

Kramer, T.C. (1942) 'The partitioning of the truncus and conus and the formation of the membranous portion of the interventricular septum in the human heart', *American Journal of Anatomy*, 71(3), pp. 343–370. Available at: https://doi.org/10.1002/aja.1000710303.

Kreicher, K.L. *et al.* (2018) 'Characteristics and Progression of Hearing Loss in Children with Down Syndrome', *The Journal of Pediatrics*, 193, pp. 27-33.e2. Available at: https://doi.org/10.1016/j.jpeds.2017.09.053.

Krishnan, A. *et al.* (2014) 'A detailed comparison of mouse and human cardiac development', *Pediatric Research*, 76(6), pp. 500–507. Available at: https://doi.org/10.1038/pr.2014.128.

Kruithof, B.P.T. *et al.* (2003) 'Cardiac muscle cell formation after development of the linear heart tube', *Developmental Dynamics: An Official Publication of the American Association of Anatomists*, 227(1), pp. 1–13. Available at: https://doi.org/10.1002/dvdy.10269.

Lana-Elola, E. *et al.* (2016) 'Genetic dissection of Down syndrome- associated congenital heart defects using a new mouse mapping panel', *eLife*, 5(JANUARY2016). Available at: https://doi.org/10.7554/eLife.11614.001.

Lana-Elola, E. *et al.* (2021) 'Comprehensive phenotypic analysis of the Dp1Tyb mouse strain reveals a broad range of Down syndrome-related phenotypes', *Disease Models & Mechanisms*, 14(10), p. dmm049157. Available at: https://doi.org/10.1242/dmm.049157.

Lana-Elola, E. *et al.* (2023) 'Congenital heart defects in Down syndrome are caused by increased dosage of DYRK1A'. bioRxiv, p. 2023.09.18.558244. Available at: https://doi.org/10.1101/2023.09.18.558244.

Lashkarinia, S.S. *et al.* (2023) 'Embryonic aortic arch material properties obtained by optical coherence tomography-guided micropipette aspiration', *Journal of Biomechanics*, 146, p. 111392. Available at: https://doi.org/10.1016/j.jbiomech.2022.111392.

Lejeune, J., Gauthier, M. and Turpin, R. (1959) '[Human chromosomes in tissue cultures]', *Comptes Rendus Hebdomadaires Des Seances De l'Academie Des Sciences*, 248(4), pp. 602–603.

Lewis, A.E. *et al.* (2013) 'The widely used Wnt1-Cre transgene causes developmental phenotypes by ectopic activation of Wnt signaling', *Developmental Biology*, 379(2), pp. 229–234. Available at: https://doi.org/10.1016/j.ydbio.2013.04.026.

Li, J., Chatzeli, L., *et al.* (2016) 'Epithelial stratification and placode invagination are separable functions in early morphogenesis of the molar tooth', *Development*, 143(4), pp. 670–681. Available at: https://doi.org/10.1242/dev.130187.

Li, Jingjing, Miao, L., *et al.* (2016) 'Single-Cell Lineage Tracing Reveals that Oriented Cell Division Contributes to Trabecular Morphogenesis and Regional Specification', *Cell Reports*, 15(1), pp. 158–170. Available at: https://doi.org/10.1016/j.celrep.2016.03.012.

Li, Z. *et al.* (2007) 'Duplication of the entire 22.9 Mb human chromosome 21 syntenic region on mouse chromosome 16 causes cardiovascular and gastrointestinal abnormalities', *Human Molecular Genetics*, 16(11), pp. 1359–1366. Available at: https://doi.org/10.1093/hmg/ddm086.

Lin, J.-H.I. *et al.* (2020) 'Mutation of LRP1 in cardiac neural crest cells causes congenital heart defects by perturbing outflow lengthening', *Communications Biology*, 3(1), pp. 1–12. Available at: https://doi.org/10.1038/s42003-020-1035-9.

Lindberg, M.F. *et al.* (2023) 'Chemical, Biochemical, Cellular, and Physiological Characterization of Leucettinib-21, a Down Syndrome and Alzheimer's Disease Drug Candidate', *Journal of Medicinal Chemistry*, 66(23), pp. 15648–15670. Available at: https://doi.org/10.1021/acs.jmedchem.3c01888.

Liu, C. *et al.* (2011a) 'Genetic analysis of Down syndrome-associated heart defects in mice', *Human Genetics*, 130(5), pp. 623–632. Available at: https://doi.org/10.1007/s00439-011-0980-2.

Liu, C. *et al.* (2011b) 'Genetic analysis of Down syndrome-associated heart defects in mice', *Human Genetics*, 130(5), pp. 623–632. Available at: https://doi.org/10.1007/s00439-011-0980-2.

Liu, C. *et al.* (2014) 'Engineered chromosome-based genetic mapping establishes a 3.7-Mb critical genomic region for Down syndrome-associated heart defects in mice', *Human genetics*, 133(6), pp. 743–753. Available at: https://doi.org/10.1007/s00439-013-1407-z.

Liu, H. *et al.* (2022) 'Migration deficits of the neural crest caused by CXADR triplication in a human Down syndrome stem cell model', *Cell Death & Disease*, 13(12), pp. 1–12. Available at: https://doi.org/10.1038/s41419-022-05481-6.

Li-Villarreal, N. *et al.* (2023) 'Three-dimensional microCT imaging of mouse heart development from early post-implantation to late fetal stages', *Mammalian Genome*, 34(2), pp. 156–165. Available at: https://doi.org/10.1007/s00335-022-09976-7.

Loane, M. *et al.* (2013) 'Twenty-year trends in the prevalence of Down syndrome and other trisomies in Europe: impact of maternal age and prenatal screening', *European Journal of Human Genetics*, 21(1), pp. 27–33. Available at: https://doi.org/10.1038/ejhg.2012.94.

Lockhart, M. *et al.* (2011) 'Extracellular Matrix and Heart Development', *Birth defects research. Part A, Clinical and molecular teratology*, 91(6), pp. 535–550. Available at: https://doi.org/10.1002/bdra.20810.

van der Loo, J.J., Jacot, J. and Bovendeerd, P.H.M. (2008) 'The Development in Cardiac Stiffness in Embryonic, Neonatal and Adult Mice Evaluated with Atomic Force Microscopy', *BMTE 08.45, Univ. California, San Diego (UCSD), Tech. Univ., San Diego* [Preprint]. Available at: http:// www.mate.tue.nl/mate/pdfs/9706.pdf.

Lopez, A.L. and Larina, I.V. (2019) 'Second harmonic generation microscopy of early embryonic mouse hearts', *Biomedical Optics Express*, 10(6), pp. 2898–2908. Available at: https://doi.org/10.1364/BOE.10.002898.

Lyle, R. *et al.* (2009) 'Genotype-phenotype correlations in Down syndrome identified by array CGH in 30 cases of partial trisomy and partial monosomy chromosome 21', *European journal of human genetics: EJHG*, 17(4), pp. 454–466. Available at: https://doi.org/10.1038/ejhg.2008.214.

Lyubchenko, Y.L., Gall, A.A. and Shlyakhtenko, L.S. (2014) 'Visualization of DNA and Protein-DNA Complexes with Atomic Force Microscopy', *Methods in molecular biology (Clifton, N.J.)*, 1117, pp. 367–384. Available at: https://doi.org/10.1007/978-1-62703-776-1_17.

Ma, L. *et al.* (2005) 'Bmp2 is essential for cardiac cushion epithelial-mesenchymal transition and myocardial patterning', *Development (Cambridge, England)*, 132(24), pp. 5601–5611. Available at: https://doi.org/10.1242/dev.02156.

MacGrogan, D. *et al.* (2016) 'Sequential Ligand-Dependent Notch Signaling Activation Regulates Valve Primordium Formation and Morphogenesis', *Circulation Research*, 118(10), pp. 1480–1497. Available at: https://doi.org/10.1161/CIRCRESAHA.115.308077.

Majkut, S., Dingal, P.C.D.P. and Discher, D.E. (2014) 'Stress sensitivity and mechanotransduction during heart development', *Current biology: CB*, 24(10), pp. R495-501. Available at: https://doi.org/10.1016/j.cub.2014.04.027.

Malt, E.A. *et al.* (2013) 'Health and disease in adults with Down syndrome', *Tidsskrift for Den Norske Laegeforening: Tidsskrift for Praktisk Medicin, Ny Raekke*, 133(3), pp. 290–294. Available at: https://doi.org/10.4045/tidsskr.12.0390.

Markwald, R.R. *et al.* (1981) 'Endocardial cushion tissue development: structural analyses on the attachment of extracellular matrix to migrating mesenchymal cell surfaces', *Scanning Electron Microscopy*, (Pt 2), pp. 261–274.

Marlow, E.C. *et al.* (2021) 'Leukemia Risk in a Cohort of 3.9 Million Children With and Without Down Syndrome', *The Journal of pediatrics*, 234, pp. 172-180.e3. Available at: https://doi.org/10.1016/j.jpeds.2021.03.001.

Mathew, P. and Bordoni, B. (2023) 'Embryology, Heart', in *StatPearls*. Treasure Island (FL): StatPearls Publishing. Available at: http://www.ncbi.nlm.nih.gov/books/NBK537313/ (Accessed: 8 December 2023).

McCormick, M.K. *et al.* (1989) 'Molecular genetic approach to the characterization of the "Down syndrome region" of chromosome 21', *Genomics*, 5(2), pp. 325–331. Available at: https://doi.org/10.1016/0888-7543(89)90065-7.

McDonald-McGinn, D.M. *et al.* (2015) '22q11.2 deletion syndrome', *Nature Reviews Disease Primers*, 1(1), pp. 1–19. Available at: https://doi.org/10.1038/nrdp.2015.71.

McVicker, R.W., Shanks, O.E. and McClelland, R.J. (1994) 'Prevalence and associated features of epilepsy in adults with Down's syndrome', *The British Journal of Psychiatry: The Journal of Mental Science*, 164(4), pp. 528–532. Available at: https://doi.org/10.1192/bjp.164.4.528.

Meilhac, S.M. *et al.* (2004) 'Oriented clonal cell growth in the developing mouse myocardium underlies cardiac morphogenesis', *Journal of Cell Biology*, 164(1), pp. 97–109. Available at: https://doi.org/10.1083/jcb.200309160.

Meng, E.C. *et al.* (2023) 'UCSF ChimeraX: Tools for structure building and analysis', *Protein Science*, 32(11), p. e4792. Available at: https://doi.org/10.1002/pro.4792.

Michos, O. *et al.* (2004) ‘Gremlin-mediated BMP antagonism induces the epithelial-mesenchymal feedback signaling controlling metanephric kidney and limb organogenesis’, *Development (Cambridge, England)*, 131(14), pp. 3401–3410. Available at: https://doi.org/10.1242/dev.01251.

Miyake, T., Cameron, A.M. and Hall, B.K. (1996) ‘Detailed staging of inbred C57BL/6 mice between Theiler’s [1972] stages 18 and 21 (11-13 days of gestation) based on craniofacial development’, *Journal of Craniofacial Genetics and Developmental Biology*, 16(1), pp. 1–31.

Miyake, T., Cameron, A.M. and Hall, B.K. (1997) ‘Variability of embryonic development among three inbred strains of mice’, *Growth, development, and aging*, 61(3–4), pp. 141–155.

Miyamoto, M. and Kwon, C. (2022) ‘Uncovering the origins and lineage markers of human heart fields’, *Cell stem cell*, 29(9), pp. 1285–1287. Available at: https://doi.org/10.1016/j.stem.2022.08.004.

Mogra, R., Zidere, V. and Allan, L.D. (2011) ‘Prenatally detectable congenital heart defects in fetuses with Down syndrome’, *Ultrasound in Obstetrics & Gynecology: The Official Journal of the International Society of Ultrasound in Obstetrics and Gynecology*, 38(3), pp. 320–324. Available at: https://doi.org/10.1002/uog.8977.

Mohun, T.J. and Anderson, R.H. (2020) ‘3D Anatomy of the Developing Heart: Understanding Ventricular Septation’, *Cold Spring Harbor Perspectives in Biology*, p. a037465. Available at: https://doi.org/10.1101/cshperspect.a037465.

Mohun, T.J. and Weninger, W.J. (2011) ‘Imaging heart development using high-resolution episcopic microscopy’, *Current Opinion in Genetics & Development*, 21(5), pp. 573–578. Available at: https://doi.org/10.1016/j.gde.2011.07.004.

Mollo, N. *et al.* (2022) ‘Overexpression of the Hsa21 Transcription Factor RUNX1 Modulates the Extracellular Matrix in Trisomy 21 Cells’, *Frontiers in Genetics*, 13, p. 824922. Available at: https://doi.org/10.3389/fgene.2022.824922.

Moore, C.S. (2006) ‘Postnatal lethality and cardiac anomalies in the Ts65Dn Down Syndrome mouse model’, *Mammalian Genome*, 17(10), pp. 1005–1012. Available at: https://doi.org/10.1007/s00335-006-0032-8.

Moorman, A. *et al.* (2003) ‘DEVELOPMENT OF THE HEART: (1) FORMATION OF THE CARDIAC CHAMBERS AND ARTERIAL TRUNKS’, *Heart*, 89(7), pp. 806–814.

Morrison, M.L. *et al.* (2018) ‘Congenital Heart Disease in Down Syndrome’, in *Advances in Research on Down Syndrome*. IntechOpen. Available at: https://doi.org/10.5772/intechopen.71060.

Mostefa-Kara, M. *et al.* (2015) ‘Anatomy of the ventricular septal defect in outflow tract defects: Similarities and differences’, *The Journal of Thoracic and Cardiovascular Surgery*, 149(3), pp. 682-688.e1. Available at: https://doi.org/10.1016/j.jtcvs.2014.11.087.

Musy, M. *et al.* (2018) 'A quantitative method for staging mouse embryos based on limb morphometry', *Development*, 145(7), p. dev154856. Available at: https://doi.org/10.1242/dev.154856.

Nagaoka, S.I., Hassold, T.J. and Hunt, P.A. (2012) 'Human aneuploidy: mechanisms and new insights into an age-old problem', *Nature Reviews Genetics*, 13(7), pp. 493–504. Available at: https://doi.org/10.1038/nrg3245.

Neeb, Z. *et al.* (2013) 'Cardiac outflow tract anomalies', *Wiley interdisciplinary reviews. Developmental biology*, 2(4), pp. 499–530. Available at: https://doi.org/10.1002/wdev.98.

Nixon, D.W. (2018) 'Down Syndrome, Obesity, Alzheimer's Disease, and Cancer: A Brief Review and Hypothesis', *Brain Sciences*, 8(4), p. 53. Available at: https://doi.org/10.3390/brainsci8040053.

Nomura-Kitabayashi, A. *et al.* (2009) 'Outflow tract cushions perform a critical valve-like function in the early embryonic heart requiring BMPRIA-mediated signaling in cardiac neural crest', *American Journal of Physiology - Heart and Circulatory Physiology*, 297(5), pp. H1617–H1628. Available at: https://doi.org/10.1152/ajpheart.00304.2009.

Norman, M.D.A. *et al.* (2021) 'Measuring the elastic modulus of soft culture surfaces and three-dimensional hydrogels using atomic force microscopy', *Nature Protocols*, 16(5), pp. 2418–2449. Available at: https://doi.org/10.1038/s41596-021-00495-4.

O'Doherty, A. *et al.* (2005) 'Genetics: An aneuploid mouse strain carrying human chromosome 21 with Down syndrome phenotypes', *Science*, 309(5743), pp. 2033–2037. Available at: https://doi.org/10.1126/science.1114535.

O'Donnell, A. and Yutzey, K.E. (2020) 'Mechanisms of heart valve development and disease', *Development*, 147(13), p. dev183020. Available at: https://doi.org/10.1242/dev.183020.

Okishima, T., Ohdo, S. and Hayakawa, K. (1986) 'Pathogenesis of Persistent Truncus Arteriosus Produced by Bis-Diamine in Rats', *Pediatrics International*, 28(3), pp. 403–418. Available at: https://doi.org/10.1111/j.1442-200X.1986.tb00741.x.

Oliver, T.R. *et al.* (2008) 'New Insights into Human Nondisjunction of Chromosome 21 in Oocytes', *PLoS Genetics*, 4(3), p. e1000033. Available at: https://doi.org/10.1371/journal.pgen.1000033.

Olson, L.E. *et al.* (2004) 'A Chromosome 21 Critical Region Does Not Cause Specific Down Syndrome Phenotypes', *Science*, 306(5696), pp. 687–690. Available at: https://doi.org/10.1126/science.1098992.

O'Toole, S. *et al.* (2019) 'Investigation into the validity of WearCompare, a purpose-built software to quantify erosive tooth wear progression', *Dental Materials*, 35(10), pp. 1408–1414. Available at: https://doi.org/10.1016/j.dental.2019.07.023.

Pandey, P. *et al.* (2018) 'Cardiomyocytes Sense Matrix Rigidity through a Combination of Muscle and Non-muscle Myosin Contractions', *Developmental Cell*, 45(5), p. 661. Available at: https://doi.org/10.1016/j.devcel.2018.05.016.

Papageorgiou, M. *et al.* (2020) 'Age- and Strain-Related Differences in Bone Microstructure and Body Composition During Development in Inbred Male Mouse Strains', *Calcified Tissue International*, 106(4), pp. 431–443. Available at: https://doi.org/10.1007/s00223-019-00652-8.

Peña, B. *et al.* (2022) 'Atomic Force Microscopy (AFM) Applications in Arrhythmogenic Cardiomyopathy', *International Journal of Molecular Sciences*, 23(7), p. 3700. Available at: https://doi.org/10.3390/ijms23073700.

Peterson, J.C. *et al.* (2021) 'The Role of Cell Tracing and Fate Mapping Experiments in Cardiac Outflow Tract Development, New Opportunities through Emerging Technologies', *Journal of Cardiovascular Development and Disease*, 8(5), p. 47. Available at: https://doi.org/10.3390/jcdd8050047.

Petridou, N.I. and Heisenberg, C. (2019) 'Tissue rheology in embryonic organization', *The EMBO Journal*, 38(20), p. e102497. Available at: https://doi.org/10.15252/embj.2019102497.

Piotrowski, T. and Nüsslein-Volhard, C. (2000) 'The endoderm plays an important role in patterning the segmented pharyngeal region in zebrafish (Danio rerio)', *Developmental Biology*, 225(2), pp. 339–356. Available at: https://doi.org/10.1006/dbio.2000.9842.

Pond, A.J.R. *et al.* (2021) 'A deep learning approach for staging embryonic tissue isolates with small data', *PLoS ONE*, 16(1), p. e0244151. Available at: https://doi.org/10.1371/journal.pone.0244151.

Pugnaloni, F. *et al.* (2020) 'Genetics of atrioventricular canal defects', *Italian Journal of Pediatrics*, 46, p. 61. Available at: https://doi.org/10.1186/s13052-020-00825-4.

Qiu, H. *et al.* (2010) 'Short Communication: Vascular Smooth Muscle Cell Stiffness As a Mechanism for Increased Aortic Stiffness With Aging', *Circulation Research*, 107(5), pp. 615–619. Available at: https://doi.org/10.1161/CIRCRESAHA.110.221846.

Redhead, Y. *et al.* (2023) 'Craniofacial dysmorphology in Down syndrome is caused by increased dosage of Dyrk1a and at least three other genes', *Development*, 150(8), p. dev201077. Available at: https://doi.org/10.1242/dev.201077.

Ren, H. *et al.* (2022) 'High-Resolution 3D Heart Models of Cardiomyocyte Subpopulations in Cleared Murine Heart', *Frontiers in Physiology*, 13. Available at: https://www.frontiersin.org/articles/10.3389/fphys.2022.779514 (Accessed: 17 December 2023).

Risebro, C.A. and Riley, P.R. (2006) 'Formation of the Ventricles', *The Scientific World Journal*, 6, pp. 1862–1880. Available at: https://doi.org/10.1100/tsw.2006.316.

Robinson, S.W. *et al.* (2003) 'Missense mutations in CRELD1 are associated with cardiac atrioventricular septal defects', *American Journal of Human Genetics*, 72(4), pp. 1047–1052. Available at: https://doi.org/10.1086/374319.

Rolfe, S.M., Whikehart, S.M. and Maga, A.M. (2023) 'Deep learning enabled multi-organ segmentation of mouse embryos', *Biology Open*, 12(2), p. bio059698. Available at: https://doi.org/10.1242/bio.059698.

Roper, R.J. *et al.* (2009) 'A neural crest deficit in Down syndrome mice is associated with deficient mitotic response to Sonic hedgehog', *Mechanisms of development*, 126(3–4), p. 212. Available at: https://doi.org/10.1016/J.MOD.2008.11.002.

Sader, J.E., Chon, J.W.M. and Mulvaney, P. (1999) 'Calibration of rectangular atomic force microscope cantilevers', *Review of Scientific Instruments*, 70(10), pp. 3967–3969. Available at: https://doi.org/10.1063/1.1150021.

Sago, H. *et al.* (1998) 'Ts1Cje, a partial trisomy 16 mouse model for Down syndrome, exhibits learning and behavioral abnormalities', *Proceedings of the National Academy of Sciences of the United States of America*, 95(11), pp. 6256–6261. Available at: https://doi.org/10.1073/pnas.95.11.6256.

Sait, S., Alamoudi, S. and Zawawi, F. (2022) 'Management outcomes of otitis media with effusion in children with down syndrome: A systematic review', *International Journal of Pediatric Otorhinolaryngology*, 156, p. 111092. Available at: https://doi.org/10.1016/j.ijporl.2022.111092.

Samsa, L.A., Yang, B. and Liu, J. (2013) 'Embryonic Cardiac Chamber Maturation: Trabeculation, Conduction and Cardiomyocyte Proliferation', *American journal of medical genetics. Part C, Seminars in medical genetics*, 163(3), pp. 157–168. Available at: https://doi.org/10.1002/ajmg.c.31366.

Sandu, A.-L. *et al.* (2008) 'Fractal dimension analysis of MR images reveals grey matter structure irregularities in schizophrenia', *Computerized Medical Imaging and Graphics: The Official Journal of the Computerized Medical Imaging Society*, 32(2), pp. 150–158. Available at: https://doi.org/10.1016/j.compmedimag.2007.10.005.

Sarno, L.A. *et al.* (2020) 'Significant Improvements in Mortality After the Fontan Operation in Children With Down Syndrome', *The Annals of Thoracic Surgery*, 109(3), pp. 835–841. Available at: https://doi.org/10.1016/j.athoracsur.2019.07.085.

Savolainen, SaijaM., Foley, J.F. and Elmore, S.A. (2009) 'Histology Atlas of the Developing Mouse Heart', *Toxicologic Pathology*, 37(4), pp. 395–414. Available at: https://doi.org/10.1177/0192623309335060.Histology.

Savolainen, S.M., Foley, J.F. and Elmore, S.A. (2009) ‘Histology Atlas of the Developing Mouse Heart with Emphasis on E11.5 to E18.5’, *Toxicologic pathology*, 37(4), pp. 395–414. Available at: https://doi.org/10.1177/0192623309335060.

Schmidt, U. *et al.* (2018) ‘Cell Detection with Star-Convex Polygons’, in A.F. Frangi et al. (eds) *Medical Image Computing and Computer Assisted Intervention – MICCAI 2018*. Cham: Springer International Publishing (Lecture Notes in Computer Science), pp. 265–273. Available at: https://doi.org/10.1007/978-3-030-00934-2_30.

Schölkopf, B., Smola, A. and Müller, K.-R. (1997) ‘Kernel principal component analysis’, in W. Gerstner et al. (eds) *Artificial Neural Networks — ICANN’97*. Berlin, Heidelberg: Springer (Lecture Notes in Computer Science), pp. 583–588. Available at: https://doi.org/10.1007/BFb0020217.

Scholl, A.M. and Kirby, M.L. (2009) ‘Signals controlling neural crest contributions to the heart’, *Wiley interdisciplinary reviews. Systems biology and medicine*, 1(2), pp. 220–227.

Scott, K.E., Fraley, S.I. and Rangamani, P. (2021) ‘A spatial model of YAP/TAZ signaling reveals how stiffness, dimensionality, and shape contribute to emergent outcomes’, *Proceedings of the National Academy of Sciences*, 118(20), p. e2021571118. Available at: https://doi.org/10.1073/pnas.2021571118.

Sewell-Loftin, M.K. *et al.* (2014) ‘Myocardial contraction and hyaluronic acid mechanotransduction in epithelial-to-mesenchymal transformation of endocardial cells’, *Biomaterials*, 35(9), pp. 2809–2815. Available at: https://doi.org/10.1016/j.biomaterials.2013.12.051.

Shan, H. *et al.* (2023) ‘Persistent fifth aortic arch: a comprehensive literature review’, *Frontiers in Pediatrics*, 11. Available at: https://doi.org/10.3389/fped.2023.1183345.

Sharma, P.R. *et al.* (2004) ‘Spatiotemporal analysis of programmed cell death during mouse cardiac septation’, *The Anatomical Record Part A: Discoveries in Molecular, Cellular, and Evolutionary Biology*, 277A(2), pp. 355–369. Available at: https://doi.org/10.1002/ar.a.20006.

Shen, Y., Schmidt, T. and Diz-Muñoz, A. (2020) ‘Protocol on Tissue Preparation and Measurement of Tumor Stiffness in Primary and Metastatic Colorectal Cancer Samples with an Atomic Force Microscope’, *STAR Protocols*, 1(3), p. 100167. Available at: https://doi.org/10.1016/j.xpro.2020.100167.

Shinohara, T. *et al.* (2001) ‘Mice containing a human chromosome 21 model behavioral impairment and cardiac anomalies of Down’s syndrome’, *Human Molecular Genetics*, 10(11), pp. 1163–1175. Available at: https://doi.org/10.1093/hmg/10.11.1163.

Silva, A.C. *et al.* (2021) ‘Bearing My Heart: The Role of Extracellular Matrix on Cardiac Development, Homeostasis, and Injury Response’, *Frontiers in Cell and Developmental Biology*, 8. Available at:

https://www.frontiersin.org/articles/10.3389/fcell.2020.621644 (Accessed: 8 December 2023).

Simon, C. *et al.* (2012) 'Sox10-iCreERT2 : a mouse line to inducibly trace the neural crest and oligodendrocyte lineage', *Genesis (New York, N.Y.: 2000)*, 50(6), pp. 506–515. Available at: https://doi.org/10.1002/dvg.22003.

Snarr, B.S., Kern, C.B. and Wessels, A. (2008) 'Origin and fate of cardiac mesenchyme', *Developmental Dynamics*, 237(10), pp. 2804–2819. Available at: https://doi.org/10.1002/dvdy.21725.

Snider, P. and Conway, S.J. (2011) 'Probing Human Cardiovascular Congenital Disease Using Transgenic Mouse Models', *Progress in molecular biology and translational science*, 100, p. 10.1016/B978-0-12-384878-9.00003–0. Available at: https://doi.org/10.1016/B978-0-12-384878-9.00003-0.

Stadtfeld, M., Ye, M. and Graf, T. (2007) 'Identification of interventricular septum precursor cells in the mouse embryo', *Developmental Biology*, 302(1), pp. 195–207. Available at: https://doi.org/10.1016/j.ydbio.2006.09.025.

Stefanovic, S., Etchevers, H.C. and Zaffran, S. (2021) 'Outflow Tract Formation—Embryonic Origins of Conotruncal Congenital Heart Disease', *Journal of Cardiovascular Development and Disease*, 8(4), p. 42. Available at: https://doi.org/10.3390/jcdd8040042.

Stoll, C. *et al.* (2015) 'Associated congenital anomalies among cases with Down syndrome', *European Journal of Medical Genetics*, 58(12), pp. 674–680. Available at: https://doi.org/10.1016/j.ejmg.2015.11.003.

Su, Z. *et al.* (2022) 'Global, regional, and national time trends in mortality for congenital heart disease, 1990-2019: An age-period-cohort analysis for the Global Burden of Disease 2019 study', *EClinicalMedicine*, 43, p. 101249. Available at: https://doi.org/10.1016/j.eclinm.2021.101249.

Sugi, Y. *et al.* (2003) 'Fibroblast growth factor (FGF)-4 can induce proliferation of cardiac cushion mesenchymal cells during early valve leaflet formation', *Developmental Biology*, 258(2), pp. 252–263. Available at: https://doi.org/10.1016/s0012-1606(03)00099-x.

Takeuchi, J.K. *et al.* (2003) 'Tbx5 specifies the left/right ventricles and ventricular septum position during cardiogenesis', *Development (Cambridge, England)*, 130(24), pp. 5953–5964. Available at: https://doi.org/10.1242/dev.00797.

Tan, H. *et al.* (2013) 'Fluid flow forces and rhoA regulate fibrous development of the atrioventricular valves', *Developmental Biology*, 374(2), pp. 345–356. Available at: https://doi.org/10.1016/j.ydbio.2012.11.023.

Tang, W. *et al.* (2019) 'Cardiac neural crest contributes to cardiomyocytes in amniotes and heart regeneration in zebrafish', *eLife*, 8, pp. 1–16. Available at: https://doi.org/10.7554/elife.47929.

Theiler, K. (1972) ‘The house mouse. Development and normal stages from fertilization to 4 weeks of age.’, *The house mouse. Development and normal stages from fertilization to 4 weeks of age.* [Preprint]. Available at: https://www.cabdirect.org/cabdirect/abstract/19730104208 (Accessed: 15 December 2023).

Thiel, R. *et al.* (1993) ‘Time-dependent differences in the development of somites of four different mouse strains’, *Teratogenesis, Carcinogenesis, and Mutagenesis*, 13(6), pp. 247–257. Available at: https://doi.org/10.1002/tcm.1770130602.

Thom, T. *et al.* (2006) ‘Heart disease and stroke statistics--2006 update: a report from the American Heart Association Statistics Committee and Stroke Statistics Subcommittee’, *Circulation*, 113(6), pp. e85-151. Available at: https://doi.org/10.1161/CIRCULATIONAHA.105.171600.

Timin, G. and Milinkovitch, M.C. (2023) ‘High-resolution confocal and light-sheet imaging of collagen 3D network architecture in very large samples’, *iScience*, 26(4). Available at: https://doi.org/10.1016/j.isci.2023.106452.

Toussaint, N. *et al.* (2019) ‘Application of high-resolution landmark-free morphometrics to a mouse model of Down Syndrome reveals a tightly localised cranial phenotype’, *bioRxiv*, p. 711259. Available at: https://doi.org/10.1101/711259.

Toussaint, N. *et al.* (2021) ‘A landmark-free morphometrics pipeline for high-resolution phenotyping: application to a mouse model of Down syndrome’, *Development*, 148(18), p. dev188631. Available at: https://doi.org/10.1242/dev.188631.

Tuckett, F. and Morriss-Kay, G. (1988) ‘Alcian blue staining of glycosaminoglycans in embryonic material: effect of different fixatives’, *The Histochemical Journal*, 20(3), pp. 174–182. Available at: https://doi.org/10.1007/BF01746681.

Tyser, R.C.V. *et al.* (2021) ‘Characterization of a common progenitor pool of the epicardium and myocardium’, *Science*, 371(6533), p. eabb2986. Available at: https://doi.org/10.1126/science.abb2986.

Tyser, R.C.V. (2023) ‘Formation of the Heart: Defining Cardiomyocyte Progenitors at Single-Cell Resolution’, *Current Cardiology Reports*, 25(6), pp. 495–503. Available at: https://doi.org/10.1007/s11886-023-01880-z.

Verma, A. *et al.* (2023) ‘Management of Down Syndrome–Associated Leukemias: A Review’, *JAMA Oncology*, 9(9), pp. 1283–1290. Available at: https://doi.org/10.1001/jamaoncol.2023.2163.

Verzi, M.P. *et al.* (2005) ‘The right ventricle, outflow tract, and ventricular septum comprise a restricted expression domain within the secondary/anterior heart field’, *Developmental Biology*, 287(1), pp. 134–145. Available at: https://doi.org/10.1016/j.ydbio.2005.08.041.

Vraneković, J. *et al.* (2012) 'Down Syndrome: Parental Origin, Recombination, and Maternal Age', *Genetic Testing and Molecular Biomarkers*, 16(1), pp. 70–73. Available at: https://doi.org/10.1089/gtmb.2011.0066.

Waldo, K. *et al.* (1998) 'Cardiac Neural Crest Cells Provide New Insight into Septation of the Cardiac Outflow Tract: Aortic Sac to Ventricular Septal Closure', *Developmental Biology*, 196(2), pp. 129–144. Available at: https://doi.org/10.1006/DBIO.1998.8860.

Waldo, K.L. *et al.* (2005) 'Secondary heart field contributes myocardium and smooth muscle to the arterial pole of the developing heart', *Developmental Biology*, 281(1), pp. 78–90. Available at: https://doi.org/10.1016/j.ydbio.2005.02.012.

Waller III, B. r. *et al.* (2000) 'Conotruncal anomalies in the trisomy 16 mouse: An immunohistochemical analysis with emphasis on the involvement of the neural crest', *The Anatomical Record*, 260(3), pp. 279–293. Available at: https://doi.org/10.1002/1097-0185(20001101)260:3<279::AID-AR65>3.0.CO;2-2.

Wang, J., Greene, S.B. and Martin, J.F. (2011) 'Bmp Signaling in Congenital Heart Disease: New Developments and Future Directions', *Birth defects research. Part A, Clinical and molecular teratology*, 91(6), pp. 441–448. Available at: https://doi.org/10.1002/bdra.20785.

Wang, M. *et al.* (2023) 'Shear and hydrostatic stress regulate fetal heart valve remodeling through YAP-mediated mechanotransduction', *eLife*. Edited by K. Yutzey, D.Y. Stainier, and J. Vermot, 12, p. e83209. Available at: https://doi.org/10.7554/eLife.83209.

Ward, C. *et al.* (2005) 'Ablation of the secondary heart field leads to tetralogy of Fallot and pulmonary atresia', *Developmental Biology*, 284(1), pp. 72–83. Available at: https://doi.org/10.1016/j.ydbio.2005.05.003.

Webb, S., Brown, N.A. and Anderson, R.H. (1996) 'The structure of the mouse heart in late fetal stages', *Anatomy and Embryology*, 194(1), pp. 37–47. Available at: https://doi.org/10.1007/BF00196313.

Webb, S., Brown, N.A. and Anderson, R.H. (1998) 'Formation of the Atrioventricular Septal Structures in the Normal Mouse', *Circulation Research*, 82(6), pp. 645–656. Available at: https://doi.org/10.1161/01.RES.82.6.645.

Wei, L. *et al.* (2001) 'Rho kinases play an obligatory role in vertebrate embryonic organogenesis', *Development (Cambridge, England)*, 128(15), pp. 2953–2962. Available at: https://doi.org/10.1242/dev.128.15.2953.

Weigert, M. *et al.* (2020) 'Star-convex Polyhedra for 3D Object Detection and Segmentation in Microscopy', in. *2020 IEEE Winter Conference on Applications of Computer Vision (WACV)*, IEEE Computer Society, pp. 3655–3662. Available at: https://doi.org/10.1109/WACV45572.2020.9093435.

Weijerman, M.E. and de Winter, J.P. (2010) 'Clinical practice', *European Journal of Pediatrics*, 169(12), pp. 1445–1452. Available at: https://doi.org/10.1007/s00431-010-1253-0.

Weninger, W.J. *et al.* (2006) 'High-resolution episcopic microscopy: a rapid technique for high detailed 3D analysis of gene activity in the context of tissue architecture and morphology', *Anatomy and Embryology*, 211(3), pp. 213–221. Available at: https://doi.org/10.1007/s00429-005-0073-x.

Weninger, W.J. *et al.* (2014) 'Phenotyping structural abnormalities in mouse embryos using high-resolution episcopic microscopy', *Disease Models & Mechanisms*, 7(10), pp. 1143–1152. Available at: https://doi.org/10.1242/DMM.016337.

Wessels, A. and Sedmera, D. (2003) 'Developmental anatomy of the heart: a tale of mice and man', *Physiological Genomics*, 15(3), pp. 165–176. Available at: https://doi.org/10.1152/physiolgenomics.00033.2003.

Wiegering, A., Rüther, U. and Gerhardt, C. (2017) 'The role of Hedgehog signalling in the formation of the ventricular septum', *Journal of Developmental Biology*, 5(4). Available at: https://doi.org/10.3390/jdb5040017.

Winston, J.B. *et al.* (2012) 'Complex Trait Analysis of Ventricular Septal Defects Caused by Nkx2-5 Mutation', *Circulation. Cardiovascular genetics*, 5(3), pp. 293–300. Available at: https://doi.org/10.1161/CIRCGENETICS.111.961136.

Wong, M.D. *et al.* (2015) '4D Atlas of the Mouse Embryo for Precise Morphological Staging', *Development (Cambridge)*, 142(20), pp. 3583–3591. Available at: https://doi.org/10.1242/dev.125872.

Wu, B. *et al.* (2011) 'Nfatc1 Coordinates Valve Endocardial Cell Lineage Development Required for Heart Valve Formation', *Circulation Research*, 109(2), pp. 183–192. Available at: https://doi.org/10.1161/CIRCRESAHA.111.245035.

Xin, M. *et al.* (2011) 'Regulation of Insulin-Like Growth Factor Signaling by Yap Governs Cardiomyocyte Proliferation and Embryonic Heart Size', *Science signaling*, 4(196), p. ra70. Available at: https://doi.org/10.1126/scisignal.2002278.

Xu, H. *et al.* (2004) 'Tbx1 has a dual role in the morphogenesis of the cardiac outflow tract', *Development (Cambridge, England)*, 131(13), pp. 3217–3227. Available at: https://doi.org/10.1242/dev.01174.

Ya, J. *et al.* (1998) 'Normal Development of the Outflow Tract in the Rat', *Circulation Research*, 82(4), pp. 464–472. Available at: https://doi.org/10.1161/01.RES.82.4.464.

Yamagishi, H. (2021) 'Cardiac Neural Crest', *Cold Spring Harbor Perspectives in Biology*, 13(1). Available at: https://doi.org/10.1101/cshperspect.a036715.

You, A.Y.F. *et al.* (2017) 'Raman spectroscopy imaging reveals interplay between atherosclerosis and medial calcification in the human aorta', *Science Advances*, 3(12), p. e1701156. Available at: https://doi.org/10.1126/sciadv.1701156.

Yu, Z. *et al.* (2022) 'Long-term trends in the incidence of congenital anomalies in Central China from 1997 to 2019', *Public Health*, 203, pp. 47–52. Available at: https://doi.org/10.1016/j.puhe.2021.12.007.

Zaman, S. and Fortea, J. (2022) 'The crucial history of Down syndrome', *The Lancet Neurology*, 21(3), p. 222. Available at: https://doi.org/10.1016/S1474-4422(22)00047-3.

Zhang, H. *et al.* (2014a) 'Yap1 Is Required for Endothelial to Mesenchymal Transition of the Atrioventricular Cushion*', *Journal of Biological Chemistry*, 289(27), pp. 18681–18692. Available at: https://doi.org/10.1074/jbc.M114.554584.

Zhang, H. *et al.* (2014b) 'Yap1 Is Required for Endothelial to Mesenchymal Transition of the Atrioventricular Cushion', *The Journal of Biological Chemistry*, 289(27), pp. 18681–18692. Available at: https://doi.org/10.1074/jbc.M114.554584.

Zhang, M. *et al.* (2018) 'TBX1 loss-of-function mutation contributes to congenital conotruncal defects', *Experimental and Therapeutic Medicine*, 15(1), pp. 447–453. Available at: https://doi.org/10.3892/etm.2017.5362.

Zhang, T. *et al.* (2023) 'Fractal analysis: Left ventricular trabecular complexity cardiac MRI adds independent risks for heart failure with preserved ejection fraction in participants with end-stage renal disease', *International Journal of Cardiology*, 391. Available at: https://doi.org/10.1016/j.ijcard.2023.131334.

Zhang, Z., Huynh, T. and Baldini, A. (2006) 'Mesodermal expression of Tbx1 is necessary and sufficient for pharyngeal arch and cardiac outflow tract development', *Development (Cambridge, England)*, 133(18), pp. 3587–3595. Available at: https://doi.org/10.1242/dev.02539.

Zheng, Y. and Pan, D. (2019) 'The Hippo Signaling Pathway in Development and Disease', *Developmental cell*, 50(3), pp. 264–282. Available at: https://doi.org/10.1016/j.devcel.2019.06.003.

Zhou, L. *et al.* (2017) 'Gata4 potentiates second heart field proliferation and Hedgehog signaling for cardiac septation', *Proceedings of the National Academy of Sciences of the United States of America*, 114(8), pp. E1422–E1431. Available at: https://doi.org/10.1073/pnas.1605137114.